

**ANALYSIS TOOLS FOR THE DESIGN OF
ACTIVE STRUCTURAL ACOUSTIC
CONTROL SYSTEMS**

Marco Oude Nijhuis

De promotiecommissie is als volgt samengesteld:

Voorzitter en secretaris:

Prof.dr.ir. H.J. Grootenboer Universiteit Twente

Promotor:

Prof.dr.ir. A. de Boer Universiteit Twente

Leden:

Prof.dr.ir. J.B. Jonker Universiteit Twente

Prof.dr. A.J. van der Schaft Universiteit Twente

Prof.dr. H. Nijmeijer Technische Universiteit Eindhoven

Prof.dr.ir. F. van Keulen Technische Universiteit Delft

Dr.ir. A.P. Berkhoff Universiteit Twente/TNO-TPD

Analysis Tools for the Design of Active Structural Acoustic Control Systems
Oude Nijhuis, Marco Hendrikus Hermanus
PhD thesis, University of Twente, Enschede, The Netherlands
November 2003

ISBN 90-365-1983-7

Subject headings: active structural acoustic control, piezoelectric actuators
and sensors, numerical modelling

Copyright ©2003 by M.H.H. Oude Nijhuis, Enschede, The Netherlands
Printed by Ponsen & Looijen bv., Wageningen, The Netherlands

**ANALYSIS TOOLS FOR THE DESIGN OF
ACTIVE STRUCTURAL ACOUSTIC
CONTROL SYSTEMS**

PROEFSCHRIFT

ter verkrijging van
de graad van doctor aan de Universiteit Twente,
op gezag van de rector magnificus,
prof.dr. F.A. van Vught,
volgens besluit van het College voor Promoties
in het openbaar te verdedigen
op woensdag 5 november 2003 om 13.15 uur

door

Marco Hendrikus Hermanus Oude Nijhuis

geboren op 29 mei 1975

te Oldenzaal

Dit proefschrift is goedgekeurd door de promotor

Prof.dr.ir. A. de Boer

Summary

Acoustic noise is an important problem in the modern society and provides much of the impetus for the development of noise reduction techniques. Passive methods, such as the use of sound absorbing materials, provide an adequate solution to many noise problems, but for noise reduction at low frequencies (below 1000 Hz) they often lead to an unacceptable increase in mass and volume. Active control methods are better suited for low frequency noise problems. This thesis deals with an active control method for reducing the noise produced by vibrating structures, which is referred to as active structural acoustic control (ASAC). In ASAC, the minimisation of the sound radiation is achieved by modifying the vibration using actuators directly attached to the structure. In this research, emphasis is on the use of piezoelectric patches as control actuators. The key benefits of using piezoelectric patches instead of other actuator principles are their low weight and volume, low cost, and furthermore the possibility of integration into the structure. The goal of this research is to develop and validate efficient analysis tools for ASAC, and to apply them for the design of active control systems. In contrast to work that was presented in the literature, in this thesis a wide range of analysis tools are combined, resulting in an analysis environment for the design of ASAC systems.

As a first step, the dynamical behaviour of a structure with surface bonded piezoelectric patches is studied with an analytical beam model. This analytical model proved very useful for studying the fundamental issues of ASAC, but is not suitable for realistic structures with complex geometries. Therefore, numerical techniques are applied to model the structural vibration and sound radiation of arbitrary structures with piezoelectric patches. The structural and acoustic responses are determined with an uncoupled analysis. The dynamical behaviour of the structure including piezoelectric patches is modelled with the finite element method. A model reduction technique is applied to obtain a model which can be evaluated with low computational effort. The free field sound radiation associated with the structural vibration is modelled with

the Rayleigh integral method. Both the structural and acoustic models were successfully validated with experiments performed on a clamped plate setup with surface bonded piezoelectric patches.

The analysis tool was applied to investigate the effect of two control strategies. First, the feedforward control of harmonic disturbances was demonstrated for a control system consisting of piezoelectric patches as actuators, and accelerometers or microphones as error sensors. Second, the concept of multiple independent feedback loops, each consisting of a piezoelectric actuator patch, an accelerometer and a direct velocity feedback loop, was applied to reduce the sound radiation of a lightly damped structure in a broad frequency range. The numerical and experimental results show that significant reductions in sound power can be obtained with both strategies. Furthermore, the predicted control performances, in terms of sound power, are in good agreement with the experimental results.

Finally, a strategy is proposed for the optimisation of ASAC systems, which is based on the numerical model. A genetic algorithm is applied as the optimisation routine because it is suited for solving optimisation problems with multiple optima. The optimisation strategy was successfully applied for the optimal placement of independent direct velocity feedback controllers. It was found that a setup with optimally located controllers gives a better control performance than a setup with arbitrarily located controllers. Furthermore, there is a good agreement between the predicted and measured sound powers for the optimised setup.

Samenvatting

Geluidsoverlast is een belangrijk probleem in de hedendaagse maatschappij en vormt een belangrijke impuls tot de ontwikkeling van geluidsreductie-technieken. Passieve methoden, zoals het gebruik van geluidsabsorberende materialen, zijn in veel gevallen een adequate oplossing, maar leiden vaak tot een onacceptabele toename in gewicht en volume voor laagfrequente geluidsproblemen. Actieve regeltechnieken zijn beter geschikt voor laagfrequente geluidsproblemen. Dit proefschrift behandelt een actieve regeltechniek om het geluid dat door trillende constructies geproduceerd wordt te reduceren, namelijk active structural acoustic control (ASAC). Het minimaliseren van geluid wordt met ASAC bereikt door een verandering van de trillingen met actuatoren die met de structuur geïntegreerd zijn. In dit onderzoek ligt de nadruk op het gebruik van piezoelektrische patches als actuatoren. De belangrijkste voordelen van het gebruik van piezoelektrische actuatoren in plaats van andere actuatorprincipes zijn het lage gewicht en volume, de lage kosten en de mogelijkheid tot integratie met de structuur. Het doel van dit onderzoek is om efficiënte analysegereedschappen voor ASAC te ontwikkelen en valideren, en om deze toe te passen voor het ontwerpen van actieve regelsystemen. In tegenstelling tot het werk dat gepresenteerd is in de literatuur, wordt in dit proefschrift een breed scala van analysegereedschappen gecombineerd, hetgeen resulteert in een analyse-omgeving voor het ontwerp van ASAC systemen.

In eerste instantie wordt het dynamisch gedrag van een structuur met aan het oppervlak bevestigde piezoelektrische patches bestudeerd met een analytisch balkmodel. Dit analytisch model bleek erg nuttig te zijn om de fundamentele problemen van ASAC te bestuderen, maar is niet geschikt voor realistische constructies met complexe geometrieën. Daarom zijn numerieke technieken gebruikt om de trillingen en de geluidsafstraling van willekeurige constructies met piezoelektrische patches te modelleren. De structurele en akoestische responsie worden bepaald door middel van een ongekoppelde analyse. Het dynamisch gedrag van de constructie met piezoelektrische patches wordt gemodelleerd met de eindige elementen methode. Een reductiemethode is

toegepast om een model te verkrijgen dat met weinig rekenkracht geëvalueerd kan worden. De geluidsafstraling naar het vrije veld van de trillende constructie wordt gemodelleerd met de Rayleigh integraalmethode. Zowel het structurele als akoestische model is met succes gevalideerd met experimenten die uitgevoerd zijn aan een ingeklemde plaat met aan het oppervlak bevestigde piëzoelektrische patches.

Het analysegereedschap is toegepast om het effect van twee regelstrategieën te onderzoeken. Ten eerste is het feedforward regelen van harmonische verstoringen gedemonstreerd voor een regelsysteem bestaande uit piëzoelektrische patches als actuatoren, en versnellingsopnemers of microfoons als sensoren. Ten tweede is het concept van meerdere onafhankelijke feedback regelaars, elk bestaande uit een piëzoelektrische actuator patch, een versnellingsopnemer en een directe snelheidsterugkoppeling, toegepast om de geluidsafstraling van een lichtgedempte constructie te verminderen in een breed frequentiegebied. De numerieke en experimentele resultaten laten zien dat met beide strategieën het afgestraalde geluidsvermogen aanzienlijk gereduceerd kan worden. Tevens zijn de voorspelde reducties van het geluidsvermogen in goede overeenstemming met de experimentele resultaten.

Tenslotte is een strategie voor de optimalisatie van ASAC systemen voorgesteld, die gebaseerd is op het numerieke model. Een genetisch algoritme wordt toegepast als optimalisatieroutine, omdat het geschikt is voor het oplossen van optimalisatieproblemen met meerdere optima. De optimalisatiestrategie is met succes toegepast voor de optimale plaatsing van onafhankelijke regelaars met directe snelheidsterugkoppeling. Een configuratie met optimaal geplaatste regelaars geeft een betere regelprestatie dan een configuratie met willekeurig geplaatste regelaars. Voor de geoptimaliseerde configuratie komen het voorspelde en gemeten geluidsvermogen goed overeen.

Contents

Summary	v
Samenvatting	vii
Contents	ix
1 Introduction	1
1.1 Background	1
1.2 Sound, vibration, reduction	1
1.3 Active control of sound and vibration	2
1.4 Smart structures	4
1.5 Active structural acoustic control	5
1.6 Problem definition	8
1.7 Outline of the thesis	8
2 Piezoelectric Materials	11
2.1 Introduction	11
2.2 Piezoelectric actuators and sensors	12
2.3 Piezoceramics	18
2.4 Basic equations	20
2.5 Piezoelectric coupling	25
2.6 Concluding remarks	28
3 Analytical Study of Active Structural Acoustic Control	31
3.1 Introduction	31
3.2 Literature survey	32
3.3 Beam model	35
3.4 Modal behaviour	45
3.5 Active structural acoustic control	48
3.6 Concluding remarks	55

4	Numerical Modelling and Experimental Validation	57
4.1	Introduction	57
4.2	Structural model	59
4.3	Acoustic model	71
4.4	Experimental validation	82
4.5	Concluding remarks	98
5	Feedforward Control	99
5.1	Introduction	99
5.2	Optimal control	101
5.3	Error criteria	103
5.4	Experiments	113
5.5	Concluding remarks	122
6	Feedback Control	125
6.1	Introduction	125
6.2	Collocated feedback control	126
6.3	Collocated control with piezoelectric patches	133
6.4	Decentralised velocity feedback control	138
6.5	Experiments	144
6.6	Concluding remarks	150
7	Optimisation	151
7.1	Introduction	151
7.2	General approach	152
7.3	Genetic algorithms	158
7.4	Optimal placement of patch/accelerometer pairs	160
7.5	Test case	167
7.6	Concluding remarks	172
8	Conclusions and Recommendations	173
8.1	Conclusions	173
8.2	Recommendations	174
	List of Symbols	177
A	Additional Information on Piezoelectricity	183
A.1	Alternative constitutive equations	183
A.2	PIC-151 material properties	184
A.3	Thermopiezoelectricity	185

B	Additional Information on Beam Models	187
B.1	Derivation of the dynamic stiffness matrix	187
B.2	Uniform electric field assumption	192
B.3	Model for the coupled longitudinal and transverse vibrations	193
C	A Plate with Surface Bonded Patches	199
C.1	Analytical model	199
C.2	Numerical model: ANSYS implementation	204
C.3	Comparison	206
D	Radiation Filters	209
D.1	Derivation of the radiation filters	209
D.2	Structural-acoustic model	212
D.3	Test case	213
E	Adaptive Notch Filter	215
F	Description of the Genetic Algorithm	219
F.1	Genetic algorithm	219
F.2	Handling constraints	224
	Bibliography	225
	Nawoord	235

Chapter 1

Introduction

1.1 Background

In the field of acoustics *noise* is generally defined as an unpleasant or disliked sound. This definition is straightforward, but the difference between sound and noise is by no means precise. For example, in the opinion of some (older) people, the sound of modern music is the equivalent of noise. On the other hand, there are few who would say that the sound produced by passing traffic or a vacuum cleaner is pleasant.

Noise problems have been around for a long time, but the development of noise reduction technology is increasingly stimulated for several reasons. One reason is the realisation that long-term exposure to high sound levels leads to hearing damage or even hearing loss. Furthermore, because of the tendency towards lightweight design, noise problems arise more often. In addition, sound is nowadays an important quality issue for consumer products and is even used as a marketing tool.

There are various methods for tackling noise problems. In the present work, a relatively new method is considered, which is based on the application of active control techniques. Emphasis is on the development of analysis tools, the validation of these tools, and their application for designing control systems for noise reduction.

1.2 Sound, vibration, reduction

Noise problems are often the result of structural vibration. The vibrations of a structure (e.g. car body or aircraft fuselage) due to some excitation source (e.g. engine) are transmitted to the medium surrounding the structure, in

most cases air, and cause pressure disturbances which are experienced as noise. This exchange of vibrational and acoustic energy is referred to as *acousto-elastic interaction*. Acousto-elastic interaction is described by time and space dependent disturbances, which propagate through the two media as waves, and are characterised by the wave propagation speed, frequency, wavelength and amplitude. The human ear is able to detect sound in the frequency range between 20 Hz and 20 kHz.

Integration of noise and vibration issues in the design of consumer products, cars, machines, etc. can certainly improve the sound quality of such products, but it will not prevent noise problems. It is therefore common to tackle noise problems with additional means. The traditional way is to use *passive methods*, which are based on absorption and/or reflection of acoustic energy. Examples of absorption-based techniques are sound absorbing materials such as glasswool and foam and (coupled) tube resonators [1, 2]. Sound can be reflected with single or double wall panels [3], for instance as shielding for noisy machinery. Passive methods provide an adequate solution to many noise problems, but have the drawback that they tend to be more attractive for the higher frequencies (> 1000 Hz). At low frequencies, passive methods often lead to an unacceptable increase in mass and volume.

In contrast to passive methods, *active control methods* rely on an external energy source. Active control systems can take many forms, but such a system typically consists of *sensors*, to detect a response, an electronic *controller*, to suitably manipulate the sensor signals, and *actuators*, to influence the response. Active control is mainly suited for the low frequency range, where passive methods are less attractive [4]. The complementary use of active and passive methods is thus an attractive solution to noise (or vibration) problems. The subject of this thesis is an active control method for reducing the noise produced by vibrating structures. More precisely, the objective is to change the vibration of the structure in such a way that the sound radiation is reduced.

1.3 Active control of sound and vibration

The idea of active control of sound and vibration is not new. In 1936, Paul Lueg [5] patented a technique for controlling sound with additional sound. His idea is illustrated in Figure 1.1 for the control of a plane sound wave in a duct. An acoustic source A produces a sound wave s_1 , which propagates through the duct (from left to right). The components of the active control system are a microphone M , an electric controller V and a loudspeaker L . The

signal measured by the detection microphone is passed through the controller to the loudspeaker. If the controller is tuned such that the speaker produces a sound wave s_2 with the amplitude of the original wave, but shifted 180 degrees in phase, then the original wave is totally cancelled. A person at the right hand end of the duct would in that case experience no sound. An essential assumption for this to be true is that all components in the system behave in a *linear* way, i.e. the principle of superposition applies.

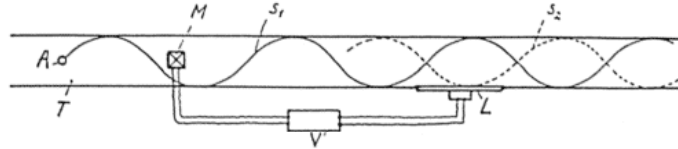


Figure 1.1: A figure from the illustration page of Lueg's patent [5].

The concept of using a control system with speakers as actuators and microphones as sensors to reduce sound is referred to as *active noise control* (ANC) [6]. The practical use of ANC was for a long time limited because the technology means were not available. For high levels of sound reduction the amplitude and phase of the control signal must be accurate, which was difficult with analogue controllers. With the arrival of digital signal processing techniques ANC became more feasible. Nowadays, ANC technology is for example used in active headsets (e.g. by Sennheiser) and to reduce cabin noise in propeller aircraft (e.g. by Lord Corporation).

A drawback of ANC is that when the acoustic source is distributed over multiple surfaces, as in vibrating plate-like structures, many speakers are required to provide global control. In this context, global control refers to a reduction of sound in a large spatial domain. Based on this observation, Fuller and co-workers [7, 8, 9] introduced an alternative to ANC, in which the control inputs are directly applied to the structure. The idea is to change the vibration with the objective of reducing the overall sound radiation. This technique has been termed *active structural acoustic control* (ASAC). It is an extension of a technique called *active vibration control* (AVC) to the range of audio frequencies. Conventional AVC methods, which were developed parallel to ANC methods, were for instance used to control the vibrations of precision instruments in space structures. Such control problems are generally characterised by much lower frequencies than those in noise control problems. ASAC also differs from AVC in that it attempts to control only the vibrations which are important to sound radiation [10]. In AVC the vibration level is reduced to the best possible extent, with no concern regarding the overall sound.

The first references to ASAC concentrated on using point forces (“shakers”) to control the sound radiated by a plate [7, 8, 9]. Furthermore, the control system consisted of microphone error sensors that measure the sound in front of the plate. More recently, distributed piezoelectric actuators have been used instead of point forces [11, 12]. A distributed piezoelectric actuator is a layer of piezoelectric material that is bonded to the surface of a structure. These actuators have the practical advantage that they can be integrated with the structure. As well as using actuators integrated with the structure, there has been growing interest in replacing error microphones by error sensors integrated within the structure [13, 14]. A system with both actuators and sensors integrated can be used when it is impractical to have microphones in the acoustic field.

1.4 Smart structures

The idea of integrating actuators and sensors into the structure is considered in many other engineering fields besides ASAC. Such a structure with integrated actuators and sensors is often referred to as a *smart structure*: a structure with a high degree of integration of the actuators and sensors inside the structure, such that the structural response can be adjusted to varying loading conditions [4]. In a smart structure, actuating and sensing is performed by so-called *smart materials*. A smart material is a material that responds (e.g. deforms) to a particular stimulus, such as an electric field (piezoelectric materials), temperature (shape memory alloys) or magnetic field (magnetostrictive materials). A number of engineering problems which can possibly be solved with smart structures is given below. For each item, one or more example references are given, but it is noted that a very large amount of literature is available on each subject.

- **Tail buffet alleviation** [15, 16]. The tail buffet problem of fighter aircraft occurs when the vortical flow breaks down ahead of the vertical tails. The resulting loads on the tails (buffet loads) result in a premature fatigue failure of the tails. Buffet alleviation is obtained with an active control system which attempts to add damping to the tail structure.
- **Smart aircraft wings** [17]. The idea of using smart structures technology for shape control of aircraft wings is aimed at providing improved aerodynamic and aeroelastic performance compared to conventional wings. Researchers have for instance looked at hingeless trailing edge control surfaces (“flaps”).
- **Active rotor blades** [18, 19, 20]. During flight, helicopter rotor blades are exposed to unsteady aerodynamic loading conditions which results in high vi-

bration levels of the blades. These vibrations may be reduced with smart structure concepts (“active twist rotor”, “active blade tips”) to improve the flight performance and to extend the structural life of components.

Although different engineering problems are characterised by different control objectives, there is certainly similarity between these problems. For instance, the same modelling techniques can be used for the analysis of different smart structures. Some of the issues described in this thesis are therefore useful for other smart structure applications.

1.5 Active structural acoustic control

1.5.1 ASAC in general

In a complex system such as a car, many disturbance sources and transmission paths can give rise to noise problems. In some cases the noise problem can possibly be solved with ASAC. Since the introduction of ASAC, research has evolved in various directions for solving different noise problems. These directions differ in the sense that the considered noise problems involve various types of disturbance sources, structures, acoustic environment, actuators and sensors and control strategy. Some of these issues are discussed briefly.

Enclosed or free sound field

An active control system for reducing the noise produced by a car could be used to improve the comfort of passengers in the car, but as well to reduce the sound experienced by people outside the car (“traffic noise”). Control of an *enclosed sound field* (inside the car), i.e. sound in a volume of air enclosed by reflective boundaries, involves resonant behaviour of both the structure and the acoustic enclosure [21]. On the other hand, control of a *free sound field* (outside the car), i.e. sound propagating away from the structure into an in theory unconfined space, does not involve acoustic resonant behaviour. *In this thesis the control of free field sound radiation is considered.*

Disturbance source

In terms of frequency, disturbance sources can be characterised as *narrowband* and *broadband*. A narrowband signal is one with the energy concentrated in a small frequency band. In a broadband signal the energy is more or less equally distributed over a wide frequency band. In the case of a car, a running engine can be seen as a narrowband source, whereas the problem of wind noise is

more broadband in nature. *The control of both narrowband and broadband disturbances is considered in this work.*

Actuators and sensors

A large portion of the work on ASAC is concerned with the use of distributed piezoelectric actuators. Besides the possibility to integrate such actuators within the structure, piezoelectric actuators have the advantage of low weight and low cost. There are also several drawbacks such as the limited maximum strain (up to 0.1 %), and the fact that the material is brittle. *In this work, emphasis is on the development of models of structures with piezoelectric actuators. In addition, the use of the sensors on the structure for control of sound radiation is considered.*

Feedforward or feedback control

Active control strategies can be divided into two categories: *feedforward* and *feedback*. The principles of feedforward and feedback control are shown in Figure 1.2. The essential difference between the two is that feedforward control relies on the availability of a reference signal correlated to the disturbance source, whereas feedback control does not.

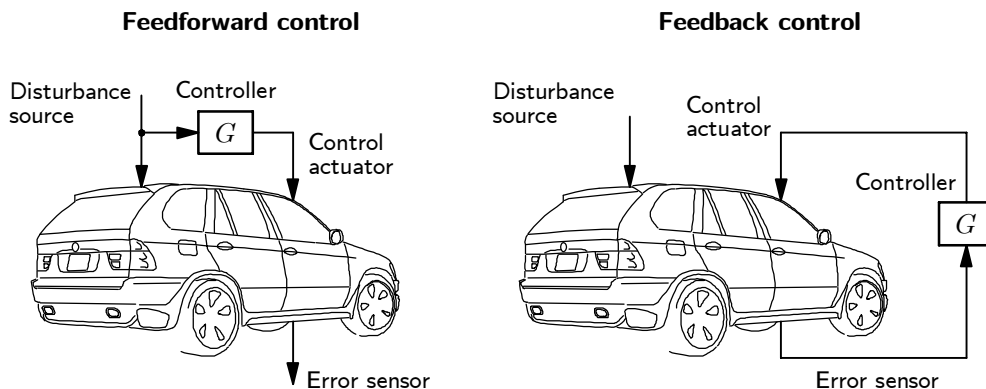


Figure 1.2: Basic representations of feedforward and feedback control.

Lueg’s idea of controlling sound in a duct is an example of feedforward control. As shown in Figure 1.1, the speaker input is derived from the reference signal measured by the detection microphone. On the other hand, in a feedback control system the control signal is derived from an “error sensor” measuring the system response. The choice of which control scheme to use strongly

depends on what is known about the disturbance source. *In this thesis both feedforward and feedback control will be considered.*

1.5.2 Present approach

Adequate design of an active control system requires an understanding of the underlying physics. It is therefore important to have a model of the system under consideration. Furthermore, with a model the performance of various control strategies can be investigated. In this respect, it is important to note that the design of a control system does not only involve the choice of the control strategy and associated control parameters, but also issues such as the dimensions and placement of actuators and sensors.

A large portion of the literature on ASAC (and smart structures) concerns the modelling of structures with distributed piezoelectric actuators and sensors. The early works deal with analytical models of beam and plate systems (see Chapter 3). These models are very useful for studying the underlying physics, but are not suitable for representing “real life” structures with complex geometries. On the other hand, the finite element method (FEM) is suitable for the dynamical modelling of structures with complex geometries at low frequencies, where active control is attractive. The growing interest in the design of complex structures with piezoelectric patches has stimulated the development of “piezoelectric elements”, i.e. finite elements with piezoelectric capabilities.

An additional argument for using FEM comes from the fact that an accurate knowledge of the transfer functions between the actuators and sensors is required for control system design. Local effects such as added mass and stiffness significantly influence these transfer functions, and an erroneous prediction of the control performance is obtained if the local effects are neglected. With FEM the mass and stiffness effects of piezoelectric patches are easily included, in contrast to analytical models.

This research deals with the development of analysis tools for ASAC, or to put it in a more general context, for smart structures. FEM is applied to model a structure with piezoelectric patches. The use of FEM for the analysis of ASAC systems is not new, but most earlier works were devoted to the development of piezoelectric elements rather than the use of FEM models for control system design. A FEM model is generally described by a large number of degrees of freedom. This feature makes such a model not suitable for the design of an active control system. Therefore, a model reduction technique is applied to obtain an efficient analysis tool, which can serve as a basis for the design of a control system.

In order to design a control system for noise reduction, a model for predicting the acoustic radiation of the structure must be available. It is noted that in this work emphasis is on a model for the structural vibration. The acoustic radiation is analysed with a model that is only valid for flat plates, which is sufficient for the test problems considered in the present investigation.

1.6 Problem definition

In view of the considerations in the previous section, the goal of this study is formulated as follows:

- Development and validation of efficient analysis tools to predict the dynamical behaviour of structures with integrated piezoelectric patches and the corresponding sound radiation.
- Application of the analysis tools for the design and optimisation of active control systems for reducing the sound radiation of plate-like structures.

1.7 Outline of the thesis

This thesis is divided in two parts according to the previous problem definition. The first part (Chapters 2, 3 and 4) deals with the modelling issues and validation of the models. In the second part (Chapters 5, 6 and 7) these models are used to investigate the performance of two control strategies and to perform an optimisation study.

In Chapter 2 it is described how piezoelectric materials are applied in ASAC as actuators and sensors. Also, the basic equations governing the dynamical behaviour of piezoelectric materials are introduced.

An analytical model for beam structures with surface bonded piezoelectric actuators and sensors is presented in Chapter 3. This model is used to study the influence of the mass and stiffness of the actuators and sensors on the dynamical behaviour, and to study the fundamental issues of ASAC. Furthermore, the analytical model serves as a validation tool for numerical codes.

In Chapter 4 the numerical approach for the modelling of ASAC systems is presented and validated. The size of a FEM model of a structure with surface bonded piezoelectric actuators and sensors rapidly increases with the complexity of the structure. Therefore a technique for reducing the number of degrees

of freedom is applied. In this way, calculation times are drastically reduced, which is essential for control system design and parameter studies. Next, a model for predicting the acoustic radiation of the structure is described. The structural and acoustic models are validated with the results of experiments performed on a clamped plate setup.

The numerical model provides the basis to simulate and investigate the performance of various control strategies. Two control strategies are considered in this thesis. First, feedforward control for reducing acoustic radiation due to a narrowband disturbance source is studied in Chapter 5. Second, the control problem considered in Chapter 6 involves a broadband disturbance, for which feedback control is applied. In both chapters numerical results are compared with experimental results, again for the clamped plate setup.

A further application of the numerical model is demonstrated in Chapter 7. In this chapter an approach for the optimisation of ASAC systems is presented. The approach is applied and validated for a test case involving the optimal placement of actuators and sensors.

Finally, conclusions and recommendations are presented in Chapter 8.

Chapter 2

Piezoelectric Materials

2.1 Introduction

Piezoelectric materials have the ability to convert mechanical energy into electrical energy, and vice versa, the ability to convert electrical energy into mechanical energy. In 1880 Pierre and Jacques Curie (21 and 24 years of age!) discovered that certain crystals produce an electrical charge under deformation, where the amount of charge depends on the deformation magnitude. This effect, which is shown in Figure 2.1, is called the *direct piezoelectric effect*. The inverse of the direct effect, the so-called *converse piezoelectric effect*, was demonstrated by the Curie brothers in 1881, after Gabriel Lippman deduced it from thermodynamic principles. The converse effect is that such a crystal becomes strained when an electric field is applied, and the magnitude of the developed strain depends on the field strength.

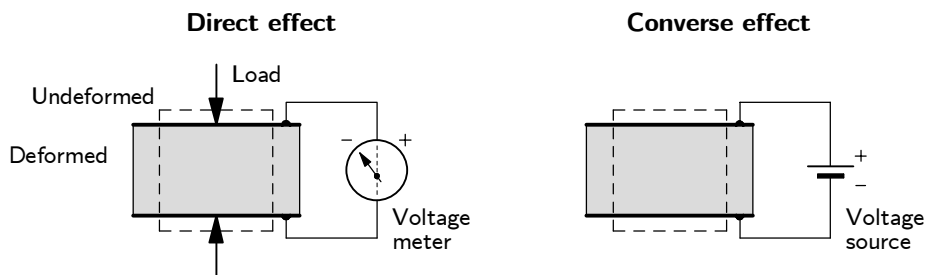


Figure 2.1: The *direct* and *converse* piezoelectric effects.

The Curie brothers carried out experiments with crystal materials such as Rochelle salt, tourmaline and quartz. The first applications of these natural

piezoelectric materials date from the first world war, when quartz was used in ultrasonic submarine detectors. Because the piezoelectric effect is very small in natural crystals, the number of applications was limited for a long time. Still, some famous applications, such as the phonograph pick-up, were already conceived at that time. The development of piezoelectric ceramic materials (*piezoceramics*) started during the second world war. Piezoceramics are prepared by sintering metallic oxide powders. The piezoelectric properties of these materials are up to 100 times greater than those of natural crystals. The most widely used piezoceramic is *lead-zirconate-titanate*, which is usually referred to as PZT. Since the introduction of piezoceramics, the number of applications has increased rapidly. Piezoceramics are nowadays used in for instance audio buzzers, ignition systems, microphones and accelerometers.

In the field of active control, piezoelectric materials are also widely used, both as actuators and sensors. This chapter provides an overview of how piezoelectric materials are applied in active (structural acoustic) control. Furthermore some issues related to the modelling of the dynamical behaviour of such materials are presented.

2.2 Piezoelectric actuators and sensors

Figure 2.2 shows a piece of piezoelectric material with electrodes attached to the top and bottom surfaces. An electrode is a thin metallic layer with high electrical conductivity, e.g. silver or gold, to create a uniform distribution of the electric potential on a surface. When a DC voltage source is connected to the electrodes an *electric field* E is induced in the material pointing from the positive to the negative electrode. The so-called *poling direction* P is along the vertical 3-axis. Poling and poling direction are more clearly explained in Section 2.3. For now, it is sufficient to know that if the poling direction and the direction of the electric field are equal, the material will extend in the direction of the field (3-axis) and contract in the directions perpendicular to the field (1,2-axes). On the other hand, if the electric field is opposite to the poling direction, the material contracts in the direction of the field and extends in the directions perpendicular to the field.

The amount of strain due to an applied electric field is specified by the piezoelectric strain constant d . For the deformation of a piezoceramic element the strain constants d_{33} , d_{31} and d_{32} are of interest, where the first index denotes the direction of the field and the second index denotes the direction of mechanical strain. The deformation in the direction of the field is in analogy with the piezoelectric strain constant referred to as the *d_{33} -effect*. The defor-

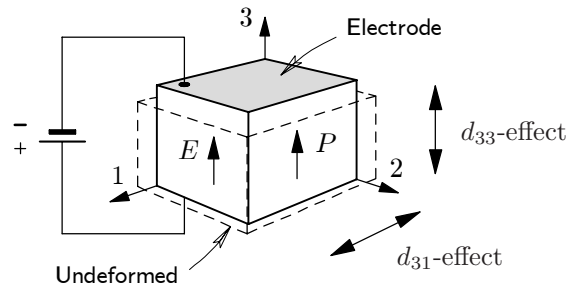


Figure 2.2: The d_{33} -effect and d_{31} -effect.

mation in the directions perpendicular to the field is the so-called d_{31} -effect. Piezoceramic materials are isotropic in the plane normal to the poling direction, so $d_{31} = d_{32}$. The d_{31} constant of piezoceramics is usually one-half of the d_{33} constant.

The d_{33} -effect and the d_{31} -effect in piezoelectric materials are widely used for actuation and sensing purposes. Piezoelectric actuators rely on the converse effect, whereas piezoelectric sensors rely on the direct effect. Different types of piezoelectric actuators and sensors used in the field of active (structural acoustic) control are considered in the following.

2.2.1 Actuators

Piezoelectric stacks

The d_{33} -effect is used in piezoceramic *stack* actuators. The elongation along the 3-axis of a piezoceramic element such as shown in Figure 2.2 is proportional to the applied electric field, which is equal to the voltage across the electrodes divided by the length of the piezoceramic element. The maximum strain that can be developed in piezoceramics by electrical actuation is approximately 0.1 %. Therefore, for “large” actuator displacements, which are desired in many applications, a long piezoceramic element is required. A long piezoceramic element, however, requires a high voltage to obtain an electric field of sufficient magnitude. This problem is overcome in piezoelectric stack actuators by using *stacked* thin piezoceramic layers, usually PZT, separated by electrodes (see Figure 2.3). In this way, a sufficiently large electric field is induced in each layer with a low voltage. Stack actuators are mainly used for position precision control and vibration control where only small actuator strokes, and possibly large forces, are required (see reference [22] for an example).

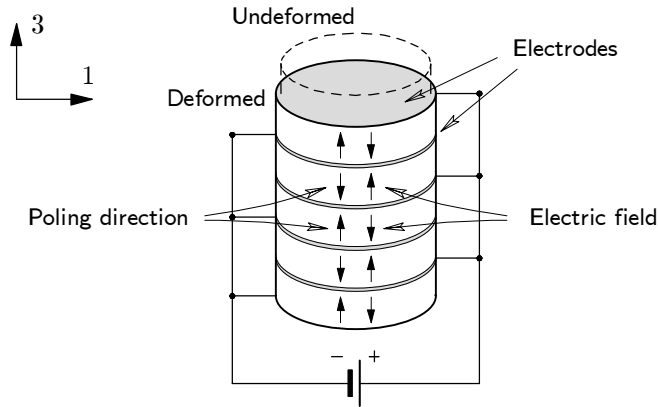


Figure 2.3: Schematic layout of a piezoelectric stack actuator.

Piezoelectric patches

The d_{31} -effect is used in so-called laminar piezoelectric actuators (see Figure 2.4). Such actuators will be called piezoelectric *patches* in this thesis. A patch is a thin layer of piezoelectric material, often PZT, covered with electrodes on both sides. The patches used in the experiments presented in this work are PZT patches with in-plane dimensions of 50×30 mm and thicknesses up to 1 mm.

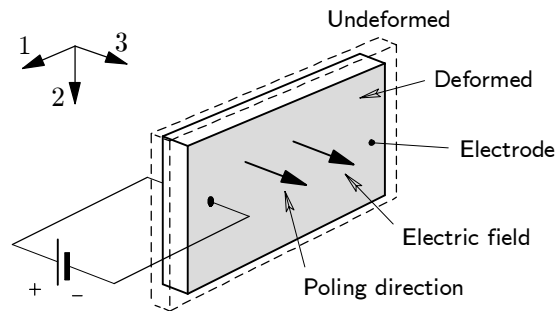


Figure 2.4: Deformation of an unconstrained piezoelectric patch due to an electric potential.

The voltage is applied across the thickness of the patch and the electrodes create an equal potential distribution. An electric field in the poling direction results in a contraction in the plane of the patch (1-2 plane). The geometric layout of the patch ensures that the deformation is mainly in-plane.

When two glued patches with opposite poling directions are subjected to

the same field (in sign and strength), then the extension of one patch and the contraction of the other results in out-of-plane bending. Such actuators are so-called *bimorph* actuators. Likewise, piezoelectric patches can be bonded to a thin plate-like structure to obtain a bending of the structure (see Figure 2.5). As a result of an applied voltage the patch attempts to extend but is constrained somewhat due to the stiffness of the plate. The result is an out-of-plane bending of the plate. It is the out-of-plane vibration of plate-like structures that causes a noise problem. The piezoelectric patch is therefore an attractive option for the use as an actuator in active structural acoustic control.

In Figure 2.5 two configurations of surface bonded piezoelectric patches are shown. The bonding layer between the structure and a patch is usually much thinner than the patch and plate, and is therefore not shown. In the so-called *symmetric configuration* two patches are bonded symmetrically on opposite sides of the structure. If the electric fields across the patches have equal magnitudes but opposite directions, a pure bending of the structure is obtained. However, if the electric fields are equal in both magnitude and direction, a pure extension is the result. It is noted that this is true if the poling directions of the two patches are equal. In Figure 2.5 the case of pure bending is shown. The configuration with one surface bonded patch is referred to as the *asymmetric configuration*. In this configuration, both extension and bending of the structure is obtained. A more detailed analysis of the two configurations will be given in Chapter 3.

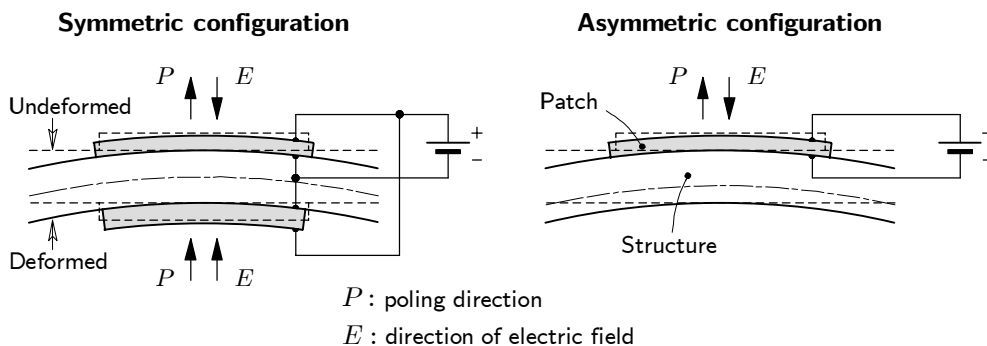


Figure 2.5: Symmetric and asymmetric configurations.

The key benefits of using piezoelectric patches for ASAC instead of other actuator principles are their low weight and volume, low cost, and furthermore the possibility of integration into the structure. On the other hand, piezoelectric patches have a number of drawbacks which could make the ASAC concept in-

feasible. Piezoelectric patches are brittle (i.e. thus not robust with respect to damage), not easily conformable to curved structures and, most importantly, have a low maximum strain (“low control authority”). To overcome these drawbacks researchers are exploring new actuation concepts. An example is given in the next section.

Piezoelectric fibre composites

One new actuator concept which is not further considered in this thesis but certainly worth mentioning is the *piezoelectric fibre composite* [23]. A piezoelectric fibre composite (PFC) consists of piezoceramic fibres aligned in a polymer matrix, see Figure 2.6. The fibres, which are manufactured by extrusion techniques, are approximately 100 – 130 microns in diameter. A so-called *interdigitated electrode* (IDE) is etched on the top and bottom surfaces of the matrix material. The electrode fingers have alternating polarity, which causes the electric field to be aligned primarily along the fibres. In this way poling is mainly along the x -axis, allowing the use of the d_{33} -effect.

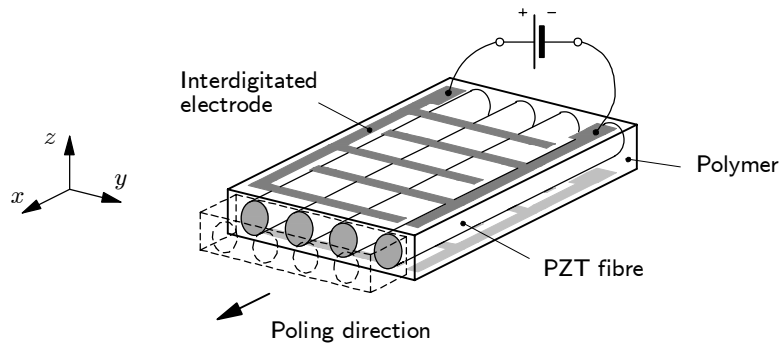


Figure 2.6: A piezoelectric fibre composite (PCF) with interdigitated electrode.

PFCs have several advantages over standard piezoelectric patches. The maximum strain is higher since the poling direction is along the fibre direction. Because of the combination of ceramic fibres and soft matrix polymer, PFCs are much more robust to damage. The elastic and electrical properties of the matrix material may be enhanced with additives such as glass fibres or PZT filler. Furthermore, PFCs can be fully integrated into a host structure, and are conformable to curved structures.

2.2.2 Sensors

Piezoelectric patches and polymers

Because of the direct piezoelectric effect, piezoelectric patches can also be used for sensing the structural vibration. For instance, the symmetric configuration of Figure 2.5 can serve as an actuator/sensor pair, where one patch is the actuator and the other patch is the sensor (see Chapter 6).

Actuator patches are mostly made of the piezoceramic material PZT. For sensing purposes, however, also a *polymer* material exhibiting the piezoelectric effect is suitable. The most used piezoelectric polymer is probably *polyvinylidene fluoride* (PVDF or PVF₂). The material properties of PVDF are compared to those of PZT in Table 2.1. Because of the small piezoelectric constant and Young's modulus, PVDF has a moderate ability for transforming electrical energy into mechanical energy. This characteristic makes PVDF not very suitable for use as an actuator. The high compliance, however, has the advantage that the material hardly influences the dynamical behaviour of the host structure. For this reason PVDF films are mainly used as sensors in active noise and vibration control. The use of PVDF films as distributed sensors (or actuators) is beyond the scope of this thesis. There is however a large amount of literature on this topic, see for example references [24, 25, 26].

Property		PZT	PVDF
Density	ρ [kg/m ³]	7800	1800
Young's modulus	$1/S_{33}^E$ [N/m ²]	$50 \cdot 10^9$	$2.0 \cdot 10^9$
Piezoelectric constant	d_{33} [m/V]	$420 \cdot 10^{-12}$	$-33 \cdot 10^{-12}$
Dielectric constant	ϵ_{33}^s [F/m]	$190 \cdot 10^{-10}$	$1.1 \cdot 10^{-10}$
Max. electric field	[V/m]	$1 \cdot 10^6$	$30 \cdot 10^6$
Temperature range	[°C]	up to 150	-40 to 80

Table 2.1: Typical values for material properties of PZT and PVDF.

Accelerometers

In this work extensive use is made of piezoelectric accelerometers. The type of accelerometer considered here is a so-called *compression mode* accelerometer, which is based on the d_{33} -effect. The basic design of a piezoelectric compression mode accelerometer is shown in Figure 2.7.

A piezoelectric element is placed between the mounting base of the accelerometer and a so-called seismic mass. When the accelerometer is subjected

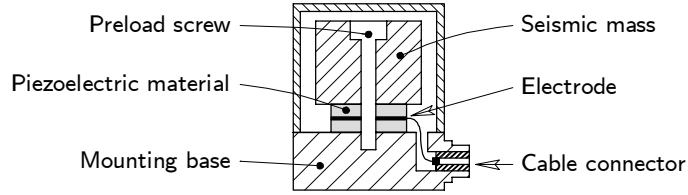


Figure 2.7: Illustration of a piezoelectric compression mode accelerometer.

to a vibration, a force acts on the piezoelectric element which is proportional to the acceleration of the seismic mass. The charge on the electrodes of the piezoelectric element is proportional to the applied force and thus to the acceleration. An external charge amplifier is used to convert the charge signal into a voltage, which can be used as an error signal for control.

2.3 Piezoceramics

For a basic understanding of the piezoelectric effect in piezoceramics, the material is considered on an atomic scale. The polycrystalline structure of a piezoceramic is made up of negatively and positively charged atoms (ions) occupying specific positions in a repeating *unit cell*. The unit cell of the piezoceramic PZT has two states, which are shown in Figure 2.8. Above the so-called *Curie temperature* T_c the crystal structure has a centre of symmetry. In this state, where the centres of positive and negative charge both correspond to the centre of symmetry, the unit cell is electrically neutral. However, the unit cell has no centre of symmetry (non-centrosymmetric) below the Curie temperature. Now the centres of positive and negative electric charge within the unit cell are not located in the same place, i.e. the unit cell now possesses a natural dipole¹. In this state, the material has so-called *spontaneous polarisation*. The polarisation direction is the direction when pointing from the centre of negative charge to the centre of positive charge.

Below the Curie temperature, a deformation of the unit cell due to mechanical loading is accompanied by a shift of the ions (direct effect). Also, when the unit cell is exposed to an external electric field, a shift of the ions is accompanied by a deformation of the structure (converse effect).

¹A dipole consists of two equal point charges of opposite sign separated by a certain distance.

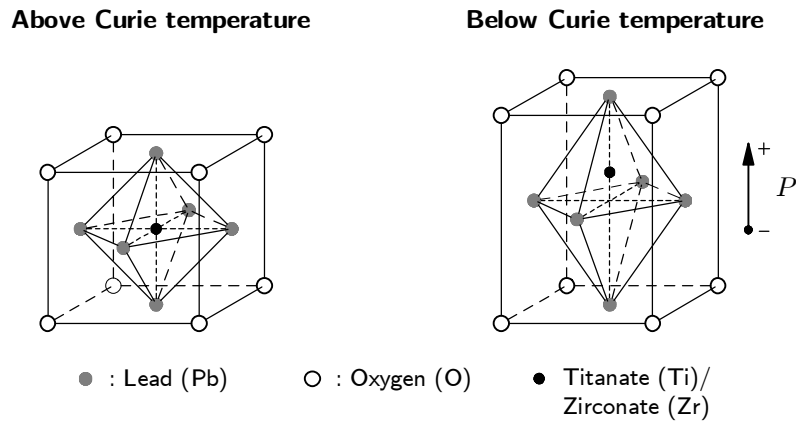


Figure 2.8: PZT unit cell: $T > T_c$, neutral (left); $T < T_c$, electric dipole (right).

Poling

In a fabricated piezoceramic there are many domains consisting of unit cells with the same polarisation direction. Because of the random distribution of domain orientations in the material, the net electric dipole summed over the whole material is zero. Therefore, the material has isotropic material properties and does not exhibit the piezoelectric effect. With a process called *poling* the electric dipoles are reoriented in order to create macroscopic spontaneous polarisation. Figure 2.9 gives a schematic illustration of the domain orientations before and after the poling process.

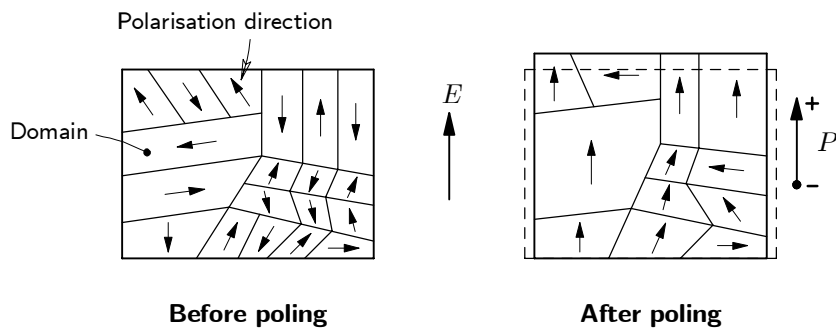


Figure 2.9: Poling of piezoceramics (such as PZT): before poling, random orientation of domains (left); after poling, macroscopic polarisation due to oriented dipoles (right). E is the direction of the electric field during poling, P is the resulting direction of macroscopic polarisation.

During poling, a strong DC electric field (> 2 kV/mm) is applied to the piezoceramic. With the electric field applied, the domains are aligned in the direction of the field. The material expands along the axis of the field and contracts perpendicular to that axis. After removal of the field, the electric dipoles stay roughly in alignment. The material has now what is called a remanent polarisation. The net dipole is normally not detectable because the surface charges are rapidly neutralised by ambient charged particles. The piezoelectric effect is maintained as long the material is not exposed to extreme temperature, electric or mechanical conditions. In Appendix A additional information on piezoelectricity is given. For thorough discussions on this subject the reader is referred to for instance the textbooks of Tiersten [27] and Cady [28].

2.4 Basic equations

In this section the basic equations governing the dynamical behaviour of piezoelectric materials are presented. These equations form the basis for the analytical and numerical models of structures with surface bonded piezoelectric patches. The following assumptions are made:

- *Linear piezoelectric material behaviour.* Ferroelectric hysteresis is neglected and there is no polarisation reversal or depoling due to extreme thermal, electrical, or mechanical loading.
- *No thermal effects.* This assumption is valid if the piezoelectric material operates in an environment with small temperature variations. Some notes on the modelling of thermal effects are given in Appendix A.3.
- *Quasi-static electric field behaviour.* In a piezoelectric material the characteristic wavelength of mechanical vibration is much shorter than the electromagnetic wavelength [27]. Therefore, the magnetic effects are negligible compared to the electrical effects.

2.4.1 Constitutive relations

The linear material behaviour relating the *stress* and *strain* in an elastic body is described in Cartesian coordinates by the constitutive relation (using index notation and Einstein's summation convention):

$$\epsilon_{ij} = S_{ijkl} \sigma_{kl}, \quad (2.1)$$

where ϵ_{ij} and σ_{kl} are the components of the strain and stress tensors, and S_{ijkl} are the components of the compliance tensor. This equation is the more general form of Hooke's law.

The linear constitutive behaviour of a dielectric medium is described in terms of the *electric flux density*² and *electric field strength*. In index notation, this equation reads:

$$D_i = \varepsilon_{ij} E_j, \quad (2.2)$$

where D_i and E_j are the components of the electric flux density and electric field vectors and ε_{ij} are the components of the dielectric permittivity tensor. In a vacuum, the electric flux density and electric field are related by $\varepsilon_0 = 8.85 \cdot 10^{-12}$ F/m (= Farad/m). The electric permittivity in other dielectric media is often expressed relative to ε_0 .

For a piezoelectric material, the mechanical and electrical constitutive equations are coupled:

$$\epsilon_{ij} = S_{ijkl}^E \sigma_{kl} + d_{kij} E_k, \quad (2.3a)$$

$$D_i = d_{ikl} \sigma_{kl} + \varepsilon_{ik}^\sigma E_k, \quad (2.3b)$$

where d_{ijk} are the components of the piezoelectric charge coefficient tensor. The piezoelectric charge coefficient tensor measures the amount of strain developed in an electric field in the absence of stress (unconstrained), or the amount of electric flux density due to a stress in a zero electric field. Tensor S^E is the compliance for a constant electric field and ε^σ is the permittivity tensor evaluated under constant stress. The strain and electric field are related to the components of the displacement field w_i and the electric potential field ϕ by the compatibility equations:

$$\epsilon_{ij} = \frac{1}{2} (w_{i,j} + w_{j,i}), \quad (2.4)$$

$$E_i = -\phi_{,i}. \quad (2.5)$$

where a subscript $,i$ denotes the differentiation with respect to coordinate direction x_i . Because of the symmetry of the tensors, the piezoelectric constitutive relations can be written in matrix notation as:³

$$\begin{Bmatrix} \boldsymbol{\epsilon} \\ \mathbf{D} \end{Bmatrix} = \begin{bmatrix} \mathbf{S}^E & \mathbf{d}^T \\ \mathbf{d} & \underline{\underline{\varepsilon}}^\sigma \end{bmatrix} \begin{Bmatrix} \boldsymbol{\sigma} \\ \mathbf{E} \end{Bmatrix}, \quad (2.6)$$

²Electric flux density is also called *dielectric displacement*. However, electric flux density is used rather than dielectric displacement to prevent confusion with mechanical displacement.

³In this thesis, a bold lower case symbol denotes a vector (e.g. \mathbf{v}), while a matrix is denoted by a bold upper case symbol (e.g. \mathbf{M}). In some cases, however, this convention is ignored to keep the notation consistent with the literature. Then, a vector may be written as \mathbf{V} and a matrix as $\underline{\underline{\mathbf{m}}}$ (see equation 2.6).

where ϵ is the vector with the components of the strain tensor. This vector will be called the strain vector. Similar terminology is used for all other vectors and matrices in equation (2.6). The strain and stress vectors are defined as follows:

$$\epsilon = \begin{Bmatrix} \epsilon_{11} \\ \epsilon_{22} \\ \epsilon_{33} \\ 2\epsilon_{23} \\ 2\epsilon_{31} \\ 2\epsilon_{12} \end{Bmatrix}, \quad \sigma = \begin{Bmatrix} \sigma_{11} \\ \sigma_{22} \\ \sigma_{33} \\ \sigma_{23} \\ \sigma_{31} \\ \sigma_{12} \end{Bmatrix}. \quad (2.7)$$

The storage order of the shear strains and stresses is according to the IEEE standard on piezoelectricity. It is noted that this notation is not always followed in the field of mechanical engineering. In addition, in the literature the constitutive relations (2.6) are sometimes presented in an alternative way. These alternative formulations can be found in Appendix A.

Piezoceramics

It was already mentioned that an unpoled piezoceramic has isotropic material properties. When the material is poled, the isotropy is destroyed in the direction of the electric field, but maintained in the plane normal to the field. Therefore, all piezoceramics have the same type of constitutive matrix. Due to symmetry within the unit cell, the compliance, piezoelectric and dielectric matrices have few non-zero elements [28].

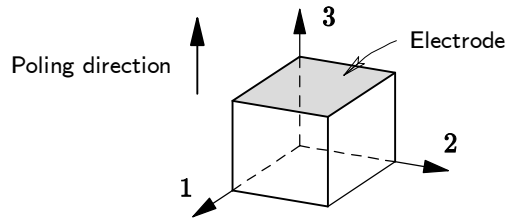


Figure 2.10: Definition of the coordinate system.

It is assumed that the poling direction is along the 3-axis, see Figure 2.10. After the poling process, the symmetry of the piezoceramic is equivalent to that of a hexagonal crystal. The elastic compliance matrix under constant

electric field is:

$$\mathbf{S}^E = \begin{bmatrix} S_{11}^E & S_{12}^E & S_{13}^E & 0 & 0 & 0 \\ S_{12}^E & S_{11}^E & S_{13}^E & 0 & 0 & 0 \\ S_{13}^E & S_{13}^E & S_{33}^E & 0 & 0 & 0 \\ 0 & 0 & 0 & S_{44}^E & 0 & 0 \\ 0 & 0 & 0 & 0 & S_{44}^E & 0 \\ 0 & 0 & 0 & 0 & 0 & S_{66}^E \end{bmatrix}. \quad (2.8)$$

The components of the elastic compliance matrix are often expressed in terms of the Young's moduli, the Poisson's ratios and shear moduli. The following relations are valid:

$$S_{11}^E = 1/E_{11}, \quad S_{12}^E = -\nu_{12}/E_{11}, \quad (2.9a)$$

$$S_{33}^E = 1/E_{33}, \quad S_{13}^E = -\nu_{13}/E_{11} = -\nu_{31}/E_{33}, \quad (2.9b)$$

$$S_{44}^E = 1/G_{23}, \quad S_{66}^E = 2(1 + \nu_{12})/E_{11} \quad (2.9c)$$

The piezoelectric charge coefficient matrix $\underline{\mathbf{d}}$ and the dielectric matrix under constant stress $\underline{\boldsymbol{\varepsilon}}^\sigma$ reduce to:

$$\underline{\mathbf{d}} = \begin{bmatrix} 0 & 0 & 0 & 0 & d_{15} & 0 \\ 0 & 0 & 0 & d_{15} & 0 & 0 \\ d_{31} & d_{31} & d_{33} & 0 & 0 & 0 \end{bmatrix}, \quad (2.10)$$

and

$$\underline{\boldsymbol{\varepsilon}}^\sigma = \begin{bmatrix} \varepsilon_{11}^\sigma & 0 & 0 \\ 0 & \varepsilon_{11}^\sigma & 0 \\ 0 & 0 & \varepsilon_{33}^\sigma \end{bmatrix}. \quad (2.11)$$

A total number of ten independent material properties define the constitutive behaviour of a piezoceramic.

2.4.2 Equations of motion

The equilibrium of continuous piezoelectric media is described by two equations. The first equation follows from Newton's law and describes the *balance of mechanical forces*. In Cartesian coordinates this equation is given by:

$$\sigma_{ij,j} + f_i = \rho \ddot{w}_i + c_d \dot{w}_i, \quad (2.12)$$

where f_i are the components of the body force vector, ρ is the mass density and c_d is the viscous damping factor. Symbols \dot{w}_i and \ddot{w}_i denote the first and second

time derivatives of displacement components w_i , respectively. The second equilibrium equation describes the *balance of electrical charges*. Since it was assumed that the electric field behaviour is quasi-static, Maxwell's equation for quasi-static electric fields is applied:

$$D_{i,i} - q = 0, \quad (2.13)$$

where q is the free charge density. In integral form, this equation states that the electric flux emanating from a closed surface is equal to the total charge enclosed by that surface. The equilibrium equations (2.12) and (2.13), constitutive relations (2.3) and compatibility equations (2.4) and (2.5) can be combined to four differential equations in terms of the displacements w_i and the electric potential ϕ . The surface boundary conditions that are required to solve the equations of motion can take four forms. On surfaces where the displacement or electric potential is prescribed, the boundary conditions are:

$$w_i = \tilde{w}_i, \quad \text{or} \quad \phi = \tilde{\phi}, \quad (2.14)$$

where the “tilde” symbol denotes a prescribed value. On surfaces where the stress or electric flux density is prescribed the boundary conditions are:

$$n_i \sigma_{ij} = \tilde{\sigma}_j, \quad \text{or} \quad n_i D_i = \tilde{D}, \quad (2.15)$$

where n_i are the components of the unit normal vector on the surface.

It is in general not an easy task to find a closed form solution for the dynamical behaviour of a piezoelectric material. In most cases the geometry and boundary conditions are very complex, so one has to use a numerical approach such as the finite element method (see Chapter 4). However, in a few cases where special assumptions apply, the dynamical behaviour can be studied with an analytical model. An example is given in the next section.

2.5 Piezoelectric coupling

The basic technique for solving the coupled electromechanical response is illustrated with an example consisting of a piezoelectric bar. A one-dimensional model for the longitudinal vibration of the bar is derived, which can be seen as a simple representation of a piezoelectric stack actuator. Both the free and forced undamped vibrations are considered. Emphasis is on how the dynamical behaviour is determined by the piezoelectric properties and the electrical boundary conditions.

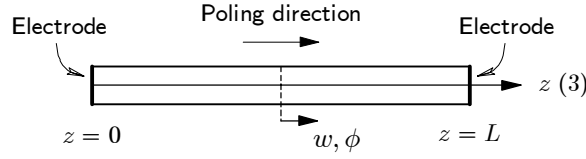


Figure 2.11: A prismatic piezoelectric bar.

Consider a prismatic piezoelectric bar of length L which is poled along the length of the bar (see Figure 2.11). It is assumed that all points on a cross section in the bar have an equal longitudinal displacement and an equal electric field. Lateral deformation (Poisson contraction) is allowed. If the length is large compared to the cross-sectional dimensions of the bar, then the effect of lateral displacements upon longitudinal vibration is negligible. The assumptions made correspond with non-zero stress in the longitudinal direction, whereas all other stresses are zero. In addition, there is only an electric field along the length of the bar. For this particular case, the constitutive relations (2.6) reduce to:

$$\epsilon_{33} = S_{33}^E \sigma_{33} + d_{33} E_3, \quad (2.16a)$$

$$D_3 = d_{33} \sigma_{33} + \epsilon_{33}^\sigma E_3. \quad (2.16b)$$

The elastic compliance is replaced by $S_{33}^E = 1/E_{pe}$, where E_{pe} is Young's modulus in the z -direction. Equations (2.16) can also be written as:

$$\sigma_{33} = E_{pe} \epsilon_{33} - d_{33} E_{pe} E_3, \quad (2.17a)$$

$$D_3 = d_{33} E_{pe} \epsilon_{33} + \epsilon_{33}^\sigma (1 - k_{33}^2) E_3, \quad (2.17b)$$

where $k_{33} = d_{33} \sqrt{E_{pe}/\epsilon_{33}^\sigma}$ is the so-called *electromechanical coupling factor* [29]. This factor measures how well a piezoelectric material converts mechanical energy into electrical energy or converts electrical energy into mechanical energy. The electromechanical coupling factor can have values between 0 (no coupling) and 1, but is up to 0.7 for piezoceramics.

The equations of motion (2.12) and (2.13) reduce to a much easier form for this one-dimensional problem. The combination of these equations and the constitutive relations (2.17), and substitution of equations (2.4) and (2.5), gives two equations in terms of the displacement $w(z, t)$ and electrical potential $\phi(z, t)$:

$$\frac{\partial^2 w(z, t)}{\partial t^2} = E_{pe} \frac{\partial^2 w(z, t)}{\partial z^2} + d_{33} E_{pe} \frac{\partial^2 \phi(z, t)}{\partial z^2}, \quad (2.18a)$$

$$\frac{\partial^2 \phi(z, t)}{\partial z^2} = \frac{k_{33}^2}{d_{33}(1 - k_{33}^2)} \frac{\partial^2 w(z, t)}{\partial z^2}, \quad (2.18b)$$

where ρ_{pe} is the density of the piezoelectric material. Note that the body forces and damping are neglected in equation (2.18a). Equations (2.18a) and (2.18b) can be combined to a *one-dimensional wave equation* in terms of the mechanical displacement:

$$\frac{\partial^2 w(z, t)}{\partial t^2} = c_{pe}^2 \frac{\partial^2 w(z, t)}{\partial z^2}, \quad (2.19)$$

where

$$c_{pe} = \sqrt{\frac{E_{pe}}{\rho_{pe}(1 - k_{33}^2)}}. \quad (2.20)$$

In this equation c_{pe} is the propagation speed of longitudinal waves travelling through the bar. This constant clearly depends on the piezoelectric properties of the bar. If the piezoelectric coupling is zero ($d_{33} = 0$), the wave propagation speed reduces to that in an elastic bar: $c_e = \sqrt{E_{pe}/\rho_{pe}}$.

The frequency domain equivalent of the wave equation is obtained when assuming harmonic time dependence, i.e. $w(z, t) = w(z) e^{j\omega t}$, where $w(z)$ is the displacement amplitude, j is the imaginary unit and ω is the angular frequency. The solution of the resulting ordinary differential equation is:

$$w(z) = C_1 \sin(k_l z) + C_2 \cos(k_l z), \quad (2.21)$$

where $k_l = \omega/c_{pe}$ is the longitudinal wave number. The solution for the electric potential follows from equation (2.18b), and is given by:

$$\phi(z) = \frac{k_{33}^2}{d_{33}(1 - k_{33}^2)} [C_1 \sin(k_l z) + C_2 \cos(k_l z)] + C_3 z + C_4. \quad (2.22)$$

The electric potential distribution is thus a linear field superposed on a field similar to that for the displacement.

The integration coefficients C_1 to C_4 can be solved with two mechanical and two electrical boundary conditions. In the following, the zero displacement and zero stress boundary conditions are referred to as *fixed* and *free*, respectively. If the electric potential on an electrode is zero, then the electrode is said to be *grounded*. The combination of two grounded electrodes is called a *short circuit*. The combination of a grounded electrode and an electrode subjected to a zero electric flux density boundary condition is called an *open circuit*.

First, the modal properties are considered for various boundary conditions at $z = L$, whereas the bar is fixed and grounded at $z = 0$. Substitution of the general solution into a set of boundary conditions leads to an equation of the form $\mathbf{M}(\omega) \mathbf{a} = \mathbf{0}$ (unforced), where \mathbf{a} is the vector with integration coefficients. The eigenfrequencies follow from solving the characteristic equation $|\mathbf{M}(\omega)| = 0$. In Table 2.2 the eigenfrequencies are given for the possible combinations of boundary conditions at $z = L$.

	Short circuit ($\phi = 0$)	Open circuit ($D_3 = 0$)	Elastic
Fixed ($w = 0$)	$\frac{i\pi c_{pe}}{L}$	$\frac{i\pi c_{pe}}{L}$	$\frac{i\pi c_e}{L}$
Free ($\sigma_{33} = 0$)	$k_{33}^2 \tan(k_l L) = k_l L$	$\frac{(2i-1)\pi c_{pe}}{2L}$	$\frac{(2i-1)\pi c_e}{2L}$

Table 2.2: Eigenfrequencies ω_i ($i = 1, 2, \dots$) of the bar for different boundary conditions at $z = L$. The bar is fixed and grounded at $z = 0$. Also the eigenfrequencies of an elastic bar are given ($k_{33} = 0$).

The eigenfrequencies do not depend on the electrical boundary conditions if the bar is fixed at both ends. The expression for the eigenfrequency is similar to that of an elastic bar, but with a different wave propagation speed. Since the electromechanical coupling factor is between 0 and 1 ($c_{pe} > c_e$), the piezoelectric bar has higher eigenfrequencies than its elastic counterpart. If the bar is free at $z = L$, then the eigenfrequencies associated with the short circuit and open circuit are different. In the case of the short circuit boundary condition, no closed-form solution is available. The roots of the corresponding characteristic equation are smaller than those for the open circuit case, but the difference rapidly decreases with increasing mode number. The first three displacement eigenmodes $\hat{w}_i(z)$ and electric potential eigenmodes $\hat{\phi}_i(z)$ of a fixed-free bar are shown in Figure 2.12 for open circuit and closed circuit conditions. In the figure the values of $\hat{w}_i(z)$ and $\hat{\phi}_i(z)$ are plotted as functions

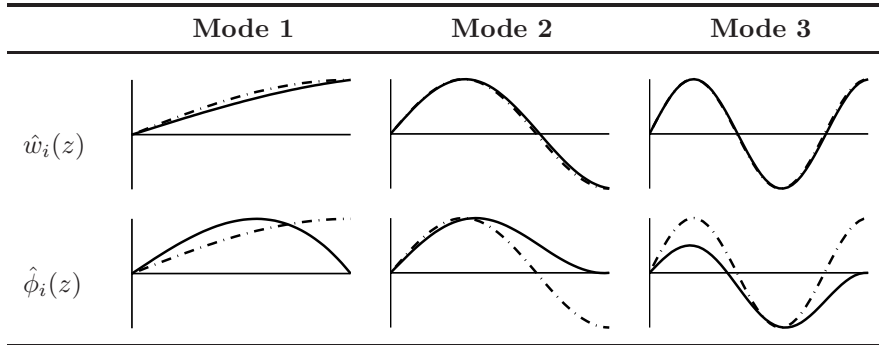


Figure 2.12: Comparison of displacement eigenmodes $\hat{w}_i(z)$ and potential eigenmodes $\hat{\phi}_i(z)$ ($i = 1, 2, 3$) for *short circuit* (—) and *open circuit* (----) conditions. The bar is free at $z = L$, and fixed and grounded at $z = 0$ ($k_{33} = 0.7$).

of the coordinate along the bar.⁴ It can be observed that both the displacement and electric potential eigenmodes depend on whether the bar is subjected to a short circuit or open circuit condition.

The frequency domain response of the displacement at $z = L$ on a longitudinal stress applied in the same point is shown in Figure 2.13. As before, the bar is fixed at $z = 0$ and subjected to either a short circuit or open circuit boundary condition. A clear difference can be observed between the response of a piezoelectric bar and an elastic bar. Furthermore, the dynamical response of the piezoelectric bar depends on the type of electrical boundary condition.

To conclude, the dynamical behaviour clearly depends on the piezoelectric properties of the bar. Furthermore, just as is the case for the mechanical boundary conditions, the dynamics are as well influenced by the electrical boundary conditions. It will be shown in Chapter 3 that the piezoelectric coupling is of minor concern for the dynamical behaviour of structures with surface bonded piezoelectric patches.

2.6 Concluding remarks

In this chapter some background information was given on piezoelectricity and on the application of piezoelectric materials in active (structural acoustic) control. With the growing interest in active control, a number of new sensor and actuator concepts have been developed. In this thesis mainly the use of piezoceramic patches (PZT) is considered. The basic equations governing the

⁴The shapes must not be confused with the bending mode shapes of a beam.

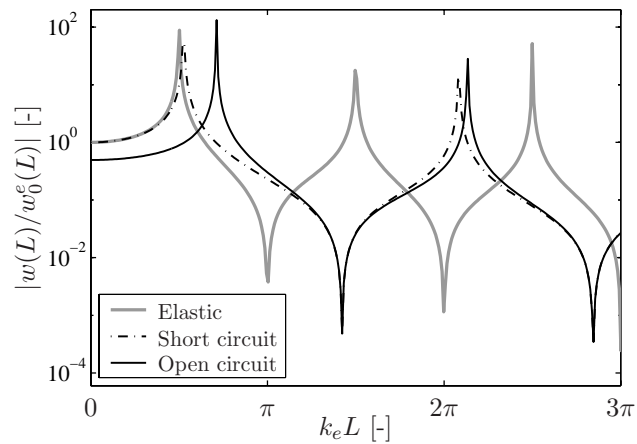


Figure 2.13: Transfer function between force and displacement at the free end of a piezoelectric bar ($k_{33} = 0.7$, *short circuit* or *open circuit*) and an elastic bar ($k_{33} = 0$). The results are normalized to the static displacement of an elastic bar.

coupled electromechanical behaviour of such materials were introduced. It was shown that the dynamical behaviour of piezoelectric materials is determined by their mechanical and electrical properties, and the mechanical and electrical boundary conditions.

Chapter 3

Analytical Study of Active Structural Acoustic Control

3.1 Introduction

In the previous chapter, it was explained how piezoelectric patches are used as actuators and sensors in active structural acoustic control (ASAC) and in other smart structure applications. In this chapter, the basic physical aspects of structures with surface bonded piezoelectric patches are considered in more detail. In the first part of this chapter, an analytical model of a beam with surface bonded piezoelectric patches is presented. This model is applied in the second part in a preliminary study of ASAC.

To put the current model into perspective, a short review of various analytical models of beam and plate structures with piezoelectric patches is presented in Section 3.2. It is stressed that the current model, which is described in Section 3.3, is not new. The model is based on the same assumptions and includes the same effects as the models presented in several other works. However, the current model is different from previous works in the sense that it is implemented in such a way that beams with multiple patches can easily be modelled. In Section 3.4 it is demonstrated that the mass and stiffness effects of the piezoelectric patches, which are included in the model, can be of significant influence on the dynamical behaviour of the structure. The beam model is applied in Section 3.5 in a preliminary study of ASAC. It must be said that the test problem concerns a highly idealised structure and that furthermore a highly idealised control system is used. On the other hand, the problem gives insight in the fundamental issues of ASAC. More realistic problems will be dealt with in Chapter 4.

3.2 Literature survey

Since the early 1980s many papers have been published concerning the use of piezoelectric materials for the active control of sound and vibration. A selection of relevant papers concerning analytical models of beam and plate structures with surface bonded piezoelectric patches is given in Table 3.1.

Bailey and Hubbard [30] were among the first who explored the use of piezoelectric actuators for active vibration control. They demonstrated vibration reduction of a beam fully covered with a thin layer of PVDF by means of analytical and experimental work.

Crawley and De Luis [31] presented a rigorous study of “symmetric actuation” by two piezoelectric patches bonded symmetrically on opposite sides of a thin beam. They demonstrated a number of important results, such as increased actuation effectiveness for stiffer and thinner bonding layers and for a stiffer piezoelectric material. For an increasingly stiffer and thinner bonding layer, the shear forces between the patches and the beam are transferred over a small zone near the ends of the patches. In the limit, for an infinitely stiff and thin bonding layer (i.e. a *perfect bonding* condition), the load on the beam can be represented by a pair of opposite bending moments if the actuators are driven “out-of-phase”. On the other hand, if the patches are driven “in-phase”, the load is equivalent to a pair of opposite normal forces. The magnitude of the bending moments or normal forces is proportional to the applied voltage.

Many papers have been published since the work of Crawley and De Luis. Dimitriadis, Fuller and Rogers [32] considered the application of symmetrically bonded piezoelectric patches to a simply supported plate structure, under the assumption of perfect bonding. Kim and Jones [33] extended the model of Dimitriadis et al. by introducing a bonding layer between the plate and the patches.

In other works, the “asymmetric actuation” by a single surface bonded patch was investigated. The asymmetric configuration induces longitudinal and transverse motions simultaneously in the structure. Gibbs and Fuller [34] used a static analysis to determine the equivalent external loads on a beam, i.e. normal forces and bending moments at the ends of the patch, and they developed a dynamical model to calculate the beam response to these loads. They neglected the mass and stiffness of the patch in the dynamical model. Charette, Guigou, Berry and Plantier [35], presented a model which accounts for the mass and stiffness effect of a patch. They used a Rayleigh-Ritz approach to model a beam with a surface bonded PZT actuator patch on one side and a PVDF sensor layer on the other side. Their model describes the

coupled longitudinal and transverse motion of the beam. In all of the previously mentioned works on beam models, the patches are aligned with the beam axis. However, if a patch is arbitrarily oriented with respect to the beam axis, then the actuation also couples to the torsional motion. This effect is included in the models presented by Park, Walz and Chopra [36] and Park and Chopra [37].

It is stressed that the current beam model is not new. It is based on the same assumptions and incorporates the same effects as some of the previously mentioned models. However, the current model differs from existing models in the sense that it is implemented using a so-called *dynamic stiffness matrix* formulation. This implementation makes it easy to model beams with multiple, non-identical, piezoelectric actuator or sensor patches, in asymmetric or symmetric configurations. The analysis presented in this section is restricted to a beam setup. A plate model is included in Appendix C.

Authors	Year	Ref.	Beam/ plate	Symmetric/ asymmetric	m/k effects	Bonding layer	Remarks
Bailey and Hubbard	1985	[30]	beam	symmetric	no	no	includes experimental work
Crawley and De Luis	1987	[31]	beam	symmetric	no	yes	detailed strain-stress analysis
Crawley and Anderson	1990	[38]	beam	symmetric	no	no	
Dimitriadis, Fuller and Rogers	1991	[32]	plate	symmetric	no	no	
Kim and Jones	1991	[33]	plate	symmetric	no	yes	correction of "Dimitriadis-model"
Gibbs and Fuller	1992	[34]	beam	asymmetric	no	no	on wave responses
Pan, Hansen and Snyder	1992	[39]	beam	symmetric	yes	no	
Charette et al.	1994	[35]	beam	asymmetric	yes	no	Rayleigh-Ritz approach
Rivory, Hansen and Pan	1994	[40]	beam	symmetric	yes	no	also experimental work
Park, Walz and Chopra	1996	[36]	beam	asymmetric	yes	yes	longitudinal, transverse and torsional vibration
Ha and Kim	2002	[41]	beam	both	yes	yes	multimorph configuration
Lee, Gardonio and Elhott	2002	[42]	beam	symmetric	yes	no	triangularly shaped actuator/sensor pair
This thesis			beam	both	yes	no	longitudinal and transverse vibration
This thesis			plate	asymmetric	no	no	included in Appendix C

Table 3.1: A selection of literature on analytical models of beams and plates with piezoelectric patches.

3.3 Beam model

In this section an analytical model for the dynamical behaviour of beam-like structures with surface bonded piezoelectric patches is presented. An example of such a system is shown in Figure 3.1. It is perhaps more appropriate to call this structure a strip rather than a beam, but the term “beam model” is used to be consistent with the literature. The main features of the model are:

- A perfect bonding condition is assumed, which is true for thin bonding layers with a stiffness comparable to that of the beam and piezoelectric material [31].
- Variations along the width (y -axis) are neglected.
- Both the symmetric and asymmetric configurations are modelled.
- The mass and stiffness effects of the patches are accounted for.

Furthermore, linear piezoelectric material behaviour and small deformations are assumed (see Section 2.4). In the following, first the equations of motion are derived for a beam part with a single patch and with two symmetrically bonded patches. Next, a so-called dynamic stiffness matrix formulation is presented. With this formulation it is relatively easy to model a beam with multiple patches.

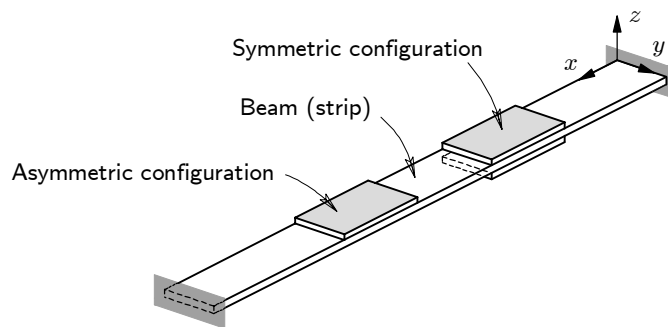


Figure 3.1: A beam with surface bonded piezoelectric patches.

3.3.1 Asymmetric configuration

A piezoelectric patch can be used as an actuator or a sensor. First, the case that the patch is a (voltage driven) actuator is considered. Subsequently, the additional equations required to model a sensor are introduced.

Strains and stresses

The *Euler-Bernoulli hypothesis* is used to describe the deformation of the asymmetric configuration. This means that a cross-sectional plane normal to the neutral axis remains plane and normal to this axis during deformation. A graphical representation of this assumption is shown in Figure 3.2. The longitudinal displacement field $u(x, z, t)$ can therefore be written as:¹

$$u(x, z, t) = u_0(x, t) - z \frac{\partial w(x, t)}{\partial x}, \quad (3.1)$$

where $u_0(x, t)$ and $w(x, t)$ are the longitudinal and transverse displacements, respectively, of the beam mid-plane. Note that coordinate z is measured from the mid-plane of the beam.

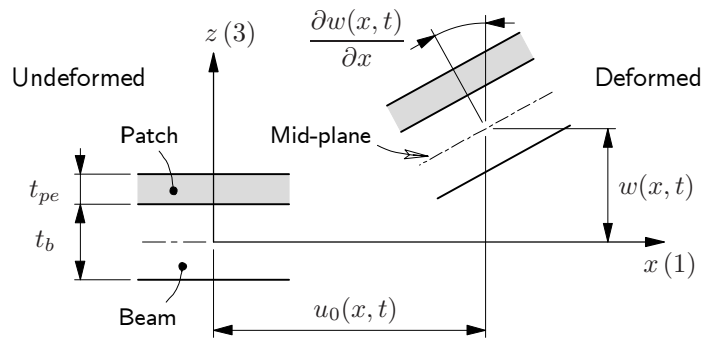


Figure 3.2: Euler-Bernoulli displacement field.

In the rest of the analysis, the space and time dependence of the variables is omitted. The longitudinal strain ϵ_{11} associated with the Euler-Bernoulli displacement field is given by (see Figure 3.3):

$$\epsilon_{11} = \frac{\partial u}{\partial x} = \epsilon_0 - \kappa z, \quad (3.2)$$

¹The displacements in the x - and z -directions are referred to as *longitudinal* and *transverse*, respectively.

where $\epsilon_0 = \partial u_0 / \partial x$ is the mid-plane membrane strain and $\kappa = \partial^2 w / \partial x^2$ is the curvature. The strain variation along the thickness is thus the sum of a uniform strain field (i.e. longitudinal component) and a linear strain field (i.e. transverse component). Because of the strain continuity at the interface of beam and patch, the perfect bonding condition is automatically satisfied.

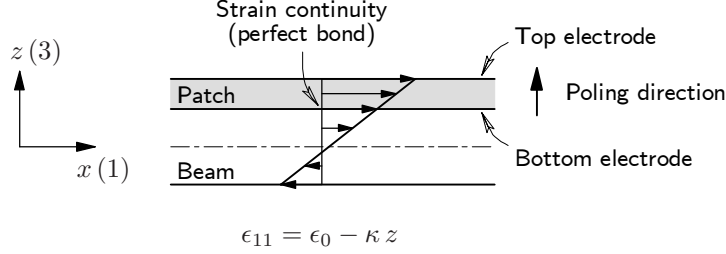


Figure 3.3: Asymmetric Euler-Bernoulli strain distribution ($\epsilon_0 > 0$, $\kappa < 0$).

The normal stresses (in the x -direction) in the beam and patch are found with the constitutive equations for a uni-axial stress field (see Section 2.4):

$$\text{Beam : } \quad \epsilon_{11} = \sigma_{11}^b / E_b, \quad (3.3a)$$

$$\text{Patch : } \quad \epsilon_{11} = \sigma_{11}^{pe} / E_{pe} + d_{31} E_3, \quad (3.3b)$$

where σ_{11}^b and σ_{11}^{pe} are the normal stresses in the beam and patch, E_b and E_{pe} are the Young's moduli of the beam and patch, and d_{31} is the piezoelectric strain constant. It is assumed that the electric field between the electrodes on the top and bottom surfaces of the patch is uniform:

$$E_3 = -\frac{V}{t_{pe}}, \quad (3.4)$$

where V is the voltage applied across the electrodes and t_{pe} is the patch thickness. Instead of using this assumption, the electric field can also be solved from Maxwell's law. The resulting electric field is the sum of a uniform part, as in equation (3.4), and a linear part, which is proportional to the curvature κ . It is shown in Appendix B that the contribution of the linear part to the electric field is negligible. For this reason the assumption of a uniform electric field is used.

Equations (3.2), (3.3) and (3.4) can be combined to:

$$\sigma_{11}^b = E_b(\epsilon_0 - \kappa z), \quad (3.5a)$$

$$\sigma_{11}^{pe} = E_{pe}(\epsilon_0 - \kappa z + \epsilon_{pe}), \quad (3.5b)$$

where

$$\epsilon_{pe} = \frac{d_{31}V}{t_{pe}}. \quad (3.6)$$

When a voltage V is applied to an unconstrained patch (i.e. not bonded), the resulting longitudinal strain is equal to ϵ_{pe} . This quantity is referred to as the *free piezoelectric strain*.

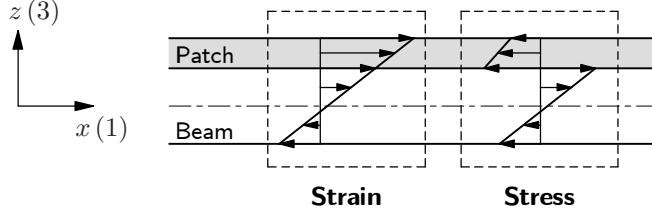


Figure 3.4: Assumed strain and stress distributions ($E_b > E_{pe}$).

As a result of the strain continuity at the interface of the beam and patch, the stress will show a discontinuity at the interface if the Young's moduli of the materials are different (see Figure 3.4). The discontinuity is also created by the “external” stress caused by ϵ_{pe} .

Normal force and bending moment

The internal normal force N and bending moment M are found by integration of the stresses over a cross section:

$$N = b_b \int_{-t_b/2}^{t_b/2} \sigma_{11}^b dz + b_{pe} \int_{t_b/2}^{t_b/2+t_{pe}} \sigma_{11}^{pe} dz, \quad (3.7a)$$

$$M = -b_b \int_{-t_b/2}^{t_b/2} \sigma_{11}^b z dz - b_{pe} \int_{t_b/2}^{t_b/2+t_{pe}} \sigma_{11}^{pe} z dz. \quad (3.7b)$$

where t_b is the beam thickness, b_b is the beam width, and b_{pe} is the patch width. After substitution of equations (3.5), the following relation is obtained:

$$\begin{Bmatrix} N \\ M \end{Bmatrix} = \begin{bmatrix} E_b A_b + E_{pe} A_{pe} & -E_{pe} Q_{pe} \\ -E_{pe} Q_{pe} & E_b I_b + E_{pe} I_{pe} \end{bmatrix} \begin{Bmatrix} \epsilon_0 \\ \kappa \end{Bmatrix} + \begin{Bmatrix} E_{pe} A_{pe} \\ -E_{pe} Q_{pe} \end{Bmatrix} \epsilon_{pe}, \quad (3.8)$$

where

$$A_b = b_b t_b, \quad I_b = \frac{b_b t_b^3}{12},$$

$$A_{pe} = b_{pe} t_{pe}, \quad I_{pe} = b_{pe} t_{pe} \left(\frac{t_b^2}{4} + \frac{t_b t_{pe}}{2} + \frac{t_{pe}^2}{3} \right), \quad Q_{pe} = \frac{b_{pe} t_{pe} (t_b + t_{pe})}{2}.$$

The off-diagonal terms in the matrix in equation (3.8) are the result of the setup being non-symmetric with respect to the x -axis.

Essentially, the foregoing formulation is valid only if the beam and patch are infinitely long. In practice the patch only partially covers the beam. The stress distribution shown in Figure 3.4 does not hold near the free edges of the patch since the equilibrium conditions require the normal stress to be zero at an edge. However, the stress field is unaffected up to a small distance from the edge, which is of the order of the patch thickness. Therefore, if the length of a patch is large compared to the thickness, the stress field is valid in the largest part of the actuator, and edge effects can be neglected.

From this point, it is assumed that the beam width and patch width are constant along the length (i.e. independent of x). Then, a voltage applied to the patch induces a normal force and a bending moment, which are uniform within the edges of the patch (no edge effects). The loading induced by the patch can be seen to be equivalent with two equal and opposite normal forces (x -direction) and two equal and opposite bending moments. The magnitudes of the normal forces and bending moments are proportional to the applied voltage. If the patch width varies along the x -direction, transverse loads are also induced by the patch [4, 42].

Equations of motion

The mechanical equilibrium in the longitudinal and transverse directions of an infinitesimal part of the beam with patch is given by (no external mechanical loads):

$$(\rho A)_{\text{eq}} \frac{\partial^2 u_0}{\partial t^2} - \rho_{pe} Q_{pe} \frac{\partial^3 w}{\partial x \partial t^2} - \frac{\partial N}{\partial x} = 0, \quad (3.9a)$$

$$(\rho A)_{\text{eq}} \frac{\partial^2 w}{\partial t^2} + \frac{\partial^2 M}{\partial x^2} = 0, \quad (3.9b)$$

where $(\rho A)_{\text{eq}} = \rho_b A_b + \rho_{pe} A_{pe}$ is the mass per unit length. The rotary inertia is neglected in equation (3.9b). Substitution of equations (3.8) into the above set gives the following result:

$$(\rho A)_{\text{eq}} \frac{\partial^2 u_0}{\partial t^2} - \rho_{pe} Q_{pe} \frac{\partial^3 w}{\partial x \partial t^2} - (EA)_{\text{eq}} \frac{\partial^2 u_0}{\partial x^2} + E_{pe} Q_{pe} \frac{\partial^3 w}{\partial x^3} = 0, \quad (3.10a)$$

$$(\rho A)_{\text{eq}} \frac{\partial^2 w}{\partial t^2} - E_{pe} Q_{pe} \frac{\partial^3 u_0}{\partial x^3} + (EI)_{\text{eq}} \frac{\partial^4 w}{\partial x^4} = 0, \quad (3.10b)$$

where $(EA)_{\text{eq}} = E_b A_b + E_{pe} A_{pe}$ and $(EI)_{\text{eq}} = E_b I_b + E_{pe} I_{pe}$. It is important to note that because of the assumption of a constant beam and patch width, there

are no right hand side terms related to the piezoelectric strain ϵ_{pe} . The load induced by the patch is introduced in the model with the boundary conditions.

Equations (3.10) clearly indicate that the longitudinal and transverse vibrations are coupled. For sound radiation (and ASAC) the transverse vibration of the structure is of interest. If only a small part of the beam is covered with patches, a good estimate for the transverse vibration at low frequencies is obtained when the normal force is set to zero (see Appendix B). In this way the coupling between the longitudinal and transverse vibrations vanishes. When the normal force is set to zero, the equations of motion (3.10) reduce to a single equation in terms of the transverse displacement:²

$$(\rho A)_{\text{eq}} \frac{\partial^2 w}{\partial t^2} + (EI)_{\text{eq}}^a \frac{\partial^4 w}{\partial x^4} = 0, \quad (3.11)$$

where

$$(EI)_{\text{eq}}^a = (EI)_{\text{eq}} - \frac{(E_{pe} Q_{pe})^2}{(EA)_{\text{eq}}}. \quad (3.12)$$

Surface charge

So far the analysis was restricted to the case of an actuator patch. The additional equations required to model a sensor patch are given here. It is common to use the charge produced by the patch as the sensor signal. The surface charge Q on the top electrode is found by integration of the electric flux density D_3 over the electrode area. The electric flux density is related to the mechanical deformation and piezoelectric strain by means of the constitutive equation (see Section 2.4):

$$D_3 = d_{31} E_{pe} \epsilon_{11} + \epsilon_{33}^\sigma (1 - k_{31}^2) E_3, \quad (3.13)$$

where ϵ_{33}^σ is the dielectric constant and $k_{31} = d_{31} \sqrt{E_{pe} / \epsilon_{33}^\sigma}$ is the electromechanical coupling factor. For an Euler-Bernoulli strain field and a uniform electric field, equation (3.13) becomes:

$$D_3 = d_{31} E_{pe} \left(\left[\frac{E_{pe} Q_{pe}}{(EA)_{\text{eq}}} - z \right] \frac{\partial^2 w}{\partial x^2} - \left[\frac{1 - k_{31}^2}{k_{31}^2} + \frac{E_{pe} A_{pe}}{(EA)_{\text{eq}}} \right] \epsilon_{pe} \right). \quad (3.14)$$

In this equation the longitudinal strain component ϵ_0 has been eliminated on the assumption that the normal force is zero. It was previously assumed that

²By demanding $N = 0$, ϵ_0 can be eliminated from equation (3.8). Equation (3.11) is found when the resulting expression for the bending moment is substituted into equation (3.9b).

the electric field is uniform across the patch. As a consequence Maxwell's equation is not satisfied: the electric flux density varies across the thickness of the patch (see equation (3.14)). Therefore, the surface charge Q is defined as the integral of the *average* electric flux density:

$$Q = b_{pe} \int_0^{l_{pe}} \left(\int_{t_b/2}^{t_b/2+t_{pe}} D_3 dz \right) dx. \quad (3.15)$$

3.3.2 Symmetric configuration

In the symmetric configuration two patches are bonded symmetrically on opposite sides of the beam. In the analysis that follows, indices ① and ② refer to the patches on the top and bottom sides, respectively. The symmetric configuration is mainly attractive as an actuator, although it is also possible to use one patch as actuator and the other patch as sensor (see Chapter 6). The case that both patches serve as actuator is considered here.

It is assumed that the two patches have equal length, thickness and material properties. The normal force N and bending moment M for an Euler-Bernoulli strain field are:

$$\begin{Bmatrix} N \\ M \end{Bmatrix} = \begin{bmatrix} (EA)_{\text{eq}}^s & 0 \\ 0 & (EI)_{\text{eq}}^s \end{bmatrix} \begin{Bmatrix} \epsilon_0 \\ \kappa \end{Bmatrix} + \begin{Bmatrix} E_{pe} A_{pe} (\epsilon_{pe①} - \epsilon_{pe②}) \\ -E_{pe} Q_{pe} (\epsilon_{pe①} + \epsilon_{pe②}) \end{Bmatrix}, \quad (3.16)$$

where $\epsilon_{pe①} = d_{31} V_{①} / t_{pe}$ and $\epsilon_{pe②} = d_{31} V_{②} / t_{pe}$ are the free piezoelectric strains of the top and bottom patches, respectively, and:

$$\begin{aligned} (EA)_{\text{eq}}^s &= E_b A_b + 2E_{pe} A_{pe}, \\ (EI)_{\text{eq}}^s &= E_b I_b + 2E_{pe} I_{pe}. \end{aligned}$$

The equations of motion for the longitudinal and transverse vibrations of the symmetric configuration are given by:

$$(\rho A)_{\text{eq}}^s \frac{\partial^2 u_0}{\partial t^2} - (EA)_{\text{eq}}^s \frac{\partial^2 u_0}{\partial x^2} = 0, \quad (3.17a)$$

$$(\rho A)_{\text{eq}}^s \frac{\partial^2 w}{\partial t^2} + (EI)_{\text{eq}}^s \frac{\partial^4 w}{\partial x^4} = 0. \quad (3.17b)$$

It has again been assumed that the beam and patch widths are constant along the beam. Equations (3.16) and (3.17) show that, in contrast to the asymmetric configuration, now the longitudinal and transverse vibrations are decoupled. As a result, it is possible to excite these vibrations independently. In Figure 3.5 the “in-phase” and “out-of-phase” excitation mechanisms are

compared. In the case of in-phase excitation, both patches extend at the same time by the same amount. As a result, only the longitudinal vibration is excited. On the other hand, if the extension of one patch is accompanied by the same amount of contraction of the other patch, the excitation is out-of-phase. In this case only the transverse vibration is excited. As indicated by equation (3.16), opposite free piezoelectric strains ($\epsilon_{pe\textcircled{2}} = -\epsilon_{pe\textcircled{1}}$) result in in-phase excitation and equal free piezoelectric strains result in out-of-phase excitation ($\epsilon_{pe\textcircled{2}} = \epsilon_{pe\textcircled{1}}$). For any other combination of the two, both the longitudinal and transverse vibrations are excited. It is noted that the longitudinal and transverse vibrations are no longer decoupled if the two patches do not have equal length, thickness or material properties.

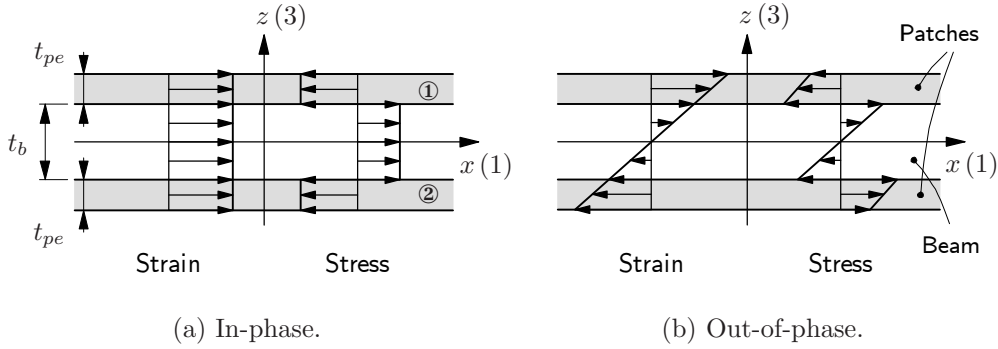


Figure 3.5: (a) In-phase ($\epsilon_{pe\textcircled{2}} = -\epsilon_{pe\textcircled{1}}$) and (b) out-of-phase ($\epsilon_{pe\textcircled{2}} = \epsilon_{pe\textcircled{1}}$) excitation mechanisms in the symmetric configuration.

3.3.3 Dynamic stiffness matrix method

The beam model is implemented using a *dynamic stiffness matrix* (DSM) formulation. This formulation is attractive for the current problem because it is easy to combine beam parts with a surface bonded patch and “regular” beam parts, i.e. without a patch. The DSM method is quite similar to what in the literature is called the *spectral element method* [43, 44, 45, 46]. In the spectral element method the frequency domain solution is subsequently transformed to the time domain using the fast Fourier transform. In the present study, only frequency domain simulations are considered.

A schematic representation of the DSM method is shown in Figure 3.6. In this example a beam with two asymmetric bonded patches is considered. The model consists of five elements, and each element has two nodes. For

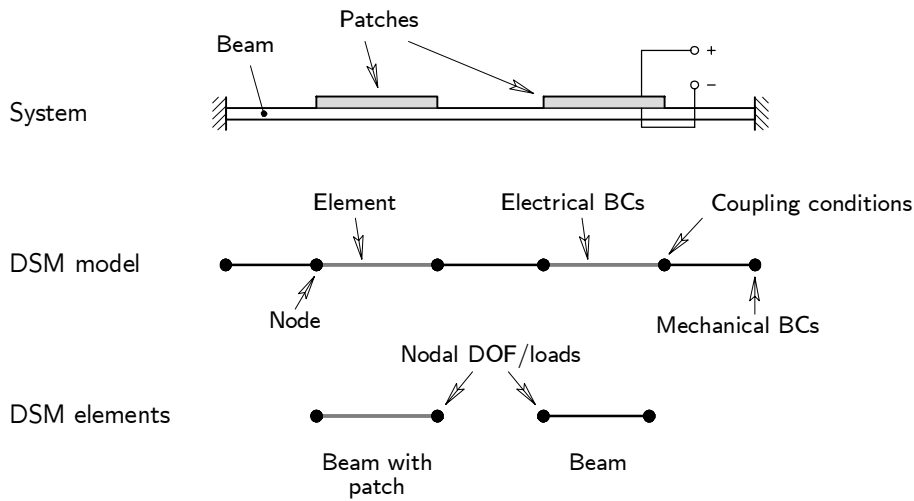


Figure 3.6: Schematic representation of the DSM method.

each element, the displacement and rotation at the nodes (nodal degrees of freedom) are related to the force and moment at the nodes (nodal loads) by means of a frequency dependent matrix, the so-called *dynamic stiffness matrix*. The exact solution of the governing equation of motion is used to create such an element matrix. Elements are coupled with the continuity and equilibrium equations at the nodes, resulting in a system matrix. Together with boundary conditions and external loads (i.e. structural and/or electrical) the system can be solved to obtain the frequency response of the nodal degrees of freedom.

The DSM method is, to some extent, similar to the finite element method. In both cases the structure is divided into a number of elements. However, the shape functions that are used to describe the spatial dependence of a variable are different. In finite element formulations linear or quadratic shape functions are often used, whereas in the DSM method the exact solution is used. Therefore, the DSM method does not require a minimum number of elements per wavelength. As a result the system matrix remains small. A drawback is that the exact solution must be available. This condition limits the DSM method to simple wave propagation problems, such as beams, for which the exact solution is available.³

³The DSM method can also be used for other one-dimensional problems, such as acoustic wave propagation in tubes [2].

The element matrix for a beam with one surface bonded patch is derived in Appendix B. Here only the result is given:

$$\begin{bmatrix} \mathbf{K}_{11} & \mathbf{k}_{12} \\ \mathbf{k}_{12}^T & k_{22} \end{bmatrix} \begin{Bmatrix} \mathbf{w} \\ V \end{Bmatrix} = \begin{Bmatrix} \mathbf{f} \\ Q \end{Bmatrix}, \quad (3.18)$$

where \mathbf{w} is the vector with nodal displacements and rotations, \mathbf{f} is the vector with nodal forces and moments, V is the voltage across the electrodes of the patch and Q is the charge on the electrodes. It is noted that in the element matrix, only \mathbf{K}_{11} is frequency dependent. The components of \mathbf{k}_{12} and k_{22} are constant. This is in correspondence with the quasi-static field assumption in the derivation of the basic equations for piezoelectricity (see Section 2.4).

Two beam parts can be coupled by demanding continuity of displacement and rotation, and force and moment equilibrium in the node that is shared by the two parts. The derivations of the element formulations for other beam parts (e.g. no patch or symmetric configuration) is similar to the analysis presented in Appendix B.

Actuator/sensor reciprocity

Because the element matrix given in equation (3.18) is symmetric, a duality exists between actuation and sensing with a piezoelectric patch. This duality is shown in Figure 3.7 for a single element with simply supported end conditions. The load on the structure induced by a voltage is equivalent with a pair of opposite bending moments at the supports. When the patch is used as a charge sensor, i.e. the electrodes are short circuited ($V = 0$), the charge on the electrodes for some deformed shape is proportional to the difference between the slopes at the beam edges.

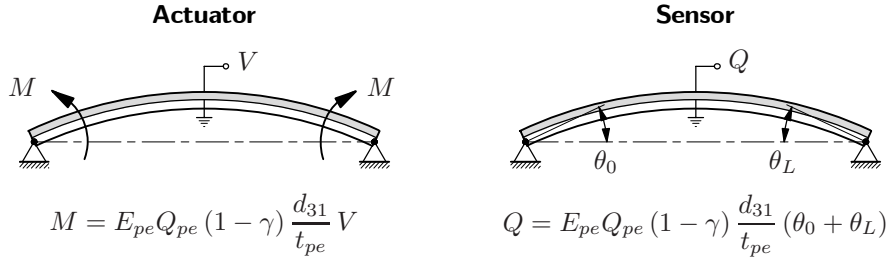


Figure 3.7: Reciprocity between actuation and sensing ($\gamma = E_{pe} A_{pe} / (EA)_{eq}$).

It is important to note that this interpretation of a piezoelectric actuator and sensor is valid only for a patch with a constant width. If for instance the width varies along the beam, then transverse forces are also introduced by an actuator [4], but the reciprocity between actuation and sensing remains.

3.4 Modal behaviour

In this section the modal behaviour of a beam with one surface bonded piezoelectric patch is considered. The setup is shown in Figure 3.8 and the model parameters are given in Table 3.2. In the following, the influence of the mass and stiffness of the patch on the eigenfrequencies is considered. It is furthermore shown how the eigenfrequencies depend on the type of electrical boundary condition on the electrodes (short circuit or open circuit). The DSM model of the setup consists of three elements. Clamped boundary conditions are applied at the beam ends. The eigenfrequencies have been determined with a numerical scheme for solving the characteristic equation $\det(\mathbf{K}_{\text{sys}}) = 0$, where \mathbf{K}_{sys} is the system matrix. Because no damping is included in the model, the eigenfrequencies are real numbers.

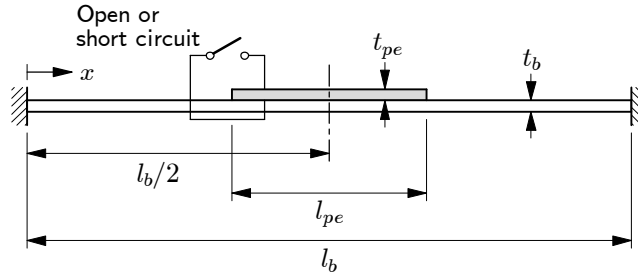


Figure 3.8: A beam clamped on both sides with one surface bonded patch.

Beam			Patch		
l_b	0.49	m	b_{pe}	0.03	m
b_b	0.03	m	ρ_{pe}	7760	kg/m ³
t_b	$1.2 \cdot 10^{-3}$	m	E_{pe}	$59.5 \cdot 10^9$	N/m ²
ρ_b	2710	kg/m ³	d_{31}	$-2.14 \cdot 10^{-10}$	m/V
E_b	$70 \cdot 10^9$	N/m ²	ε_{33}^σ	$1.87 \cdot 10^{-8}$	F/m

Table 3.2: Model parameters (see Figure 3.8). The length l_{pe} and thickness t_{pe} of the patch vary per analysis.

3.4.1 Mass and stiffness effects

The effects of mass and stiffness are demonstrated by varying the thickness and length of the patch. The patch is subjected to a short circuit boundary condition ($V = 0$). In Figure 3.9(a) the relative change of the eigenfrequencies

of the first five modes is shown as a function of the normalised patch thickness t_{pe}/t_b . The patch length is one fifth of the beam length ($l_{pe} = l_b/5$). The relative change of an eigenfrequency f_m is defined as $(f_m - f_m^b)/f_m^b$, where f_m^b is the eigenfrequency of the beam without patch and m is the mode number. Not surprisingly, thicker patches result in a bigger change of the eigenfrequencies.

A surface bonded patch introduces both mass and stiffness effects. The mass effect results in a decrease of the eigenfrequency, whereas the stiffness effect results in an increase of the eigenfrequency. The mode shapes are helpful for understanding which of the two effects is dominant.

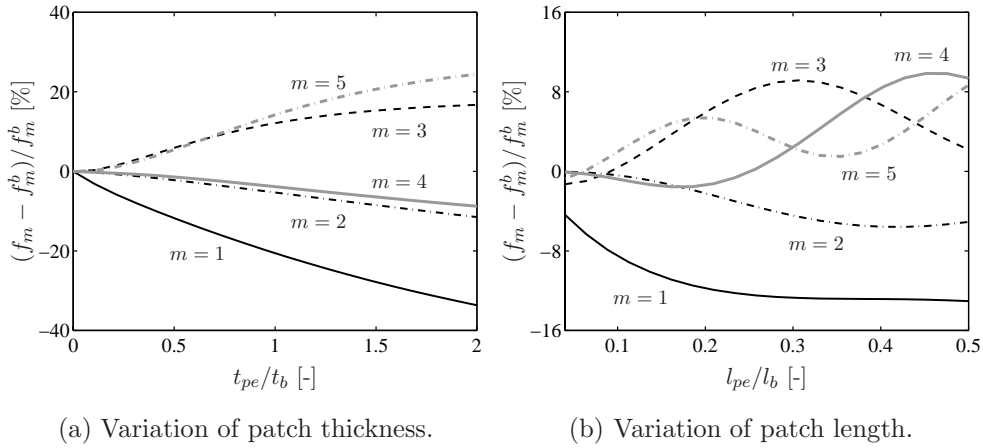


Figure 3.9: Eigenfrequency variation as a function of (a) the patch thickness ($l_{pe} = l_b/5$) and (b) the patch length ($t_{pe} = t_b/2$), where m is the mode number.

In Figure 3.10 the first four mode shapes of the beam with patch and those of the beam without patch are compared. In the case of the first mode, the location of the patch corresponds to a region where the displacement of the mode shape is high. Because the wavelength associated with the first mode is large compared to the patch length, the mass effect is dominant. Therefore, in Figure 3.9(a) the first eigenfrequency decreases with increasing patch thickness. In the case of the third mode, the patch is also in a region with high displacement. However, because the wavelength of this mode is close to the patch length, the stiffness effect is dominant for this mode. As a consequence, the corresponding eigenfrequency increases with increasing patch thickness. For the second and fourth modes, the location of the patch is close to a nodal line. Again the mass effect is dominant, although the relative decrease of the corresponding eigenfrequencies is less than for the first mode.

It is stressed that the shape of the curves in Figure 3.9(a) strongly depends on the length and location of the patch.

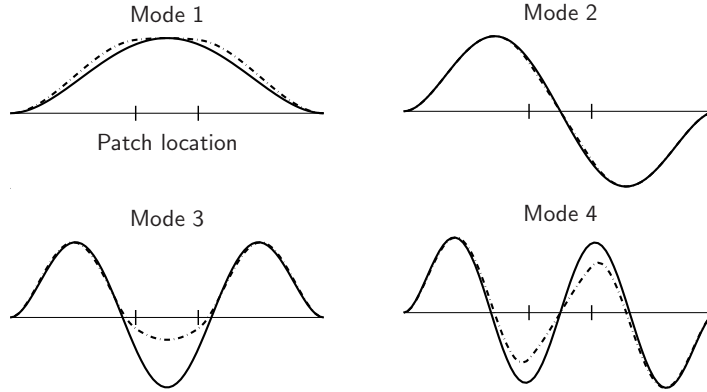


Figure 3.10: Comparison of the first four mode shapes of a beam without patch (—) and a beam with patch (----) ($l_{pe} = l_b/5$, $t_{pe} = t_b$).

A similar argumentation can be given for the results shown in Figure 3.9(b), where the relative change of the eigenfrequencies is shown as a function of the normalised patch length l_{pe}/l_b . Again the change of the eigenfrequencies is significant. The eigenfrequencies are not shown for very small patches, because the model is only valid for $t_{pe}/l_{pe} \ll 1$. As the length of the patch is increased, the relative importance of the mass and stiffness effects changes, which explains the shape of the curves. Because higher modes have shorter wavelengths, the “waveness” of the curves increases with the mode number.

3.4.2 Piezoelectric coupling effect

In Section 2.5 the effect of piezoelectric coupling was demonstrated for the longitudinal vibration of a piezoelectric bar. It was found that the eigenfrequencies depend on the piezoelectric and dielectric material properties and on the electrical boundary conditions. The effect of piezoelectric coupling is considered here for the beam setup shown in Figure 3.8.

The top electrode is divided into two separated parts, i.e. there is no direct electrical contact between the two parts. One part is subjected to a *short circuit* electrical boundary condition ($V = 0$) and the other part is subjected to an *open circuit* boundary condition ($Q = 0$).

In Figure 3.11 the relative change of the eigenfrequencies is shown as a function of the normalised length of the *short circuited* electrode l_{pe}^s/l_{pe} . Note that the cases $l_{pe}^s/l_{pe} = 0$ and $l_{pe}^s/l_{pe} = 1$ correspond to setups with a single

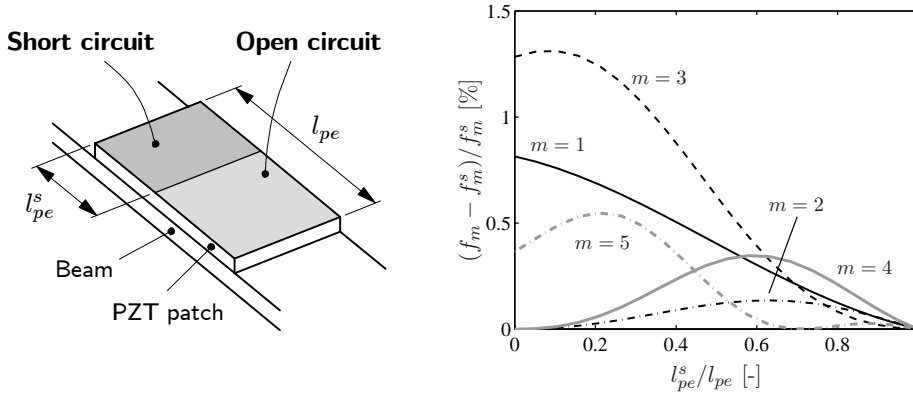


Figure 3.11: Eigenfrequency variation as a function of the length of the short circuited electrode.

electrode with an open circuit and short circuit, respectively. The relative change of an eigenfrequency f_m is defined as $(f_m - f_m^s)/f_m^s$, where f_m^s is the eigenfrequency of mode m for $l_{pe}^s/l_{pe} = 1$ (short circuit). The variation of the eigenfrequencies is very small compared to the mass and stiffness effects discussed previously ($< 1.5\%$). Therefore the piezoelectric coupling effect is only weak for a beam with a surface bonded patch.

3.5 Active structural acoustic control

In this section a basic analysis of ASAC is presented for a *strip* with surface bonded piezoelectric *actuator* patches. In this context a strip is a plate with an infinite length in one direction. The structural response of the strip is obtained with the model presented in Section 3.3. The concept of ASAC is presented for two different disturbance sources which are considered to be representative for structural and acoustic excitation of the strip. The results emphasize the difference between ASAC and active vibration control (AVC). More thorough discussions on this subject can be found for instance in references [8, 9, 11] and the book of Fuller [10].

3.5.1 Optimal control

In the present analysis a highly idealised control system is used. The control problem is formulated as to find the control input (i.e. actuator voltage) which minimises a given quadratic error criterion. A detailed outline of this control approach can be found in Chapter 5. In this section the method is only briefly

discussed. The main assumptions are that the overall system is linear (i.e. structural, electrical and acoustical) and that all signals are in steady state so that the effect of control can be considered on each frequency independently.

To illustrate the difference between ASAC and AVC, two error criteria are used. The first error criterion is the *radiated sound power*, which is a convenient measure for free field sound radiation. A numerical method for calculating the radiated sound power is presented in Chapter 4. The resulting expression for the radiated sound power \bar{W} is:

$$\bar{W} = \mathbf{v}_n^H \mathbf{R} \mathbf{v}_n, \quad (3.19)$$

where \mathbf{v}_n is the vector with velocities in the transverse direction at discrete points on the strip (normal velocity), and \mathbf{R} is the so-called *radiation resistance matrix* (see Section 4.3.1). Note that \mathbf{v}_n^H denotes the complex conjugate and transpose of \mathbf{v}_n (Hermitian).

The second error criterion is a measure for the strip vibration in the transverse direction. This criterion, which will be called the *vibration level*, is defined as the space and time average of the squared normal velocity of the strip. In discrete form, the vibration level $\langle \bar{v}_n^2 \rangle$ is given by (see Chapter 4):

$$\langle \bar{v}_n^2 \rangle = \mathbf{v}_n^H \mathbf{N} \mathbf{v}_n. \quad (3.20)$$

It is assumed that the strip is excited by a single disturbance source with amplitude f_d (e.g. point force), and that a single actuator patch with voltage V_c is available for control. With the system being linear, the normal velocity of the strip can be written as:

$$\mathbf{v}_n = \mathbf{h}_d f_d + \mathbf{h}_c V_c. \quad (3.21)$$

where \mathbf{h}_d and \mathbf{h}_c are vectors whose elements are the frequency response functions from the disturbance input and control input, respectively, to the normal velocity at each point on the strip.

Both error criteria are quadratic in terms of the normal velocity vector \mathbf{v}_n and can be written in the general form:

$$J = \mathbf{v}_n^H \mathbf{W} \mathbf{v}_n. \quad (3.22)$$

The control input that minimises this quadratic error criterion is given by (see Chapter 5):

$$V_c^{\min} = - (\mathbf{h}_c^H \mathbf{W} \mathbf{h}_c)^{-1} \mathbf{h}_c^H \mathbf{W} \mathbf{h}_d f_d, \quad (3.23)$$

provided that $\mathbf{h}_c^H \mathbf{W} \mathbf{h}_c$ is not singular. The optimal control input V_c^{\min} is substituted into equation (3.21) for the strip vibration in order to evaluate the control performance (e.g. in terms of radiated sound power or vibration level).

3.5.2 Setup

The system that is studied consists of a baffled strip which is clamped on both sides. As a first step, one piezoelectric actuator patch is bonded to the strip. Two different disturbances are considered, which are shown in Figure 3.12. First, the strip vibration is induced by a point force that is considered to be representative of a structural disturbance. Second, an acoustic plane wave incident on the strip at an oblique angle is taken as the disturbance.

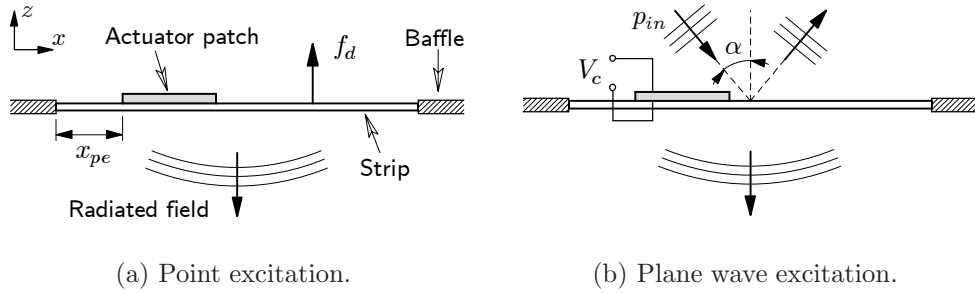


Figure 3.12: A baffled strip with one actuator patch excited by (a) a point force, or (b) a plane wave. The setup is infinitely wide in the direction perpendicular to the (x, z) -plane.

The dimensions and material properties of the beam and the material properties of the patch are given in Table 3.2. The length and thickness of the patch are 50 mm and 1.0 mm, respectively. The offset between the left ends of the beam and patch is $x_{pe} = 85$ mm (see Figure 3.12(a)). No attempt has been made to optimally configure the actuator; the choice of the location and size is made on an ad-hoc basis. The acoustic medium surrounding the strip is air ($\rho_0 = 1.2$ kg/m³ and $c_0 = 343$ m/s). Note that all results presented in the following sections are calculated per unit width.

3.5.3 Structural excitation

The disturbance is a transverse point force applied at $x = 0.3$ m with an amplitude $f_d = 1.0$ N/m.⁴ The optimal actuator voltage is calculated for the structural error criterion $J = \langle \bar{v}_n^2 \rangle$ and for the acoustic error criterion $J = \bar{W}$. In Figures 3.13 and 3.14 the corresponding vibration levels and radiated sound powers are shown for the frequency range from 10 to 1000 Hz. The vibration

⁴In fact the force is a line force because the strip is infinite in one direction.

level and radiated sound power for a strip without patch are also included in the results.

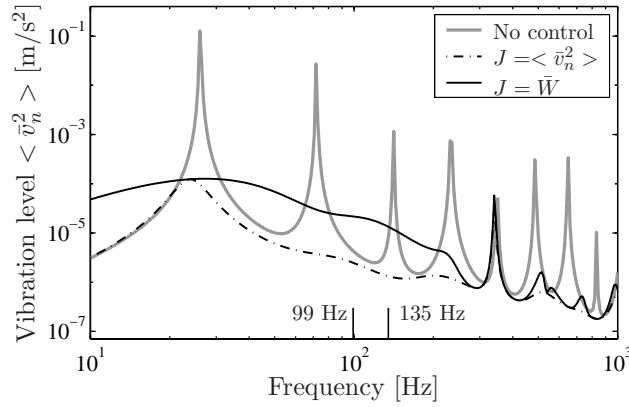


Figure 3.13: Vibration level with and without control for point force excitation.

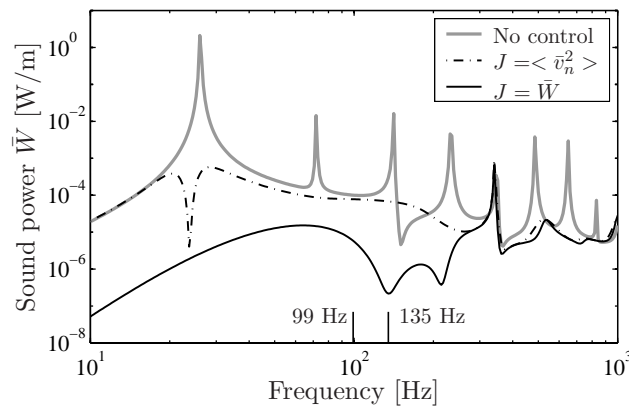


Figure 3.14: Sound power with and without control for point force excitation.

In Figure 3.13 the “dash-dotted” line ($J = \langle \bar{v}_n^2 \rangle$) corresponds to the best possible reduction of the vibration level for this location of the patch (and point force). On the other hand, in Figure 3.14 the “dashed” line ($J = \bar{W}$) corresponds to the best possible reduction of the sound power.

The results illustrate that ASAC is not simply a matter of applying AVC. When the actuator is driven such that the sound power is minimised, the vibration level is even increased at certain frequencies, when compared with the vibration level without control. A reduction of the vibration level leads

to a reduction of the radiated sound, but the performance is by no means optimal.

For both error criteria, control is more effective at low frequencies, although the response near the higher resonance frequencies is reduced. The number of vibration modes contributing to the response in off-resonance regions increases with frequency. In general only one vibration mode can be suppressed with one actuator, hence the overall reduction in off-resonance regions is less at the higher frequencies.

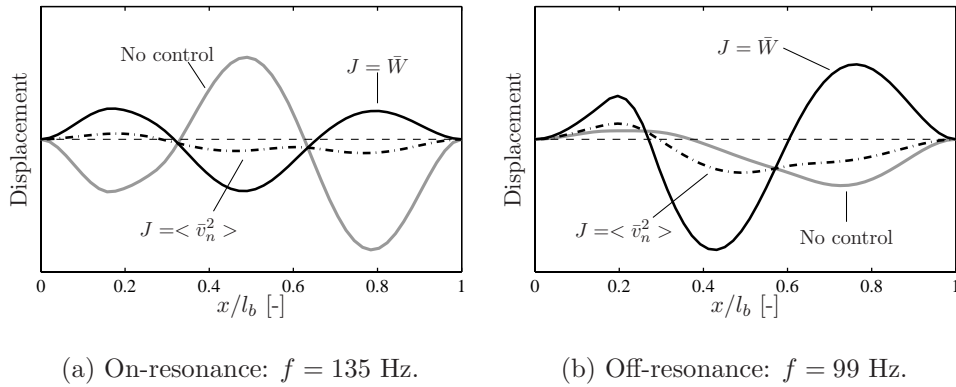


Figure 3.15: (a) On-resonance and (b) off-resonance vibration shapes, with and without control.

In Figure 3.15(a) the vibration shapes with and without control are shown for a frequency of 135 Hz. This frequency is very close to the third resonance frequency, which makes these vibration shapes correspond to an “on-resonance” excitation. For both error criteria a decrease in the vibration amplitude is observed, but the reduction is more significant when the vibration level is minimised. Near a resonance frequency the strip response is dominated by a single vibration mode. The reduction of sound radiation is obtained by suppressing the participation of the dominant mode. This mechanism is referred to as *modal suppression* [9, 10].

In Figure 3.15(b) the vibration shapes are shown for a frequency of 99 Hz, which corresponds to an “off-resonance” excitation. In an off-resonance region several vibration modes contribute to the sound radiation. In the case of minimisation of the radiated sound power, the response is changed such that the resulting vibration shape is a less efficient sound radiator. As shown in the figure, this may even result in an increase of the vibration. This mechanism for off-resonance sound radiation control is called *modal restructuring* [9, 10].

The frequency range considered here is well below the *coincidence frequency*. At the coincidence frequency the structural wavelength in the strip is equal to the acoustic wavelength in the direction along the strip. Well below coincidence, the acoustic wavelength is much larger than the structural wavelength. As a result, so-called *volumetric* vibration shapes (e.g. the odd modes) are much better radiators than *non-volumetric* vibration shapes (e.g. the even modes). It is therefore no surprise that the vibration shapes associated with the minimisation of radiated sound power are non-volumetric, both on-resonance and off-resonance.

3.5.4 Acoustic excitation

The pressure associated with an acoustic plane wave travelling in free space is given by:

$$p(x, z) = p_{in} e^{-jk(x \sin(\alpha) - z \cos(\alpha))}, \quad (3.24)$$

where $k = \omega/c_0$ is the acoustic wave number with c_0 the speed of sound, p_{in} is the amplitude of the wave, and α is the angle between the direction of propagation and the z -axis (see Figure 3.12(b)). Under the assumption that the fluid loading is small, the pressure on the strip can be described by the so-called *blocked pressure* [47]. The blocked pressure is the surface pressure on a rigid strip which totally reflects the incident wave. The disturbance load on the strip is therefore twice the incident pressure and is given by:

$$f(x) = -2p_{in} e^{-jkx \sin(\alpha)}. \quad (3.25)$$

A convenient measure for sound transmission problems is the *transmission loss* TL , which is here defined as:

$$TL = 10 \log_{10} \left(\frac{\bar{W}_{in}}{\bar{W}} \right), \quad (3.26)$$

where \bar{W} is the radiated sound power and \bar{W}_{in} is the incident sound power, which is defined as:

$$\bar{W}_{in} = \frac{|p_{in}|^2 l_b \cos(\alpha)}{2\rho_0 c_0} + \bar{W}, \quad (3.27)$$

where ρ_0 is the density of the acoustic medium. The first term on the right hand side of this equation is the power associated with the incident plane wave. The radiated sound power is added to ensure that the transmission loss is a positive number, which is a physical constraint (see Basten [3]).

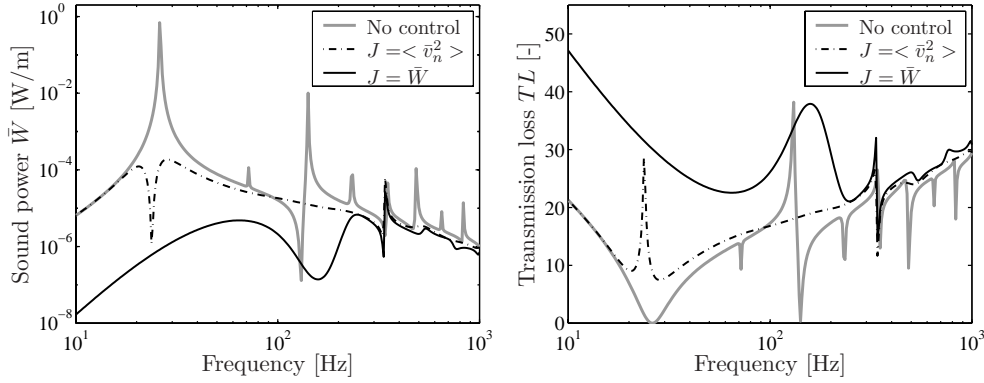


Figure 3.16: Radiated sound power (left) and transmission loss (right) with and without control for plane wave excitation ($p_{in} = 1$, $\alpha = \pi/4$).

Again the vibration level and the radiated sound power are used as error criteria. Figure 3.16 gives the results with and without control for an incident plane wave with $p_{in} = 1$ and $\alpha = \pi/4$. Both the radiated sound power and the transmission loss are shown. The results for the radiated sound power are similar to those obtained for structural excitation (see Figure 3.14). That is, the reduction of the radiated sound power is far from optimal when the vibration level is minimised.

The transmission loss that is obtained if no control is applied is typical for bounded plate structures below coincidence. There is an average increase with frequency for frequencies above the first eigenfrequency, and small dips occur at the higher resonance frequencies. It can be observed that with the current setup, i.e. with one actuator patch, the control of sound radiation is effective in a limited frequency band. As will be shown in the next section, more actuators must be applied to obtain better performance.

3.5.5 Multiple actuators

To illustrate the effect of using multiple actuators, a comparison is made between the control performances obtained with one, two and three actuator patches. Only the control of radiated sound power is considered ($J = \bar{W}$). The patches have equal dimensions ($l_{pe} = 50$ mm, $t_{pe} = 1.0$ mm). The offsets between the left end of the beam and the left ends of the patches are 85 mm, 220 mm and 355 mm respectively. Note that three different DSM models are used.

In Figure 3.17 the sound power and transmission loss are shown for each of

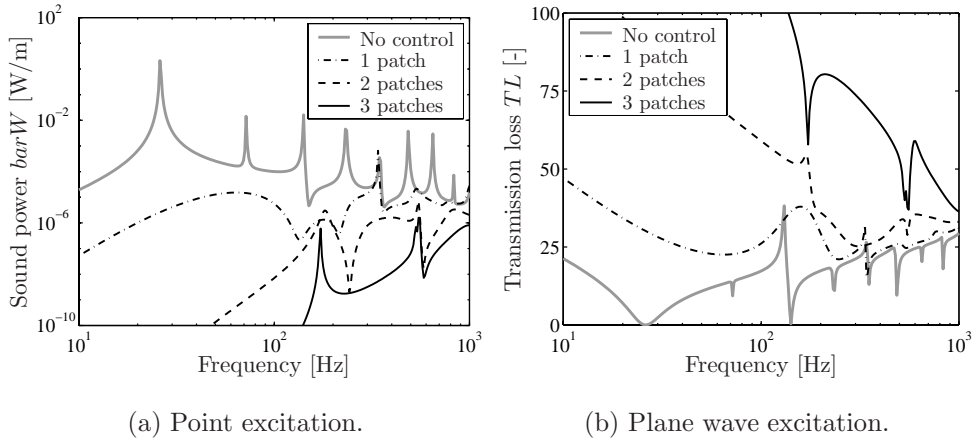


Figure 3.17: (a) Radiated sound power for point force excitation and (b) transmission loss for plane wave excitation for one, two and three control actuators.

the three configurations. The results show a clear improvement of the control performance if more actuators are used. That is, with more actuators larger reductions of the sound power and higher transmission losses are obtained.

Although the results are very promising, one should be aware that the system under consideration is highly idealised. The setup comprises a two-dimensional sound radiation problem, whereas real-life problems are three-dimensional. Real-life structures are characterised by higher modal densities than the current test problem. As a result, the control performance is limited to frequencies much lower than for the results shown in Figure 3.17. Besides, the error criteria that were considered are far from practical. A quantity such as the radiated sound power is not easily measured in practice. The use of a small number of discrete sensors, e.g. microphones, will certainly degrade the performance. These and other issues will be considered in more detail in Chapters 5 and 6.

3.6 Concluding remarks

In this chapter a model for the dynamical behaviour of a beam with surface bonded piezoelectric patches was presented. The most important features of the model are that a perfect bonding condition between the beam and a patch is assumed and that the mass and stiffness of a patch are accounted for. The dynamic stiffness matrix formulation was used to implement the model. This

implementation makes it possible to model beams with multiple piezoelectric actuator and sensor patches, in asymmetric or symmetric configurations.

It was demonstrated for a setup consisting of a beam with one surface bonded patch that the mass and stiffness of the patch can be of significant influence on the modal behaviour of the structure. When a large part of the structure is covered with piezoelectric material (e.g. multiple small patches) these effects must be included in the model to obtain an accurate prediction of the dynamical behaviour. The added stiffness introduced by the piezoelectric coupling is of minor importance for surface bonded patches and can therefore be neglected.

A preliminary study of ASAC was presented for a test problem consisting of a plate that is infinitely long in one direction with one or more actuator patches. The effect of optimal control was considered for two error criteria: one related to the structural response (vibration level) and the other related to the acoustic response (radiated sound power). It was demonstrated that ASAC is not simply a matter of applying AVC. In the off-resonance frequency ranges, control of radiated sound power can even be accompanied by an increase in vibration. Because the problem concerns a highly idealised structure and control system, the control performances that were found for the test problem must not be expected in practice.

Chapter 4

Numerical Modelling and Experimental Validation

4.1 Introduction

In the previous chapter an analytical model was used in a basic study of active structural acoustic control (ASAC). Analytical models are very useful for studying the underlying physics but are generally not suitable for representing “real life” structures with complex geometries and boundary conditions. A more advanced modelling technique is considered in this chapter. The goal is to develop an analysis tool which can serve as a basis for the design of an active control system. This tool is capable of describing the structural dynamics of plate-like structures with piezoelectric patches and the corresponding free field sound radiation. The analysis tool is validated with experiments.

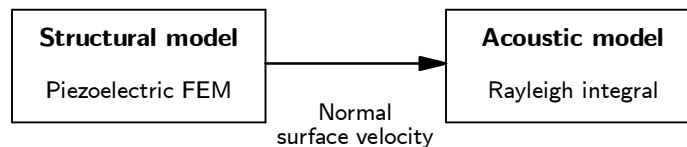


Figure 4.1: “Uncoupled” structural-acoustic analysis.

A vibrating structure which is surrounded by an acoustic medium causes pressure perturbations in the medium, which are experienced as sound. On the other hand, the pressure perturbations in the acoustic medium act as a load on the structure. When the medium is air, which is assumed in this work, the influence of the medium on the structural vibration can be neglected. It

is therefore allowed to perform an uncoupled analysis of the structural and acoustic responses, which is illustrated in Figure 4.1.

In the first part of the analysis, the structural vibration response due to one or more inputs acting on the structure is calculated. The *finite element method* (FEM) is used to model the dynamical behaviour of the structure and the piezoelectric patches bonded on the structure. This model is referred to as the *structural model*.

In the second part of the analysis, the free field sound radiation associated with the structural vibration is calculated. The normal surface velocity distribution calculated with the structural model is used as an input for this analysis. In the present work, the analysis is restricted to baffled plates for which the *Rayleigh integral method* can be applied. This model is referred to as the *acoustic model*.

For both the structural model and acoustic model, reduction techniques are applied in order to reduce computation time. In the case of the structural model the reduction is based on a superposition of the *structural modes*, whereas for the acoustic model a superposition of so-called *radiation modes* is applied. Furthermore, the governing equations are transformed to a state space representation, which is very often used for control system design.

It is stressed that the “open-loop” system is considered in this chapter. This means that the numerical and experimental results do not involve an active control system. The application of the analysis tool for ASAC will be considered in later chapters.

This chapter is divided into three parts. In Section 4.2 the structural model is discussed. The piezoelectric finite element equations are introduced and a modal reduction method for these equations is presented. Next, in Section 4.3 the acoustic model is presented. For baffled plate structures the Rayleigh integral can be used to calculate the field pressure and the radiated sound power. The calculation of the radiated sound power can be performed more efficiently using a superposition of radiation modes. In Section 4.4 the numerical method is validated with experiments. The experimental setup consists of a clamped rectangular plate with two surface bonded PZT patches. A comparison of numerical and experimental results is given for the structural and acoustic domain.

4.2 Structural model

4.2.1 Piezoelectric FEM equations

The finite element modelling of plates and shells with surface bonded or embedded piezoelectric patches has received considerable attention in recent years. As a result, a large number of finite element formulations have been developed and published, as described in the review article of Benjeddou [48]. Nowadays commercial finite element codes are equipped with elements with piezoelectric capabilities.

The finite element equations of motion for a structure exhibiting linear piezoelectric behaviour are given by:

$$\begin{bmatrix} \mathbf{M}_{uu} & \mathbf{0} \\ \mathbf{0} & \mathbf{0} \end{bmatrix} \begin{Bmatrix} \ddot{\mathbf{u}}(t) \\ \ddot{\boldsymbol{\phi}}(t) \end{Bmatrix} + \begin{bmatrix} \mathbf{C}_{uu} & \mathbf{0} \\ \mathbf{0} & \mathbf{0} \end{bmatrix} \begin{Bmatrix} \dot{\mathbf{u}}(t) \\ \dot{\boldsymbol{\phi}}(t) \end{Bmatrix} + \begin{bmatrix} \mathbf{K}_{uu} & \mathbf{K}_{u\phi} \\ \mathbf{K}_{\phi u} & \mathbf{K}_{\phi\phi} \end{bmatrix} \begin{Bmatrix} \mathbf{u}(t) \\ \boldsymbol{\phi}(t) \end{Bmatrix} = \begin{Bmatrix} \mathbf{f}(t) \\ \mathbf{g}(t) \end{Bmatrix}, \quad (4.1)$$

where $\mathbf{u}(t)$ is the vector with nodal structural displacements, and $\boldsymbol{\phi}(t)$ is the vector with nodal voltages. Matrices \mathbf{M}_{uu} , \mathbf{C}_{uu} , and \mathbf{K}_{uu} are the structural mass, damping and stiffness matrices, respectively. The piezoelectric coupling is represented by the piezoelectric stiffness matrices $\mathbf{K}_{u\phi}$ and $\mathbf{K}_{\phi u} = \mathbf{K}_{u\phi}^T$, and $\mathbf{K}_{\phi\phi}$ is the dielectric stiffness matrix. The external loads are stored in the vector with nodal forces $\mathbf{f}(t)$ and the vector with nodal charges $\mathbf{g}(t)$. In equation (4.1) no distinction is made between the structure and the piezoelectric material. Obviously, the piezoelectric stiffness matrix and dielectric stiffness matrix are zero in the structure. The basic equations for the derivation of the piezoelectric FEM formulation were introduced in Section 2.4. Quasi-static behaviour of the electric field was assumed there, which explains why the mass and damping matrices in equation (4.1) do not contain contributions related to the electric field.

The basic idea is to obtain a state space representation of the FEM model which can serve as a basis for the design of a controller. In general, a FEM model must include many degrees of freedom (DOF) in order to obtain an accurate prediction of the dynamical behaviour. A model with a large number of DOF is not really suited for the design of a controller, as its evaluation requires considerable computational effort. For this reason a model reduction technique is applied to reduce the number of DOF in the model. The method is similar to the *mode superposition technique*. The mode superposition method is often used in the field of structural dynamics, but is applied here for the piezoelectric finite element formulation. The result is a compact dynamical model, which can be evaluated with little computational effort.

A piezoelectric material can be used either to excite a structure, i.e. as a voltage or charge driven actuator, or to measure vibration, i.e. as a voltage or charge sensor. To make the reduction method applicable for all those cases, a distinction is made between two types of electrodes:

- Electrodes with a *prescribed voltage*, which applies for voltage driven actuators and charge sensors (short circuit).
- Electrodes with a *prescribed charge*, which applies for charge driven actuators and voltage sensors (open circuit).

The vector with nodal voltages and the vector with nodal charges are divided according to this subdivision of electrical boundary conditions:

$$\boldsymbol{\phi}(t) = \begin{Bmatrix} \boldsymbol{\phi}^v(t) \\ \boldsymbol{\phi}^c(t) \end{Bmatrix}, \quad \mathbf{g}(t) = \begin{Bmatrix} \mathbf{g}^v(t) \\ \mathbf{g}^c(t) \end{Bmatrix}, \quad (4.2)$$

where the superscript v refers to *prescribed voltage* and the superscript c refers to *prescribed charge*. Note that $\boldsymbol{\phi}^v(t)$ and $\mathbf{g}^c(t)$ are given inputs to the system, whereas $\boldsymbol{\phi}^c(t)$ and $\mathbf{g}^v(t)$ are outputs of the system. The electrical DOF of nodes which are not on an electrode surface are handled as prescribed charge DOF, with $\mathbf{g}^c(t) = \mathbf{0}$. With the distinction between prescribed voltage and charge DOF, the equation of motion (4.1) becomes:

$$\begin{bmatrix} \mathbf{M}_{uu} & \mathbf{0} & \mathbf{0} \\ \mathbf{0} & \mathbf{0} & \mathbf{0} \\ \mathbf{0} & \mathbf{0} & \mathbf{0} \end{bmatrix} \begin{Bmatrix} \ddot{\mathbf{u}}(t) \\ \ddot{\boldsymbol{\phi}}^v(t) \\ \ddot{\boldsymbol{\phi}}^c(t) \end{Bmatrix} + \dots + \begin{bmatrix} \mathbf{K}_{uu} & \mathbf{K}_{u\phi}^v & \mathbf{K}_{u\phi}^c \\ \mathbf{K}_{\phi u}^v & \mathbf{K}_{\phi\phi}^{vv} & \mathbf{K}_{\phi\phi}^{vc} \\ \mathbf{K}_{\phi u}^c & \mathbf{K}_{\phi\phi}^{cv} & \mathbf{K}_{\phi\phi}^{cc} \end{bmatrix} \begin{Bmatrix} \mathbf{u}(t) \\ \boldsymbol{\phi}^v(t) \\ \boldsymbol{\phi}^c(t) \end{Bmatrix} = \begin{Bmatrix} \mathbf{f}(t) \\ \mathbf{g}^v(t) \\ \mathbf{g}^c(t) \end{Bmatrix}. \quad (4.3)$$

For ease of writing the damping forces have been omitted in this equation. In the mode superposition method the response is written in terms of the eigenmodes of the system. In order to perform an eigenvalue analysis, the nodal voltages $\boldsymbol{\phi}^c(t)$ are condensed from the system. The third row in equation (4.3) can also be written as:

$$\boldsymbol{\phi}^c(t) = (\mathbf{K}_{\phi\phi}^{cc})^{-1} [-\mathbf{K}_{\phi u}^c \mathbf{u}(t) - \mathbf{K}_{\phi\phi}^{cv} \boldsymbol{\phi}^v(t) + \mathbf{g}^c(t)]. \quad (4.4)$$

Substitution of this equation into the first row in equation (4.3) gives an equation of motion in terms of the structural displacement vector $\mathbf{u}(t)$:

$$\mathbf{M}_{uu} \ddot{\mathbf{u}}(t) + \mathbf{C}_{uu} \dot{\mathbf{u}}(t) + \mathbf{K}_{uu}^* \mathbf{u}(t) = \mathbf{f}^*(t), \quad (4.5)$$

where the equivalent stiffness matrix \mathbf{K}_{uu}^* is given by:

$$\mathbf{K}_{uu}^* = \mathbf{K}_{uu} - \mathbf{K}_{u\phi}^c (\mathbf{K}_{\phi\phi}^{cc})^{-1} \mathbf{K}_{\phi u}^c, \quad (4.6)$$

and the equivalent force vector $\mathbf{f}^*(t)$ is defined as:

$$\mathbf{f}^*(t) = \mathbf{f}(t) - \mathbf{K}_{u\phi}^{v*} \phi^v(t) - \mathbf{K}_{u\phi}^c (\mathbf{K}_{\phi\phi}^{cc})^{-1} \mathbf{g}^c(t), \quad (4.7)$$

where $\mathbf{K}_{u\phi}^{v*} = \mathbf{K}_{u\phi}^v - \mathbf{K}_{u\phi}^c (\mathbf{K}_{\phi\phi}^{cc})^{-1} \mathbf{K}_{\phi u}^{cv}$. This equation shows that the electrical inputs $\phi^v(t)$ (prescribed voltages) and $\mathbf{g}^c(t)$ (prescribed charges) are written as equivalent structural loads. Once the structural displacement vector has been solved from equation (4.5), the voltages in the nodes with a prescribed charge boundary condition, $\phi^c(t)$, can be calculated with equation (4.4). The charges associated with the set of prescribed voltages, $\mathbf{g}^v(t)$, can be calculated as follows:

$$\mathbf{g}^v(t) = \mathbf{K}_{\phi u}^{v*} \mathbf{u}(t) + \mathbf{K}_{\phi\phi}^{vv*} \phi^v(t) + \mathbf{K}_{\phi\phi}^{vc} (\mathbf{K}_{\phi\phi}^{cc})^{-1} \mathbf{g}^c(t), \quad (4.8)$$

where $\mathbf{K}_{\phi u}^{v*} = (\mathbf{K}_{u\phi}^{v*})^T$ and $\mathbf{K}_{\phi\phi}^{vv*} = \mathbf{K}_{\phi\phi}^{vv} - \mathbf{K}_{\phi\phi}^{vc} (\mathbf{K}_{\phi\phi}^{cc})^{-1} \mathbf{K}_{\phi\phi}^{cv}$. This result is obtained after substitution of equation (4.4) into the second row in equation (4.3).

4.2.2 Model reduction

In the present approach the response is expanded in terms of the undamped eigenvectors of the problem. When the undamped free vibration is considered ($\mathbf{f}^*(t) = \mathbf{0}$), and harmonic time dependence is assumed ($\mathbf{u}(t) = \mathbf{u} e^{j\omega t}$), equation (4.5) reduces to the generalised eigenvalue problem:

$$\omega^2 \mathbf{M}_{uu} \mathbf{u} = \mathbf{K}_{uu}^* \mathbf{u}, \quad (4.9)$$

where ω is the angular frequency of vibration. The solution of this eigenvalue problem comprises n angular eigenfrequencies ω_i and corresponding eigenvectors $\hat{\mathbf{u}}_i$ ($i = 1 \dots n$), where n is the total number of structural DOF in the model. It was already shown in the previous chapters that the eigenfrequencies and eigenmodes (mode shapes) depend on the type of electrical boundary conditions. In equation (4.9) this effect is accounted for in the equivalent stiffness matrix \mathbf{K}_{uu}^* , see also equation (4.6). Only the electrical DOF with a prescribed charge boundary condition contribute to the equivalent stiffness matrix. The amount of change in stiffness (or a related property such as eigenfrequency) due to the piezoelectric coupling depends on the type of problem. In Section 2.5 it was shown that the piezoelectric coupling effect is significant for the longitudinal vibration of a piezoelectric bar. However, it was

concluded in Section 3.4 that the effect is negligible for a beam with surface bonded piezoelectric patches.

The matrix with eigenfrequencies Ω and the matrix with “structural” mode shapes Ψ_u are defined as:

$$\Omega = \begin{bmatrix} \omega_1 & 0 & \cdots & 0 \\ 0 & \omega_2 & \cdots & 0 \\ \vdots & \vdots & \ddots & \vdots \\ 0 & 0 & \cdots & \omega_n \end{bmatrix}, \quad \Psi_u = [\hat{\mathbf{u}}_1 \quad \hat{\mathbf{u}}_2 \quad \cdots \quad \hat{\mathbf{u}}_n]. \quad (4.10)$$

The mode shapes are normalised with respect to the mass matrix, thus satisfying the following normalisation:

$$\Psi_u^T \mathbf{M}_{uu} \Psi_u = \mathbf{I}, \quad (4.11a)$$

$$\Psi_u^T \mathbf{K}_{uu}^* \Psi_u = \Omega^2, \quad (4.11b)$$

where \mathbf{I} is the identity matrix. For each mode i , the nodal voltages $\hat{\phi}_i^v$ are calculated with equation (4.4) by substitution of a structural mode shape $\hat{\mathbf{u}}_i$, for the unforced case: $\mathbf{g}^c(t) = \mathbf{0}$ and $\phi^v(t) = \mathbf{0}$. The results are stored in the modal matrix Ψ_ϕ^c , which is related to the matrix with structural mode shapes by:

$$\Psi_\phi^c = -(\mathbf{K}_{\phi\phi}^{cc})^{-1} \mathbf{K}_{\phi u}^c \Psi_u. \quad (4.12)$$

In the mode superposition method the solution of equation (4.5) is written as:

$$\mathbf{u}(t) = \sum_{i=1}^n \hat{\mathbf{u}}_i q_i(t) = \Psi_u \mathbf{q}(t), \quad (4.13)$$

where $\mathbf{q}(t)$ is the column vector with mode participation factors, also referred to as generalised coordinates. Substitution of this solution into equation (4.5) and pre-multiplying through by Ψ_u^T yields:

$$\mathbf{I} \ddot{\mathbf{q}}(t) + \Psi_u^T \mathbf{C}_{uu} \Psi_u \dot{\mathbf{q}}(t) + \Omega^2 \mathbf{q}(t) = \Psi_u^T \mathbf{f}^*(t). \quad (4.14)$$

For this result the normalisation equations (4.11) have been used. The equation of motion in terms of the mode participation factors is only coupled through non-zero off-diagonal coefficients in matrix $\Psi_u^T \mathbf{C}_{uu} \Psi_u$. The internal damping of a structure is in many cases poorly known. It is often assumed that the structure exhibits *proportional* damping, which means that the viscous damping matrix is proportional to a linear combination of the mass and

stiffness matrices. In the case of proportional damping the generalised damping matrix reduces to a diagonal matrix of the form:

$$\mathbf{\Psi}_u^T \mathbf{C}_{uu} \mathbf{\Psi}_u = \text{diag}(2\zeta_i \omega_i) = 2 \mathbf{\Xi} \mathbf{\Omega}, \quad (4.15)$$

where ζ_i is damping ratio of mode i , and $\mathbf{\Xi} = \text{diag}(\zeta_i)$ is the so-called modal damping matrix. For a proportionally damped system the generalised equations of motion can thus be written as:

$$\mathbf{I} \ddot{\mathbf{q}}(t) + 2 \mathbf{\Xi} \mathbf{\Omega} \dot{\mathbf{q}}(t) + \mathbf{\Omega}^2 \mathbf{q}(t) = \mathbf{\Psi}_u^T \mathbf{f}^*(t), \quad (4.16)$$

or, because these generalised equations of motion comprise n uncoupled equations, as:

$$\ddot{q}_i(t) + 2\zeta_i \omega_i \dot{q}_i(t) + \omega_i^2 q_i(t) = \hat{\mathbf{u}}_i^T \mathbf{f}^*(t), \quad i = 1 \dots n. \quad (4.17)$$

Truncated modal expansion and residual flexibility

The response of a structure which is excited by a band-limited input is usually dominated by the modes with an eigenfrequency in or close to the frequency band of interest. A good estimate of the response in that frequency band is then obtained with only a small number of modes included in the modal expansion (4.13). However, in some cases truncating the modal expansion can lead to errors in the prediction of the dynamical behaviour (see Section 4.2.3 for an example).

With the concept of *residual flexibility* the accuracy of the truncated modal expansion can be improved [4]. This concept is explained with a frequency domain analysis, thus harmonic time dependence is introduced for all time dependent variables. It is assumed that an accurate prediction of the dynamical behaviour is desired in the frequency band $[0, \omega_b]$. The exact frequency domain solution of equation (4.5) can be written as:

$$\mathbf{u} = \sum_{i=1}^m \hat{\mathbf{u}}_i q_i + \sum_{i=m+1}^n \hat{\mathbf{u}}_i q_i, \quad q_i = \frac{\hat{\mathbf{u}}_i^T \mathbf{f}^*}{-\omega^2 + 2j\zeta_i \omega_i \omega + \omega_i^2}. \quad (4.18)$$

The common way is to truncate the expansion to m modes, where $m \ll n$. The resulting error in the prediction of \mathbf{u} is equal to the contributions of modes $m+1$ to n . The maximum frequency of interest ω_b is much smaller than the eigenfrequencies for modes satisfying $i > m$. Therefore, the response at low frequencies can be approximated by:

$$\mathbf{u} \approx \sum_{i=1}^m \frac{\hat{\mathbf{u}}_i \hat{\mathbf{u}}_i^T \mathbf{f}^*}{-\omega^2 + 2j\zeta_i \omega_i \omega + \omega_i^2} + \sum_{i=m+1}^n \frac{\hat{\mathbf{u}}_i \hat{\mathbf{u}}_i^T \mathbf{f}^*}{\omega_i^2}. \quad (4.19)$$

In this approximation the high frequency modes ($i > m$) contribute “statically” to the system response, whereas the low frequency modes ($i \leq m$) respond “dynamically”. The second right hand side term is often called the *residual mode*. Equation (4.19) can be transformed such that the high frequency modes, which are usually not calculated with a FEM program, do not appear in the expansion. The static displacement response \mathbf{u}_0 can be written as a modal expansion by inserting $\omega = 0$ into equation (4.18):

$$\mathbf{u}_0 = \sum_{i=1}^m \frac{\hat{\mathbf{u}}_i \hat{\mathbf{u}}_i^T \mathbf{f}^*}{\omega_i^2} + \sum_{i=m+1}^n \frac{\hat{\mathbf{u}}_i \hat{\mathbf{u}}_i^T \mathbf{f}^*}{\omega_i^2}. \quad (4.20)$$

With this result, equation (4.19) becomes:

$$\mathbf{u} \approx \sum_{i=1}^m \frac{\hat{\mathbf{u}}_i \hat{\mathbf{u}}_i^T \mathbf{f}^*}{-\omega^2 + 2j\zeta_i \omega_i \omega + \omega_i^2} + \mathbf{u}_0 - \sum_{i=1}^m \frac{\hat{\mathbf{u}}_i \hat{\mathbf{u}}_i^T \mathbf{f}^*}{\omega_i^2}. \quad (4.21)$$

The harmonic displacement response \mathbf{u} is now written in terms of modes 1 to m and the static response \mathbf{u}_0 due to \mathbf{f}^* . So the cost for a more accurate estimation of \mathbf{u} is the static response analysis that must be performed. The foregoing analysis is valid for a structure without rigid body modes. For a discussion on systems with rigid body modes, the reader is referred to Preumont [4].

4.2.3 Example: Strip problem

For a test case consisting of a strip with two asymmetric bonded patches the model reduction technique was validated (see Figure 4.2). Two PZT patches of equal size ($50 \times 30 \times 1.0$ mm) and equal material properties (PIC-151, see Appendix A) were bonded on the aluminium strip of $490 \times 30 \times 1.2$ mm. One patch was a voltage driven actuator (prescribed voltage) whereas the other patch was a voltage sensor (zero charge).

Three models of the test setup are considered: a dynamic stiffness matrix model (see Chapter 3), a two-dimensional FEM model and a three-dimensional FEM model. In this work the commercial finite element program ANSYS was used. Two element types with piezoelectric capabilities are available in ANSYS: a two-dimensional four-node solid element and a three-dimensional eight-node solid element [49]. So-called extra shape functions are included to enhance the accuracy of solid elements in bending problems [50].

The two-dimensional FEM model consisted of 64 two-node beam elements along the strip, with a finer mesh in the parts where the patches were located, i.e. 12 elements along each patch. The patches were modelled with the two-dimensional piezoelectric solid elements, both patches with 2 elements across

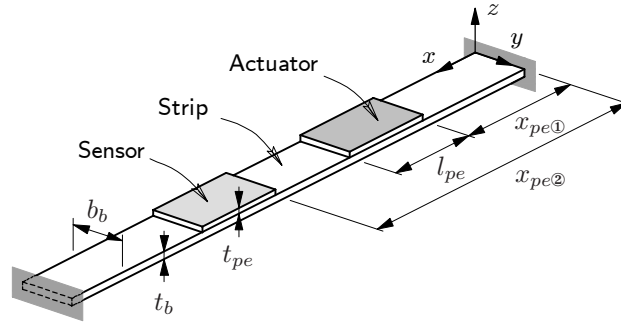


Figure 4.2: A strip clamped on both sides with two surface bonded patches.

the thickness. The three-dimensional FEM model had the same discretization along the length and 5 elements along the width of the strip. The strip and patches were modelled with four-node plate elements and three-dimensional piezoelectric solid elements. More details on the ANSYS models are given in Appendix C.

Eigenfrequencies

In Table 4.1 the first six eigenfrequencies calculated with the three models are listed. Furthermore, the eigenfrequencies of the same strip, but without patches, are shown. The three-dimensional FEM model also predicts the torsional and in-plane bending vibration modes of the system, but these are not included in the results.

Mode	No patches			Two patches		
	DSM	2D FEM	3D FEM	DSM	2D FEM	3D FEM
1	26.11	26.11	26.35	21.79	21.77	22.00
2	71.97	71.97	72.68	62.13	61.76	62.63
3	141.1	141.1	142.6	135.8	135.6	137.4
4	233.2	233.2	236.2	229.4	228.7	232.3
5	348.4	348.4	353.6	358.5	357.0	363.3
6	486.6	486.6	495.1	491.3	489.7	499.0

Table 4.1: Eigenfrequencies (in Hz) of the strip with and without patches. DSM: analytical model, 2D FEM: two-dimensional FEM model, 3D FEM: three-dimensional FEM model ($x_{pe1} = 138.3$ mm, $x_{pe2} = 342.5$ mm). Only bending modes are considered.

In both cases there is good correspondence between the eigenfrequencies. For the strip with patches, the eigenfrequencies calculated with the two-dimensional FEM model are closer to the analytical results than those calculated with the three-dimensional FEM model. The same is observed in the results of the strip without patches. The analytical model and the two-dimensional FEM model are based on the plane stress assumption, which is true if the width to thickness ratio b_b/t_p is small. For a plate infinitely wide in one direction the plane strain assumption is valid. For the strip with $b_b/t_p = 25$ the stress distribution will be somewhere in between the plane stress ($\omega_i \propto \sqrt{E}$) and plane strain ($\omega_i \propto \sqrt{E/(1-\nu^2)}$) limit cases. Therefore, it is not surprising that the three-dimensional FEM model predicts higher eigenfrequencies.

Frequency response functions

As a next step, the model reduction technique was validated with a frequency domain analysis. For this purpose, a comparison was made between frequency response functions (FRFs) which were calculated with the *three-dimensional* FEM model in three ways: a full analysis, i.e. directly solving the frequency domain equivalent of equation (4.3), a reduced analysis where the modal expansion is truncated to 15 modes, and a reduced analysis with the same number of modes, but enhanced with the residual mode.

The following form of proportional damping was used:

$$\mathbf{C}_{uu} = \alpha \mathbf{M}_{uu} + \beta \mathbf{K}_{uu}^*. \quad (4.22)$$

It can be shown that the modal damping ratios corresponding with proportional damping are given by:

$$\zeta_i = \frac{1}{2} \left(\frac{\alpha}{\omega_i} + \beta \omega_i \right). \quad (4.23)$$

In Figure 4.3 the magnitudes of the FRFs are shown for three different locations of the sensor patch (case 1, 2 and 3). The results correspond with $\alpha = 2.0$ and $\beta = 4.7 \cdot 10^{-6}$, for which the modal damping ratios of the modes in the frequency band of interest are between 0.0075 and 0.015. The full FEM analysis results are in good correspondence with results obtained with an analytical model of the setup, but these are not shown for clarity. For each case, the FRF from the actuator voltage V_1 to the normal sensor displacement u_z , and the FRF from the actuator voltage to the sensor voltage V_2 are shown. It can be observed that significant errors can occur in the prediction of the FRFs

if the residual mode is neglected. When the modal expansion is truncated after m modes, the residual mode correction $\Delta \mathbf{u}$ is:

$$\Delta \mathbf{u} = \mathbf{u}_0 - \sum_{i=1}^m \frac{\hat{\mathbf{u}}_i \hat{\mathbf{u}}_i^T \mathbf{f}^*}{\omega_i^2}, \quad (4.24)$$

where the first right hand side term is the static response and the second right hand side term is the contribution of the low frequency modes to the static response. This equation shows that the residual mode correction is significant if the static response is not well described by the low frequency modes. A substantial error in the prediction of an FRF can be expected if the residual mode correction is of the same order as the truncated modal expansion. This is the case in the off-resonant regions, which explains why the effect is more clearly visible near the anti-resonance frequencies of the FRFs. Furthermore, the effect is more pronounced in the FRF from the actuator voltage to the sensor voltage (V_2/V_1). For that particular transfer, the in-plane deformation significantly contributes to the response. Because the in-plane vibration modes are quite high in frequency, and thus not included in the truncated modal expansion, the error is the largest for this transfer.

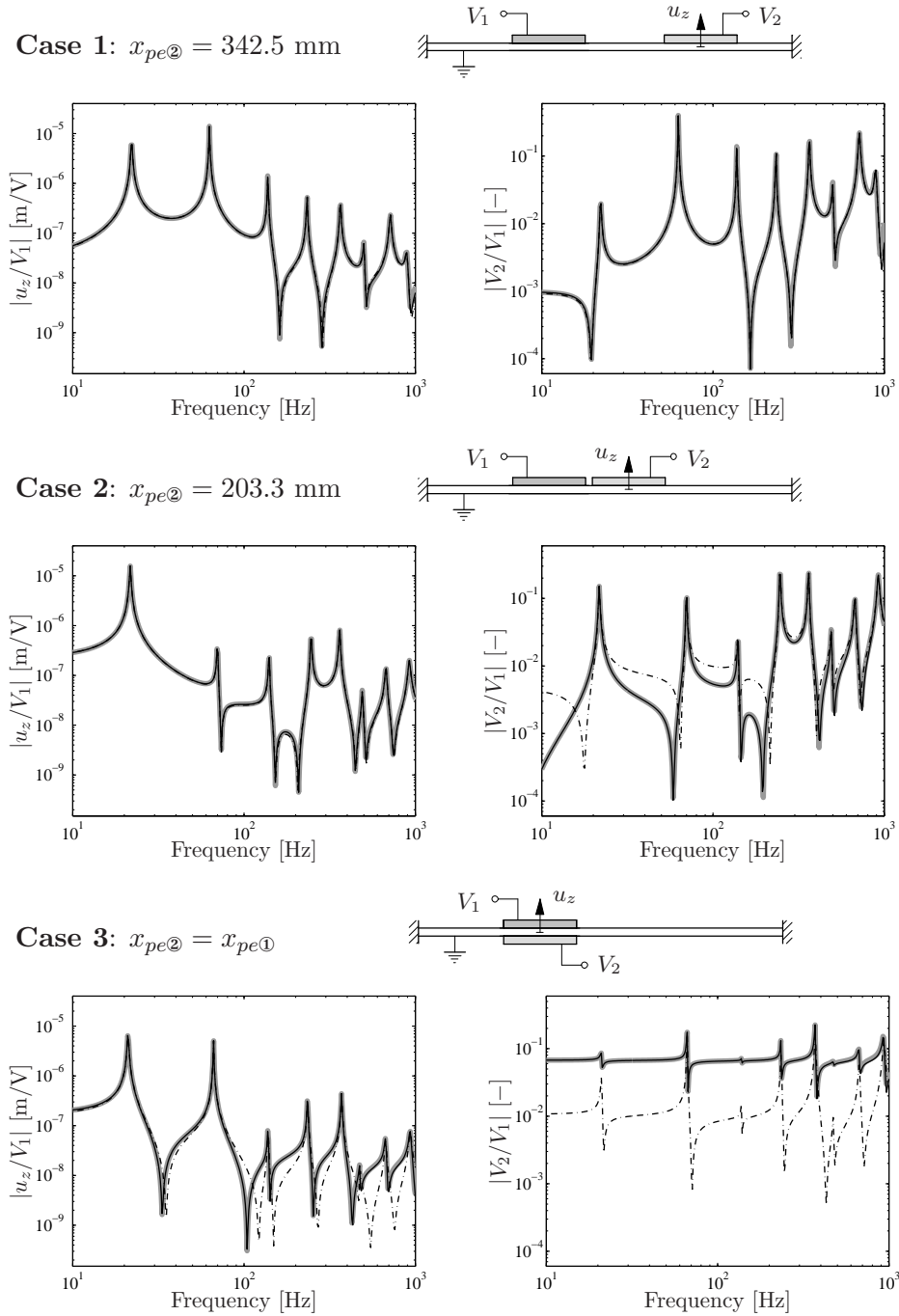


Figure 4.3: FRFs calculated with the full FEM model (—), the reduced model without residual mode (----), and the reduced model with residual mode (—) ($x_{pe①} = 138.3$ mm).

4.2.4 State space representation

So far the structural model was described in terms of second-order differential equations. Many (feedback) control design methods are based on a so-called *state space* representation, which uses a description in terms of first-order differential equations [4, 51]. In this section the state space representation of the previously described reduced model is given.

The general state space representation of a linear, time invariant¹ dynamical system is given by [4, 10]:

$$\dot{\mathbf{x}}(t) = \mathbf{A} \mathbf{x}(t) + \mathbf{B} \mathbf{v}(t), \quad (4.25a)$$

$$\mathbf{y}(t) = \mathbf{C} \mathbf{x}(t) + \mathbf{D} \mathbf{v}(t). \quad (4.25b)$$

Equation (4.25a) describes the response of the state vector $\mathbf{x}(t)$ when driven by the input vector $\mathbf{v}(t)$. In this first-order differential equation \mathbf{A} is the system matrix and \mathbf{B} is the input matrix. The outputs of the system, which are stored in $\mathbf{y}(t)$, are related to the state vector and input vector as in equation (4.25b), where \mathbf{C} is the output matrix, and \mathbf{D} is the feedthrough matrix.

Consider a structure with several piezoelectric actuators, either voltage or charge driven, which is furthermore excited by structural forces. Also, several displacement sensors and piezoelectric sensors, which measure either charge or voltage, are mounted on the structure. The input vector $\mathbf{v}(t)$ and output vector $\mathbf{y}(t)$ for such a system are defined as:

$$\mathbf{v}(t) = \begin{Bmatrix} \mathbf{f}(t) \\ \phi^v(t) \\ \mathbf{g}^c(t) \end{Bmatrix}, \quad \mathbf{y}(t) = \begin{Bmatrix} \mathbf{u}(t) \\ \mathbf{g}^v(t) \\ \phi^c(t) \end{Bmatrix}. \quad (4.26)$$

One choice of suitable state variables are the mode participation factors (generalised coordinates) and the first-order time derivatives of the mode participation factors:

$$\mathbf{x}(t) = \begin{Bmatrix} \mathbf{q}(t) \\ \dot{\mathbf{q}}(t) \end{Bmatrix}. \quad (4.27)$$

By rewriting the second-order equation of motion (4.16) in state variable form, the system matrix and input matrix become:

$$\mathbf{A} = \begin{bmatrix} \mathbf{0} & \mathbf{I} \\ -\Omega^2 & -2\Xi\Omega \end{bmatrix}, \quad \mathbf{B} = \begin{bmatrix} \mathbf{0} & \mathbf{0} & \mathbf{0} \\ \Psi_u^T & -\Psi_u^T \mathbf{K}_{u\phi}^{v*} & (\Psi_\phi^c)^T \end{bmatrix}. \quad (4.28)$$

¹A state space model is called *time invariant* if \mathbf{A} , \mathbf{B} , \mathbf{C} and \mathbf{D} do not vary in time.

The input matrix \mathbf{B} is obtained when the equivalent force vector is expanded as in equation (4.7), thereby using equation (4.12).

The displacement response, which is the sum of the truncated modal expansion and the residual mode (see equation (4.21)), is in the time domain given by:

$$\mathbf{u}(t) = \Psi_u \mathbf{q}(t) + \left(\mathbf{U}_0 - \Psi_u (\Omega^2)^{-1} \Psi_u^T \right) \mathbf{f}^*(t). \quad (4.29)$$

The static displacement response has been replaced by the matrix \mathbf{U}_0 , in which each column i is the static displacement response when element i in $\mathbf{f}^*(t)$ is equal to one, whereas all other inputs are zero. With equation (4.29) the displacement response can be calculated for time-varying inputs. In the same way, expressions can be derived for the response of the charge and voltage sensors:

$$\mathbf{g}^v(t) = \mathbf{K}_{\phi u}^{v*} \Psi_u \mathbf{q}(t) + \left(\mathbf{G}_0^v - \mathbf{K}_{\phi u}^{v*} \Psi_u (\Omega^2)^{-1} \Psi_u^T \right) \mathbf{f}^*(t), \quad (4.30a)$$

$$\phi^c(t) = \Psi_\phi^c \mathbf{q}(t) + \left(\Phi_0^c - \Psi_\phi^c (\Omega^2)^{-1} \Psi_u^T \right) \mathbf{f}^*(t), \quad (4.30b)$$

where \mathbf{G}_0^v and Φ_0^c contain the unit static charge and unit static voltage responses, respectively, to the inputs stored in $\mathbf{f}^*(t)$. With equations (4.29) and (4.30) the output matrix and feedthrough matrix become:

$$\mathbf{C} = \begin{bmatrix} \Psi_u & \mathbf{0} \\ \mathbf{K}_{\phi u}^{v*} \Psi_u & \mathbf{0} \\ \Psi_\phi^c & \mathbf{0} \end{bmatrix}, \quad (4.31)$$

$$\mathbf{D} = \begin{bmatrix} \mathbf{U}_0 \\ \mathbf{G}_0^v \\ \Phi_0^c \end{bmatrix} - \begin{bmatrix} \Psi_u \\ \mathbf{K}_{\phi u}^{v*} \Psi_u \\ \Psi_\phi^c \end{bmatrix} (\Omega^2)^{-1} \begin{bmatrix} \Psi_u^T & -\Psi_u^T \mathbf{K}_{u\phi}^{v*} & (\Psi_\phi^c)^T \end{bmatrix}. \quad (4.32)$$

Some remarks are made with respect to the implementation of the state space model. The number of modes included in the truncated modal expansion is m . The number of state variables is thus equal to $2m$. In general the number of inputs to the system is much smaller than the total number of DOF in the model n . Therefore, most elements in the nodal force vector \mathbf{f} are zero. Only the non-zero inputs are included in the input vector. Likewise, only the responses of interest are included in the output vector. In this way a compact state space model is obtained. For ease of writing, no new symbols are introduced in this section to denote vectors and matrices accounting for a few modes, inputs or outputs.

4.3 Acoustic model

In this section an acoustic model is presented to predict the free field sound radiation associated with a given vibration response of the structure. Acoustic wave propagation through a homogeneous elastic fluid such as air is described by the well known wave equation. In the case of harmonic time dependence, this equation reduces to the Helmholtz *differential* equation, which is given by:

$$\nabla^2 p(\mathbf{r}) + k^2 p(\mathbf{r}) = -j\omega\rho_0 q(\mathbf{r}), \quad (4.33)$$

where $p(\mathbf{r})$ is the complex pressure² amplitude at location \mathbf{r} , $k = \omega/c_0$ is the acoustic wave number with c_0 the speed of sound in the medium, ρ_0 is the density of the medium, and $q(\mathbf{r})$ is some external volume source. The Helmholtz differential equation can be rewritten in an integral formulation, which is called the Helmholtz *integral* equation. In this equation the surface normal velocity $v_n(\mathbf{r}_s)$ on a vibrating source with a closed boundary S and the radiated pressure field $p(\mathbf{r})$ are related by [52]:

$$\alpha(\mathbf{r}) p(\mathbf{r}) = \oint_S \left(p(\mathbf{r}_s) \frac{\partial G(\mathbf{r}, \mathbf{r}_s)}{\partial n} + j\omega\rho_0 v_n(\mathbf{r}_s) G(\mathbf{r}, \mathbf{r}_s) \right) dS, \quad (4.34)$$

where $G(\mathbf{r}, \mathbf{r}_s)$ is a Green's function. Note that \mathbf{r}_s defines a point on boundary S whereas \mathbf{r} defines a field point. The value of $\alpha(\mathbf{r})$, the so-called free space angle, depends on where the pressure is evaluated. It is equal to one if the point lies outside the closed boundary, and one half if the point is on a smooth part of the boundary S . When the vibrating surface is subjected to the free field condition (Sommerfeld radiation condition), then the Green's function is the solution of the Helmholtz differential equation excited by a Dirac pulse:

$$G(\mathbf{r}, \mathbf{r}_s) = \frac{e^{-jk|\mathbf{r}-\mathbf{r}_s|}}{4\pi|\mathbf{r}-\mathbf{r}_s|}, \quad (4.35)$$

where $|\mathbf{r}-\mathbf{r}_s|$ is the distance between a surface point and a field point. Once the surface normal velocity distribution $v_n(\mathbf{r}_s)$ has been determined with the structural model, the associated pressure field can be calculated from equation (4.34).

Sound pressure is a quantity which depends on the location of a receiver with respect to the sound source. A more convenient measure for the strength

²In this work *pressure* refers to *acoustic pressure*, i.e. the small fluctuation upon the steady state (e.g. atmospheric) pressure.

of a sound source is the *time-averaged sound power*, which is widely used for comparing sound sources. The sound power is directly related to the *time-averaged sound intensity*. In this thesis the terms sound power and sound intensity will be used as abbreviations of time-averaged sound power and time-averaged sound intensity. In the case of harmonic time dependence the sound intensity is given by:

$$\bar{\mathbf{I}}(\mathbf{r}) = \frac{1}{2} \text{Re} (p(\mathbf{r}) \mathbf{v}^*(\mathbf{r})) , \quad (4.36)$$

where $\mathbf{v}(\mathbf{r})$ is the acoustic particle velocity and superscript * denotes the complex conjugate.

The vector quantity sound intensity describes the amount and the direction of net flow of acoustic energy per unit area, at a given position. The sound power generated within a given volume is equal to the surface integral of the normal component of the sound intensity:

$$\bar{W} = \oint_S \bar{\mathbf{I}}(\mathbf{r}_s) \cdot \mathbf{n}(\mathbf{r}_s) dS , \quad (4.37)$$

where $\mathbf{n}(\mathbf{r}_s)$ is the surface normal. If the surface used for evaluation of this expression is chosen equal to the surface defining the vibrating body, the sound power can be written as:

$$\bar{W} = \frac{1}{2} \text{Re} \left(\oint_S p(\mathbf{r}_s) v_n^*(\mathbf{r}_s) dS \right) . \quad (4.38)$$

Sound power is often specified in decibels because this scale is better suited to the “human audio system” than a linear scale. The *sound power level* is defined as:

$$L_W = 10 \log_{10} \left(\frac{\bar{W}}{\bar{W}_{\text{ref}}} \right) , \quad \bar{W}_{\text{ref}} = 1 \cdot 10^{-12} \text{ W} , \quad (4.39)$$

where \bar{W}_{ref} is the reference power.

4.3.1 Rayleigh integral method

In this thesis the analysis is restricted to flat plate-like structures. When it is assumed that such a structure is placed in a baffle, the Helmholtz integral equation (4.34) reduces to the *Rayleigh integral* [52] (or Rayleigh’s second integral), which is given by:

$$p(\mathbf{r}) = \frac{j\omega\rho_0}{2\pi} \int_S v_n(\mathbf{r}_s) \frac{e^{-jk|\mathbf{r}-\mathbf{r}_s|}}{|\mathbf{r}-\mathbf{r}_s|} dS . \quad (4.40)$$

Figure 4.4 gives a geometric interpretation of the Rayleigh integral. The baffle is an infinitely extended rigid surface around the plate. The sound fields on both sides of the plate are equal in magnitude, but have opposite phase.

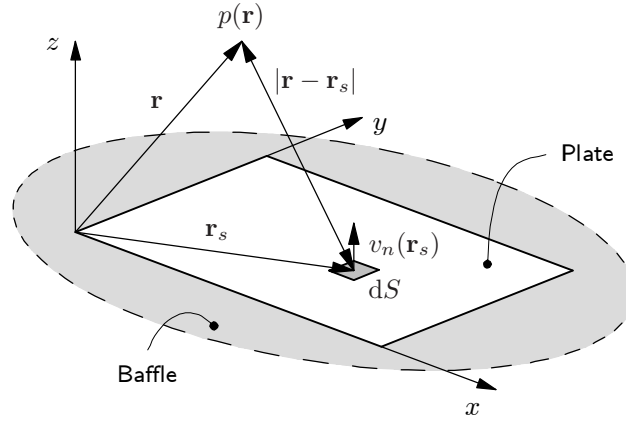


Figure 4.4: Geometric interpretation of the Rayleigh integral.

Discretization

The Rayleigh integral is solved with a primitive numerical scheme. The plate is divided into N rectangular elements of equal size, which are small compared to the acoustic wavelength. It is assumed that the normal velocity is constant across each element. One could say that the plate surface is divided into a set of elemental radiators or pistons that each move with constant harmonic velocity. For this discretization, equation (4.40) can be written as:

$$\mathbf{p}_f = \mathbf{Z}_f \mathbf{v}_n, \quad (4.41)$$

where \mathbf{p}_f is the vector with pressures in a set of *field* points, \mathbf{v}_n is the vector with normal surface velocities of the elemental radiators, and \mathbf{Z}_f is a frequency dependent transfer matrix, whose elements are given by:

$$(Z_f)_{ij} = \frac{j\omega\rho_0 S_e}{2\pi} \frac{e^{-jkr_{ij}}}{r_{ij}}, \quad (4.42)$$

where S_e is the area of an elemental radiator. The distance between a field point i and a surface point j is $r_{ij} = |\mathbf{r}_i - \mathbf{r}_j|$, where \mathbf{r}_j refers to the centre of an elemental radiator. For the same discretization, the expression for the

sound power (4.38) reduces to the summation:

$$\bar{W} = \frac{S_e}{2} \operatorname{Re} (\mathbf{v}_n^H \mathbf{p}) , \quad (4.43)$$

where \mathbf{p} is the vector with *surface* pressures, evaluated at the same points on the surface as \mathbf{v}_n . With substitution of $\mathbf{p} = \mathbf{Z}\mathbf{v}_n$, where \mathbf{Z} is the impedance matrix evaluated on the vibrating surface, the sound power can be written as:

$$\bar{W} = \frac{S_e}{2} \operatorname{Re} (\mathbf{v}_n^H \mathbf{Z} \mathbf{v}_n) = \mathbf{v}_n^H \mathbf{R} \mathbf{v}_n . \quad (4.44)$$

In this equation $\mathbf{R} = (S_e/2) \operatorname{Re}(\mathbf{Z})$ is the so-called *radiation resistance matrix*, which can be written as:

$$\mathbf{R} = \frac{\omega^2 \rho_0 S_e^2}{4\pi c_0} \begin{bmatrix} 1 & \frac{\sin(kr_{12})}{kr_{12}} & \dots & \frac{\sin(kr_{1N})}{kr_{1N}} \\ \frac{\sin(kr_{21})}{kr_{21}} & 1 & & \vdots \\ \vdots & & \ddots & \vdots \\ \frac{\sin(kr_{N1})}{kr_{N1}} & \dots & \dots & 1 \end{bmatrix} . \quad (4.45)$$

The elements of this matrix depend on the properties of the acoustic medium, the frequency, and the length and width of the plate. Here the radiated sound power is evaluated on the plate surface, but it may be developed on any surface enclosing the plate³. In an alternative approach, which is presented for instance in references [10] and [53], the radiated sound power is found by integrating the far-field sound intensity over a hemisphere surrounding the plate.

A problem arises if the surface pressure itself is of interest. The surface impedance matrix \mathbf{Z} has singular diagonal elements (i.e. because $r_{ii} = 0$). An approximation can be made to avoid the singularity. The diagonal elements in the impedance matrix are replaced by:

$$Z_{ii} = \rho_0 c_0 \left(1 - e^{-jk\sqrt{(S_e/\pi)}} \right) . \quad (4.46)$$

This expression corresponds with the impedance seen by a baffled *circular* piston with surface area S_e moving with uniform velocity. For this case the Rayleigh integral can be evaluated analytically. The singularity is not encountered in the radiation resistance matrix, because this matrix is defined only by the real part of the surface impedance matrix.

³It is thus assumed that the internal loss of the medium is negligible, which is true for free field sound propagation in air.

4.3.2 Structural-acoustic coupling

The surface velocity resulting from a structural analysis is available at the node locations of the FEM model. The centre locations of the elemental radiators, which define the acoustic mesh, will in general not coincide with the node locations. It is thus necessary to transfer the nodal results of the structural model to the centres of the elemental radiators. The use of separate meshes has the advantage that the radiation matrix can be re-used as long the length and width of the plate remain unchanged. For example, the same radiation matrix can be used to analyse a given plate geometry with different arrangements of the patches (e.g. location, number) In this way, the required computational effort in parameter and optimisation studies is limited (see Chapter 7).

In the frequency domain, the normal plate velocity can be written in terms of the mode participation factors as:

$$\mathbf{v}_n = j\omega \mathbf{\Psi}_n \mathbf{q}, \quad (4.47)$$

where $\mathbf{\Psi}_n$ contains the normal displacement components of the structural modes, transferred to the centres of the elemental radiators. The size of $\mathbf{\Psi}_n$ is equal to $N \times m$, where N is the number of elemental radiators and m is the number of modes used in the reduced structural analysis. With this equation, the sound power can be written as:

$$\begin{aligned} \bar{W} &= \mathbf{v}_n^H \mathbf{R} \mathbf{v}_n \\ &= \omega^2 \mathbf{q}^H \mathbf{M} \mathbf{q}, \end{aligned} \quad (4.48)$$

where \mathbf{M} is a real, symmetric, positive definite matrix. The diagonal and off-diagonal terms in \mathbf{M} are the so-called *self* and *mutual* radiation efficiencies, respectively, of the structural modes. It is important to note that the off-diagonal terms cannot be neglected in the prediction of the sound power. A consequence of \mathbf{M} being a fully populated matrix is that the structural modes do not contribute independently to the sound power. This also means that a reduction of the participation factor of one structural mode (e.g. by active control) does not guarantee a reduction of the sound power. This conclusion was also drawn in Section 3.5, where it was shown that control aiming at structural vibration reduction may lead to an increase of sound at some frequencies.

4.3.3 Radiation modes

It is possible to calculate a set of surface velocity distributions which are orthogonal with respect to the sound power. These surface velocity distributions,

so-called *radiation modes*, were first introduced by Borgiotti [54]. Since then a large amount of work has been published on the topic.

The radiation modes are obtained through a decomposition of a discretized radiation operator. This radiation operator follows when writing the sound power in terms of the structural mode participation factors⁴ [53, 55], such as in equation (4.48), or in terms of the normal velocities of an array of discrete elemental radiators⁵ [56, 57, 58], such as in equation (4.44). Either of these formulations can be used to determine the radiation modes. However, the latter approach is used since it separates the dynamical behaviour of the structure from the associated sound radiation [57]. The radiation modes are furthermore more accurately described with this approach [59]. An important feature is that the radiation modes depend only on the geometry of a vibrating object, and not on other properties of the structure (e.g. material, boundary conditions).

Eigenvalue analysis

The radiation efficiency is a measure for how well a vibrating object radiates sound. It is defined as the ratio of the sound power radiated per unit area by the object to the sound power radiated per unit area by a reference source. The reference source is a baffled piston vibrating at a high frequency ($kR \gg 1$, with R the effective piston radius) with a velocity equal to the space and time-averaged, squared normal velocity $\langle \bar{v}_n^2 \rangle$ of the object. The radiation efficiency is thus given by:

$$\sigma = \frac{\bar{W}}{\rho_0 c_0 S \langle \bar{v}_n^2 \rangle}, \quad (4.49)$$

where S is the total area of the object. The space and time average of the squared normal velocity is given by:

$$\langle \bar{v}_n^2 \rangle = \frac{1}{2S} \int_S |v_n(\mathbf{r}_s)|^2 dS = \mathbf{v}_n^H \mathbf{N} \mathbf{v}_n. \quad (4.50)$$

Matrix \mathbf{N} is a real, symmetric, and positive definite matrix, which for the discretization introduced previously can be replaced by $\mathbf{N} = \frac{1}{2N} \mathbf{I}$. With equations (4.44) and (4.50) the expression for the radiation efficiency becomes:

$$\sigma = \frac{\mathbf{v}_n^H \mathbf{R} \mathbf{v}_n}{\rho_0 c_0 S \mathbf{v}_n^H \mathbf{N} \mathbf{v}_n}. \quad (4.51)$$

⁴As explained by Cunefare [55], one may use any set of orthogonal shape functions.

⁵Numerical schemes more advanced than the constant velocity assumption of Section 4.3.1 are used by Naghshineh et al. [56].

As shown by Cunefare [55] the radiation modes and corresponding radiation mode efficiencies are obtained when solving the generalised eigenvalue problem for the matrices \mathbf{R} and \mathbf{N} at each frequency:

$$\lambda \mathbf{N} \mathbf{v}_n = \mathbf{R} \mathbf{v}_n. \quad (4.52)$$

The eigenvalue solution of (4.52) yields a set of real, positive eigenvalues λ_i and corresponding real eigenvectors γ_i . An eigenvector is called a radiation mode and the corresponding eigenvalue is directly proportional to the radiation efficiency of that mode ($\sigma_i = \lambda_i / \rho_0 c_0 S$). The eigenvalues and radiation modes are stored in two matrices $\mathbf{\Lambda}$ and $\mathbf{\Gamma}$:

$$\mathbf{\Lambda} = \begin{bmatrix} \lambda_1 & 0 & \cdots & 0 \\ 0 & \lambda_2 & \cdots & 0 \\ \vdots & \vdots & \ddots & \vdots \\ 0 & 0 & \cdots & \lambda_N \end{bmatrix}, \quad \mathbf{\Gamma} = [\gamma_1 \quad \gamma_2 \quad \cdots \quad \gamma_N]. \quad (4.53)$$

The normalization is as follows:

$$\mathbf{\Gamma}^T \mathbf{N} \mathbf{\Gamma} = \mathbf{I}, \quad (4.54a)$$

$$\mathbf{\Gamma}^T \mathbf{R} \mathbf{\Gamma} = \mathbf{\Lambda}. \quad (4.54b)$$

Because the radiation resistance matrix \mathbf{R} depends on frequency, the eigenvalue decomposition must be performed for each frequency step. As a result, the radiation modes and corresponding efficiencies also depend on frequency.

In Figure 4.5 the radiation efficiencies of the first eight radiation modes for a baffled, rectangular surface are shown as a function of kl_x . The aspect ratio of the surface is $l_x/l_y = 2$, where l_x and l_y are the length and width of the surface, respectively. The six most efficient radiation mode shapes are shown for three different frequencies in Figure 4.6. These results were obtained with a grid consisting of 20×10 elemental radiators. It can be seen in Figure 4.5 that for low values of kl_x the radiation efficiencies fall off very rapidly with increasing radiation mode number. In this frequency region, the shape of the most efficient radiation mode is a piston-like mode, i.e. the surface moves with uniform velocity. As the mode number increases, the shape of the corresponding radiation mode shows more oscillations. The radiation efficiencies depend on $(kl_x)^n$ for $kl_x < 2\pi$, where order n depends on the radiation mode number. In Figure 4.5 furthermore the *grouping* behaviour of the radiation modes can be seen, i.e. certain groups of modes show the same frequency dependence for their radiation efficiencies [60].

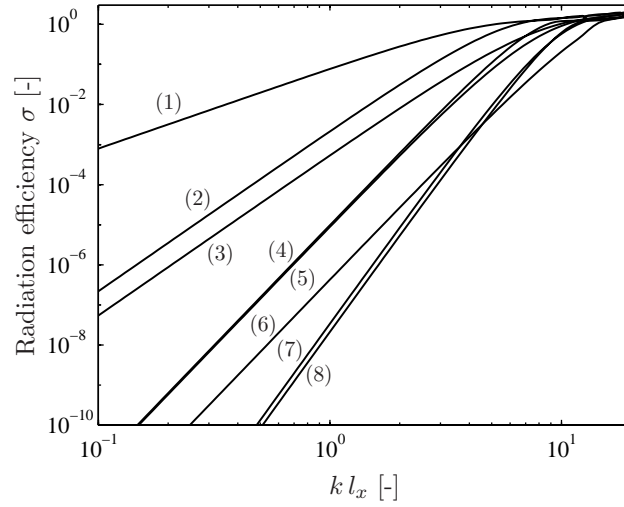


Figure 4.5: Radiation efficiencies of the first eight radiation modes of a baffled, rectangular surface as a function of kl_x ($l_x/l_y = 2$).

At higher frequencies, $kl_x > 2\pi$, when the plate length exceeds the acoustic wavelength, the efficiencies of all radiation modes become significant. It is then difficult to distinguish between “strong” and “weak” radiation modes. In Figure 4.6 it can be seen that the radiation mode shapes start to change from their low frequency shapes. However, the deviation in shape is quite small for a considerable frequency range.

Cunefare and Currey [59] presented the results of a parameter study regarding the radiation mode concept. They showed that when the number of elemental radiators is increased by one, i.e. $N \rightarrow N + 1$, a new *least efficient* radiation mode is introduced. Another important conclusion was that the radiation efficiency of the most efficient radiation mode has a finite upper bound, and converges fast with increasing number of elemental radiators.

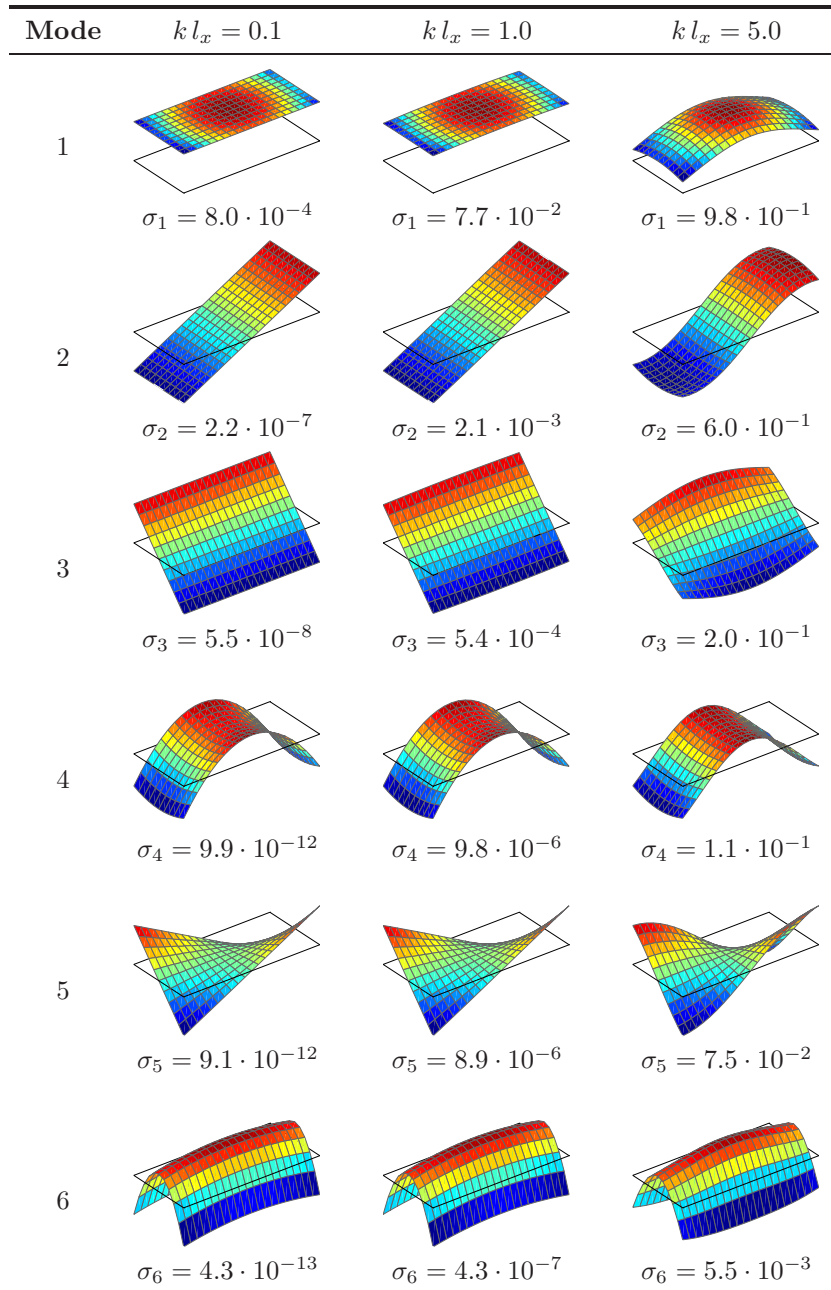


Figure 4.6: First six radiation mode shapes of a baffled, rectangular surface for $kl_x = 0.1$, $kl_x = 1.0$ and $kl_x = 5.0$.

Sound power in terms of radiation modes

The vibration response of the plate was previously expanded using the structural modes, see equation (4.47), but one can alternatively use an expansion in terms of the radiation modes:

$$\mathbf{v}_n = \mathbf{\Gamma} \mathbf{a}, \quad (4.55)$$

where \mathbf{a} is the vector with radiation mode participation factors. With this equation and normalisation equation (4.54b) the sound power can be written as:

$$\begin{aligned} \bar{W} &= \mathbf{v}_n^H \mathbf{R} \mathbf{v}_n \\ &= \mathbf{a}^H \mathbf{\Gamma}^T \mathbf{R} \mathbf{\Gamma} \mathbf{a} \\ &= \mathbf{a}^H \mathbf{\Lambda} \mathbf{a} \\ &= \sum_{i=1}^N \lambda_i |a_i|^2. \end{aligned} \quad (4.56)$$

This equation shows that the radiation modes contribute independently to the sound power. In the low frequency range ($kl_x < 2\pi$) the radiation mode efficiencies fall off very rapidly with mode number. Therefore, the sound power can be well approximated using only a small number of modes $N_r \ll N$:

$$W \approx \sum_{i=1}^{N_r} \lambda_i |a_i|^2 = \mathbf{a}_r^H \mathbf{\Lambda}_r \mathbf{a}_r, \quad (4.57)$$

where the subscript r denotes a vector or matrix that accounts for N_r radiation modes. This approximation becomes less accurate with increasing frequency. For a proper choice of N_r , not only the radiation efficiency is of importance. The sound power is also determined by the extent to which a radiation mode participates in the vibration response. The radiation mode participation factors are calculated from a given normal velocity distribution \mathbf{v}_n as follows:

$$\mathbf{a}_r = \mathbf{\Gamma}_r^T \mathbf{N} \mathbf{v}_n. \quad (4.58)$$

This result is found when equation (4.55) is pre-multiplied by $\mathbf{\Gamma}_r^T \mathbf{N}$ and normalisation equation (4.54a) is used. A further simplification is to express the radiation mode participation factors in terms of the structural mode participation factors \mathbf{q} :

$$\mathbf{a}_r = j\omega \mathbf{\Gamma}_r^T \mathbf{N} \mathbf{\Psi}_n \mathbf{q}. \quad (4.59)$$

As mentioned before, the radiation modes depend on the geometry, but not on other structural properties. Therefore the radiation modes can be re-used to calculate the sound power as long as the geometry remains unchanged.

4.3.4 Radiation filters

It was mentioned before that several control design methods rely on a state space model. A number of methods for capturing the sound radiation behaviour into a state space model have been reported in the literature. Such a model is referred to as a *radiation filter*. Baumann, Saunders and Robertshaw [61] introduced the idea of a radiation filter. They used a description of the sound power in terms of the *structural* modes to develop the radiation filter. More recently, Gibbs, Clark, Cox and Viperman [62] introduced a new method for designing radiation filters termed *radiation modal expansion*. In contrast to the work of Baumann et al., they used a description of the sound power in terms of the *radiation* modes.

A radiation filter can be combined with the state space representation of the structural model to obtain an augmented system model accounting for the structural-acoustic coupling. With the structural-acoustic state space model the performance of various control systems can be analysed. The control strategies considered in Chapters 5 and 6 are not based on a state space representation of the acoustic model. However, for the sake of completeness a comparison of the two approaches for designing a radiation filter is presented in Appendix D.

4.4 Experimental validation

The experimental validation of the numerical model is presented in this section. For this purpose, a test setup consisting of a clamped plate with two *asymmetric* bonded patches is considered. The structural model is validated by means of a comparison of predicted and measured eigenfrequencies, mode shapes and frequency response functions. The acoustic model is validated by means of a comparison of predicted and measured sound powers radiated by the setup due to the excitation of the plate with the patches. The dynamical behaviour of the setup was determined in the frequency range up to 500 Hz. In the present analysis only the open-loop behaviour is considered (i.e. no control).

4.4.1 Experimental setup

The experimental setup is shown in Figure 4.7. An aluminium plate with dimensions $490 \times 244 \times 1.2$ mm is clamped in a frame, which consists of thick aluminium bars. Two identical rectangular PZT patches (PI Ceramic) of $50 \times 30 \times 1.0$ mm were bonded to the plate with a conductive glue (Epotek H20 E). A conductive glue was used to provide an easy electrical connection to the bottom electrode, i.e. the electrode bonded to the plate surface. The patches could be driven independently by a high voltage amplifier (Piezomechanik SVR 1000/3). This amplifier has a low voltage monitor output, which was used for measuring frequency response functions.

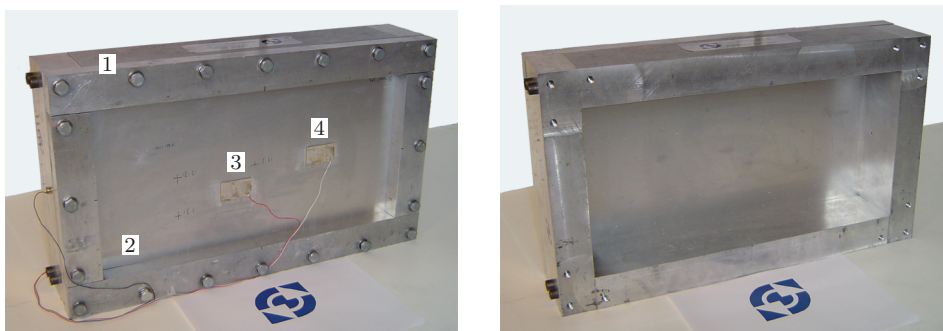


Figure 4.7: Experimental setup, 1: Frame, 2: Plate, 3: Patch 1, 4: Patch 2.

A schematic view of the setup including measurement equipment is shown in Figure 4.8. The experimental results presented in this section, but also in later chapters, were obtained with the following sensor types:

- *Accelerometers* (Brüel & Kjær (B&K) 4374). Accelerations normal to the plate surface were measured with small accelerometers. The acceleration signal was amplified by a B&K 2690 Nexus conditioning amplifier.
- *Microphones* (B&K 4192). Half-inch microphones measured the acoustic pressure in discrete field points, also in combination with the Nexus conditioning amplifier.
- *Laser vibrometer* (Polytec). The laser vibrometer was mounted on a programmable x - y table (Dantec) to measure the normal plate velocity in a large number of points (in an automated way).
- *Sound intensity probe* (B&K 2683, B&K 2260). With a two-microphone sound intensity probe the sound power radiated by the plate was measured (more details will be given in Section 4.4.4).

A DSPT SigLab dynamic signal analyser processed the sensor signals. This is a four-channel analyser so not all sensors could be used at the same time. All measurements were performed in a room of $2.8 \times 2.8 \times 2.0$ m with sound absorbing walls. The main reason for using this room was in order to isolate the experimental setup from external acoustic sources.

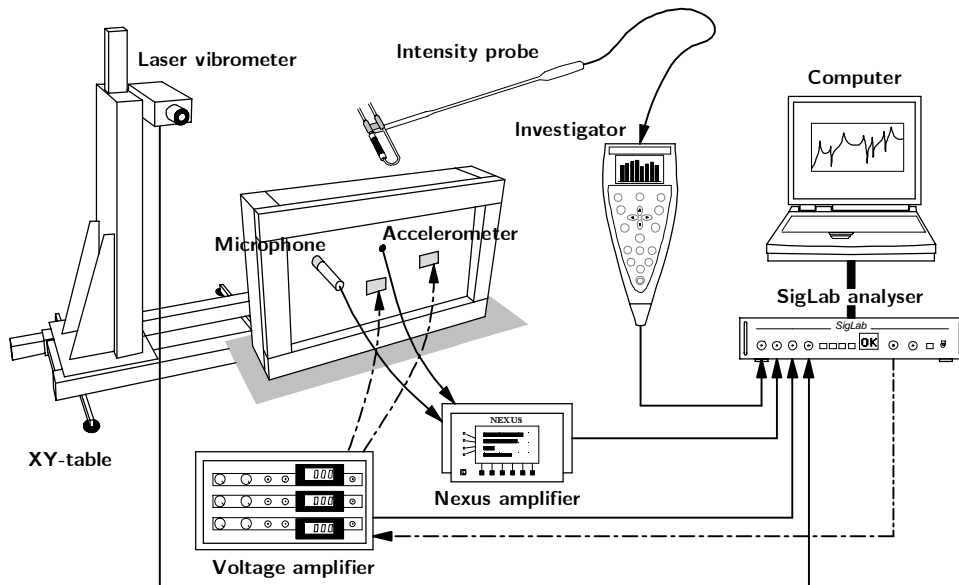


Figure 4.8: Experimental setup.

4.4.2 Numerical model

In Figure 4.9 the properties of the plate and the patches are given. The material properties of the patches can be found in Appendix A. The eigenfrequency of the first structural mode of the setup showing considerable displacement of the frame is well above 500 Hz. Therefore the frame was not included in the structural model.

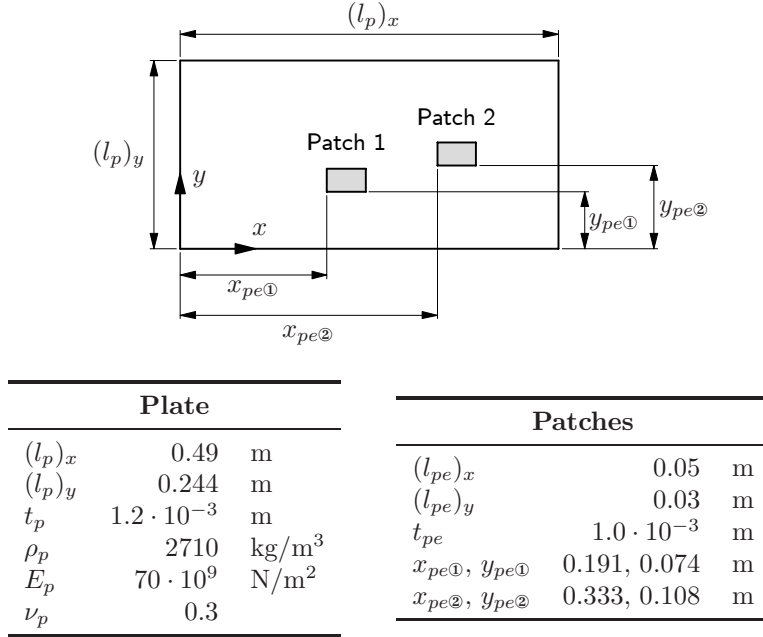


Figure 4.9: Model parameters (material properties of the patches are given in Appendix A).

The FEM program ANSYS was used to model the setup. The plate was meshed with 48 and 24 four-node plate elements along its length and width, respectively. In the regions near the PZT patches the mesh was refined to correspond with the mesh of the patches, which consisted of $10 \times 6 \times 2$ eight-node piezoelectric solid elements (see Appendix C for more details). Two steps were required to create a reduced structural model. First, the eigenfrequencies and mode shapes were determined with a modal analysis. Second, for each input to the system (e.g. actuator voltage) a static analysis was performed. This second step was required to include the residual mode. The results were imported in MATLAB where the reduced structural model was assembled. The acoustic model, which consisted of 20×10 elemental radiators, was also de-

finned in MATLAB. The properties of air are $\rho_0 = 1.2 \text{ kg/m}^3$ and $c_0 = 343 \text{ m/s}$. The results were obtained with 20 structural modes and 10 radiation modes. It is important to note that the acoustic model predicts the sound power radiated on one side of the plate under the assumption that the plate is baffled. However, in the experimental setup no baffle was used.

4.4.3 Structural response

The structural model presented in Section 4.2 was validated in two ways. First, a comparison was made of calculated and measured eigenfrequencies and mode shapes. As a next step, some frequency response functions were considered.

Eigenfrequencies and mode shapes

The modal properties of the experimental setup were determined in the frequency range up to 500 Hz from measured frequency response function data. For this purpose a broadband driving signal was applied to “patch 1” (see Figure 4.9), which excites all modes in this frequency range. The plate response was measured with the laser vibrometer. Transfer functions between the voltage applied to the patch and the normal plate velocity were measured on a grid of 15×7 points. The eigenfrequencies were identified as the amplitude resonance frequencies in the frequency response functions.⁶

The numerical and experimental results of the eigenfrequency analysis are shown in Figure 4.10. There is a good agreement between the predicted and measured eigenfrequencies of the plate with patches. The numerical results for a clamped plate without patches are also shown. The eigenfrequencies of the plate without patches are for most of the modes higher than the eigenfrequencies of the plate with patches. This is because the patches mainly introduce a mass effect for the low frequency modes (see also Section 3.4). A remarkable aspect is that the mass effect results in a substantial difference between some of the mode shapes of the two setups. It appears that modes 4 and 5 of the plate with patches are linear combinations of the 4-1 and 1-2 modes of the plate without patches. This effect is also visible in the experimental results. Although the difference between these two mode shapes is considerable, the eigenfrequencies are nearly equal.

⁶With the numerical model the *undamped* eigenfrequencies were calculated, whereas the measured amplitude resonance frequencies depend on the amount of damping in the system. However, because the damping is very small (about 0.5 %), the differences between the *undamped* and *damped* eigenfrequencies are negligible.

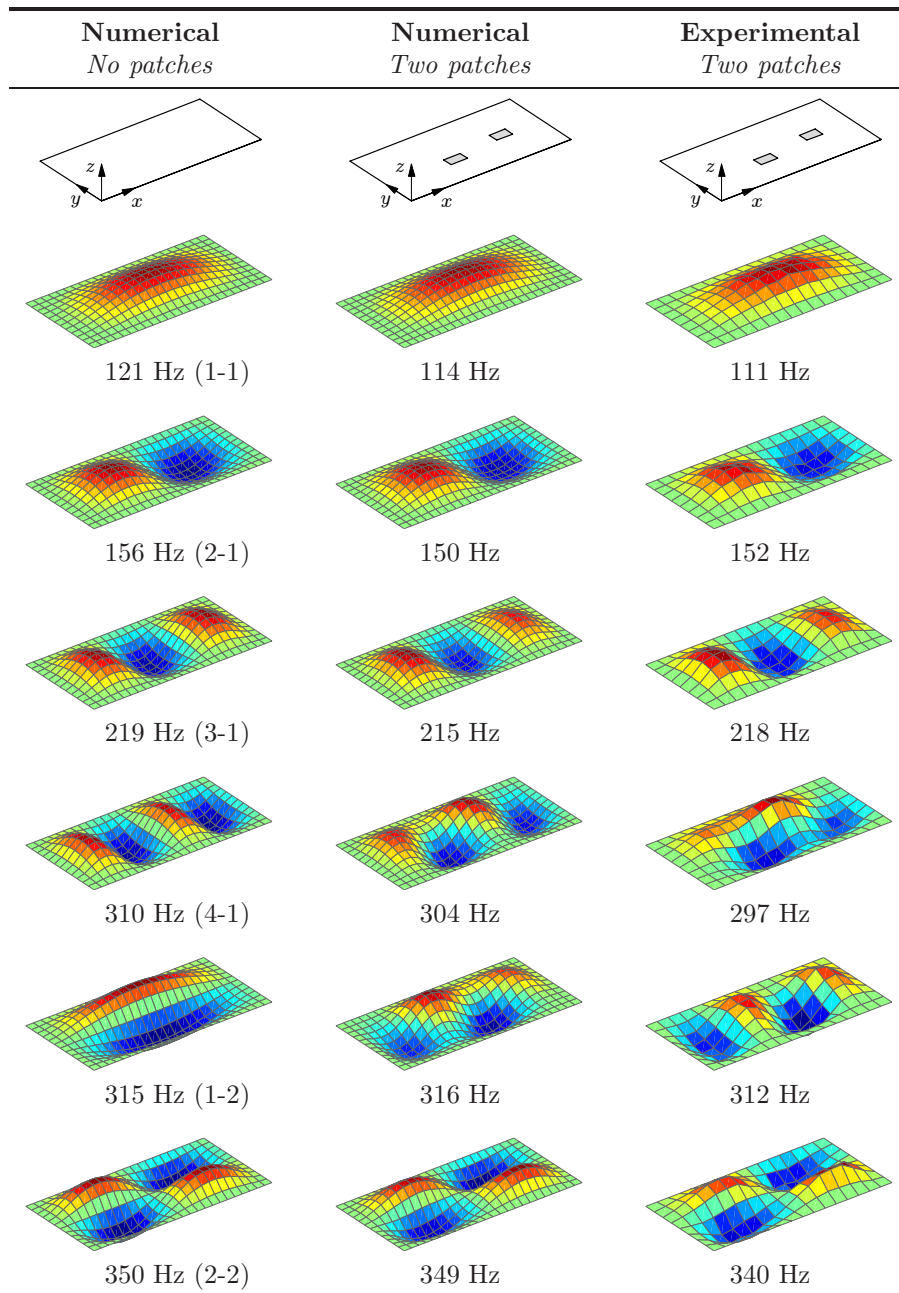


Figure 4.10: First six structural mode shapes; numerical and experimental results are shown. The numerical results are interpolated to an equidistant plot grid.

An alternative to comparing predicted and measured mode shapes by visual inspection is the *modal assurance criterion* (MAC). This criterion provides a measure for the degree of consistency between a numerical mode shape $\hat{\mathbf{u}}_i^{\text{num}}$ and an experimental mode shape $\hat{\mathbf{u}}_j^{\text{exp}}$. The MAC criterion is defined here as:

$$\text{MAC}(i, j) = \frac{\left((\hat{\mathbf{u}}_i^{\text{num}})^T \hat{\mathbf{u}}_j^{\text{exp}} \right)^2}{\left((\hat{\mathbf{u}}_i^{\text{num}})^T \hat{\mathbf{u}}_i^{\text{num}} \right) \left((\hat{\mathbf{u}}_j^{\text{exp}})^T \hat{\mathbf{u}}_j^{\text{exp}} \right)}. \quad (4.60)$$

The value of $\text{MAC}(i, j)$ lies between zero and one. A value near one indicates a good correspondence between the mode shapes, whereas a value near zero indicates that the mode shapes are not consistent. The mode shapes obtained with the FEM model (normal displacement only) are interpolated to the measurement grid to make the comparison by MAC possible.

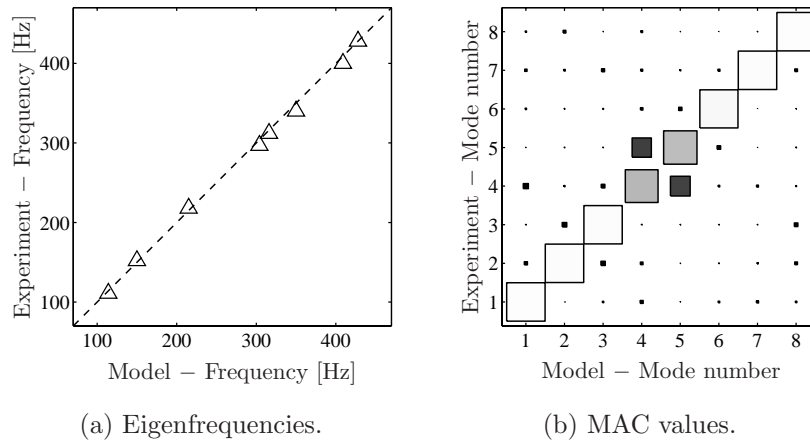


Figure 4.11: Comparison of numerical and experimental eigenfrequency analysis results: (a) eigenfrequencies and (b) MAC values, where the area of a square corresponds to $\text{MAC}(i, j)$.

In Figure 4.11(b) the MAC values for the first eight modes are shown. For each pair (i, j) , the area of the square corresponds to the value of $\text{MAC}(i, j)$. For most of the modes the MAC values for $i = j$ are close to one indicating a good correspondence between the predicted and measured mode shapes.⁷ For modes 4 and 5 the consistency is less.

⁷It is noted that for a perfect match, i.e. $\hat{\mathbf{u}}_i^{\text{num}} = \hat{\mathbf{u}}_j^{\text{exp}}$, the MAC values for $i \neq j$ are not equal to zero. This is because structural modes are orthogonal with respect to the mass and stiffness rather than to each other.

In Figure 4.11(a) the measured eigenfrequencies are plotted against the predicted eigenfrequencies. All triangles are close to the dashed line, which indicates that there is a good correspondence between the results.

Frequency response functions

In addition to the modal properties, frequency response functions for two separate excitations were considered. First, the plate was excited by a voltage applied to “patch 1” (actuator patch). An accelerometer was located at the centre of the patch, on the plate side opposite to where the patch is bonded. Also, the voltage across the electrodes of “patch 2” was measured (sensor patch). To measure the voltage across a patch the electrodes were connected to the SigLab analyser without an amplifier. In the numerical model the sensor patch was simulated by a zero charge boundary condition on the top electrode of the patch (open circuit).

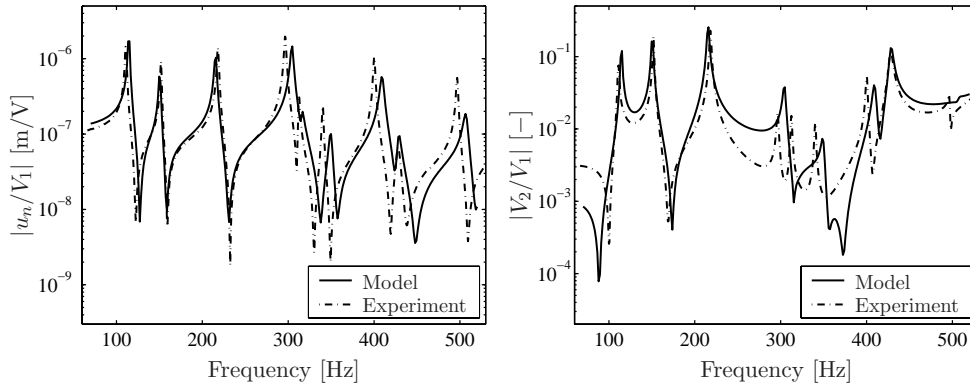


Figure 4.12: Calculated and measured FRFs from voltage applied to patch 1 V_1 to (left) accelerometer displacement u_n and (right) voltage across patch 2 V_2 .

The FRF from the actuator patch to the accelerometer and the FRF from the actuator patch to the sensor patch are shown in Figure 4.12. The measured acceleration signal is integrated twice for a comparison with the numerical model. There is a reasonable agreement between the predicted and measured results. The error is more significant in the FRF of the sensor patch, especially in the range from 300 to 400 Hz, but no plausible explanation was found for this. In the FRF of the accelerometer, in every interval between two consecutive resonance frequencies, there is an anti-resonance frequency. This property of a “co-located” actuator/sensor pair is important for feedback control design [4], as will be shown in Chapter 6.

Next, the plate was excited by PZT patch 2 and the acceleration (accelerometer co-located with patch 2), and the voltage across patch 1 was measured. The numerical and experimental results are shown in Figure 4.13.

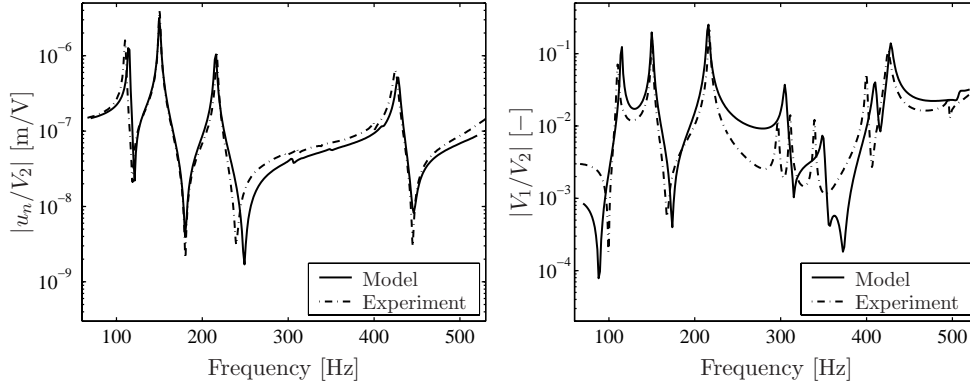


Figure 4.13: Calculated and measured FRFs from voltage applied to patch 2 V_2 to (left) accelerometer displacement u_n and (right) voltage across patch 1 V_1 .

The location of patch 2 is such that the first, second, third and eighth modes are well excited by the patch. The other modes are excited too, as can be seen in the FRF of the PZT sensor, but less effective. It is noted that the location of the sensor strongly determines whether a certain resonance frequency is visible in an FRF.

As a result of piezoelectric reciprocity the FRFs between the actuator patch and sensor patch must be identical for the two excitations. This is confirmed both numerically and experimentally in Figures 4.12 and 4.13 (right-hand side figures). In this respect reciprocity implies that the voltage measured by patch 2 when driving patch 1 is equal to the voltage measured by patch 1 when driving patch 2.

4.4.4 Sound radiation

Sound intensity method

The sound power radiated by an acoustic source is found by integrating the sound intensity, which is the product of acoustic pressure and particle velocity, over a surface enclosing the source. In practice the pressure is relatively easily measured with microphones, but it is not so easy to measure acoustic particle

velocity.⁸ In some special cases the sound intensity can be related directly to pressure, thereby circumventing the measurement of the particle velocity. It is then possible to calculate the sound power from pressure levels measured on a surface enclosing the source in the far field. Such pressure based methods must be carried out in special measurement facilities, where the conditions for the relation between intensity and pressure are satisfied. One example is the *anechoic room*, in which sound waves travelling from an acoustic source are absorbed by the walls, thus simulating a *free field* condition (ISO 3745). A second example is the *reverberant room*, in which sound is reflected so many times that it travels in all directions with equal magnitude and probability, in order that the *diffuse field* condition is satisfied (ISO 3741).

Sound intensity based sound power measurements do not require special measurement rooms. In this work an intensity probe with two closely spaced microphones is used to estimate the sound intensity (see Figure 4.14). The microphones are separated by a *solid spacer* and mounted head-to-head. The basic idea is to find an estimate of the sound intensity at the centre of the spacer.

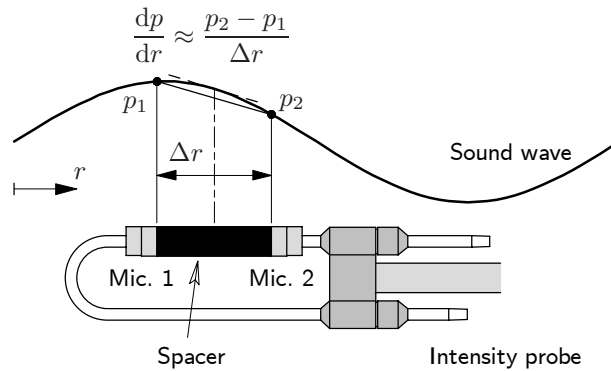


Figure 4.14: Estimation of the pressure gradient with a sound intensity probe.

In a linear sound field the particle velocity is related to the pressure gradient by Euler's equation, which for propagation in one direction reads:

$$\rho_0 \frac{\partial v_r(t)}{\partial t} = -\frac{\partial p(t)}{\partial r}, \quad (4.61)$$

where $v_r(t)$ is the particle velocity in the direction r . The particle velocity is estimated by replacing the pressure gradient with a finite difference approximation using the two microphone signals, as illustrated in Figure 4.14. In

⁸There exist acoustic particle velocity sensors, e.g. the *microflown*, but the use of such sensors in sound intensity measurements is not considered in this work.

practice the time domain microphone signals are transformed to the frequency domain using FFT, so the particle velocity estimation becomes:

$$v_r \approx -\frac{1}{j\rho_0\omega} \frac{p_2 - p_1}{\Delta r}, \quad (4.62)$$

where p_1 and p_2 are the complex pressure amplitudes measured with the microphones on the intensity probe, and Δr is the spacer length. The pressure at the centre of the spacer is approximated by $p = (p_1 + p_2)/2$. Thus, with equation (4.62) the sound intensity in direction r can be written as:

$$\bar{I}_r = \frac{1}{2} \text{Re}(p^* v_r) \approx -\frac{1}{2\rho_0\omega\Delta r} \text{Im}(p_1^* p_2). \quad (4.63)$$

Equation (4.63) gives an estimate of the sound intensity at a single point on the surface enclosing the acoustic source. The sound power is obtained by multiplying the space average of the sound intensity $(\bar{I}_r)_{\text{avg}}$ with the surface area S :

$$\bar{W} = (\bar{I}_r)_{\text{avg}} S. \quad (4.64)$$

There are two standardised procedures to obtain the space-averaged sound intensity. The *discrete point method* (ISO 9614-1) consists of many measurements, where for each measurement the probe is held at a single point. With an equal distribution of points across the measurement surface, the space-averaged intensity equals the average of the measured point intensities. In the *scanning method* (ISO 9614-2) the intensity probe is moved with constant speed across a path on the measurement surface. Both the discrete point method and scanning method are used in this work.

Intensity based sound power measurements are attractive because there is no need for a special measurement facility, one can measure close to the source (near field) where signal-to-noise ratios are high, and a source does not have to be isolated from other acoustic sources. The method can however not be applied without constraints. One should carefully consider the following limits:

- *High frequency limit.* The finite difference approximation is only valid if the acoustic wavelength is large compared to the spacer length. This poses an upper frequency limit on the intensity method.
- *Low frequency limit.* The estimation of the sound intensity in equation (4.63) can also be written as:

$$\bar{I}_r \approx \frac{1}{2\rho_0\omega\Delta r} |p_1| |p_2| \sin(\Delta\theta),$$

where $\Delta\theta$ is the phase angle between the microphone signals. At low frequencies, where the wavelength is much larger than the spacer length, this phase angle is small. In all analysing systems there will be a *phase mismatch* between the two measurement circuits, e.g. because the microphones are slightly different. The sound intensity estimation will be substantially under- or overestimated if the phase change across the spacer is of the same order as the phase mismatch.

The frequency limits are to a large extent determined by the spacer length and the quality of the measurement hardware. In the above, some possible errors in sound intensity estimations were given, but this is certainly not a complete list. More details can be found for instance in references [63, 64, 65, 66].

Implementation

The experiments were carried out with the B&K 2683 intensity probe with two half inch microphones (B&K 4181) separated by a spacer of 50 mm. The B&K 2260 signal analyser can be used to determine the sound power, but it gives results in octave or one-third octave frequency bands. In the present study the narrowband behaviour is of interest and therefore the B&K 2260 was used only as a pre-amplifier of the microphone signals. The outputs of the B&K 2260 were processed by the SigLab analyser and postprocessing, to obtain the sound power, was carried out in MATLAB.

The estimation of the sound intensity in equation (4.63) is proportional to the imaginary part of the cross-spectrum of the microphone signals. The FRFs from the voltage across the actuator patch to the microphone signals were used to calculate the cross-spectrum. The result is the sound intensity corresponding to a unit excitation voltage (perfect white noise). The measurement result is thus independent of the gain setting of the voltage amplifier, which makes it easy to compare numerical and experimental results.

Spatial averaging

The standards for the discrete point method and scanning method prescribe that a hypothetical measurement surface be defined, which encloses the acoustic source. The use of flat surfaces makes it easy to position the sound intensity probe, but as shown in Figure 4.15 the averaged sound intensity must be measured in multiple surfaces. Such a measurement is time consuming, which is not attractive if one wants to investigate the control performance in terms of sound power for different control strategies.

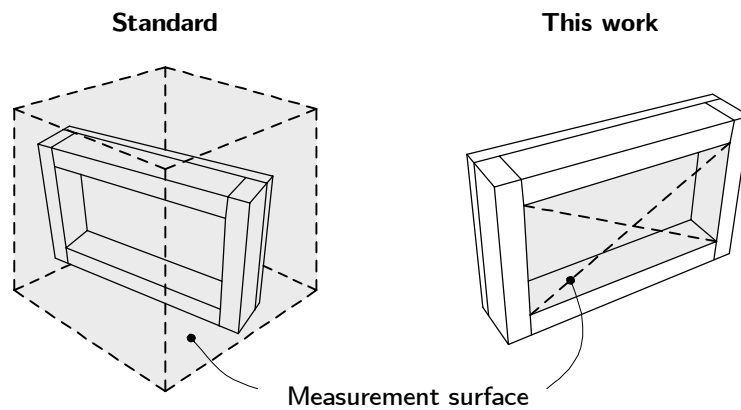


Figure 4.15: Standard definition of measurement surfaces and the method used in this work.

Hence, in this work the sound power radiated from one side of the plate is considered. The measurement surface is defined as shown in Figure 4.15. This simplified approach speeds up the sound power measurements, but as a consequence the results do not represent the total sound power radiated by the structure. This aspect is further discussed when the experimental method is compared with numerical results.

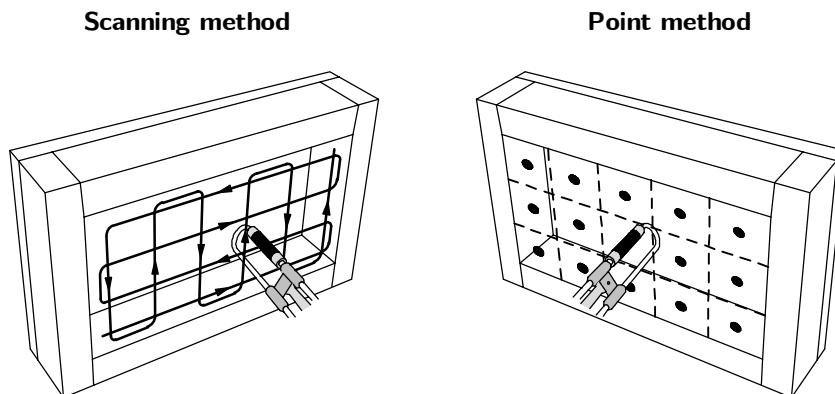


Figure 4.16: Illustration of the sound power measurement with the scanning method and the discrete point method.

Figure 4.16 shows how the discrete point method and the scanning method were used for spatial averaging of the sound intensity. The discrete point method can be expected to be more accurate and repeatable, but with the scanning method sound power measurements can be carried out much faster.

The scanning method is therefore preferable for parameter studies.

An experimental comparison of the discrete point method and scanning method is presented next. The discrete point method was performed on a grid consisting of 9×5 points, using an automated measurement procedure in which the intensity probe was mounted on the x - y table. Finer grids were also applied, but no significant improvement of the sound power was found. Several measurements were carried out using the scanning method, each lasting about 20 seconds, and following the path shown in Figure 4.16. Some differences between the sound powers measured with consecutive scans were obtained in frequency ranges in which the sound power was relatively small, but in general the repeatability was good. The plate was excited by patch 1 in the frequency range from 86 Hz to 486 Hz (pink noise). As mentioned before, the sound intensity was estimated using the FRFs of the microphones mounted on the intensity probe. Therefore, the results represent the sound power radiated by the plate when driving the patch by a *unit* voltage. The actual sound power is much higher; the input voltage was about 30 V (rms).⁹

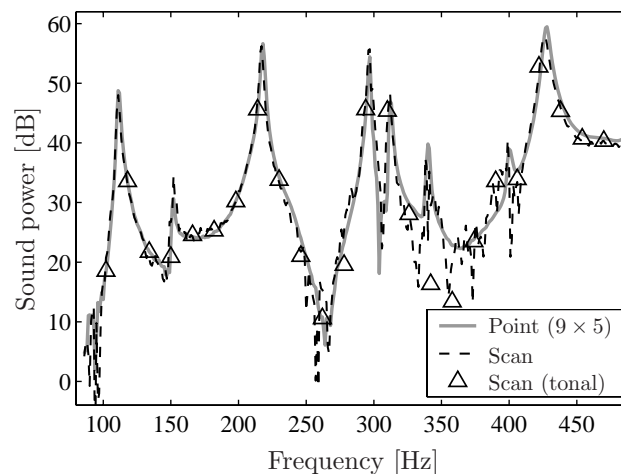


Figure 4.17: Comparison of scanning method and discrete point method: sound power radiated when patch 1 is driven (unit input).

In Figure 4.17 the sound power levels measured with the discrete point and scanning methods are shown. The scanning method was also performed for a number of tonal inputs, i.e. the sound power was measured when driving the patch by a single frequency input. This approach was used to measure the

⁹For a linear system: if the input voltage is doubled, then the increase in sound power level is 6 dB.

sound power in the case of narrowband feedforward control, as will be shown in Chapter 5. There is a good agreement between the results in the frequency ranges where the sound power is relatively high. However, in frequency ranges in which the sound power is small, e.g. near 350 Hz, there is a clear difference between the results. In such ranges the sound power measured with the scanning method shows an irregular frequency dependence. In the same ranges the repeatability of the scanning method is bad.

Comparison with model

The numerical prediction of the sound power is compared with the experimental results in Figure 4.18. Results are shown for the case that the plate is excited by patch 1 and for the case that the plate is excited by patch 2. The agreement between the prediction and measurement is far from excellent, but the numerical model certainly predicts the trends in the experimental results.

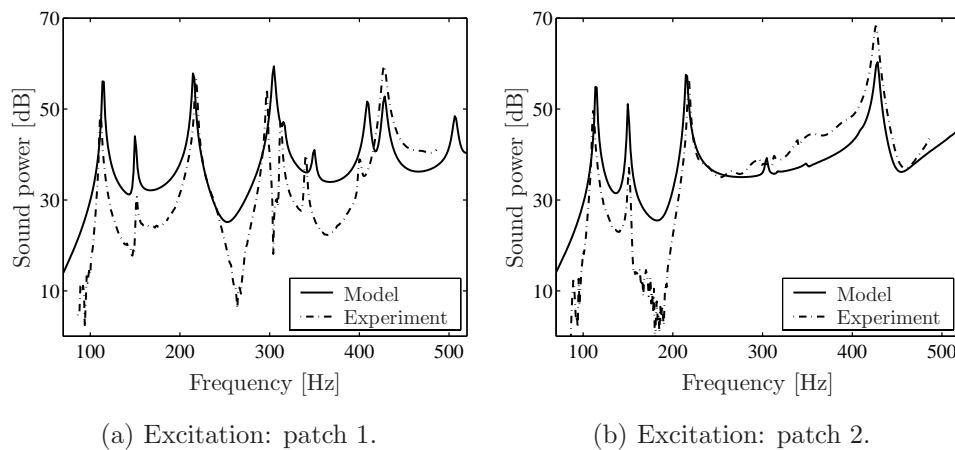


Figure 4.18: Calculated and measured sound power radiated by the plate for two excitations (unit input).

In Figure 4.19 the predicted and measured structural responses are shown in terms of the space and time average of the squared normal plate velocity (see equation (4.50)). The plate is excited by patch 1. The experimental result was obtained from the measured FRFs used for the eigenfrequency analysis (see Section 4.4.3). The agreement between the numerical and experimental results is much better for the structural response than for the acoustic response shown

in Figure 4.18(a). It is therefore concluded that the error in the prediction of the sound power is the result of an inaccurate acoustic model.

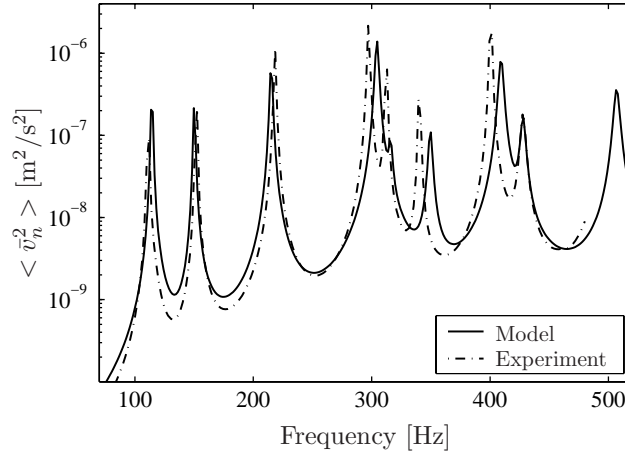


Figure 4.19: Calculated and measured structural response (excitation: patch 1, unit input).

The Rayleigh integral is based on the assumption of a baffled plate. However, the experimental setup was not placed in a baffle. Therefore, the radiation conditions in the model and the experiment are different. In order to quantify the effect of a baffle, an acoustic model of the experimental setup was created with the so-called *boundary element method* (BEM) [67, 68]. In the boundary element method (BEM) the radiating surface of an object is divided into elements. The Helmholtz integral equation (4.34) forms the basis of the boundary element method.

In Figure 4.20 the sound powers predicted with the BEM model and the Rayleigh integral model are compared with the measured sound power. These numerical results were obtained using the *measured* plate velocity distributions as input to the models. The prediction of the BEM model is very close to the measured sound power. For the largest part of the frequency range shown in the figure, the Rayleigh model overestimates the measured sound power. At low frequencies the wavelength is large compared to the dimensions of the experimental setup. A baffle prevents interaction between the sound fields on both sides of the plate. However, if no baffle is used, there is interaction of the sound fields, and as a result the plate radiates less efficiently.

The results in Figure 4.20 show that the BEM model is better suited for the current test problem. It is stressed that the BEM analysis is included only to illustrate the effect of a baffle of the sound power. The application of BEM

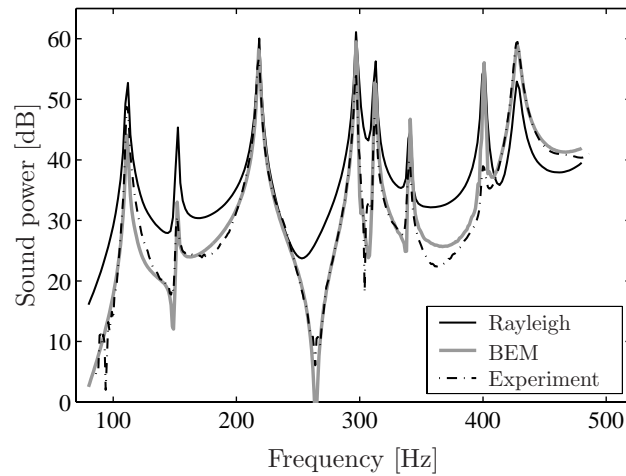


Figure 4.20: Comparison between Rayleigh model and BEM model (excitation: patch 1, unit input).

models is beyond the scope of this thesis. Hence, in the following chapters the Rayleigh model is used. Although the prediction of the sound power is far from excellent, the Rayleigh model certainly predicts the trends found in the experimental results. This simple model is therefore sufficiently accurate for the purpose of the subsequent chapters: to illustrate the effect of active control.

4.5 Concluding remarks

In this chapter an approach to model the structural-acoustic behaviour of plate-like structures with surface bonded piezoelectric patches was presented and validated. In this numerical approach, the structural and acoustic responses are modelled in an uncoupled way. First, the vibration response of the structure is calculated with the structural model. The resulting surface velocity distribution is used as the input for the acoustic model for calculating the sound radiation. The finite element method is applied to obtain an accurate description of the dynamical behaviour of the structure with piezoelectric patches. The associated free field sound radiation is calculated with the Rayleigh integral method. With model reduction techniques the number of degrees of freedom in the model is greatly reduced. The result is an efficient analysis tool which can serve as a basis for the design of a controller.

For an experimental setup consisting of a plate with two surface bonded patches the structural model and acoustic model were validated. The structural model was successfully validated with an experimental eigenfrequency analysis and an FRF analysis. A remarkable aspect is that the added mass and stiffness of the (small) patches can significantly change the mode shapes, whereas the eigenfrequencies are hardly affected. Sound power measurements were performed to validate the acoustic model. Although the agreement between predicted and measured acoustic responses is far from excellent, the numerical model certainly predicts the trends found with the experiments.

The modelling approach is general in the sense that the structure is modelled with FEM. It is therefore possible to model structures with complex geometries and boundary conditions. Less general is the Rayleigh integral method for predicting the sound field, since it is based on the assumption that the structure is a baffled plate. For structures with complex geometries, a more advanced technique such as the boundary element method must be used. However, for the analysis of the plate setup considered in this thesis, the Rayleigh integral model is sufficiently accurate.

The numerical model provides a basis to simulate and investigate the behaviour and performance of various control strategies. In the following chapters, the model is used in the analysis of a feedforward controller and a feedback controller for reducing acoustic radiation.

Chapter 5

Feedforward Control

5.1 Introduction

In this chapter the feedforward control of sound radiation of plate-like structures is considered, thereby using piezoelectric patches as part of the active control system. A feedforward control strategy is possible only if there is information about the primary disturbance excitation of the structure. If this is not the case, one has to resort to feedback control strategies, which is the topic of Chapter 6. Figure 5.1 shows a schematic representation of an elastic structure with a feedforward control system. This control problem is similar to the idea of Paul Lueg [5] for controlling sound propagation in a tube (see Chapter 1), but this case concerns the propagation of elastic flexural waves.

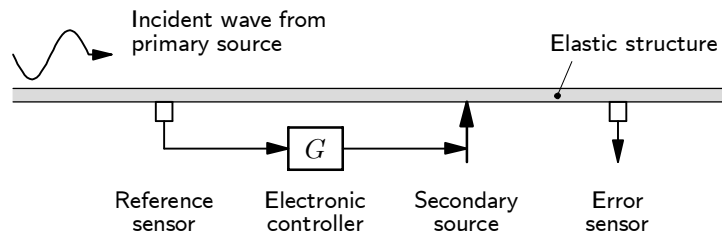


Figure 5.1: A feedforward control system for the control of wave propagation in an elastic structure.

Due to some *primary source* (disturbance source) a flexural wave travels through the elastic structure. In general the input from the primary source cannot be measured directly, so a *reference sensor* is used to detect the incoming wave. The signal from the reference sensor is fed to the *electronic controller*, which then drives the *secondary source* (control actuator). The ob-

jective is to design the controller such that the output from the *error sensor* is minimised.

An electronic controller is generally implemented on a digital signal processor (DSP). There is an inevitable delay associated with the controller due to the processing time of the DSP, but also due to amplifiers that are present in the feedforward path. The feedforward control of *random* disturbances is only effective if the delay in the path from the reference sensor to the error sensor through the controller is smaller than the time required for the elastic wave to travel from the reference sensor to the error sensor through the structure. In control theory this is referred to as the *causality constraint*. The causality constraint is of no importance if the incident wave is *deterministic*, e.g. harmonic. Then, only the fundamental driving frequency in the primary signal needs to be detected.

In this chapter the feedforward control of harmonic disturbances is considered. In Section 5.2 quadratic optimisation is applied to estimate the performance of feedforward control systems with one or more secondary sources and one or more error sensors. This method, which is referred to here as optimal control, is applied in Section 5.3 for studying the control of sound radiation of a plate structure, with surface bonded patches as secondary sources. Several arrangements of the controller are considered and error sensors are used that measure either the structural response or the acoustic response of the system. In Section 5.4.2 a number of feedforward control arrangements for harmonic disturbances are tested on the experimental setup that was introduced in the previous chapter. The experimental results are compared with numerical results, which are calculated with the structural and acoustic models presented in Chapter 4.

5.2 Optimal control

In this section a procedure is outlined for the analysis of feedforward control systems. A feedforward control system can, for example, be used to control the sound radiation of a structure such as shown in Figure 5.2. The primary excitation of the structure is due to a point force in the transverse direction, i.e. perpendicular to the plate surface. This disturbance will put the plate into motion and as a result, the error sensor, which is an accelerometer, will produce an error signal. The secondary control source is a surface bonded piezoelectric patch. In the analysis that follows, the objective is to find the control signal that must be applied to the secondary source to minimise the error signal.

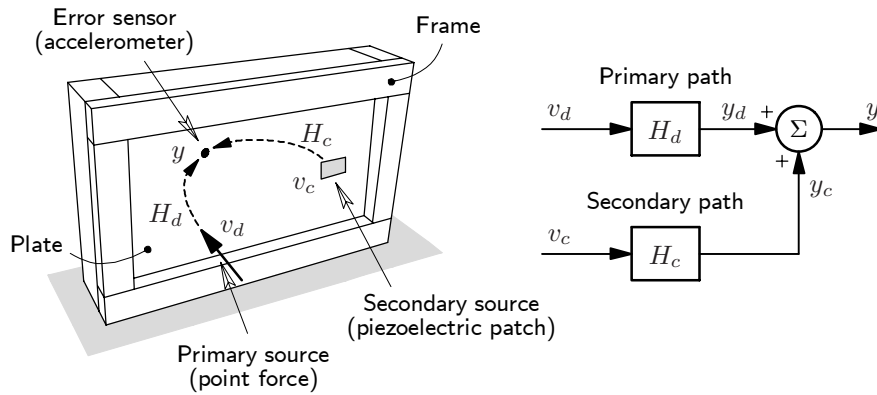


Figure 5.2: Example of a feedforward control system.

It is assumed that all parts of the system, that is structural, piezoelectric and electrical, are *linear*. Furthermore, all signals are in their *steady state*, so the effect of feedforward control is considered for each frequency independently. With the system being linear, in the frequency domain the complex output from the error sensor, y , is the superposition of the complex output due to the primary source operating alone, y_d , and the complex output due to the secondary source operating alone, y_c . The error signal can furthermore be expressed in terms of the complex amplitude of the point force, v_d , and the complex amplitude of the voltage applied to the patch, v_c :

$$y = y_d + y_c = H_d v_d + H_c v_c. \quad (5.1)$$

In this equation H_d represents the so-called *primary path*, which is the FRF from the primary source to the error sensor. The so-called *secondary path* H_c is

the FRF from the secondary source to the error sensor. It is assumed that the signals applied to the primary and secondary sources are perfectly coherent, i.e. no other uncorrelated signals are present that would act as noise. Then, the acceleration signal can be set to zero at any frequency by introducing a secondary input equal to:

$$v_c^{\min} = -\frac{H_d}{H_c} v_d. \quad (5.2)$$

This equation illustrates that the secondary input must be such that the difference in amplitude and the phase shift between the primary and secondary paths are compensated. Obviously, the secondary path FRF may not be zero in order to prevent an unbounded optimal secondary input. Such a singular condition is avoided if there is some damping in the system, but the secondary input can still be very large near certain frequencies (see Section 5.3).

Very often the control system consists of multiple error sensors and multiple secondary sources. Equation (5.1) can be written for the multiple-input-multiple-output (MIMO) case as:

$$\mathbf{y} = \mathbf{H}_d \mathbf{v}_d + \mathbf{H}_c \mathbf{v}_c, \quad (5.3)$$

where it has been assumed that there are also multiple primary sources. Note that the (i,j) -th element in matrix \mathbf{H}_c is the FRF between error sensor i and secondary source j . If the number of error sensors and the number of secondary sources are equal, the vector with optimal secondary inputs setting all error sensor outputs to zero is given by:

$$\mathbf{v}_c^{\min} = -\mathbf{H}_c^{-1} \mathbf{H}_d \mathbf{v}_d, \quad (5.4)$$

provided that \mathbf{H}_c is not singular. In many cases, however, the number of sensors and the number of secondary sources are not equal. Then, the secondary input can be found by minimising a *quadratic error criterion* of the form:

$$J = \mathbf{y}^H \mathbf{W}_y \mathbf{y} + \mathbf{v}_c^H \mathbf{W}_c \mathbf{v}_c, \quad (5.5)$$

where \mathbf{W}_y is the error weighting matrix and \mathbf{W}_c is the effort weighting matrix. With the error weighting matrix, some error signals can be given greater priority than others. The effort weighting matrix has the effect of preventing small reductions of the error signals at the expense of large control inputs. With equation (5.3) the error criterion can be written in the so-called *Hermitian quadratic form* [6]:

$$J = \mathbf{v}_c^H \mathbf{A} \mathbf{v}_c + \mathbf{v}_c^H \mathbf{b} + \mathbf{b}^H \mathbf{v}_c + c, \quad (5.6)$$

where the individual terms are given by:

$$\mathbf{A} = \mathbf{H}_c^H \mathbf{W}_y \mathbf{H}_c + \mathbf{W}_c, \quad (5.7a)$$

$$\mathbf{b} = \mathbf{H}_c^H \mathbf{W}_y \mathbf{H}_d \mathbf{v}_d, \quad (5.7b)$$

$$c = \mathbf{v}_d^H \mathbf{H}_d^H \mathbf{W}_y \mathbf{H}_d \mathbf{v}_d. \quad (5.7c)$$

It should be noted that the matrix \mathbf{A} is not the same as the state space matrix used in Section 4.2. The cost function J is quadratic in the vector with control inputs \mathbf{v}_c , and possesses a unique minimum if \mathbf{A} is not singular, which is guaranteed if \mathbf{A} is positive definite. In order to ensure the positive definiteness of \mathbf{A} , the weighting matrices \mathbf{W}_y and \mathbf{W}_c must be positive definite.¹ When this condition is satisfied, the control inputs for which the error criterion is minimal (5.6) are given by [6]:

$$\mathbf{v}_c^{\min} = -\mathbf{A}^{-1} \mathbf{b}, \quad (5.8)$$

and the minimum of the error criterion is:

$$J^{\min} = c - \mathbf{b}^H \mathbf{A}^{-1} \mathbf{b}. \quad (5.9)$$

Note that if there are as many secondary sources as error sensors and no effort weighting is included (i.e. $\mathbf{W}_c = \mathbf{0}$), the vector with optimal secondary inputs given in equation (5.8) is equal to the result in equation (5.4). In equation (5.8) the optimal secondary inputs are given relative to the primary inputs. It is however not necessary to explicitly know the complex amplitudes of the primary disturbances. The only necessity is a harmonic reference signal with a frequency equal to that of the primary input (see Section 5.4).

5.3 Error criteria

In Chapter 4 the sound power was introduced as a measure for the free field sound radiation of a vibrating structure. It was shown that the sound power, when solved with a numerical method, can be written as:

$$\bar{W} = \mathbf{v}_n^H \mathbf{R} \mathbf{v}_n, \quad (5.10)$$

where \mathbf{v}_n is the vector with normal plate velocities and \mathbf{R} is the radiation resistance matrix. This equation is quadratic in \mathbf{v}_n , which on its turn is proportional to the primary and secondary inputs acting on the system. Therefore,

¹The positive definiteness of \mathbf{W}_c ensures positive definiteness of \mathbf{A} even if $\mathbf{H}_c^H \mathbf{W}_y \mathbf{H}_c$ is singular, which can be the case if there are fewer error sensors than secondary sources.

the sound power can be used as an error criterion in optimal control theory. This error criterion defines the best possible reduction in sound power that can be achieved with a predetermined configuration of the secondary sources. It is, however, not easy to implement this kind of control strategy in practice. A practical implementation consists either of sensors that measure the structural response, such as accelerometers, or of sensors that measure the acoustic response, such as microphones. In this section the use of these more realistic error sensors in active structural acoustic control is considered.

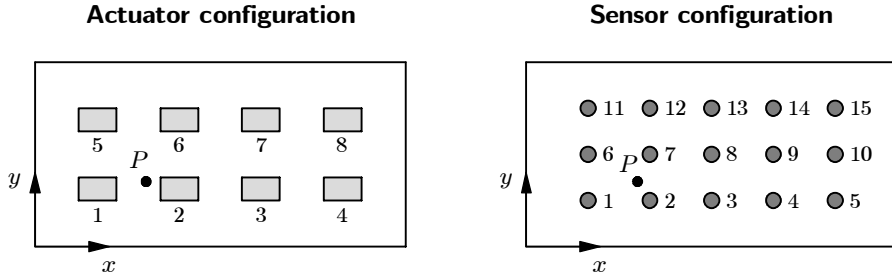


Figure 5.3: Uniform distribution of actuator patches (left), and velocity or microphone error sensors (right).

In this section results are presented for a clamped rectangular aluminium plate of $490 \times 244 \times 1.2$ mm. Eight voltage driven actuator patches ($50 \times 30 \times 1.0$ mm) are uniformly distributed over the plate in a 4×2 arrangement, as shown in Figure 5.3.² The feedforward control system consists of error sensors, uniformly distributed in a 5×3 arrangement, that measure either the normal plate velocity or the acoustic field pressure. In the case acoustic error sensors are used the sensor grid is adjacent to the plate surface with an offset of 100 mm. The primary excitation is due to a transverse point force located at $(x, y) = (147, 86.3)$ mm (indicated by P in Figure 5.3).

In the following sections several feedforward control arrangements will be considered, thereby varying the number of patches used for control and the number and type of error sensors. Clearly, the goal is to reduce the sound radiated by the plate. The results are therefore presented in terms of the sound power radiated by the controlled system, rather than by comparing the outputs of the error sensors. All results correspond to the case where the point force has an amplitude of 1 Newton.

²The material properties of the plate and the patches can be found in Figure 4.9 and Appendix A.

5.3.1 Single channel control

As a first step, a feedforward control system consisting of one secondary source and one *velocity* error sensor is considered. The associated error criterion is the squared amplitude of the normal plate velocity at the error sensor: $J = |v_n|^2$. The performance of two such single channel configurations, consisting of patch 6 and either sensor 4 or sensor 12, is shown in Figure 5.4. The best possible performance that can be obtained with this secondary source, i.e. when the error criterion is the sound power ($J = \bar{W}$), is also shown in the figure. In optimal control theory the secondary input is calculated for each frequency independently. The results will therefore be the same if the error sensor measures the normal plate displacement or acceleration rather than the plate velocity. In practice, this type of control is probably the most easily implemented with accelerometers (see Section 5.4.3).

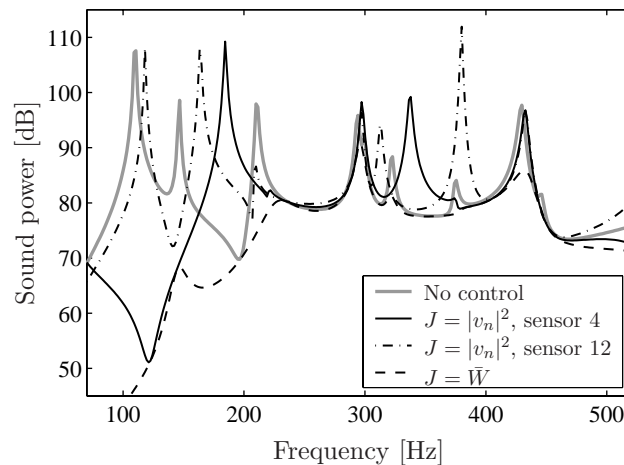


Figure 5.4: Control performance when patch 6 is the secondary source and either error sensor 4 or 12 is used ($J = |v_n|^2$), or the sound power is the error criterion ($J = \bar{W}$).

The single channel controllers give a perfect cancellation of the normal plate velocity at the error sensor. The effect of reducing the velocity at one error sensor on the overall sound radiation is not straightforward. It can be observed in Figure 5.4 that the sound powers are reduced at some frequencies, when compared with the uncontrolled system, but increased at other frequencies. A remarkable aspect is that this type of controller presents resonant behaviour at frequencies different from the eigenfrequencies of the uncontrolled system. These “new” resonance frequencies depend on the location of the error sensor.

For instance, when the displacement at error sensor 12 is driven to zero, resonant behaviour is observed at a frequency just below the first eigenfrequency of the uncontrolled system, whereas the first new resonance frequency is visible in-between the second and third eigenfrequencies of the uncontrolled system when sensor 4 is the error sensor.

The output of the single channel controller is proportional to the FRF H_d/H_c , where H_d and H_c are the FRFs from the point force and control voltage, respectively, to the error sensor (see equation (5.2)). The secondary source will have an unbounded input if the secondary path FRF H_c is zero. This singular condition is avoided by the damping in the system, but since the damping is only small the secondary input still becomes very large at certain frequencies.

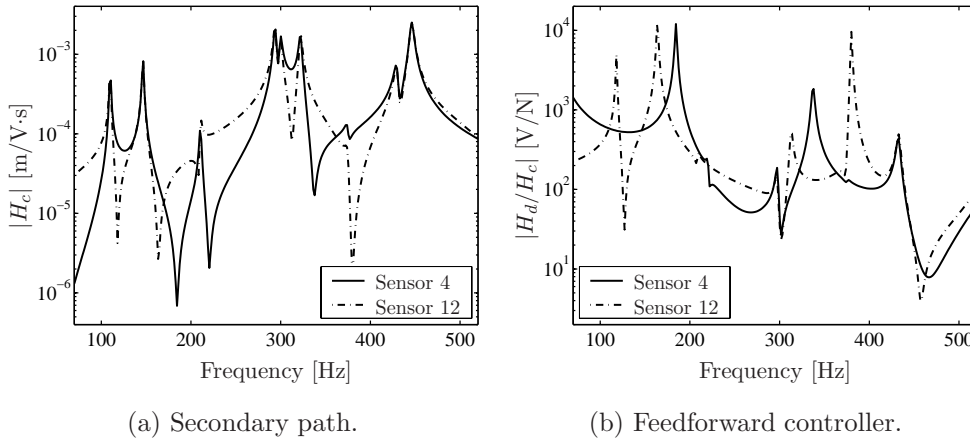


Figure 5.5: FRFs of the secondary path and the feedforward controller when either sensor 4 or 6 is used in combination with patch 6.

In Figure 5.5 the secondary path FRF H_c and the FRF of the feedforward controller H_d/H_c are shown for the two single channel control configurations. It can be observed that the output from the controller is very large near the frequencies that correspond with the anti-resonance frequencies in the secondary path FRF. A comparison of Figures 5.4 and 5.5(b) reveals that at the same frequencies the results for the sound power show resonant behaviour. An interpretation of this effect is that because there is a “weak” transfer between the secondary source and the error sensor, the control input must be very large in order to cancel the response at the error sensor. Although there is a perfect cancellation of the plate vibration at the error sensor, the overall

plate vibration increases due to the large control inputs, thus leading to high sound power levels. This effect can also occur if a microphone is used rather than a velocity sensor, as shown in the work of Burdisso and Fuller [69, 70].

A very large output from a single channel controller can be prevented by adding an effort weighting term to the error criterion: $J = |v_n|^2 + W_c |v_c|^2$. This error criterion is in fact the single channel version of equation (5.5). Effort weighting has the effect of preventing small reductions of the error signal at the expense of a large secondary input. A similar effect is obtained when a second error sensor is used, without weighting of the secondary input. It is then required that the anti-resonance frequencies in the two secondary path FRFs do not coincide, or else the secondary input will still be very large. Both methods have the effect that the output from the error criterion is no longer reduced to zero.

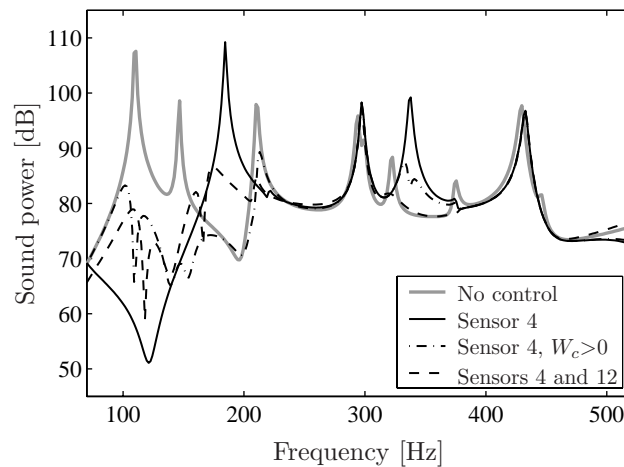


Figure 5.6: Preventing resonant behaviour of single channel feedforward controller by effort weighting or by adding a second error sensor.

In Figure 5.6 the performance of the original configuration, which consists of sensor 4 and patch 6, is compared with two alternative controllers, one implemented with control effort weighting and one implemented with a second error sensor (sensor 12). It can be observed that the resonant behaviour, which is clearly visible near frequencies of 180 Hz and 330 Hz for the original configuration, is not present in the case of the alternative controllers. On the other hand, in the low frequency range the reduction in radiated sound power is less, when compared to the original configuration.

5.3.2 Multiple channel control

As a next step, feedforward controllers consisting of multiple secondary sources and multiple error sensors are considered. In contrast to the single channel control system described previously, which used a velocity error sensor, the multiple channel control system is equipped with error sensors that measure the *acoustic pressure* in front of the plate. The error criterion is defined as the sum of the squared amplitudes of the field pressures: $J = \mathbf{p}^H \mathbf{p}$. Again the primary excitation of the structure is a point force (unit amplitude).

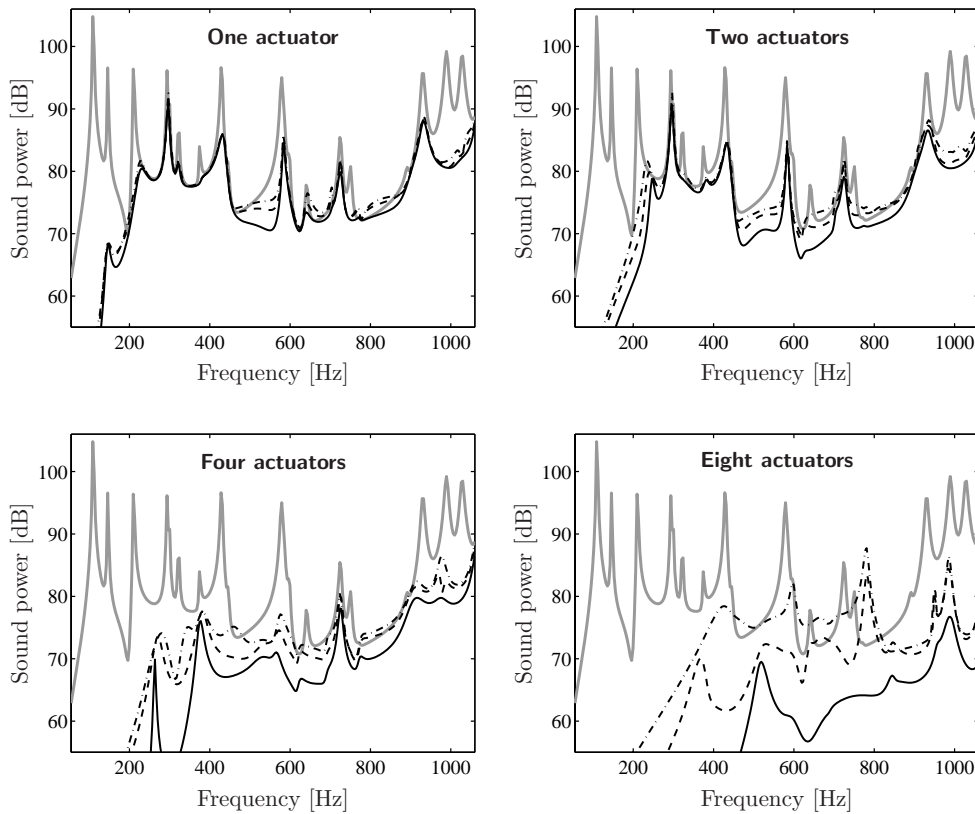


Figure 5.7: Sound power without control (—) and when the field pressure is minimised at nine error sensors (----), at fifteen error sensors (- - -), or the sound power (—) is minimised with one, two, four or eight secondary sources.

In Figure 5.7 the performance of several multiple channel configurations are compared. The control system consists of either *one* secondary source (patch 6), *two* secondary sources (patches 3 and 6), *four* secondary sources (patches 1, 3, 6 and 8) or all *eight* secondary sources (see Figure 5.3). Three error cri-

teria are considered: minimisation of the pressure at *nine* error microphones (microphones 1, 2, 3, 7, 8, 9, 13, 14 and 15), minimisation of the pressure at all *fifteen* error microphones, and minimisation of the sound power. For each configuration of the secondary sources, the control performances associated with these error criteria are compared to the case when no control is applied.

The results show that, in general, the performance improves with an increasing number of secondary sources. That is, the frequency range in which a significant reduction of the sound power is achieved broadens if more secondary sources are used. The reduction obtained with a control system consisting of one secondary source and nine (or fifteen) error microphones is close to the best possible reduction with this secondary source. Apparently, the minimisation of the near-field pressure is a good strategy for reducing the sound power at low frequencies. If more secondary sources are used, a larger offset between the best possible performance and the performance associated with the minimisation of pressure is found. Also, the reduction in sound power of a controller with microphone error sensors becomes more sensitive to the number of sensors. More sensors are then needed to “converge” to the best possible performance.

The effect of resonant behaviour, such as found with single channel control, cannot be observed in Figure 5.7. It can, however, also occur in multiple channel feedforward control systems, for example if there are as many error sensors as secondary sources. Such behaviour is encountered if the matrix \mathbf{A} in the quadratic Hermitian formulation, see equation (5.6), is ill-conditioned or singular. The results given in Figure 5.7 all correspond to configurations with more error sensors than secondary sources. It must be noted that using more error sensors than secondary sources does not necessarily prevent the controller from producing very large outputs. For example, as a result of bad placement of the error sensors, matrix \mathbf{A} can still become singular at certain frequencies. Such a situation can, however, be prevented with control effort weighting.

5.3.3 Radiation modes

It can be inconvenient or impossible to place microphones in front of the plate surface. One alternative approach, which has received considerable attention in the literature, is to measure the vibration level with sensors that are integrated in the structure. It was already demonstrated in Section 3.5 that control of the structural vibration can result in a poor performance in terms of the radiated sound power. An alternative method is to weigh the error signals measured with a grid of velocity sensors such that the resulting error criterion is a measure for the sound power [57, 58]. Such a sensing strategy is briefly discussed in this section.

The sensing strategy is based on the *radiation modes*, which were introduced in Chapter 4. At low frequencies, i.e. when the acoustic wavelength is large compared to the dimensions of the vibrating surface, the radiation efficiencies associated with the radiation modes fall off very rapidly with increasing mode number. In Chapter 4, this property was used to obtain a good approximation of the sound power by taking into account only a small number of radiation modes. This property also implies that the contribution of only a few radiation modes must be controlled to obtain high reductions in sound power. This is illustrated using an error criterion of the form:

$$J = \mathbf{a}_r^H \mathbf{\Lambda}_r \mathbf{a}_r, \quad (5.11)$$

where \mathbf{a}_r is the vector with the participation factors of a small number of radiation modes, and $\mathbf{\Lambda}_r$ is the diagonal matrix with the corresponding radiation efficiencies (see Section 4.3.3). Note that this error criterion represents an estimate of the radiated sound power.

Figure 5.8 shows the control performance, in terms of sound power, obtained with a control system consisting of four secondary sources (patches 1, 3, 6 and 8) that minimise the error criterion (5.11) when the first *six* radiation modes are included. Besides, the control performance for the error criterion ($J = \mathbf{a}_r^H \mathbf{a}_r$) is shown. In this case all radiation modes are weighted equally. It can be observed that minimisation of the radiation mode error criterion gives a control performance nearly equal to the best possible reduction in sound power, except at high frequencies (> 900 Hz). In the case where the radiation mode participations are weighted equally, the performance degrades a little at the low frequencies.

Previously, it was assumed that the radiation mode participation factors are available for control. In practice, the mode participations must be estimated with some kind of sensing strategy. One way to do this is by weighting the error signals from a grid of velocity sensors by the radiation mode shapes.

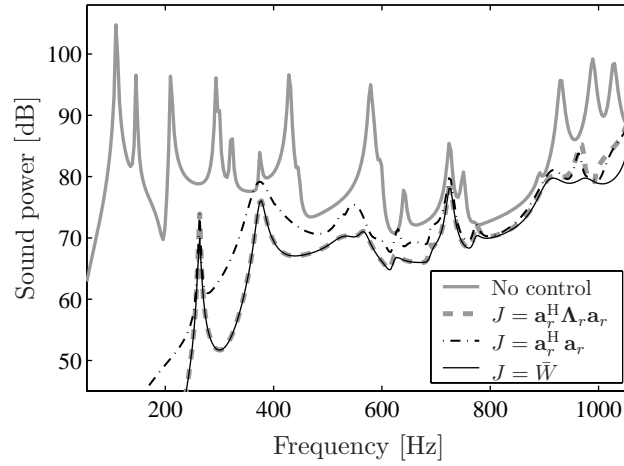


Figure 5.8: Control performance for minimisation of the participations of six radiation modes (weighted and unweighted) with four secondary sources (patches 1, 3, 6 and 8).

A disadvantage of using such a “spatial filter” is that the radiation modes depend on frequency, which would lead to a complicated implementation of the control system. It is shown by Berkhoff [58] that at low frequencies a good estimation is made with a set of radiation modes determined at a single frequency. Furthermore, weighting the estimated participation factors by the radiation efficiencies has a small influence on the control performance. In line with these observations, the following error criterion is defined:

$$J = \tilde{\mathbf{a}}_r^H \tilde{\mathbf{a}}_r, \quad \text{where} \quad \tilde{\mathbf{a}}_r = \tilde{\mathbf{\Gamma}}_r^T \mathbf{v}_n, \quad (5.12)$$

where $\tilde{\mathbf{a}}_r$ are the estimated radiation mode participation factors, \mathbf{v}_n are the error signals from the velocity sensors and $\tilde{\mathbf{\Gamma}}_r$ is a matrix with frequency independent radiation modes, at the locations of the velocity sensors.

In Figure 5.9 the performance for minimisation of the error criterion (5.12) is compared to that of the error criterion defined as the sum of the squared amplitudes of the surface velocities ($J = \mathbf{v}_n^H \mathbf{v}_n$). All fifteen velocity error sensors on the plate are used and the spatial filter is constructed with the first six radiation modes at 50 Hz. In the low frequency range, a better performance is obtained when using the frequency independent spatial filters. Besides the improved performance, this approach has the practical advantage that the number of input channels to the controller is smaller, i.e. equal to the number of radiation modes included.

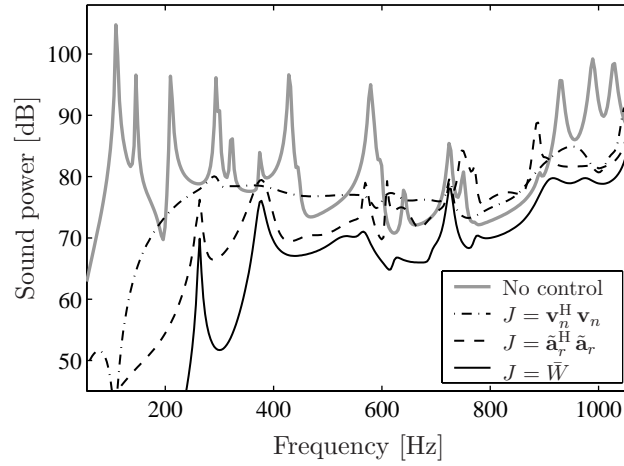


Figure 5.9: Effect of using six frequency independent radiation modes to filter surface velocities measured with fifteen error sensors (four secondary sources: patches 1, 3, 6 and 8).

The foregoing approach is related to the concept of reducing the “volume velocity” of a radiating structure. The volume velocity corresponds to the shape of the first radiation mode at low frequencies. Therefore, if only one radiation mode is accounted for in error criterion (5.12), then the (estimated) volume velocity of the plate is controlled. In this approach, the spatial filter reduces to summing the outputs from the velocity sensors [14]. Note that only one secondary source is needed to control the volume velocity. Other sensing strategies to estimate the volume velocity have also been reported in the literature, such as with shaped PVDF film [71] or by using multiple piezoelectric patches [72].

5.4 Experiments

In this section the practical application of the feedforward control of harmonic disturbances is considered. The main purpose is to show that the numerical model is capable of predicting the experimental results rather than to design a feedforward control system which most effectively reduces the sound radiation. First, the practical implementation of a feedforward controller is briefly discussed.

5.4.1 Adaptive feedforward control

An important feature of a feedforward control system is that the performance is very sensitive to small variations in the amplitude and phase of the secondary inputs. This effect is illustrated in Figure 5.10 for a strip with a single channel feedforward control system.³ In the figure the radiated sound power is shown as a function of the secondary input v_c , which is varied in a small range around the optimal secondary input v_c^{\min} . The sound power has been normalised with the sound power without control. The results, which show the control performance when the strip is excited at the first, second or third eigenfrequency of the uncontrolled system, clearly indicate that for an optimal performance the secondary input must be set with close precision.

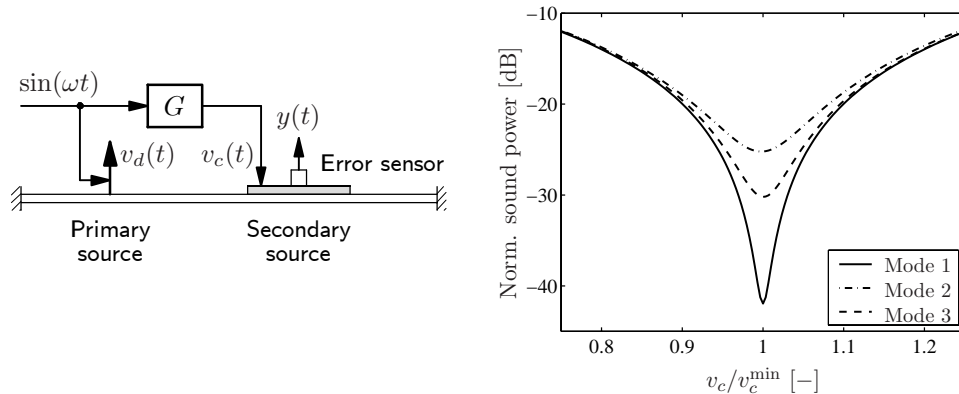


Figure 5.10: The effect of a suboptimal secondary input on the control performance, in terms of sound power, of a single channel feedforward controller.

The optimal secondary input depends on the primary source and on the primary and secondary path FRFs (see for example equation (5.2)). In practice the characteristics of the primary source are often non-stationary (e.g. change

³A more detailed analysis of this strip problem can be found in Section 3.5.

of frequency or amplitude). The primary and secondary paths will also vary slowly in time due to changes in environmental conditions (e.g temperature). A time-invariant feedforward controller, designed using the procedure presented in Section 5.2, will perform suboptimally as a result of time-variant behaviour of the system under control. Since the performance is very sensitive to small amplitude and phase mismatches of the secondary source, even small changes in the behaviour of the system can significantly degrade the control performance. A feedforward controller is therefore in general implemented as an adaptive controller, which is able to track changes in the system.

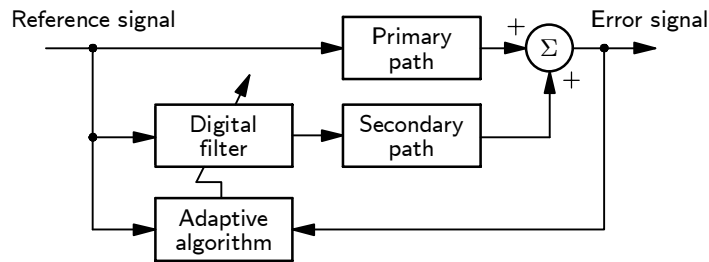


Figure 5.11: General block diagram of an adaptive feedforward control system.

An adaptive feedforward controller is usually implemented on a DSP, which allows easy adjustment of the control action. An electronic controller running on a DSP is referred to as a digital filter. A general block diagram representation of an adaptive feedforward controller is shown in Figure 5.11. The adaptive control system involves two basic parts: a *digital filter* whose output drives the secondary source (assuming a single channel system), and an *adaptive algorithm* that adjusts the coefficients of the filter.

An update of the digital filter is determined from the reference signal, but also from the error signal. It is stressed that the purpose of this “feedback path” is different from what is normally done in feedback control (see also Chapter 6). In a feedback controller, the control input is directly derived from the error signal. In an adaptive feedforward controller, the feedback path is used only to adjust the way in which the control input is derived from the reference signal. If for instance the error sensor is damaged, then the adaptive feedforward controller still operates, although it can no longer adjust to changes. If the same happens to a feedback controller, the control input becomes zero, i.e. the controller is turned off.

It is usually the goal to adjust the filter in such a way that the error signal is reduced to zero. There are various combinations of digital filters and adaptive algorithms for both broadband and narrowband control problems

(see the textbooks of Kuo and Morgan [73], and Nelson and Elliott [6]). One of the most popular implementations is the so-called filtered- x LMS algorithm. In this work a narrowband version of this algorithm, which is often referred to as *adaptive notch filter*, is used. A description of the adaptive notch filter is included in Appendix E.

5.4.2 Experimental setup

The experimental setup used for validation of the numerical model in Chapter 4 was also used in the feedforward control experiments. Most of the hardware in the experimental setup was already discussed in Section 4.4.1. The adaptive notch filter was implemented on a dSPACE DS1103 controller board.

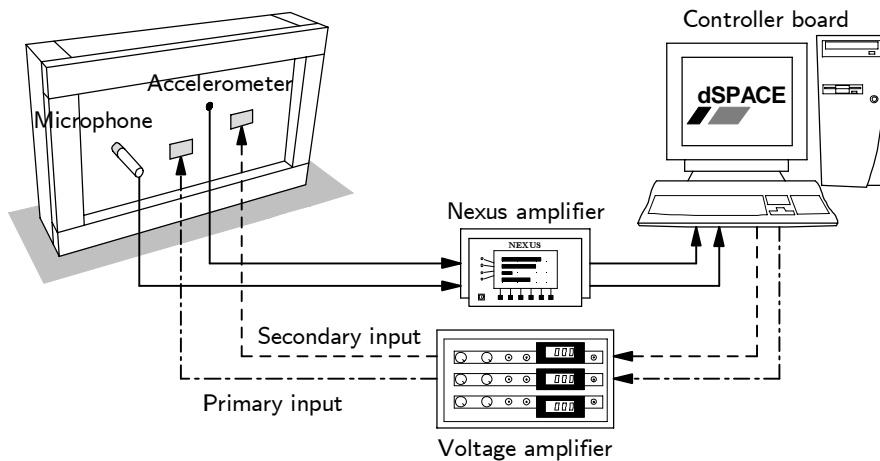


Figure 5.12: Setup for experiments with control. Hardware that is used to monitor the control performance is not shown (see Figure 4.8).

One of the two patches on the plate served as the primary source in the experiments. This type of disturbance excitation is not very realistic but allows a comparison of experimental and numerical results since the excitation due to a patch is well defined. The other patch was the secondary source; the control system had one secondary input. The effect of feedforward control was considered for a number of cases, where either accelerometers or microphones were used as error sensors. For each case, the adaptive notch filter was tested at several frequencies. At each frequency, after convergence of the controller, the sound power radiated by the plate was measured with the sound intensity

method. The scanning method was used to obtain the space-averaged sound intensity (see Section 4.4.4).

A number of general remarks are made regarding the implementation of the adaptive notch filter:

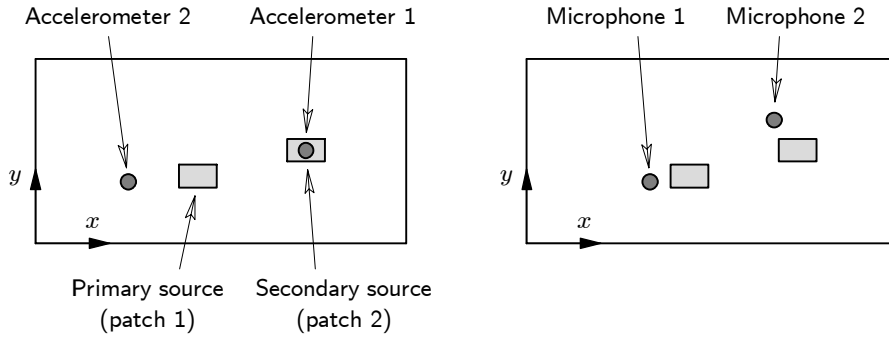
- The sample frequency of the dSPACE controller board was 20 kHz.
- The harmonic signal driving the primary source was provided by the dSPACE controller board. The same signal was used as the reference signal for the adaptive notch filter, thus no sensing device was used to detect the disturbance frequency. Furthermore, the frequency was adjusted stepwise.
- The estimation of the secondary path FRFs, used by the adaptive notch filter, were determined off-line, i.e. before the experiments with control were conducted. The secondary path FRFs were measured in the frequency range of interest using the DSPT SigLab analyser. For each frequency, before the adaptive notch filter was turned on, the corresponding amplitude and phase angle of a secondary path FRF were set.
- No weighting of the error signals (performance weighting⁴) and no weighting of the secondary inputs (effort weighting) was performed. Because there was no effort weighting, the effect of introducing new resonance frequencies caused by the feedforward controller could be investigated (see Section 5.3.1).

The current implementation of the adaptive notch filter was sufficient for studying the general properties of narrowband feedforward control. It is however not suitable for a practical problem since the filter cannot adjust to changes in the primary disturbance (e.g. frequency) or changes in the secondary path. More advanced implementations of the adaptive notch filter, which do include these features, can for instance be found in reference [73].

5.4.3 Results

The performance of the adaptive notch filter was measured for sensor arrangements consisting of either one or two accelerometers mounted on the plate, and one or two microphones placed in front of the plate. In all four cases one secondary source was used to attenuate the response at the error sensors. The locations of the primary and secondary sources and the locations of the error sensors are given in Figure 5.13.

⁴Note that performance weighting is only of interest if there are at least two error sensors.



Sensor	x [m]	y [m]	z [m]
Accelerometer 1	0.358	0.123	–
Accelerometer 2	0.123	0.081	–
Microphone 1	0.163	0.081	0.10
Microphone 2	0.327	0.163	0.10

Figure 5.13: Locations of primary and secondary sources (patches) and error sensors (accelerometers or microphones). Locations of the patches can be found in Figure 4.9.

For each arrangement of the error sensors, the adaptive notch filter was tested at about 35 frequencies in the range up to 500 Hz. At each frequency, the sound power radiated on one side of the plate was measured in order to evaluate the control performance. The complex amplitude of the signal driving the primary source was also measured in order to provide an absolute comparison between the numerical and experimental results. Also, the signal driving the secondary source was measured in order to determine the control effort. The performance of the controller was also predicted with a numerical model. More details regarding the numerical model of the experimental setup can be found in Section 4.4.2.

Structural error sensing

First, the control systems with one and two *accelerometers* are considered. Figure 5.14 shows the predicted and measured control performances in terms of the radiated sound power. The sound power due to the primary source operating alone is also depicted (no control).⁵ It is important to note that the

⁵The sound power due to the primary source alone shown in Figure 5.14(b) was measured with a high frequency resolution and using the discrete point method, whereas the results with control were measured at discrete frequencies using the scanning method.

results in the figure represent the sound power when a unit voltage is applied to the primary patch. The measurements were carried out using primary inputs up to 30 V, thus the actual sound power levels are higher. In Figure 5.15 the voltage applied to the secondary patch is shown relative to the voltage applied to the primary patch.

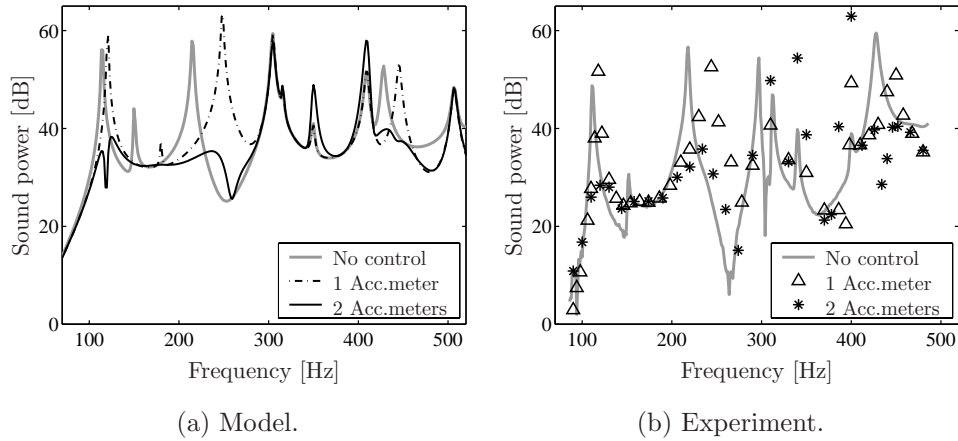


Figure 5.14: Predicted and measured performances of a narrowband feedforward controller with one accelerometer and with two accelerometers.

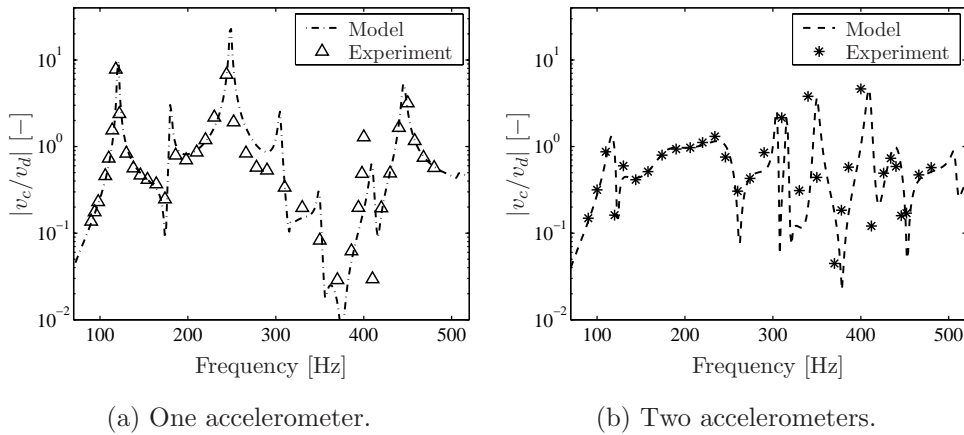


Figure 5.15: Predicted and measured values of the secondary patch voltage v_c relative to the primary patch voltage v_d .

In general, the numerical and experimental results show the same trends. The following observations can be made regarding the predicted and measured behaviour of the controlled systems:

- The results for the controller with one accelerometer clearly show resonant behaviour at frequencies not corresponding to the eigenfrequencies of the uncontrolled system, i.e. near frequencies of 120 Hz, 250 Hz and 450 Hz. As shown in Figure 5.15(a), a high control voltage is required at such a frequency in order to cancel the acceleration signal. The overall vibration level of the plate is increased and, as a result, the sound power level becomes very high. It was shown in Section 5.3.1 that these “new” resonance frequencies correspond to the anti-resonance frequencies in the secondary path FRF.
- With a second accelerometer, the effect of resonant behaviour is prevented. A comparison of Figures 5.15(a) and 5.15(b) reveals that the secondary input is much smaller near frequencies of 120 Hz, 250 Hz and 450 Hz if two accelerometers are used. The sound power is reduced by more than 15 dB at the first, third and eighth eigenfrequencies of the uncontrolled system (i.e. at 111 Hz, 218 Hz and 428 Hz). However, for some frequencies in the range between 300 and 400 Hz the radiated sound power is significantly increased by the feedforward controller.

The plate vibration response of the controlled system was measured at several interesting frequencies with the laser vibrometer in a grid consisting of 13×7 points (see also Section 4.4). The experimental results are shown together with the numerical results for the control systems with one and two accelerometers in Figures 5.16 and 5.17, respectively. Each vibration shape shown in the figures has its own scaling (for clarity), but one must be aware that there is a significant difference in vibration level between the uncontrolled and controlled systems. A second important note is that either the *real part* or the *imaginary part* of the transfer between the primary input voltage and the normal plate displacement is shown. Since the damping is small, in off-resonance frequency ranges the real part is much larger than the imaginary part (nearly 0° or 180° phase shift). In a resonance frequency, however, the imaginary part of the plate response is much larger (nearly 90° phase shift, proportional damping). It is indicated in the figure whether the real or imaginary part of the displacement response is depicted.

In the case of the control system with one accelerometer, the plate response was measured at the new resonance frequencies of the controlled system (118 Hz, 244 Hz and 450 Hz). The results are shown in Figure 5.16, together

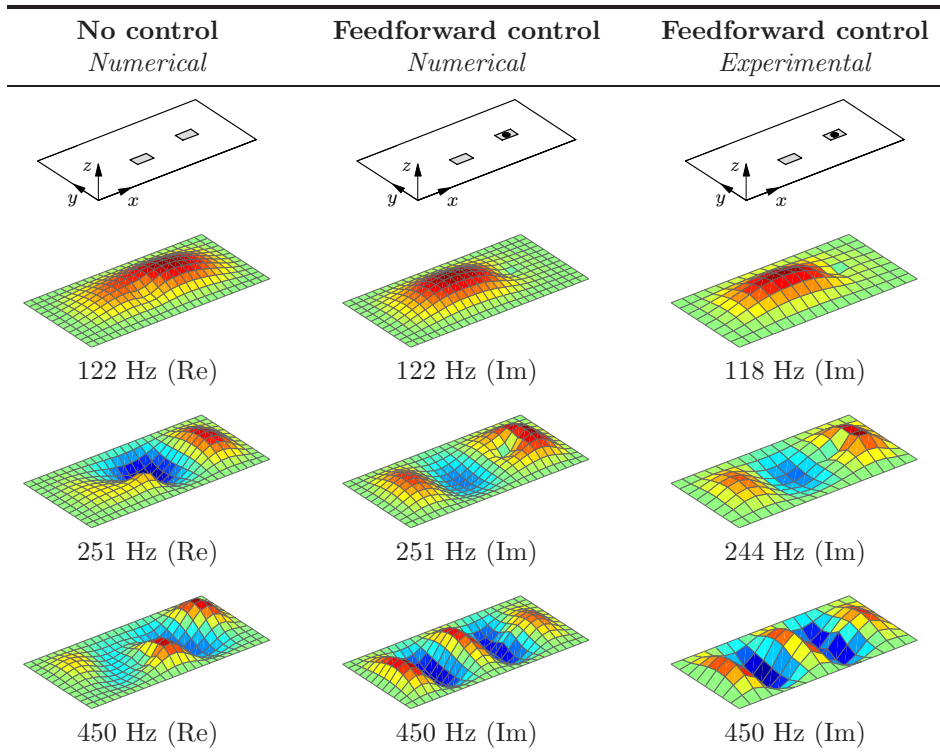


Figure 5.16: Normal plate displacement shapes without control (numerical) and with control using *one accelerometer* (numerical, experimental) for three frequencies ('Re' or 'Im' denotes whether the real or the imaginary part is shown).

with the predicted plate responses of the uncontrolled and controlled systems. The frequencies for which the numerical results are shown correspond to the predicted new resonance frequencies. These are slightly different from the frequencies for which the measured plate responses are shown.

There is a good agreement between the predicted and measured vibration shapes at all three frequencies. It can be seen that the vibration shape is changed by the feedforward control system. The output from the accelerometer is totally cancelled by the control system so the plate is effectively pinned at the location of the accelerometer. The three frequencies for which the results are shown are not far from the first, third and eighth eigenfrequencies of the uncontrolled system. The corresponding uncontrolled mode shapes are the 1-1, 3-1 and 5-1 modes, respectively. The vibration shapes of the controlled system are similar to these modes, except that the plate is pinned at the location of the accelerometer.

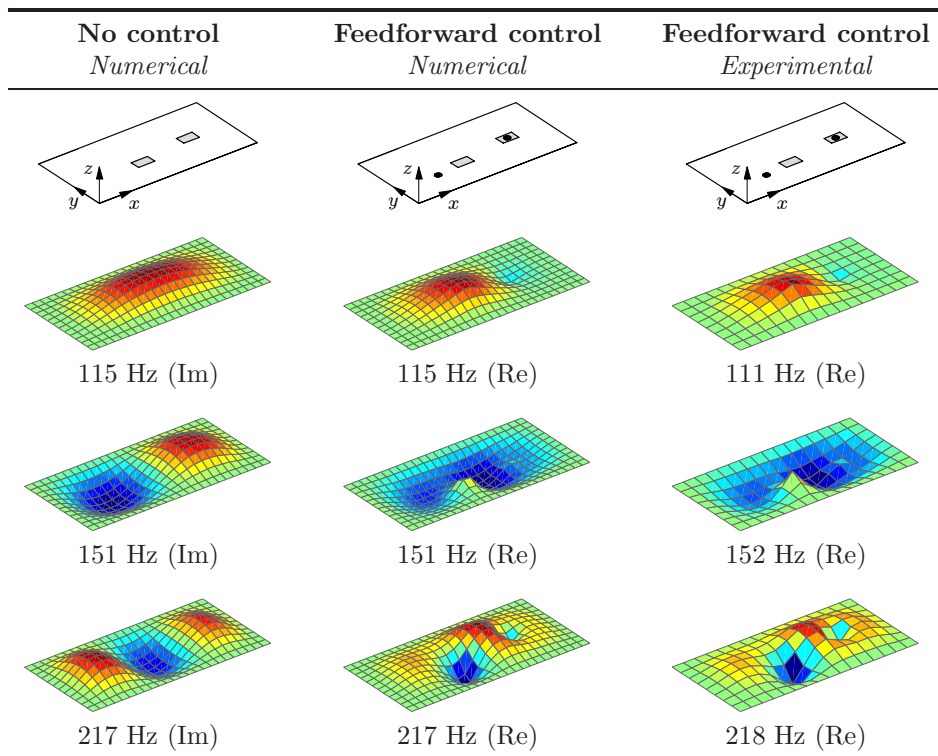


Figure 5.17: Normal plate displacement shapes without control (numerical) and with control using *two accelerometers* (numerical, experimental) for three frequencies ('Re' or 'Im' denotes whether the real or the imaginary part is shown).

In Figure 5.17 results are shown for the control system with two accelerometers. The frequencies for which the uncontrolled and controlled plate responses are shown correspond to the first three eigenfrequencies of the uncontrolled system. The predicted and measured vibration shapes are again in good agreement.

Acoustic error sensing

Next the control systems with one and two *microphones* are considered (see Figure 5.13). The predicted and measured control performances are shown in Figure 5.18. As before, the results correspond to the sound power that is radiated by the plate when a unit voltage is applied to the primary patch.

It can be observed that the trends in the experimental results are also predicted by the numerical model. For example, the dip in the sound power

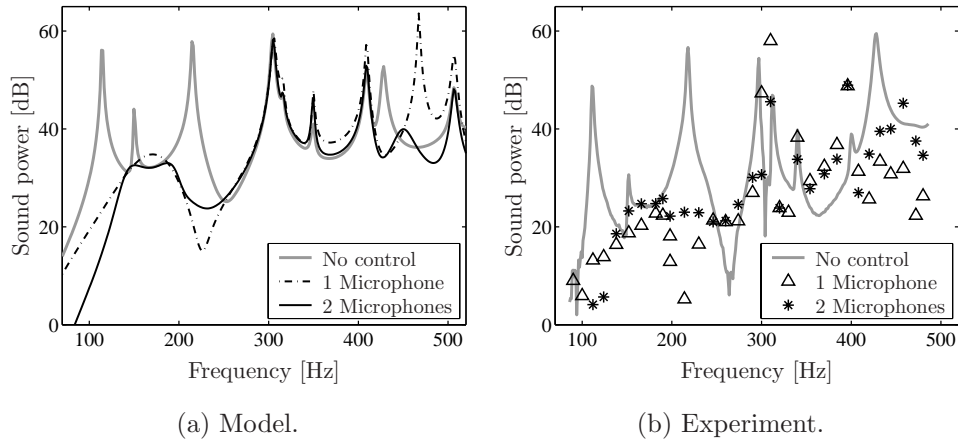


Figure 5.18: Predicted and measured performances of a narrowband feedforward controller with one microphone and with two microphones.

when one microphone signal is minimised and the increase of the sound power at higher frequencies can be observed in both Figure 5.18(a) and 5.18(b). Furthermore, it is shown in the numerical and experimental results that a second sensor does not necessarily improve the performance of the control system.

Near the first, second and eighth eigenfrequencies of the uncontrolled system, the sound power is significantly reduced by both controllers. The levels by which the sound power is reduced are certainly higher than when structural error sensors are applied. It was also demonstrated in Section 5.3 that better control performances are obtained with near-field pressure sensing than with (unweighted) structural error sensing.

5.5 Concluding remarks

In this chapter, feedforward control of harmonic disturbances was considered. Quadratic optimisation theory (optimal control) is a convenient way to analyse the behaviour of a feedforward control system with multiple secondary sources and error sensors. In a numerical study a number of features of feedforward control were demonstrated, such as the effect of “new” resonances at frequencies different from the eigenfrequencies of the uncontrolled system, and the improvement of control performance with the number of secondary sources.

An experimental validation was performed for the purpose of showing that

the numerical model is a useful tool for designing feedforward control systems. The feedforward controller is implemented as an adaptive controller, which is able to track small changes in the system under control. For control systems consisting of one piezoelectric patch and one or two accelerometers or microphones, a good correspondence between the numerical and experimental results was found. With these configurations of the feedforward controller, a significant reduction in sound power is obtained at some of the eigenfrequencies of the system. The level by which the sound power is reduced is certainly higher with microphones than with accelerometers. However, in practice it can be inconvenient or impossible to place microphones in front of the structure. An interesting alternative to this is to use vibration sensors integrated within the structure (e.g. accelerometers) whose error signals are weighted by spatial filters, i.e. the radiation modes at a fixed frequency. It was shown numerically that this approach can give improved control performance and furthermore reduces the dimensionality of the controller when compared to a control system which minimises the unweighted error signals.

Chapter 6

Feedback Control

6.1 Introduction

In the previous chapter it was assumed that information is available concerning the primary disturbance excitation. It is then possible to apply feedforward control. In many applications, however, the disturbance excitation is unknown or cannot be directly observed. In such cases where no suitable reference signal for feedforward control is available, a feedback control strategy can be employed to reject the disturbance excitation.

A major problem in the design of feedback control systems is to guarantee stability of the controlled system even when it is subject to changes in environmental or operational conditions. The general way to decrease the risk of instability is to use *collocated* actuator/sensor pairs. An actuator/sensor pair is referred to as collocated if the actuator and sensor are physically located at the same place and are energetically conjugated. A well known example in active vibration control is the combination of a point force actuator and a velocity sensor. This chapter is devoted to the implementation of a feedback control system consisting of a piezoelectric actuator patch and an accelerometer. This actuator/sensor pair is essentially not collocated, though it does possess properties similar to those of collocated systems.

The stability robustness is furthermore to a large extent determined by the type of feedback strategy. In this work the “classical” method *direct velocity feedback* (DVF) is applied because of its ease of implementation and good stability properties. Direct velocity feedback control attempts to increase the damping in the structure. As a result, the structural response to primary disturbance excitations is reduced, indirectly reducing the sound radiation. This approach can be attractive to reduce the sound radiation of lightly

damped structures. In the case of multiple pairs of piezoelectric patches and accelerometers, the control system consists of multiple independent single-input-single-output (SISO) feedback loops. This approach will be referred to as *decentralised velocity feedback* control.

This chapter starts with a brief discussion on the advantages of using collocated rather than non-collocated actuator/sensor pairs (Section 6.2). In Section 6.3 the combination of a piezoelectric actuator patch and an accelerometer is considered. This actuator/sensor pair is not truly collocated, but it is shown that such a pair exhibits similar behaviour as that of collocated systems. The analysis is extended in Section 6.4 to a plate structure with multiple piezoelectric patch/accelerometer pairs. In a numerical study, the control performance in terms of sound power reduction of a decentralised velocity feedback control system is considered. In Section 6.5 the practical implementation of the control system is discussed. A digital controller and an analogue controller are tested on the same experimental setup as used in the previous chapters. The measured control performance of these controllers is compared with the performance predicted using the numerical model.

6.2 Collocated feedback control

A major problem in the design of feedback control systems is to guarantee the stability of the controlled system. The general way to decrease the risk of a feedback control system becoming unstable is to use collocated actuator/sensor pairs [4]. An example of such a system, which consists of a point force actuator and a velocity sensor (both in the transverse direction), is shown in Figure 6.1.

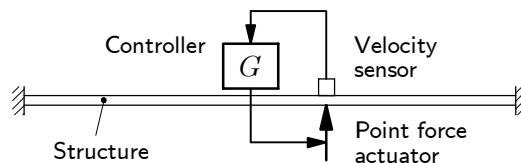


Figure 6.1: A feedback control system with a collocated point force actuator and point velocity sensor.

Collocated actuator/sensor pairs are widely applied in active control of sound and vibration and their advantages are discussed for instance in the book of Preumont [4]. For the sake of completeness a brief discussion is included here. A block diagram representation of a SISO feedback control system is shown in Figure 6.2. It is common in (classical) control theory to use the

Laplace transform for analysing feedback control systems, since it can, in contrast to the Fourier transform, be used to represent both stable and unstable systems [6, 51].

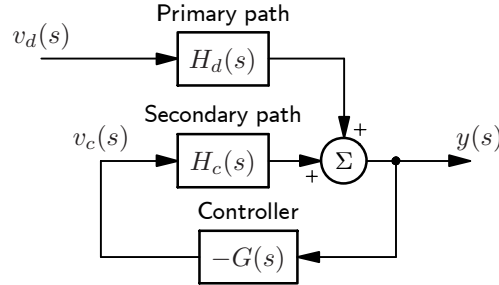


Figure 6.2: Block diagram of a single channel feedback control system.

Under the assumption that all system components are linear, in the Laplace domain the output from the error sensor $y(s)$ can be expressed as:

$$y(s) = H_d(s) v_d(s) + H_c(s) v_c(s), \quad (6.1)$$

where $v_d(s)$ and $v_c(s)$ are the primary and secondary inputs, respectively, and $H_d(s)$ and $H_c(s)$ are the primary and secondary path transfer functions, respectively. In feedback control the secondary input is derived directly from the sensor output and can be written as:

$$v_c(s) = -G(s) y(s), \quad (6.2)$$

where $G(s)$ is the Laplace transform of the controller transfer function. Equations (6.1) and (6.2) can be combined to obtain the transfer function with feedback control between the primary input and the sensor output:

$$y(s) = \frac{H_d(s)}{1 + H_c(s)G(s)} v_d(s) = H(s) v_d(s), \quad (6.3)$$

where $H(s)$ is the closed-loop transfer function.

The stability of this SISO system can be determined by an inspection of the *poles* of the closed-loop transfer function. If the poles of $H(s)$ are denoted by p_i and the *zeros* are denoted by z_i , the closed-loop transfer function can be written in the factored form:

$$H(s) = h \frac{\prod_{i=1}^m (s - z_i)}{\prod_{i=1}^n (s - p_i)}, \quad (6.4)$$

where h is a constant gain. The poles and zeros are either real numbers or conjugate pairs of complex numbers. A convenient definition of stability is that a system should produce a bounded output when subjected to a bounded input. This condition is satisfied only if all poles of $H(s)$ have *negative* real parts [51].

In the following the stability of SISO feedback control systems is investigated with the *root locus* method. The root locus shows the evolution of the poles of the closed-loop system as a function of some parameter of the control system (e.g. feedback gain). For the control system described by equation (6.3), the root locus is the set of values of s for which the characteristic equation:

$$1 + H_c(s)G(s) = 0, \quad (6.5)$$

is satisfied as the parameter goes from zero to infinity. This equation is determined only by the secondary path and controller transfer functions. Therefore no knowledge of the primary excitation is required in a stability analysis. The root locus is presented in the so-called complex plane (see e.g. Figure 6.3), in which the real part of s is shown along the horizontal axis (*real axis*) and the imaginary part of s is shown along the vertical axis (*imaginary axis*). A system is stable if all of its poles lie in the left half of the complex plane ($\text{Re}(s) < 0$). The complex plane is symmetric about the real axis ($\text{Im}(s) = 0$), so only the upper part of the complex plane will be shown in the root locus plots.

In the case of *direct velocity feedback* (DVF) control, the signal provided to the actuator is proportional to the velocity measured by the error sensor, i.e. the controller is a fixed gain $G(s) = g$. The root locus of a DVF control system with point force actuator and velocity sensor is shown in Figure 6.3. The evolution of the poles of the closed-loop system is shown for positive values of the feedback gain g . In the figure also the open-loop poles and zeros of the transfer function $gH_c(s)$ are shown.¹ The zeros and poles are shifted somewhat into the left half of the complex plane ($\text{Re}(s) < 0$) because of the small amount of (modal) damping in the model.

As the feedback gain is increased, the poles move further into the left half of the complex plane. This indicates an increase in the damping in the system, which is typical for a DVF strategy. If the gain is increased beyond a certain value, the poles move back towards the imaginary axis, to the zeros of the transfer function $gH(s)$. A physical interpretation of this effect is that for an infinite feedback gain, the point where the sensor is located remains fixed: the control acts as a support, thereby not adding any damping to the structure.

¹The zeros of the transfer function $gH_c(s)$ are, in general, not equal to the zeros of the closed-loop transfer function described by equation (6.3).

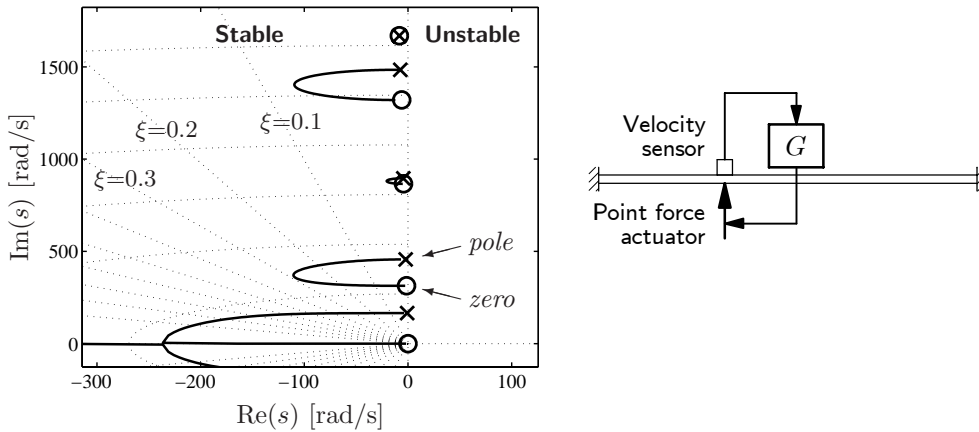


Figure 6.3: Typical root locus of a *collocated* point force actuator and velocity sensor with proportional feedback gain ($\xi = 0.1$, $\xi = 0.2$, $\xi = 0.3$ indicate lines of constant damping).

A further observation is that the maximum amount of damping that can be achieved is different for each pole. The location of the collocated actuator/sensor pair strongly determines the shape of the root locus and thus the amount of damping that is associated with a certain pole. In general, the poles and zeros should be well separated in order to obtain significant damping ratios. From a mechanical point of view, this implies that the actuator and sensor must couple well into the vibration mode associated with a certain pole. In the ultimate case, where the location of the actuator/sensor pair corresponds to a nodal line, the control system will not be able to add damping to that mode.

The root locus shown in Figure 6.3 stays in the left half of the complex plane. This means that the system is stable for all positive feedback gains g [4] (the loci associated with the “high frequency” poles, which are not shown in the figure, also stay in the left half of the complex plane). One must be aware of that the poles would move into the unstable, right half of the complex plane if the feedback gain were varied from 0 to $-\infty$. The minus sign has been included in the feedback law (6.2) so that positive values of g correspond to a stable system.

A typical root locus of a *non-collocated* DVF control system is shown in Figure 6.4. It can be seen that the locus departing from the third pole moves through right half of the complex plane ($\text{Re}(s) > 0$). Therefore the closed loop system is unstable for certain values of g .

It can be observed in Figure 6.3 that the collocated system has alternating

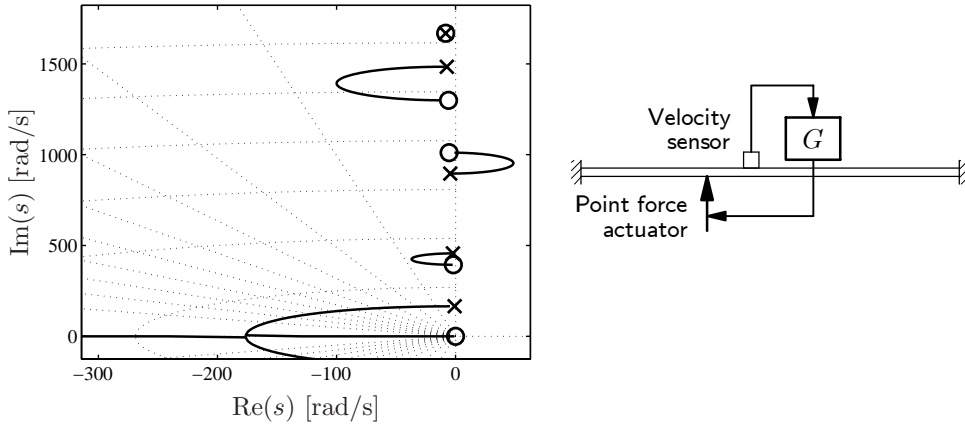


Figure 6.4: Typical root locus of a *non-collocated* point force actuator and velocity sensor with proportional feedback gain.

poles and zeros near the imaginary axis, i.e. there is a zero in-between two subsequent poles. Because of this property, a control scheme such as DVF has *guaranteed* stability [4]. The alternating pole-zero pattern does not hold for the non-collocated control arrangement, as can be seen in Figure 6.4. The importance of this property with respect to stability can be explained with a frequency response approach. The closed-loop transfer function (6.3) is transformed to the frequency domain by substitution of $s = j\omega$:

$$y(j\omega) = \frac{H_d(j\omega)}{1 + H_c(j\omega)G(j\omega)} v_d(j\omega). \quad (6.6)$$

At the point of *neutral stability*, where the root locus crosses the imaginary axis, the following relations hold:

$$|H_c G| = 1, \quad \angle(H_c G) = -180^\circ \text{ (degrees)}, \quad (6.7)$$

where the explicit notation of frequency dependence has been dropped. The closed-loop system is stable if the phase angle $\angle(H_c G)$ is larger than -180° for all frequencies where the magnitude $|H_c G|$ is larger than 1. The system is unstable if this condition is violated.

The open-loop FRF gH_c of the collocated and non-collocated configurations are shown in Figure 6.5 ($g = 1$). For a lightly damped system, with poles and zeros close to the imaginary axis, the *poles* can be recognised in a frequency response as the *resonance frequencies*, whereas the *zeros* correspond to the *anti-resonance frequencies*. Accordingly, a resonance frequency

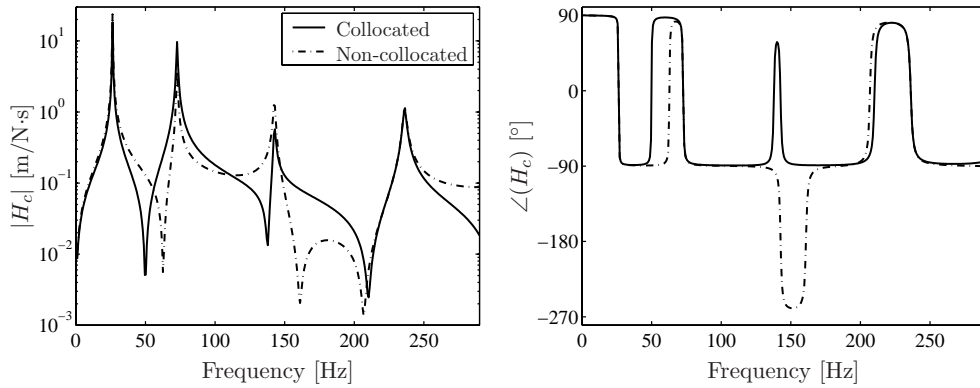


Figure 6.5: Open-loop FRF gH_c of the collocated and non-collocated configuration of Figures 6.3 and 6.4 for $g = 1$.

produces a phase shift of nearly -180° (phase *lag*) and an anti-resonance frequency produces a phase shift of nearly $+180^\circ$ (phase *lead*).

In the case of the non-collocated setup there is no anti-resonance frequency between the second and third resonance frequencies (or no zero between the second and third pole, see Figure 6.4). As a consequence, the phase angle becomes smaller than -180° . Thus, according to the stability criterion mentioned previously, for DVF control the closed-loop system will be unstable if $|gH_c| > 1$.² For the collocated setup, however, the phase is always between -90° and $+90^\circ$ because of the alternating pole-zero pattern, which implies that the closed-loop system is stable for all values of g . It is this property that makes collocated systems attractive for active damping purposes.

So far the proportional feedback of velocity was considered. Alternatively, a controller can be constructed such that its output has three components, which are proportional to the displacement, velocity and acceleration. In time-domain notation, the control law is:

$$v_c(t) = -g_d u(t) - g_v \dot{u}(t) - g_a \ddot{u}(t), \quad (6.8)$$

where g_d , g_v and g_a are the feedback gains associated with the displacement, velocity and acceleration, respectively. If only one sensor is available to measure velocity, the displacement and acceleration can be derived using an electronic integrator and differentiator.³ It is easy to show that if the actuator/sensor pair are collocated, the controller effectively modifies the mass,

²A change in g corresponds to a shift of the magnitude plot along the vertical axis.

³This control strategy would then be what in control theory is referred to as 'proportional-integral-derivative' or PID-control.

damping and stiffness of the mechanical structure. The behaviour of the closed-loop system is the same as that of the mechanical system shown in Figure 6.6, where a mass-spring-damper combination is attached to the strip with spring stiffness g_d , viscous damping constant g_d and mass g_a .

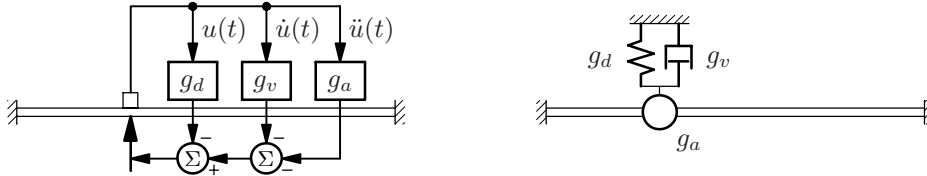


Figure 6.6: Mechanical equivalent of collocated displacement, velocity and acceleration feedback.

In the root locus of a control system with an output proportional to either acceleration or displacement, the poles move in a straight line towards the zeros. In other words, the damping of the structure is not increased. This is as expected since mass and stiffness, which are the mechanical equivalents of such control strategies, can store energy rather than dissipating it. The proportional feedback of displacement or acceleration alone is therefore not very attractive for reducing the sound radiation of lightly damped structures.

The property of alternating poles and zeros exhibited by a collocated actuator/sensor pair provides the theoretical basis for the design of feedback controllers with guaranteed stability. An important practical limitation to this concept, however, is the inevitable phase lag in the transfer function $H_c(s)G(s)$ due to sampling in digital controllers and dynamics of amplifiers, actuators and sensors. Therefore, in practice there is always a frequency where the phase of H_cG will become smaller than -180° . The only way of preventing instability of the closed-loop system is that a significant *roll off* appears in $H_c(s)G(s)$ in order that the magnitude of the associated FRF is well below 1 at that frequency. More details on this problem are given in Section 6.5.

6.3 Collocated control with piezoelectric patches

6.3.1 Collocation concepts

The practical advantages of piezoelectric actuator patches compared to point force actuators were already mentioned in Chapter 2. Figure 6.7 shows three collocation concepts that have been suggested in the literature for implementing feedback control with piezoelectric patches. These three concepts are summarised below:

- (a) A *matched piezoelectric actuator/sensor pair*, which consists of two piezoelectric patches with the same shape and size that are located at the same position, but on either side, of the structure [24, 25].
- (b) A *piezoelectric sensor/actuator*, which is a piezoelectric patch that works simultaneously as actuator and sensor [74].
- (c) The combination of a *piezoelectric actuator patch* and an *accelerometer*, where the accelerometer is located at the centre of the patch to measure the normal velocity [75].

It is noted that in order to implement DVF control for concepts (a) and (b), the sensor output must be differentiated, whereas the sensor output must be integrated for concept (c).

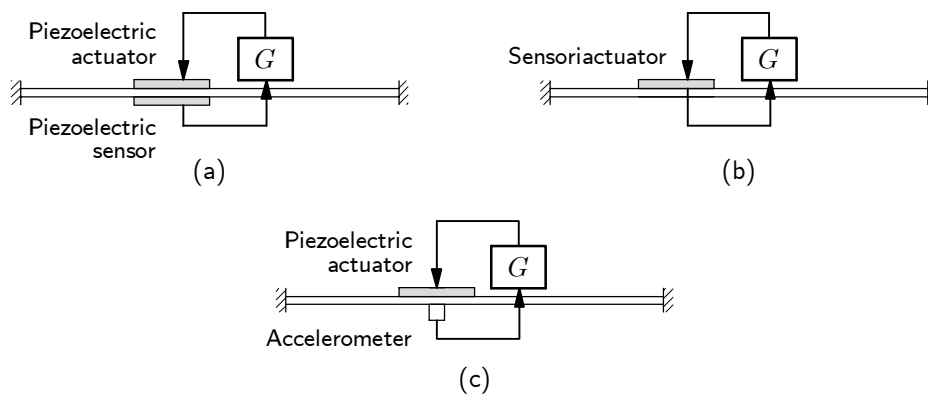


Figure 6.7: (a) Piezoelectric actuator/sensor pair, (b) Piezoelectric sensor/actuator, (c) Piezoelectric actuator patch with accelerometer.

The matched piezoelectric actuator/sensor pair seems to be an attractive concept but there is an important drawback. In this arrangement both the in-plane and out-of-plane vibration modes are excited and measured by the actuator and sensor, respectively. It has been shown for instance by Lee, Gardonio and Elliott [42, 76] that the FRF of the actuator/sensor pair is not strictly positive real because of the in-plane vibration coupling. At low frequencies the phase angle of the FRF is limited to values between -90° and $+90^\circ$, but in the range above the eigenfrequency of the first in-plane mode⁴ the phase angle is limited to values between -270° and -90° . Furthermore, at the first in-plane resonance frequency the FRF has a much larger amplitude than at the low frequencies. Therefore the implementation of a DVF strategy leads to a stability problem. This problem can be circumvented by using a strategy with sufficient roll off, such as *positive position feedback* (PPF) considered by Petitjean, Legrain, Sion and Pautin [77] or *integral force feedback* (IFF) considered by Henriouille and Sas [26]. However, at low frequencies the in-plane coupling effect is similar to that of a static feedthrough which leads to closely spaced poles and zeros and, as a result, limits the control performance.

The sensor/actuator is in contrast to the previous concept a truly collocated system. An arrangement with a single patch such as shown in Figure 6.7 suffers from in-plane coupling effects, but these can be overcome by placing a second sensor/actuator on the opposite side of the structure (see also Section 3.3.2). The charge response of the sensor/actuator consists of two contributions: the charge as a result of the mechanical deformation of the structure and the charge as a result of the voltage applied across the piezoelectric capacitance. The latter contribution is more significant and must be removed from the sensor output in order to obtain a signal proportional to the structural response. With an electrical circuit it is possible to resolve the part related to the mechanical response. However, this circuit must be adaptive in order to cope with variations in environmental conditions and operation [74]. This requires a rather complex circuit which is not always attractive for practical implementation. The application of adaptive piezoelectric sensor/actuators in feedback control has been demonstrated for instance in references [78] and [79], but is not considered in this work.

The combination of an actuator patch and an accelerometer (a *patch/accelerometer pair*) is again not a truly collocated setup. However, this pair does not suffer from in-plane coupling effects since the accelerometer measures the out-of-plane vibration component. It is therefore possible to implement the DVF

⁴In a thin plate structure the in-plane modes have much higher frequencies than the out-of-plane modes.

strategy. The consequences of this setup being not truly collocated are further discussed in the following section.

6.3.2 Patch/accelerometer pairs

A typical root locus of a control system with a piezoelectric actuator patch, accelerometer and DVF controller is shown in Figure 6.8. As before, the evolution of the poles of the closed-loop system is shown as a function of the feedback gain. The root locus was calculated using a reduced FEM model of the setup (see Chapter 4). In order to implement DVF control, the acceleration signal must be integrated to velocity. In practice, integration can be performed by the controller but also by the conditioning amplifier connected to the accelerometer (see Section 6.5). The position of the patch/accelerometer pair is equal to that of the collocated force/velocity pair considered previously, such that it is allowed to compare the two control arrangements.

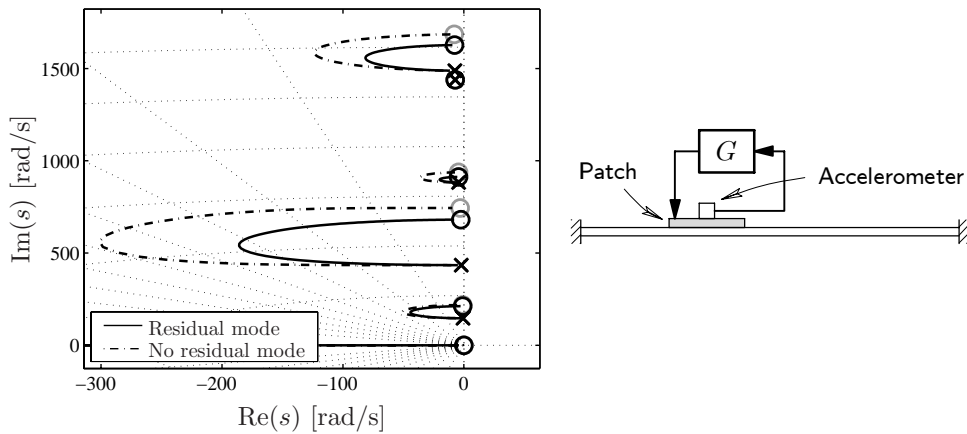


Figure 6.8: Root locus of a patch/accelerometer pair with DVF control.

The open-loop transfer function of the patch/accelerometer pair shows an alternating pole-zero pattern, similar to that of a truly collocated system. As a consequence the closed-loop system is stable for the frequency range shown in the figure (up to 300 Hz), i.e. the root locus moves through the left half of the complex plane. A comparison between the root loci shown in Figures 6.3 and 6.8 reveals that the amount of damping obtained with the patch/accelerometer pair is of the same order as for the force/velocity pair. However, the damping associated with the individual poles can be significantly smaller or higher for the two arrangements. For example, for this location of

the secondary source, the damping associated with the first pole is much higher for the force/velocity pair than for the patch/accelerometer pair.

Figure 6.8 also depicts the root locus determined with a model not accounting for the *residual mode*. It was shown in Section 4.2.3 for a similar setup, that the residual mode is particularly important for an accurate prediction of the anti-resonance frequencies. The effect of neglecting the residual flexibility is in the complex plane observed as a shift of the zeros with respect to their true locations. It can be seen that the root locus travels further into the left half of the complex plane for the model without the residual mode. Therefore, the closed-loop damping is overestimated.

Stability

The combination of a piezoelectric actuator patch and an accelerometer is not truly collocated, i.e. the property of alternating poles and zeros holds in a limited frequency band. Therefore, in the case of DVF control the stability of the closed-loop system is not guaranteed. It is possible to discriminate between two causes of an unstable closed-loop system, which are here referred to as a “high frequency” stability problem and a “low frequency” stability problem.

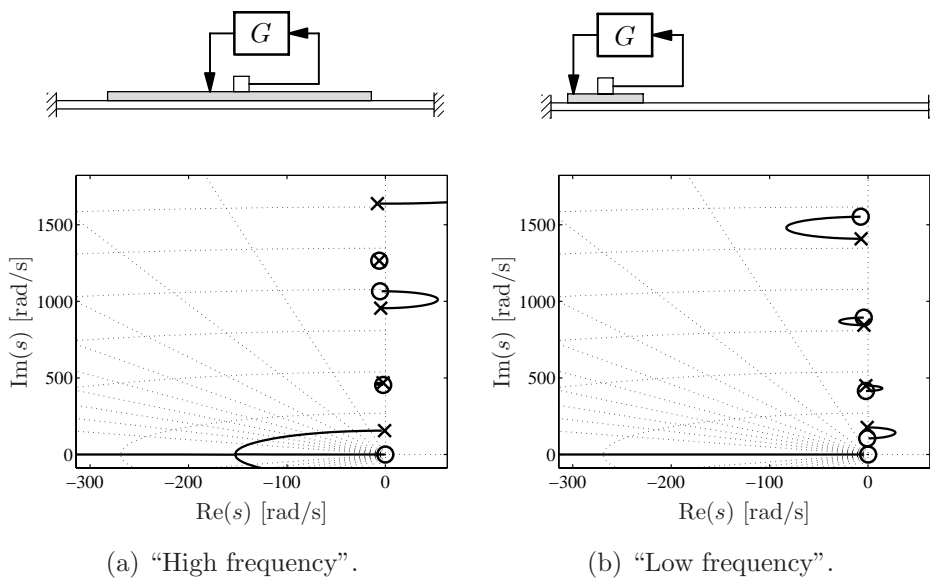


Figure 6.9: High frequency (left) and low frequency (right) instabilities for a piezoelectric patch/accelerometer pair with DVF control.

The first case is shown in Figure 6.9(a). It can be seen that there is a zero in-between the first and second poles but not in-between the second and third poles. This effect is related to the ratio between the patch length and the structural wavelength. Because in this example the patch is relatively large, the third pole already becomes unstable. For smaller patches, this instability moves up to higher frequencies, i.e. the alternating pole-zero pattern holds in a larger frequency range (see Figure 6.8). The frequency up to which the alternating pole-zero pattern holds can be controlled by the size of the patch.

The second case is shown in Figure 6.9(b). Now the instability occurs at a low frequency. The first and second poles are preceded by a zero, and as a result these poles become unstable with DVF control. In this case the instability occurs because the actuator/sensor pair is located close to a *clamped* edge. This type of instability can be prevented by proper placement of the pair, i.e. not close to a clamped edge. It is stressed that this stability problem is related to the type of boundary conditions. In case of simply support boundary conditions, this effect does not occur.

6.4 Decentralised velocity feedback control

Feedback control of structure-borne sound radiation has been dealt with by many researchers in recent years. A selection of relevant papers on this topic is given in Table 6.1. The list is certainly not complete but it gives an idea of the various actuator/sensor configurations and control strategies that have been considered. It is common to use collocated actuator/sensor pairs but the feedback law that derives the control inputs from the sensor outputs can be implemented in many ways. Feedback control strategies are often divided into two classes based upon whether or not the feedback law relies on a model of the system. The two classes are referred to here as *model-based* and *non-model-based* control, but in the literature terminology such as *modern* and *classical* control or *high-authority* and *low-authority* control is also used.

The direct velocity feedback controller considered previously does not rely on a model and is therefore robust to changes in environmental conditions. For instance, the control system remains stable if the eigenfrequencies shift as a result of a change of temperature. This may however be problematic for a model-based strategy such as LQR/LQG or H_2/H_∞ since an erroneous model may lead to an unstable system. A further drawback of model-based strategies is that the practical realisation is quite involved, especially if the model must capture the dynamics of a lightly damped system with high modal density. On the other hand, the implementation of a strategy such as DVF is not limited by computational burdens.

The remainder of this chapter is devoted to the implementation of direct velocity feedback control. The use of this simple strategy rather than a model-based strategy is motivated by its good robustness properties and ease of implementation. The plate with eight surface bonded PZT patches that was considered in Section 5.3 for feedforward control is also used to investigate the effect of direct velocity feedback. Eight accelerometers are positioned at the centres of the patches as shown in Figure 6.10. The voltage applied to a certain patch is determined only by the accelerometer located at the centre of that patch. In this way the control system consists of multiple independent feedback loops. Such an array of independent control units implementing DVF is referred to here as *decentralised velocity feedback control*. Similar approaches were followed by Elliott, Gardonio, Sors and Brennan [75] and Gardonio, Bianchi and Elliott [80, 81, 82].

Authors	Year	Ref.	Actuator(s)	Sensor(s)	Strategy	Remarks
Baumann, Saunders, Robertshaw	1991	[61]	point force	–	LQR	theoretical work, full state feedback
Ren, Seto, Doi	1997	[83]	electromagnetic	displacement	LQG	emphasis on phase-lag in feedback loop
Clark Smith, Clark	1998	[78]	point force, sensoria- ctor	point velocity	MIMO DVF	frequency shaped cost functionals
Griffin, Hansen, Cazzolato	1999	[84]	point force	displacement	LQG	flexible structure enclosing an acoustic cavity
Vipperman, Clark	1999	[79]	sensoria- ctor		H_2	
Bingham, Atalla, Hagood	2001	[85]	active fibre com- posite	accelerometer	DVF, LQG	LQG design with radiation filters
Gardonio, Bianchi, Elliott	2002	[80, 81, 82]	PZT patch	accelerometer	DVF	multiple SISO loops
Lee, Gardonio, Elliott	2002	[86]	PVDF uniform force	accelerometer array	DVF	accelerometer array estimates volume velocity
Petitjean, Legrain, Simon, Pautin	2002	[77]	PZT, shaker	PVDF, accelerometer	PPF	multiple SISO loops
Henriouille, Sas	2003	[26]	PVDF uniform force	PVDF volume velocity, accelerometers	IFF, DVF	

Table 6.1: A selection of literature on active structural acoustic feedback control.

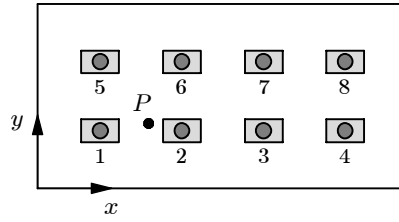


Figure 6.10: Uniform distribution of actuator patches and accelerometers.

In the case of a control system with multiple actuators and sensors the feedback law can be written as (frequency domain notation):

$$\mathbf{v}_c = -\mathbf{G} \mathbf{y}, \quad (6.9)$$

where \mathbf{v}_c is the vector with control inputs, \mathbf{y} is the vector with sensor outputs and \mathbf{G} is the matrix with controller FRFs. Provided the control system is stable, the closed-loop frequency domain response of the error sensors is given by:

$$\mathbf{y} = (\mathbf{I} + \mathbf{H}_c \mathbf{G})^{-1} \mathbf{H}_d \mathbf{v}_d, \quad (6.10)$$

where \mathbf{H}_d and \mathbf{H}_c are the matrices with the primary path and secondary path FRFs, respectively, and \mathbf{v}_d is the vector with the primary inputs. It is assumed that the signals supplied to the controller have already been integrated from acceleration to velocity. As the control is decentralised and implemented with direct velocity feedback, \mathbf{G} becomes a frequency independent diagonal matrix. Elliott et al. [75] showed that if a truly collocated system (with force/velocity pairs) with multiple independent feedback loops is implemented with fixed gains, then the system is stable provided that each of the individual gains is positive. In this work the feedback gains are furthermore chosen equal for all individual feedback loops such that $\mathbf{G} = g \mathbf{I}$, where g is a positive fixed gain. Alternatively, \mathbf{G} could be implemented as a fully populated matrix with fixed gains, as in references [78] and [87]. However, such an approach is less attractive for practical implementation because of the MIMO nature of this strategy, and the choice of the feedback gains is also not straightforward.

It was shown in Section 6.3 that stability cannot be guaranteed when the DVF control system consists of patches and accelerometers (see Figure 6.9). The stability problem at low frequencies is easily prevented by proper placement of the patches. All eight patches are located sufficiently far away from the plate edges. The stability problem at high frequencies can be determined by inspection of the open-loop secondary path FRFs. It was found that the

phase of all eight FRFs was between -90° and $+90^\circ$ in the frequency range considered in the simulation (up to 1000 Hz).

Optimal feedback gain

An example of the performance of the control system is shown in Figure 6.11. The primary excitation is due to a transverse point force⁵ (indicated by P in Figure 6.10). In the figure the sound power is shown without control and when subject to control using four of the eight feedback loops with various feedback gains. The sound power levels correspond to a primary force amplitude of 1 Newton.

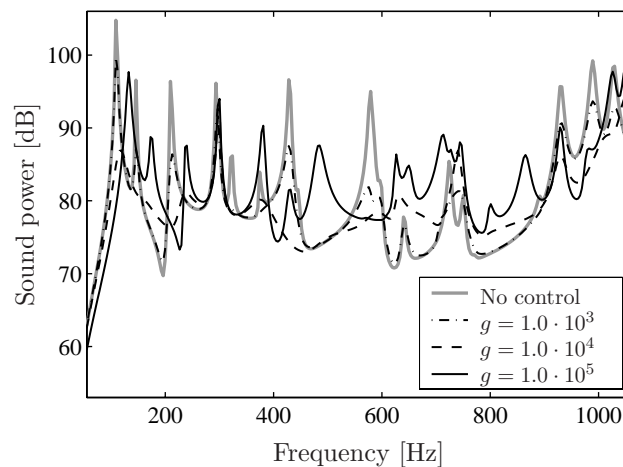


Figure 6.11: Performance of *four* decentralised velocity feedback controllers for three feedback gains (loops 1, 3, 6 and 8).

The resonance frequencies of the lightly damped plate structure are clearly visible in the result corresponding to the sound power without control. As the gain of the four feedback loops is increased, the resonances become more heavily damped. For a gain of $g = 1.0 \cdot 10^4$ V·s/m the sound power is significantly reduced at most of the resonances in this frequency range. If the gain is increased beyond a certain value the response displays new peaks, which become more pronounced as the gain is increased further. This effect was also observed in the root locus shown in Figure 6.8. When the gain is varied from zero to infinity the poles first move away from the imaginary axis, but beyond a certain gain the poles move back towards the zeros close to the imaginary

⁵The point force is applied at the same location as in the analysis of feedforward control presented in Section 5.3.

axis, which indicates a decrease of the damping. It is noted that the outputs of the accelerometers monotonically decrease as the feedback gain is increased. However, the overall plate response and associated sound radiation is minimal for a certain feedback gain. One could say that for very high gains the plate is effectively pinned at the sensor locations.

The overall performance of the control system is presented in terms of the *total sound power*, which is the sound power integrated over the frequency band of interest, i.e. up to 1000 Hz in this case. In Figure 6.12 the total sound power is plotted against the feedback gain for control systems with either two, four or all eight feedback loops turned on. The results have been normalised with the total sound power without control, so a negative value represents a reduction of the total sound power.

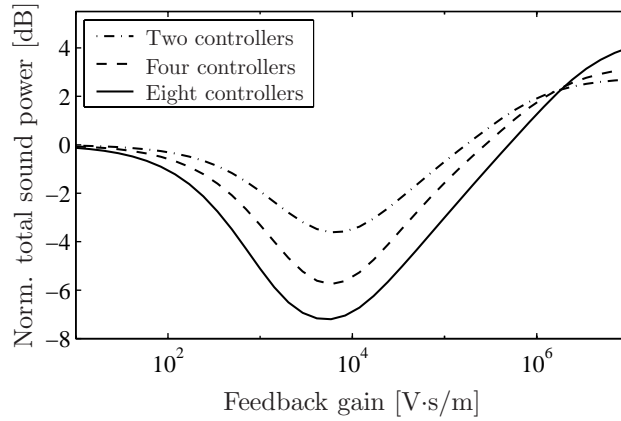


Figure 6.12: Total sound power radiated by the plate as a function of the feedback gain if either two (loops 3 and 6), four (loops 1, 3, 6 and 8) or all eight feedback loops are operating.

The trends in the figure are similar to those found by Elliott et al. [75] and Gardonio et al. [80]. A clear minimum in total sound power is observed, which shifts slightly to the left as the number of feedback loops is increased. It is not surprising that the reduction in total sound power increases with the number of feedback loops. The optimal reduction is about 3.6 dB with two feedback loops, 5.7 dB with four feedback loops, and 7.2 dB with all eight feedback loops. A further observation is that for high feedback gains the total sound power with control is higher than it is without control.

Performance

The performances of the three configurations when operating with the optimal feedback gain are shown in Figure 6.13. In this context, optimal refers to the gain for which the reduction in total sound power is a maximum (see Figure 6.12). For the configuration with two feedback loops, some of the resonances are damped. Some modes are not *observable*, i.e. not detected by the accelerometers, or not *controllable*, i.e. not excited by the patches, and the sound power is therefore not reduced at the corresponding eigenfrequencies. By extending the number of feedback loops to four, the performance is increased. If all eight feedback loops are used the sound power is significantly reduced for all efficiently radiating vibration modes in the range up to 1000 Hz. At the individual resonances the sound power is reduced by 20 dB. The reduction in total sound power is limited to 7.2 dB mainly due to the high sound power level near 1000 Hz.

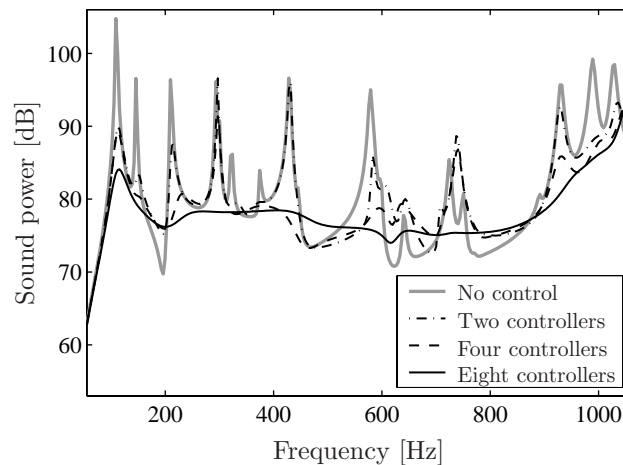


Figure 6.13: Optimal control performance with two (loops 3 and 6, $g = 6.5 \cdot 10^3 \text{ V}\cdot\text{s}/\text{m}$), four (loops 1, 3, 6 and 8, $g = 5.9 \cdot 10^3 \text{ V}\cdot\text{s}/\text{m}$) or all eight ($g = 5.3 \cdot 10^3 \text{ V}\cdot\text{s}/\text{m}$) decentralised velocity feedback controllers.

It is important to note that the DVF strategy simply adds damping to the system. As a consequence, the vibration level of the structure is reduced, but the damping mechanism does not necessarily reduce the sound power radiated by the structure. At some frequencies, mainly in off-resonant regions, a reduction of the vibration level is accompanied by an increase of the sound power.

The results shown in Figure 6.13 are only weakly sensitive to a variation of the feedback gain. One should be aware that the range along the horizontal axis in Figure 6.12 is extremely broad. In practice, for a fixed gain (near the optimal value) the performance will not degrade very much due to changes in environmental conditions. In other words, there is no need for adaptivity as was the case for the feedforward strategy considered in Chapter 5.

6.5 Experiments

The direct velocity feedback controller was implemented on the same experimental setup as used for the feedforward control experiments (see Sections 4.4.1 and 5.4.2). One of the two patches on the plate serves as the primary disturbance source (patch 1). An accelerometer is positioned at the centre of the other patch (patch 2), on the side opposite to where the patch is bonded. The DVF controller is implemented on this actuator/sensor pair. In this section the control system is limited to a single feedback loop. Decentralised velocity feedback control will be considered in Chapter 7 for a setup with two patch/accelerometer pairs.

Since the location of the secondary actuator patch is not close to the (clamped) plate edges, the low frequency stability problem discussed in Section 6.3.2 is of no concern. However, stability at high frequencies is not guaranteed with this actuator/sensor pair, as the property of alternating poles and zeros does not hold at high frequencies. Another source of stability problems, which is important in practice but was not considered in the numerical modelling, is the phase lag introduced by the hardware in the feedback loop, such as the DSP (with A/D and D/A convertors) and conditioning and power amplifiers. Because of the phase lag, the system will become unstable if the feedback gain is increased beyond a certain value, which may be well below the value corresponding to the best possible reduction in radiated sound power.

6.5.1 Implementation

The hardware used for the practical implementation of DVF is shown in Figure 6.14. The charge output from the accelerometer (B&K 4374) is converted to a voltage by a B&K 2635 charge amplifier. This amplifier is equipped with an analogue integrator⁶, which is used to produce an output proportional to the velocity. With a high-pass (HP) filter and a low-pass (LP) filter, both of fourth order, the dynamic range of the charge amplifier can be set.

⁶The B&K 2690 Nexus amplifier that was used in the experimental setups of Chapters 4 and 5 does not have a built-in integrator.

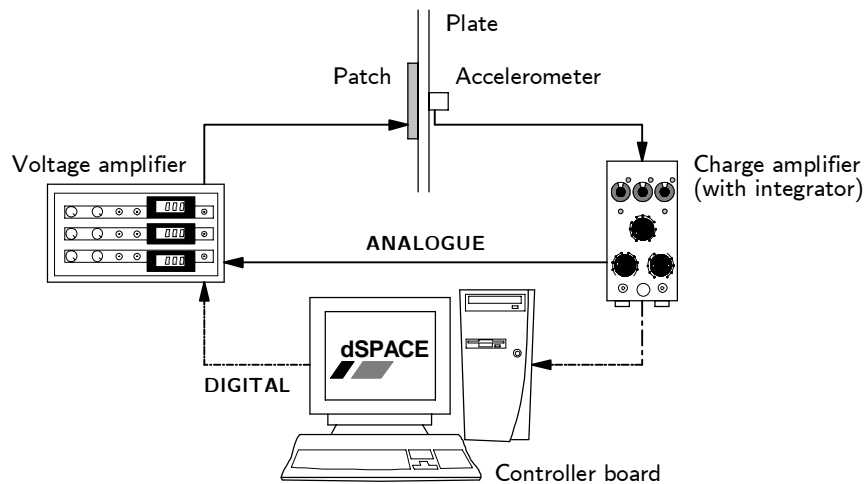


Figure 6.14: Experimental setup: *digital* and *analogue* implementation of the feedback control system.

The DVF strategy was implemented as a *digital* controller and as an *analogue* controller. In the case of the analogue implementation the output from the charge amplifier, proportional to velocity, was fed directly to the voltage amplifier (Piezomechanik SVR 1000/3). By manual adjustment of the gain of this amplifier, the gain in the feedback loop was varied. In the case of the digital implementation the dSPACE DS1103 controller board was in-between the charge amplifier and the voltage amplifier. For DVF only a proportional gain needed to be implemented on the board (the gain of the voltage amplifier is now fixed). The sample frequency was 25 kHz.

It may seem superfluous to implement this simple strategy in a digital way, but it is done here to investigate the effect of the phase lag introduced by the controller board. Note that integration of the acceleration could also be performed on the controller board. However, such an implementation introduces an additional phase lag in the feedback loop which is directly related to the sample time. Analogue integration is therefore preferable.

The dynamical behaviour of the voltage amplifier is similar to that of a *first order* LP filter. When the transfer function of a collocated actuator/sensor pair is combined with that of a first order LP filter, the resulting phase response is between -90° and $+90^\circ$ in the frequency range well below the cutoff frequency of the filter, but between -180° and 0° well above the cutoff frequency. In addition, the magnitude response displays roll off above the cutoff frequency. Such behaviour can be observed in Figure 6.15, which shows the

measured FRF from the amplifier *output* (i.e. voltage applied to patch) to the accelerometer velocity and the FRF from the amplifier *input* to the accelerometer velocity. The magnitude of the latter FRF has been scaled for an easy comparison.

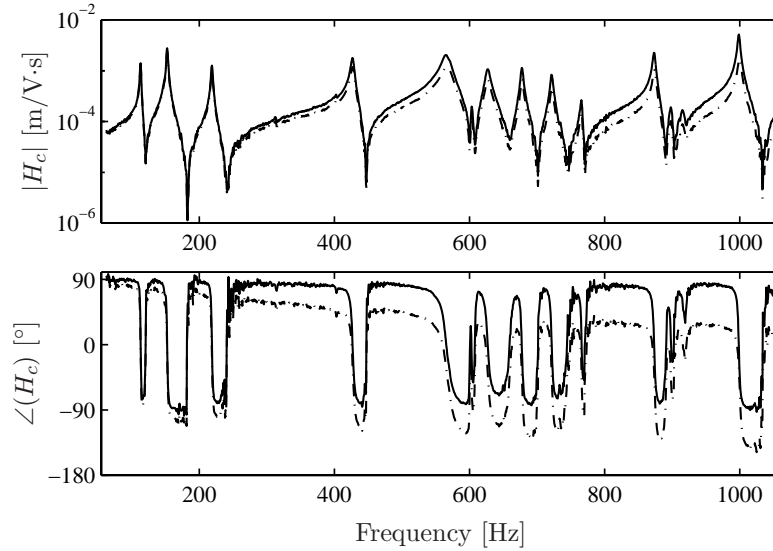


Figure 6.15: Measured secondary path FRFs: relative to amplifier output (—) and relative to amplifier input (----).

The cutoff frequency of the LP filter is determined by the capacitive load connected to the amplifier. It was found from an inspection of the measured FRF that for this patch the cutoff frequency is about 650 Hz. A first order LP filter is modelled by the transfer function:

$$H_{LP}(s) = \frac{\omega_{LP}}{s + \omega_{LP}}, \quad (6.11)$$

where ω_{LP} is the cutoff frequency. The influence of the first order LP filter on the performance of the control system is illustrated in the root locus plot in Figure 6.16. This result was obtained with the numerical model of the experimental setup. When the LP filter is included in the feedback loop, the lobes of the root locus do not travel as far into the left half of the complex plane. Therefore, the best possible damping is decreased as a result of the low pass behaviour of the voltage amplifier. Modes with eigenfrequencies well above the cutoff frequency are no longer damped. The phase is then between -180° and 0° which implies that the control system effectively feeds back a signal proportional to the displacement.

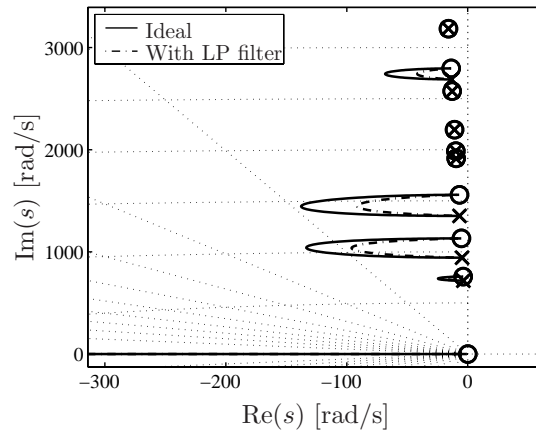


Figure 6.16: Effect of a first order LP filter on the root locus for DVF control.

6.5.2 Results

For both the digital and analogue DVF controllers, the control performance in terms of radiated sound power was measured for various feedback gains. For each gain, the sound power radiated from one side of the plate was measured with the *point* sound intensity method (5×3 grid, see Section 4.4.4). The total sound power was then calculated by integration of the sound power over frequency in the measurement range from 86 Hz to 486 Hz. This range includes the first eight modes of the system, which are all excited by the primary actuator patch.

In Figure 6.17 the total sound power, when normalised with the total sound power without control, is plotted against the feedback gain⁷. First the discussion is devoted to a comparison of the two experimental results shown in the figure. For the digital and analogue controllers, the gain was increased up to the point where the closed-loop system becomes unstable. The “critical” feedback gain is higher for the analogue controller than for the digital controller. Additional phase lag in the feedback loop, such as introduced by the DSP hardware, decreases the frequency for which the phase of the secondary path FRF (including hardware) becomes smaller than -180° . Because the magnitude of the secondary path FRF decreases with frequency (due to roll off), additional phase lag results in a smaller critical feedback gain. The critical feedback gain for the digital controller is about $2.3 \cdot 10^3$ V·s/m, whereas in the case of the analogue implementation the feedback gain can be

⁷In case of the analogue controller, the gain is not exactly known (manual adjustment). The gain is determined afterwards from measured FRF data.

increased further to about $9.1 \cdot 10^3$ V·s/m before the point of instability is reached. For the analogue controller, the critical point is close to the feedback gain corresponding to the best possible reduction of the total sound power. In the range where both controllers are stable, nearly equal performances are observed.

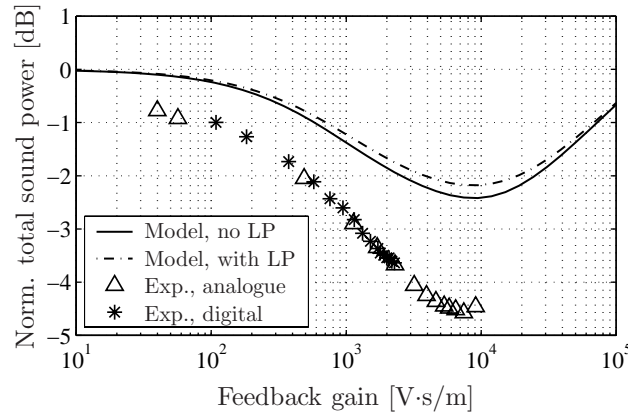


Figure 6.17: Predicted and measured total sound powers radiated by the plate as a function of the feedback gain.

In Figure 6.17 also the control performance calculated with the numerical model is shown. Results are presented for an ideal controller and for a controller that includes a first order LP filter with a cutoff frequency of 650 Hz. The effect of the LP filter is a small degradation of the control performance. More remarkable is how the control performance is underestimated by the numerical model: the best possible reduction of the total sound power is 2.2 dB in theory (with LP filter) but 4.6 dB in practice (analogue controller). This result can be explained by means of Figure 6.18, which shows the sound power as a function of frequency without control, and with control for the gain corresponding to the best possible reduction of the total sound power. Figure 6.18(b) reveals that the measured sound power level before control is most significant for modes *three* and *eight*. The total sound power without control is therefore to a large extent determined by these modes. For the same modes the sound power level is clearly reduced by the control system, which in total gives a 4.6 dB reduction of the total sound power. On the other hand, the total sound power level without control predicted with the numerical model is more or less determined by modes *one*, *three* and *four* (see Figure 6.18(a)). The control system is effective in reducing the sound power at modes one and three but cannot control mode four. Therefore, the total

sound power reduction is only 2.2 dB in theory. However, the predicted and measured reductions at the individual modes are of the same order. Note that the quantitative mismatch between the numerical and experimental results is due to inaccurate acoustic model. The Rayleigh integral model for predicting the sound power is based upon the assumption of a baffled plate, whereas the experiments were conducted without a baffle (see Section 4.4.4).

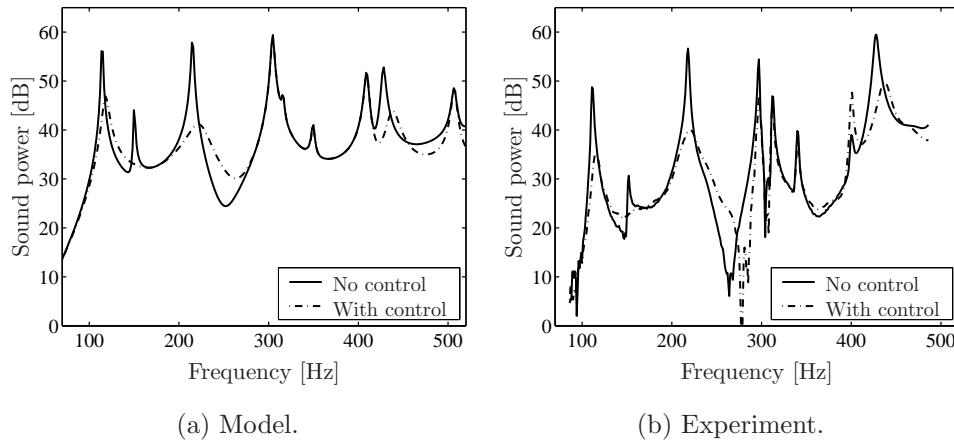


Figure 6.18: Predicted and measured performances of the DVF controller. Model: $g = 8.6 \cdot 10^3 \text{ V}\cdot\text{s}/\text{m}$, Experiment: $g = 7.4 \cdot 10^3 \text{ V}\cdot\text{s}/\text{m}$.

The acoustic radiation is clearly reduced by the single DVF controller for some of the modes in the frequency range up to 500 Hz. For example, in the experiments the sound power is reduced by 13 dB, 16 dB and 10 dB at the resonances corresponding to modes one, three and eight respectively. On the other hand, some of the other modes in this band are not controlled at all. The 4.6 dB reduction of the total sound power is audible to the human ear, but only just. To improve the control performance, more of the SISO feedback loops must be applied (see Section 6.4). A further important feature is that the best possible damping associated with a certain mode strongly depends on the location of the actuator/sensor pair. These and other aspects will be considered in more detail in the Chapter 7, which deals with the optimisation of the locations of multiple actuator/sensor pairs with respect to control of acoustic radiation.

6.6 Concluding remarks

In this chapter the feedback control of structure-borne sound radiation was investigated and demonstrated. In feedback control the use of collocated actuator/sensor pairs decreases the risk of an unstable closed-loop system. In the present work, the control system consists of a piezoelectric actuator patch and an accelerometer, which is located at the centre of the patch. This actuator/sensor pair is attractive from a practical point of view, because it is integrated within the structure, but it is not truly collocated so that stability of the closed loop system cannot be guaranteed.

A direct velocity feedback strategy is implemented on the patch/accelerometer pair, which attempts to increase the damping of the system, and indirectly, to reduce the sound radiation. This strategy has good robustness properties and is easily implemented in practice. When several patch/accelerometer pairs are used, the control system consists of multiple independent feedback loops. With such a decentralised velocity feedback strategy the radiated sound power can be reduced over a broad frequency range. The control performance is not strongly dependent of the feedback gain, so the control system does not have to be adaptive.

Based on the results for the experimental setup with one feedback unit it can be stated that a control system consisting of a piezoelectric patch, accelerometer and DVF controller has potential for reducing structure-borne sound radiation. The sound power is significantly reduced at the resonance frequencies that can be controlled by the patch/accelerometer pair. However, in terms of the total sound power, the control performance is limited. More patch/accelerometer pairs are required to improve the performance. The agreement between the predicted and measured control performance, in terms of sound power, is fairly good.

Chapter 7

Optimisation

7.1 Introduction

In the chapters on feedforward and feedback control, the control system consisted of piezoelectric patches of which the number, shape, size and location were chosen prior to the analysis. Only the voltages applied to the patches were taken as design variables, found from quadratic optimisation theory in the case of the feedforward problem or by selecting the proper gain for feedback control. However, the performance of a control system, e.g. the extent to which the acoustic radiation is reduced, is apart from the control strategy strongly dependent on properties such as size and location of the actuator patches.

A number of simple rules for designing piezoelectric actuator patches can be derived from the analysis of beam and plate systems. For instance, the response near a resonance frequency cannot be reduced if the patch is placed on a nodal line of the corresponding mode shape. Or, as shown in the previous chapter, a patch/accelerometer pair implemented with direct velocity feedback (DVF) control must be located away from clamped plate edges in order to prevent instability. Such simple design rules are certainly valuable, but they do not quantify the performance of the control system, especially if the goal is to reduce acoustic radiation. Therefore, in this chapter a numerical approach for actuator and sensor optimisation is considered.

In Section 7.2, a general outline of the optimisation strategy is presented and compared to recent and past work in the literature. The basic ingredients for the optimisation strategy are the structural and acoustic models presented in Chapter 4 and the control methods discussed in Chapters 5 and 6. The optimisation problem generally involves non-linear (discontinuous) object func-

tions with multiple optima. *Genetic algorithms* are effective in solving such problems and are therefore utilised in this work (Section 7.3). The optimisation strategy is applied here to find the optimal locations of patch/accelerometer pairs implemented with decentralised velocity feedback control. It is also possible to optimise for the number, shape or size of the patches, or for other control methods, but this is beyond the scope of this work. In Section 7.4 several object functions are introduced and analysed for a problem involving the placement of one patch/accelerometer pair. Then, the problem is extended to finding the optimal locations of two such actuator/sensor pairs with independent feedback loops (Section 7.5). The chapter ends with an experimental validation of a setup with two optimally located pairs.

7.2 General approach

In order to obtain a system which most effectively reduces excessive noise or vibrations, one should simultaneously optimise the design of the structure, the actuators and sensors, the controller and the electronics. A typical object function would be one that incorporates several conflicting criteria: high control performance, low weight, low power consumption and low cost. This most general problem is difficult to handle due to the modelling complexity and the computational effort required to optimise such a system. In this work the problem is limited to actuator and sensor optimisation for a predetermined structure and control strategy, and furthermore without considering the electronics. Before presenting the current optimisation strategy, the focus will be on how other researchers have dealt with actuator and/or sensor optimisation for active control of sound and vibration.

7.2.1 Literature survey

Many of the works on active control of sound and vibration deal with the problem of actuator and sensor optimisation. A small portion of relevant papers on this topic are listed in Table 7.1. This short list is certainly incomplete, though it gives an indication of the various approaches that have been proposed. Many other works are for instance discussed in the review papers by Padula and Kincaid [88] and Frecker [89]. An attempt has been made to categorise the works by the type of object function, design variables, optimisation routine and the control strategy applied. In the following, some further remarks on these and other categories are given.

Structure. In almost all of the papers a beam or plate structure is considered. In a few cases the geometry is more complex, such as the box-type structure in the work of Damaren [90] and the double panel partition, which represents a section of an aircraft fuselage, in the work of De Fonseca, Sas and Van Brussel [91].

Actuators and sensors. In ASAC very often piezoelectric patch actuators are applied [92, 93, 94] but also optimisation of point force actuators has been considered [91]. Although much more often the focus is on optimisation of actuators, optimisation of sensors such as PVDF patches [92] and microphones [94] has also been reported.

Modelling. For simple beam and plate structures mostly analytical models have been used. However, FEM models have been used for more complex geometries [91] or to incorporate the dynamics of piezoelectric patches [95, 96]. Such a FEM model can be defined in advance, but sometimes it is required to update the model for each evaluation of the object function.

Control strategy. In the early works actuator and sensor optimisation was performed assuming single frequency feedforward control. More recently, feedback strategies for noise and vibration attenuation over a broad frequency range have been considered [90, 97, 98]. In a few cases the actuator voltage itself is optimised rather than assuming a control strategy [95, 96].

Object function. Many different object functions have been suggested in the literature. In most cases the object function is a measure for the control performance, such as radiated (total) sound power [92], vibration level [99] or closed-loop damping ratios [90, 97].

Design variables. In most cases the design variables are the actuator and/or sensor locations. However, in some works the number of actuators and sensors [91] or the sizes of the actuators or sensors (i.e. in case of piezoelectric patches) [95] are also included in the set of design variables.

Optimisation routine. In the early works the optimisation problem is solved with gradient-based algorithms [92, 93]. However, most often the object function is a non-convex function of the design variables, for which gradient based algorithms likely converge to a local optimum. Therefore, later works focused at more global optimisation techniques such as genetic algorithms (GA) [91, 94] and simulated annealing (SA) [100]. It is noted that in some cases the optimum is obtained from a graphical representation of the object function (indicated by “none” in Table 7.1).

Authors	Year	Ref.	Object func.	Design var.	Method	Control	Remarks
Clark and Fuller	1992	[92]	sound power	location, size	gradient	feedforward	actuator and sensor; single frequency
Wang, Burdisso and Fuller	1994	[93]	sound power	location	gradient	feedforward	single frequency
Baek and Elliott	1995	[100]	squared pressure	location	GA, SA	feedforward	ANC application, single frequency
Kim, Varadan and Varadan	1995	[95]	sound power	location, size, voltage	gradient	none	FEM model, single frequency
Kang, Park, Hwang and Han	1996	[97]	modal damping	location	none	feedback	PZT actuator/sensor pair
Li, Hansen and Qiu	1996	[99]	velocity	location, size	none	none	fixed actuator voltage
Wang	1996	[94]	sound power	location	GA	feedforward	actuator and sensor; single frequency
De Fonseca, Sas and Van Brussel	1999	[91]		number, location	GA, gradient	feedforward	broadband, comparison of strategies
De Boe, Simon and Golinval	2000	[101]	Grammians	location	none	—	
De Man, Francois and Preamont	2002	[98]	open-loop	location	GA	feedback	volume velocity sensor
Damaren	2003	[90]	damping ratio	location	none	feedback	PZT actuator/sensor pair, box-type structure

Table 7.1: A selection of the literature on optimisation in active control of sound and vibration.

7.2.2 Modelling

The previous outline illustrates that actuator and sensor optimisation can be approached in many ways. Several of the concepts used by other researchers are combined in the present work. The goal is to provide a general method for actuator and sensor optimisation for active control of free field sound radiation of plate-like structures. Emphasis is on a control system with piezoelectric patches as control actuators. However, no restrictions are imposed on the type of error sensors.

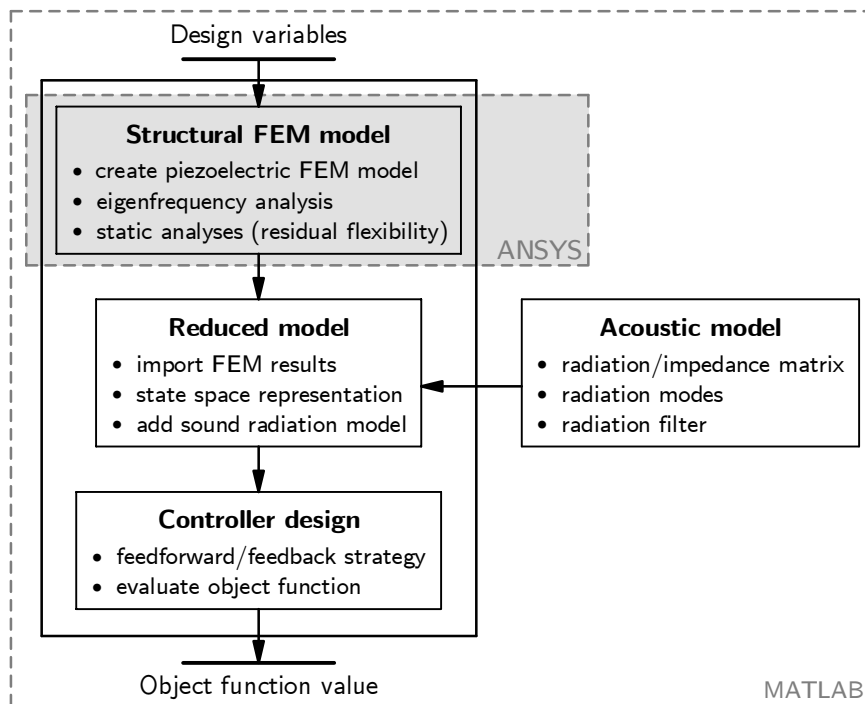


Figure 7.1: An evaluation of the object function.

Irrespective of the type of optimisation routine, an object function must be available that, when provided by a set of design values, returns a value related to the control performance. The steps required for evaluating the object function are shown in Figure 7.1. At this stage, no assumption is made regarding the exact form of the object function.

The first step is to create a FEM model of the structure with piezoelectric patches. The basis for the reduced model of the system are the results of an eigenfrequency analysis and the results of static response analyses (i.e. to

include the residual mode). These analyses are performed within the FEM program. As a next step, the equations of motion are formulated in terms of generalised coordinates and transformed into a state space description. The residual mode is accounted for in the reduced model for faster convergence of the modal expansion. More details on the model reduction technique can be found in Section 4.2.

In order to evaluate an object function related to sound radiation, the structural model is augmented with the acoustic model. It is assumed that during the optimisation the geometry of the structure remains unchanged (e.g. plate dimensions). Therefore, the sound radiation model can be defined in advance and does not have to be redefined each time the object function is evaluated. The only necessity is to interpolate the structural response to the mesh used for discretisation of the acoustic model. The sound power calculation can be based on a description in terms of radiation modes or, in the case of state space control design methods, using radiation filters. More details on the acoustic model are given in Section 4.3.

The final step is to evaluate the system response with control. The type of control strategy must be predetermined, but it can be either feedforward or feedback. The parameters of the control system (e.g. feedback gain) can in principle be handled as design variables, i.e. their optimal setting is found with the optimisation routine. However, for a given actuator and sensor configuration the optimal control parameter values can often be calculated with little effort. Because of the rapid increase of required computational effort with increasing number of design variables, it is more attractive to calculate the optimal control parameter values in this way. As an example, in case of feedforward control the optimal secondary source inputs are easily calculated with the quadratic minimisation procedure of Section 5.2.

The modelling procedure is general in the sense that the structure is modelled with the finite element method. It is therefore possible to model structures with complex geometries that cannot be modelled analytically. Less general is the Rayleigh integral method for predicting the sound field, since it is based on the assumption that the structure is a baffled plate. This model is sufficient for the analysis of the plate setup considered in this thesis, but for more complex geometries a more advanced technique like the boundary element method must be used. The description of sound power in terms of radiation modes or radiation filters is also valid for this type of advanced modelling technique.

As shown in Figure 7.1, a new FEM model is created each time the object function is evaluated. This approach is very time-consuming if the FEM model

consists of a very large number of elements, e.g. for structures with complex geometries. It may then be more attractive to use a FEM model in which the mass and stiffness contributions of the piezoelectric patches are neglected. The equivalent loading on the structure, formed by bending moments along the edges if the patch is rectangular, can be derived with an analytical model (see Appendix C). This simplification will speed up the optimisation process as the FEM model can be defined in advance and does not have to be updated during the optimisation. As a final check the optimised setup must be validated with a model that accounts for the mass and stiffness effects of the piezoelectric patches. The problem size of the plate structure that will be considered in Sections 7.4 and 7.5 is however limited. Hence, a FEM model *including* the mass and stiffness of the patches is used for those problems.

7.2.3 Optimisation routine

Several optimisation techniques are available for solving an optimisation problem. Whether or not an optimisation routine is successful in completing its task strongly depends on the type of object function. Object functions considered in optimisation of ASAC systems generally have multiple local optima. In the early works classical gradient-based routines were used to solve the problem [92, 93]. A gradient-based algorithm converges rapidly to an optimum, but the starting point (i.e. initial set of design values) is critical to whether the solution is the global optimum or one of the local optima. There is a considerable chance that the user-defined starting point is far away from the global optimum, and therefore the algorithm probably converges to a local optimum. Hence, a number of researchers utilised optimisation methods which are better suited for solving problems with multiple optima. The *genetic algorithm* is probably the most popular global optimisation technique. In the present work a genetic algorithm was also applied, since it has been shown recently that it is effective in solving ASAC related optimisation problems [91, 94, 100]. A brief description of the genetic algorithm is presented in the next section.

Two software packages were used to implement the optimisation strategy. The genetic algorithm was programmed in the MATLAB software package. The FEM model is created and analysed with the FEM program ANSYS, which can be executed from within MATLAB. Note that a parametric input file of the FEM model must be available in order to define the model for all possible combinations of the design values. The FEM results are imported into MATLAB, where all other steps for completing an object function evaluation are performed (see Figure 7.1).

7.3 Genetic algorithms

The basic idea behind genetic algorithms (GAs) is to imitate the principles of natural evolution in order to solve optimisation problems. A genetic algorithm (GA) maintains a set of potential solutions (i.e. designs) to the optimisation problem, uses some selection process based on the “fitness” of potential solutions, and uses some “genetic operators” to create new potential solutions [102]. GAs are usually described using vocabulary from natural genetics. A potential solution is called an *individual*. An individual is represented by a *chromosome* made up of a sequence of *genes*. The set of individuals maintained by the GA is the *population*. Each individual in the population has a *fitness*, which is found by evaluating some object function.

```
k=0;
initialise P(k);
evaluate P(k);
while (not termination condition) do
    k=k+1;
    select P(k) from P(k-1);
    alter P(k) by crossover and mutation;
    evaluate P(k);
end
```

Figure 7.2: The structure of a genetic algorithm.

The structure of a (simple) GA is shown in Figure 7.2. At the start of an iteration k , the algorithm maintains a population $P(k)$. For each individual in the population, the object function is evaluated to give the measure of its fitness. Then, a new population is created by selecting more fit individuals. Some of those are altered by the genetic operators *crossover* and *mutation* to form new individuals. Crossover creates two new individuals by combining chromosome segments of two individuals (*parents*). The idea behind crossover is to produce individuals with improved fitness. Mutation arbitrarily alters one of the genes of a chromosome to produce a new single individual. The idea behind mutation is to prevent convergence to a local optimum, i.e. to explore new regions of the design space. This process is repeated for several iterations (*generations*) until the algorithm converges. It is expected that the fittest individual in the final population represents a near-optimal solution to the optimisation problem.

The implementation of a GA requires a consideration of the following issues [102]: the chromosome representation of an individual, how to create an

initial population, the object function to measure fitness, the method for selecting the fittest individuals, the genetic operators, when to terminate the GA, and the choice of the GA parameters (e.g. size of the population). Especially the chromosome representation of the design variables being optimised has a large impact on the performance of the GA. In textbooks on GAs it is advised to use what is called a “natural” representation of the design variables [102, 103]. The optimisation problem considered in this work involves design variables that can take real values. Therefore, in the current implementation the genes on a chromosome are real numbers (*floating point representation*). The implementation of the GA used in this work is described in more detail in Appendix F.

A further aspect which is of great importance for the performance of the GA is the setting of the GA parameters such as population size and number of crossover or mutation operations. A number of guidelines for choosing these parameters can be found in the literature, but it is certainly not an easy task for the (unexperienced) user. Further drawbacks are that GAs have trouble finding the exact optimum and generally require a large number of function evaluations. On the other hand, there are several advantages to using GAs instead of most gradient-based methods: GAs do not require gradient information about the object function, GAs can handle discrete design variables and/or discontinuous object functions, and GAs can move away from local optima. It is not claimed here that GAs are the best option for solving the current optimisation problem. But, because of the ability to solve problems involving object functions with multiple local optima, the GA certainly is a suitable method.

7.4 Optimal placement of patch/accelerometer pairs

In the approach outlined in Section 7.2 no assumptions were made regarding the type of control strategy. In this section and the following the optimisation problem involves a control system consisting of patch/accelerometer pairs implemented with decentralised direct velocity feedback (see Chapter 6). More precisely, the *optimal placement* of these pairs is considered, whereas the actuator/sensor configuration itself is predetermined (e.g. the shape and size of the patches). The application of the present approach for optimisation of a feedforward control system is not considered in this work, but can be found in reference [104].

7.4.1 Design variables

A patch/accelerometer pair can be designed in many ways, where typical design variables are the number and locations of the pairs, and the shape, size, thickness and material properties of the piezoelectric patches. For optimal design of the control system one should take these all into account in the set of design variables for optimisation. However, in this work only the optimal placement of predetermined patch/accelerometer pairs is considered, though a number of general remarks can be made regarding the other design variables:

- *Material properties.* To maximise the excitation of the structure (i.e. effective bending moments) a material with high piezoelectric constant (d_{31}) is desirable. Furthermore, stiffer patches can induce higher loads in the structure, although the effective bending moments cannot have an arbitrary high value by stiffening a patch. PZT is currently the best available material for actuator patches.
- *Thickness.* Kim and Jones [33] studied the optimal thickness of symmetrically bonded patches for the excitation of a plate. They concluded that in the case of an aluminium plate, the optimal patch thickness is about a quarter of the plate thickness. This conclusion was deduced from a result showing the effective bending moment as a function of the thickness under the assumption of a constant electric field. If the assumption had been that of a constant applied voltage, the conclusion would in theory be: “the thinner, the better”. However, in practice the thickness is constrained by the maximum allowable electric field, which may not be exceeded to prevent the material losing its piezoelectric properties.
- *Length, width.* The length and width (i.e. size) of a patch strongly determines to what extent a certain structural mode is excited. For example,

a mode is not well excited if the patch is small compared to the structural wavelength of that particular mode. Consequently, only a small amount of damping can be added to that mode with DVF control. The size of a patch also determines the frequency up to which the patch/accelerometer pair behaves as a truly collocated actuator/sensor pair and is therefore important for stability issues [105] (see Section 6.3.2).

- *Number.* In general, an increase of the control performance can be expected when the number of patch/accelerometer pairs is increased (see Section 6.4). However, the amount by which the performance improves when an extra actuator/sensor pair is used is not straightforward. It is not worthwhile to increase the number of actuator/sensor pairs if the improvement is only marginal, especially because of the rapidly increasing cost involved. In order to optimise the number of actuator/sensor pairs, the object function must quantify the trade-off between control performance and costs [91]. However, in the current study a fixed number of patch/accelerometer pairs is assumed.

The behaviour of a control system is determined in different ways by material properties, thickness and size of a piezoelectric patch. The material properties and thickness mainly determine the effort required to obtain a certain control performance (e.g. amount of damping), but the best possible control performance hardly depends on these properties. In the case of DVF control this can be observed in the root locus plot (complex s -plane) as follows: a change of the material properties or thickness hardly affects the pole/zero locations or the shape of the root locus. However, a smaller gain is required to move the closed-loop poles as far as possible into the left-half plane if the material properties and thickness are close to optimal. On the other hand, a change in the size of a patch (length, width) can be observed in the complex plane as a change of the locations of the zeros. Consequently, the layout of the root locus and thus the damping enhancement change with the size of the patch. A similar effect is observed in the complex plane when changing the location of a patch/accelerometer pair. The damping enhancement as a result of DVF control strongly depends on the locations of the pairs. Proper placement of actuator/sensor pairs is thus of great importance for the effectiveness of this type of control strategy.

7.4.2 Object functions

So far the choice of the object function was left out of consideration. A number of object functions are introduced in this section. Because the DVF control

strategy aims at damping enhancement, it is straightforward to relate the object function to damping. The first object function is defined as the *sum of a set of weighted damping ratios*:

$$F_1 = \sum_{i=1}^n \alpha_i \zeta_i^{\text{cl}}, \quad (7.1)$$

where ζ_i^{cl} are the closed-loop damping ratios, α_i are weight factors and n is the number of modes in the summation. With the weight factors some of the modes in the summation can be given greater priority than others. Note that the goal is to find the actuator/sensor locations for which this object function is maximal.

There is a chance that the optimal solution of object function F_1 corresponds to a case where some of the damping ratios of modes included in the summation are large, whereas others nearly increase with respect to the open-loop ratios. This is circumvented with the second object function, which is defined as the *minimum in a set of weighted damping ratios*:

$$F_2 = \min(\zeta_i^{\text{cl}}/\alpha_i), \quad i = 1, \dots, n. \quad (7.2)$$

If all weight factors are equal to one, the objective is to find the solution for which the smallest damping ratio in the set is maximal. Note that in this case the damping ratio is divided by the weight factor, so that in both object functions a smaller weight factor reduces the importance of the associated mode.

If the weight factors in the foregoing object functions are set to unity, one could say that the system is optimised with respect to the structural vibration. However, the weight factors can be chosen in such a way that these object functions are more or less related to the acoustic radiation of the structure. The radiated sound power is determined by the *self* and *mutual* radiation resistances of the structural modes (see Section 4.3.2). The mutual radiation efficiencies may not be neglected in the prediction of the sound power if the structural response has contributions from several modes. However, near a resonance frequency the open-loop response is dominated by only one structural mode, and the sound power is well approximated when accounting only for the self radiation efficiency of that mode. One way to incorporate acoustic radiation into object functions F_1 and F_2 is by setting the weight factors equal to the self radiation efficiencies.

The foregoing object functions can be evaluated with an open-loop model of the system. Those functions do not rely on any knowledge about the primary

disturbance excitation of the structure. This is not the case for the third object function, which is defined as the *closed-loop total sound power* (in dB):

$$F_3 = 10 \log_{10} \left(\frac{\bar{W}_{\text{tot}}}{\bar{W}_{\text{ref}}} \right), \quad \bar{W}_{\text{tot}} = \int_{\omega_0}^{\omega_1} \bar{W}(\omega) d\omega, \quad (7.3)$$

where $\bar{W}_{\text{ref}} = 1 \cdot 10^{-12}$ W and $[\omega_0, \omega_1]$ is the frequency band over which the sound power is integrated. Since the sound power is only evaluated at discrete frequencies, this integral is evaluated numerically with the trapezoidal rule. In contrast to the previous object function, the goal is now to find the minimum.

Example results

The object functions are compared by means of the setup shown in Figure 7.3, which consists of a clamped rectangular plate with one patch/accelerometer pair with DVF controller. This problem involves two design variables, i.e. the offsets between the edges of the plate and the patch x_{pe} and y_{pe} , and can thus be represented graphically. The location of the patch/accelerometer pair was varied within the rectangular domain indicated in the figure by the dashed lines. Placement outside this domain can be regarded as an infeasible solution, because the closed-loop system is unstable (low frequency instability, see Section 6.3.2). A point force disturbance excitation was used for object function F_3 and the frequency range is from 90 to 250 Hz. This range includes the first three structural modes of the system (1-1, 2-1 and 3-1), so object functions F_1 and F_2 were evaluated with $n = 3$. The calculation of the optimal feedback gain was performed within an evaluation of the object function. The feedback gain was set to the value that minimises or maximises the object function for a given location of the patch/accelerometer pair.

In Figure 7.4 the object functions are shown as functions of the centre location of the actuator patch. The x - and y -coordinates have been normalised with the plate lengths. Object functions F_1 and F_2 are shown in Figures 7.4(a) and 7.4(b) for the case of unit weighting ($\boldsymbol{\alpha} = [\alpha_1, \alpha_2, \alpha_3] = [1, 1, 1]$). The result in Figure 7.4(c) also corresponds to object function F_2 , but there the weight factors are the self radiation efficiencies of a clamped rectangular plate.¹ The frequency dependence of the efficiencies is dealt with by setting a weight α_i equal to the self radiation efficiency of structural mode i at the eigenfrequency of that mode. After scaling to the largest self radiation efficiency in the set,

¹In fact, the self radiation efficiencies depend on the location of the actuator/sensor pair. However, since the variation of the efficiencies is only small, a good approximation is made with the results of a plate without patch.

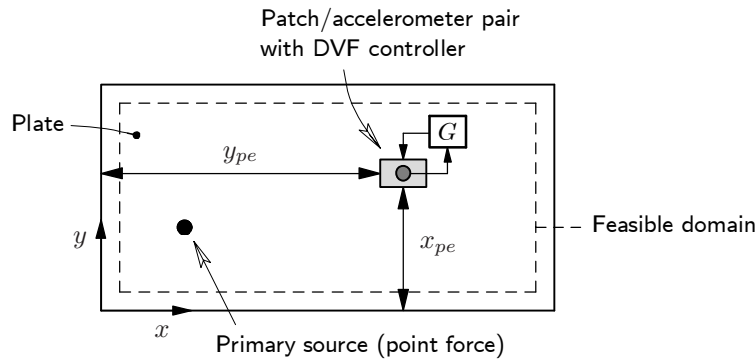


Figure 7.3: Example problem: search optimal location of one DVF loop.

the set of weight factors becomes $\alpha = [1, 0.06, 0.43]$. The “unit weighted” and “efficiency weighted” functions are denoted as F_{2a} and F_{2b} , respectively. The result in Figure 7.4(d) corresponds to object function F_3 .

For an interpretation of the results, one should realise that a structural mode cannot be controlled (or observed) if the centre of the patch/accelerometer pair is on a nodal line of that mode. The object functions are compared only with respect to their shapes; it does not make sense to compare their values. The shapes of object functions F_1 and F_{2a} , which both are a measure for damping, are clearly different. If the location of the actuator/sensor pair is such that one of the three modes cannot be controlled, then F_{2a} is minimal. The locations of the minima in Figure 7.4(b) correspond to the nodal lines of the 2-1 mode (one nodal line) and 3-1 mode (two nodal lines). The maxima in the figure correspond to locations for which all three modes can be controlled. On the other hand, a local maximum can be observed for F_1 if the actuator/sensor pair is at the plate centre (see Figure 7.4(a)). For this location, a significant amount of damping can be introduced for the 1-1 and 3-1 modes. The 2-1 mode is not controlled, but this effect is not observed in the shape of this object function.

The shape of object function F_2 clearly changes if the unit weight factors are replaced by the self-radiation efficiencies. The 1-1 mode is the most efficient radiator of the three, which explains why in Figure 7.4(c) the maximum of F_{2b} is close to the location where the 1-1 mode is best controlled, i.e. the centre of the plate. However, the optimal location is some distance from the plate centre, such that some damping is introduced for the 2-1 mode.

For object function F_3 the goal is to find the global minimum. This is in contrast to the other functions, which involve maximisation problems. A fur-

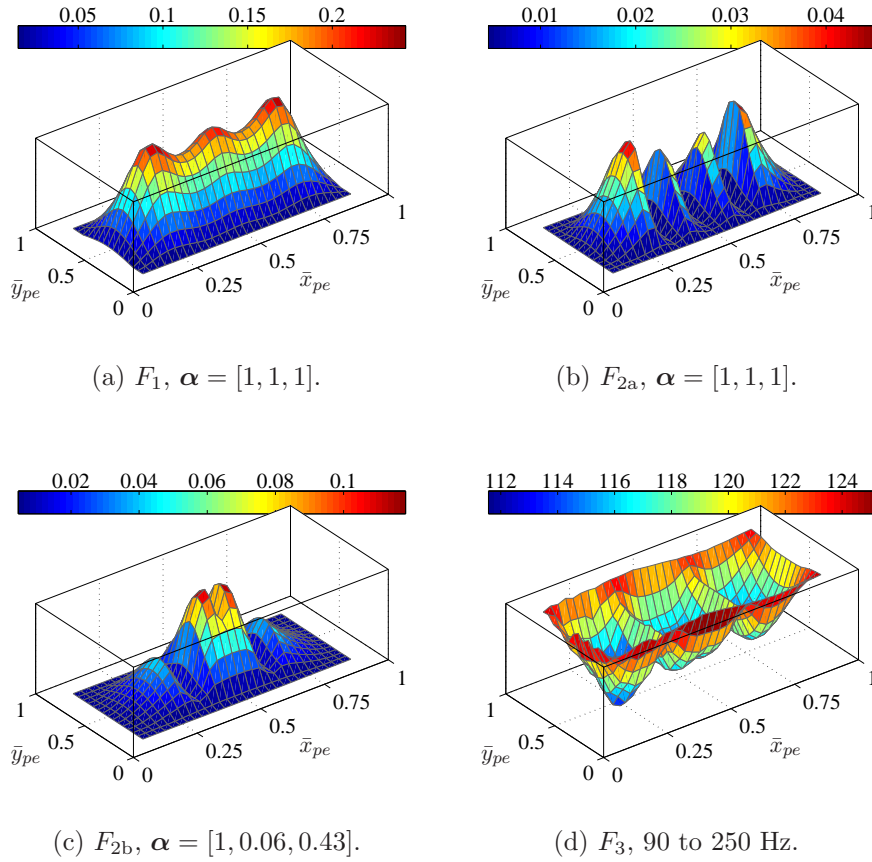


Figure 7.4: Graphical representation of the object functions, first three modes ($n = 3$) in subfigures (a),(b) and (c), frequency range including first three modes (90 to 250 Hz) in subfigure (d). Objectives F_{2a} and F_{2b} refer to two choices of the weight factors, \bar{x}_{pe} and \bar{y}_{pe} are normalised offsets between plate and patch edges.

ther difference is the non-symmetric shape of F_3 because of the non-symmetric primary point force excitation. The best possible reduction of the total sound power (90 to 250 Hz) is obtained when the location of the actuator/sensor pair is near that of the primary disturbance.

For each of the object functions the optimal location of the actuator/sensor pair was determined from the results shown in Figure 7.4. In Table 7.2 the closed-loop damping ratios corresponding to these optima are listed. Furthermore, the closed-loop total sound powers in the range 90 to 250 Hz due to

a primary point force excitation are included. The point force is located in $(x,y)=(90,90)$ mm and has an amplitude of 1 Newton. Two optimal locations are found with each of the object functions F_1 , F_{2a} and F_{2b} because of symmetry. Although the closed-loop damping ratios are equal for two such locations, the total sound powers are not equal as a result of the non-symmetric primary excitation. In the table the total sound power level is given for both optimal locations, where the left column includes the results when the location of the actuator/sensor pair is closer to the primary source.

Obj.	ζ_1^{cl} [%]	ζ_2^{cl} [%]	ζ_3^{cl} [%]	\bar{W}_{tot} [dB]	
F_1	3.37	10.81	10.44	112.0	114.5
F_{2a}	4.76	12.19	4.76	113.7	114.9
F_{2b}	11.94	0.72	9.76	114.6	114.5
F_3	2.39	6.84	9.24	111.4	

Table 7.2: Closed-loop damping ratios of the first three modes (ζ_i^{cl}) and the total sound power (\bar{W}_{tot}) in the range from 90 to 250 Hz for the optimal location of a patch/accelerometer pair found with each object function.

If no control system is applied, the total sound power radiated by the plate is about 124 dB (in the range from 90 to 250 Hz). The minimum of object function F_3 is about 111 dB and represents the best possible reduction of the total sound power that can be obtained with one patch/accelerometer pair and DVF controller, for this primary excitation. When the placement is based on one of the other object functions, the total sound power is not reduced so much, but still a good control performance is obtained. It may be a surprise that placement based on object function F_{2b} , in which the damping ratios are weighted with radiation efficiencies, does not result in a higher reduction of the total sound power when compared to placement according to object function F_{2a} . It can be observed in Table 7.2 that the closed-loop damping of the second mode remains small for object function F_{2b} . As a result, the acoustic radiation is hardly reduced near the second resonance frequency, which explains the relatively high value of the total sound power.

It is not easy to decide what object function must be used in the optimisation process. Still, a number of remarks can be made regarding the choice of an object function. The definition of object function F_3 is in closest agreement with what the control system must do: reduce the sound power radiated by the structure. However, a drawback is that the primary excitation must be known. The optimal location found with this object function depends on the properties of the disturbance source (e.g. location), and will probably be

sub-optimal if those properties change. In many cases the disturbance source is not precisely known. It is then more appropriate to use an object function like F_1 or F_2 , which does not rely on any knowledge about the disturbance source.

7.5 Test case

7.5.1 Problem description

The structure is the same clamped rectangular plate as that considered in the previous section (see Figure 7.5). Three rectangular PZT patches are bonded to the plate. One of these is used as the disturbance source. An accelerometer is located at the centre of each of the other two patches and the DVF strategy is implemented on these actuator/sensor pairs. Both feedback loops have equal feedback gain and operate independently (i.e. decentralised DVF, see Section 6.4).

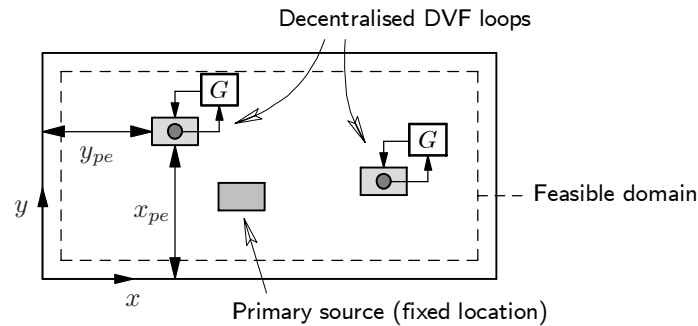


Figure 7.5: Test case: find optimal locations of two patch/accelerometer pairs with decentralised DVF loops, the primary excitation is by a third patch.

The optimisation problem is defined as finding the locations of the two patch/accelerometer pairs corresponding to minimum sound radiation. For this test problem the *object function* is the *closed-loop total sound power* (in dB), which was denoted as F_3 in the previous section. It is stressed that with this type of object function the optimal locations of the patch/accelerometer pairs depend on the location of the primary patch. A further remark is that the object function depends on the location of the actuator/sensor pairs even when the control system is turned off, since a change of location is associated with a change of the mass and stiffness distribution in the system. It was found, however, that this effect is small compared to the way in which the total sound power is reduced by the control system.

The total sound power is minimised in the frequency range from 70 Hz to 520 Hz, which includes the first nine modes of the system. All these modes are excited by the primary patch, whose location is equal to that of the primary patch in the experimental arrangement considered in the previous chapters. The dimensions of the primary patch are $50 \times 30 \times 1.0$ mm, whereas those of the secondary patches are $50 \times 30 \times 0.5$ mm.

The placement of the two patch/accelerometer pairs is restricted by demanding that the edges of a patch remain parallel to the plate edges. The location of one pair is thus defined by an x - and y -coordinate, which makes a total of four design variables. The feedback gain is determined as explained in the previous section and is thus not handled as a design variable. Obviously, the design variables are bounded since the patch/accelerometer pairs must be on the plate. With the additional constraint that the patches must be 20 mm away from the clamped plate edges, the problem of an unstable system at low frequency is circumvented. In addition, there is the constraint that the patches may not overlap. Some details on constraint handling by the genetic algorithm can be found in Appendix F.

7.5.2 Optimisation results

Five optimisation runs were performed with the genetic algorithm, each time for 50 generations with a population consisting of 30 individuals. The number of crossover and mutation operators per generation was 10 and 3, respectively (see Appendix F for more details). In four out of five runs approximately the same result was found for the placement of the patch/accelerometer pairs. This arrangement will be referred to as the *optimal* configuration. In one case the genetic algorithm converged to a local minimum. The optimal placement of the two patch/accelerometer pairs is shown in Figure 7.6. An arrangement with arbitrarily placed patch/accelerometer pairs, which will be referred to as the *alternative* configuration, is also shown. This configuration corresponds to the setup considered in Section 6.5, but extended with a second patch/accelerometer pair.

The predicted sound power levels for the optimal and alternative configurations are shown in Figure 7.7. Also shown is the sound power radiated by the plate with only the primary patch on it. These results are the sound power levels when a unit voltage is applied to the primary patch. Note that results are shown for a frequency range up to 1000 Hz whereas the setup was optimised for the range from 70 Hz to 520 Hz. Furthermore, the setting of the feedback gain is such that the best possible reduction in total sound power is

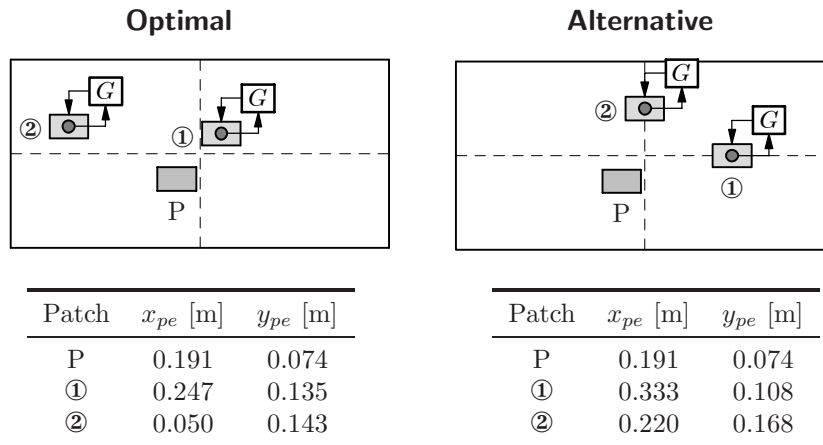


Figure 7.6: Optimal and alternative configuration.

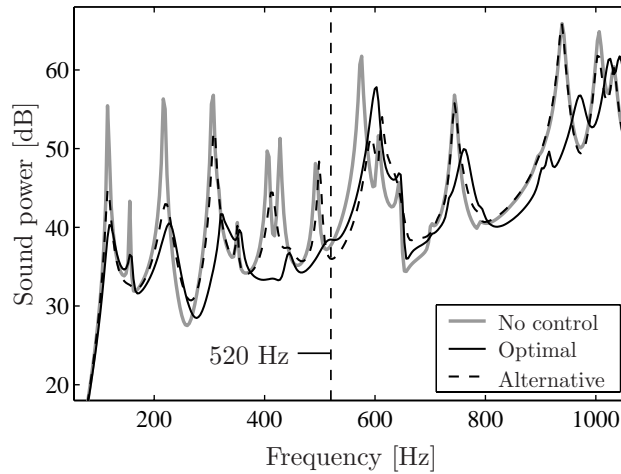


Figure 7.7: Predicted sound power levels without control and with control for optimal and alternative configurations (Optimal: $g = 3.7 \cdot 10^3$ V·s/m, Alternative: $g = 2.4 \cdot 10^3$ V·s/m).

obtained in the range from 70 Hz to 520 Hz.²

It can be observed in Figure 7.7 that below 520 Hz a better control performance is achieved with the optimal configuration. The sound power is significantly reduced at all resonance frequencies corresponding to the efficiently

²The feedback gain corresponding to the best possible reduction of total sound power is weakly dependent on the frequency range considered.

radiating structural modes. However, in the case of the alternative configuration the control system is not able to reduce the sound radiation at some resonances. One must be aware that the placement of the patch/accelerometer pairs is optimised with respect to the total sound power (i.e. the area under the sound power curve), so for some frequencies higher reductions are obtained with the alternative configuration.

7.5.3 Experiments

An experimental validation was carried out for the plate with the optimal configuration of the two patch/accelerometer pairs. More details on the realisation of such a setup can be found in Section 4.4. The two SISO feedback loops were implemented as *analogue* controllers. The analogue implementation was considered more attractive than the digital one since it allows higher feedback gains (see Section 6.5). Two identical accelerometers (B&K 4374) were connected to two identical charge amplifiers with a built-in integrator (B&K 2635). The outputs from the charge amplifiers were fed directly to the three-channel voltage amplifier (Piezomechanik SVR 1000/3). Two of the channels were used to drive the secondary patches and the other was used to drive the primary patch. The feedback gain in both loops can be varied by manual adjustment of the gain of each channel.

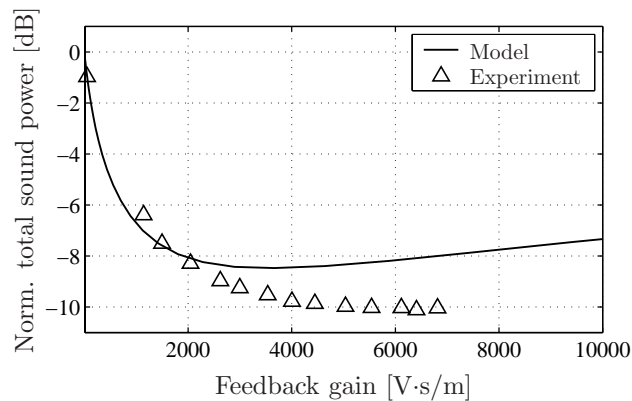


Figure 7.8: Predicted and measured total sound power radiated by the plate as a function of the feedback gain.

The feedback gain was increased stepwise up to the point of instability and for each step the sound power was measured with the point sound intensity method (see Section 4.4.4). The gain in the two feedback loops could not be set to exactly the same value (i.e. because of manual adjustment), but the

difference was always below 10 %. In Figure 7.8 the predicted and measured total sound power levels are plotted against the feedback gain. The results are normalised with the total sound power without control, so a negative value indicates a reduction in total sound power. It can be observed that the predicted and measured reductions are of the same order. The best possible reduction is obtained for a somewhat higher value in the case of the experimental results. Most probably the discrepancies between the numerical and experimental results are because of the Rayleigh model used in the prediction of the sound power. The measured reduction of the total sound power is about 10.1 dB, which is clearly better than the 4.6 dB reduction found with the setup with one feedback loop in the previous chapter (see Section 6.5.2).

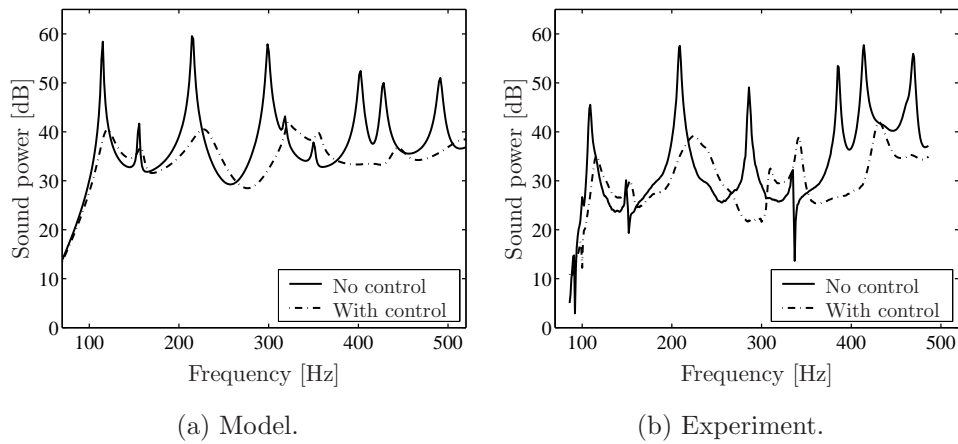


Figure 7.9: Predicted and measured sound power levels of the setup with two optimally positioned actuator/sensor pairs (Model: $g = 3.7 \cdot 10^3 \text{ V}\cdot\text{s}/\text{m}$, Experiment: $g = 6.4 \cdot 10^3 \text{ V}\cdot\text{s}/\text{m}$).

A comparison of the predicted and measured sound power levels without and with control is presented in Figure 7.9. The results with control are for the feedback gain that gives the best possible reduction of the total sound power (i.e. where the results in Figure 7.8 are minimal). It can be observed in both the numerical and experimental results that the decentralised DVF control system with optimally positioned actuator/sensor pairs is effective in controlling the sound radiation in the frequency range up to 500 Hz.

7.6 Concluding remarks

A strategy for actuator and sensor optimisation for active control of free field sound radiation of plate-like structures was presented and validated. The basic ingredients for the optimisation strategy are the structural and acoustic models presented in Chapter 4. With these models it is possible to define different types of object functions for a predetermined control strategy. The optimisation routine is a genetic algorithm, which is used for the present optimisation problem since it is suited for solving problems with multiple optima.

For the purpose of validation, the optimal placement of patch/accelerometer pairs with direct velocity feedback control was considered. The test case involved the placement of two actuator/sensor pairs on a clamped plate. It was found that a setup with optimally located actuator/sensor pairs gives better control performance than a setup with arbitrarily located pairs. With the optimal setup it is possible to reduce the sound power radiated by the plate at all resonances corresponding to efficiently radiating structural modes in the frequency range up to 500 Hz, which includes the first nine modes of the system. Furthermore, a similar performance was observed in the experimental results.

Chapter 8

Conclusions and Recommendations

8.1 Conclusions

This thesis described the development, validation and application of efficient analysis tools for active structural acoustic control. The topics covered a wide range of aspects in engineering, varying from the finite element modelling of piezoelectric materials to the practical implementation of an adaptive feedforward controller. These topics were usually dealt with separately in earlier work presented in the literature. In this thesis, a wide range of analysis tools are combined, resulting in an analysis environment for active structural acoustic control. It was demonstrated within this environment, active control systems can be designed that reduce the sound radiation of plate-like structures. With respect to this result, the following conclusions can be drawn:

- Efficient analysis tools were developed to predict the structural vibration and the free field sound radiation of plate-like structures with integrated piezoelectric patches. The linear piezoelectric finite element formulation allows an accurate modelling of the dynamical behaviour of structures with integrated piezoelectric patches, and, furthermore, enables the modelling of structures with complex geometries. The sound radiation was modelled with the Rayleigh integral method. Because of the modular architecture of the analysis tools it is possible to incorporate another method for the modelling of the sound radiation (e.g. the boundary element method). A numerical model that can be evaluated with low computational effort was obtained with model reduction techniques.

- The mass and stiffness of small surface bonded patches can significantly change the structural mode shapes, whereas the eigenfrequencies are hardly affected. Therefore, the mass and stiffness effects must be included in the model for an accurate prediction of the dynamical behaviour.
- The numerical model was successfully validated with experiments. The eigenfrequencies, mode shapes and frequency response functions predicted with the model are in good agreement with experimental results. The agreement between predicted and measured sound powers is good in a qualitative sense.
- The analysis tool was successfully applied to investigate the behaviour of two control strategies: narrowband feedforward control and velocity feedback control. These strategies can result in significant reductions of the sound power radiated by a plate. Experimental validation showed that a good estimate of the control performance, in terms of sound power, is obtained with the numerical model.
- The use of multiple independent feedback control systems, which each consist of a piezoelectric actuator patch, an accelerometer and a direct velocity feedback loop, has potential for reducing the sound radiation of lightly damped plate-like structures. This approach is attractive because of its good robustness properties and ease of implementation.
- An optimisation strategy, based on the numerical model and a genetic algorithm, was presented and validated. For a test problem involving the optimal placement of two patch/accelerometer pairs, a good agreement between numerical and experimental results was found.

8.2 Recommendations

- The Rayleigh integral model is based on the assumption that the vibrating structure is a baffled plate. This model proved to be sufficient for predicting the trends in the sound radiation behaviour of the experimental setup, but in case of structures with more complex geometries a more advanced modelling technique must be used. The boundary element method is an attractive numerical technique to model the free field sound radiation of such structures.
- In the present work two control strategies were considered, for the most part to show that the numerical model is a useful design tool. Based

on the results presented in the thesis, it can be stated that these two strategies have potential for reducing the sound radiation. However, there are many other control strategies which are possibly better suited for the current control problem. Therefore, it may be worthwhile to consider other control strategies.

- In Chapter 1 it was claimed that active control methods are better suited for low frequency noise reduction than passive methods because of the smaller weight and volume of such a system. However, the electronic hardware (i.e. controller and amplifiers) used in the experiments has a mass and volume much more than the plate itself. To make the ASAC concept interesting for commercial applications a miniaturisation of the hardware is required.

List of Symbols

Roman

a_i	Participation factor of radiation mode i	[–]
b_b	Beam width	[m]
b_{pe}	Patch width	[m]
c_0	Speed of sound in acoustic medium	[m/s]
c_e	Wave propagation speed in an elastic bar	[m/s]
c_{pe}	Wave propagation speed in a piezoelectric bar	[m/s]
D_i	Components of the electric flux density vector	[C/m ²]
d_{kij}	Components of the piezoelectric charge coefficient tensor	[m/V]
E_i	Components of the electric field vector	[V/m]
E_p	Young's modulus of plate material	[N/m ²]
$G(\mathbf{r}, \mathbf{r}_s)$	Green's function	[–]
$\bar{\mathbf{I}}$	Time-averaged sound intensity	[W/m ²]
\bar{I}_r	Time-averaged sound intensity in direction r	[W/m ²]
J	Quadratic error criterion	[–]
$j = \sqrt{-1}$	Imaginary unit	[–]
L_W	Sound power level	[dB]
l_b	Beam length	[m]
$(l_p)_x$	Plate length in x -direction	[m]
$(l_p)_y$	Plate length in y -direction	[m]
$(l_{pe})_x$	Patch length in x -direction	[m]
$(l_{pe})_y$	Patch length in y -direction	[m]
k	Acoustic wave number ($= \omega/c_0$)	[m ⁻¹]
k_{33}, k_{31}	Electromechanical coupling factors	[–]
m	Number of modes used in modal expansion	[–]
N	Number of elemental radiators	[–]
N_r	Truncated number of radiation modes	[–]
n	Number of structural DOF in FEM model	[–]
p	Acoustic pressure	[Pa]

Q	Surface charge	[C]
q_i	Participation factor of a structural mode i	[-]
\mathbf{r}	Location vector	[m]
\mathbf{r}_s	Location vector of a point on surface S	[m]
Δr	Spacer length of sound intensity probe	[m]
S	Surface area	[m ²]
S_e	Surface area of an elemental radiator	[m ²]
S_{ijkl}	Components of the compliance tensor	[N/m ²]
t_b	Beam thickness	[m]
t_p	Plate thickness	[m]
t_{pe}	Patch thickness	[m]
V	Voltage across electrodes	[V]
\mathbf{v}	Acoustic particle velocity	[m/s]
v_n	Surface normal velocity	[m/s]
\bar{W}	Time-averaged (radiated) sound power	[W]
w_i	Structural displacement field	[m]
x_{pe}	Placement of patch in x -direction	[m]
y_{pe}	Placement of patch in y -direction	[m]
x, y, z	Cartesian coordinates	[m]

Greek

α	Free space angle in Helmholtz integral equation	[-]
α, β	Coefficients for proportional damping	[-]
ϵ_{ij}	Components of the strain tensor	[-]
ϵ_0	Dielectric permittivity in vacuum ($= 8.85 \cdot 10^{-12}$)	[F/m]
ϵ_{ij}	Components of the dielectric permittivity tensor	[F/m]
λ_i	Eigenvalue of radiation mode i	[-]
ω	Angular frequency	[rad/s]
ω_i	Angular eigenfrequency of structural mode i	[rad/s]
ν_p	Poisson's ratio of plate material	[-]
ρ_0	Density of acoustic medium	[kg/m ³]
ρ_p	Density of plate material	[kg/m ³]
ρ_{pe}	Density of piezoelectric material	[kg/m ³]
σ	Radiation efficiency	[-]
σ_{ij}	Components of the stress tensor	[N/m ²]
$\Delta\theta$	Phase angle between intensity probe microphone signals	[rad]
ζ_i	Viscous damping ratio of structural mode i	[-]
ϕ	Electric potential (voltage)	[V]

Matrices

A	State space model: system matrix
B	State space model: input matrix
C	State space model: output matrix
\mathbf{C}^D	Elasticity matrix at constant electric flux density
\mathbf{C}^E	Elasticity matrix at constant electric field
\mathbf{C}_{uu}	Viscous damping matrix
D	State space model: feedthrough matrix
$\underline{\mathbf{d}}$	Piezoelectric (charge) coupling matrix
$\underline{\mathbf{e}}$	Piezoelectric (stress) coupling matrix
\mathbf{G}_0^v	Matrix with static charge responses
$\underline{\mathbf{g}}$	Piezoelectric (voltage) coupling matrix
\mathbf{H}_d	FRFs between disturbance inputs and error sensors
\mathbf{H}_c	FRFs between control inputs and error sensors
$\underline{\mathbf{h}}$	Piezoelectric (stiffness) coupling matrix
\mathbf{K}_{uu}	Structural stiffness matrix
\mathbf{K}_{uu}^*	Equivalent stiffness matrix (after static condensation)
$\mathbf{K}_{u\phi}$	Piezoelectric stiffness matrix ($= \mathbf{K}_{\phi u}^T$)
$\mathbf{K}_{\phi\phi}$	Dielectric stiffness matrix
\mathbf{M}_{uu}	Structural mass matrix
M	Matrix with radiation resistances of structural modes
R	Radiation resistance matrix
\mathbf{S}^D	Compliance matrix at constant dielectric displacement
\mathbf{S}^E	Compliance matrix at constant electric field
\mathbf{U}_0	Matrix with static structural responses
$\mathbf{W}_y, \mathbf{W}_c$	Error weighting matrix and effort weighting matrix
Z	Acoustic impedance matrix
$\underline{\beta}^\epsilon$	Dielectric matrix at constant strain
$\underline{\beta}^\sigma$	Dielectric matrix at constant stress
$\underline{\epsilon}^\epsilon$	Dielectric matrix at constant strain
$\underline{\epsilon}^\sigma$	Dielectric matrix at constant stress
Γ	Matrix with radiation modes
Λ	Matrix with eigenvalues of radiation modes
Ψ_u	Matrix with structural eigenvectors
Ψ_n	Matrix with structural eigenvectors, normal component only
Ψ_ϕ^c	Matrix with voltage eigenvectors
Φ_0^c	Matrix with static voltage responses
Ω	Matrix eigenfrequencies ($= \text{diag}(\omega_i)$)
Ξ	Viscous damping matrix ($= \text{diag}(\zeta_i)$)

Vectors

a	Vector with radiation mode participation factors
D	Electric flux density vector
E	Electric field vector
f	Vector with nodal structural forces
f*	Equivalent structural force vector
g	Vector with nodal charges
g^v	Part of g with prescribed voltage boundary condition
g^c	Part of g with prescribed charge boundary condition
p	Vector with pressures in field points
q	Vector with structural mode participation factors
u	Vector with nodal structural displacements/rotations
u₀	Static structural response
û_i	Structural eigenvector of mode <i>i</i>
v	State space model: input vector
v_d	Vector with primary disturbance inputs
v_c	Vector with secondary control inputs
v_n	Vector with normal velocities of elemental radiators
x	State space model: state vector
y	State space model: output vector
y_d	Vector with responses to primary disturbance inputs
y_c	Vector with responses to secondary control inputs
ε	Strain vector
φ	Vector with nodal voltages
φ^v	Part of φ with prescribed voltage boundary condition
φ^c	Part of φ with prescribed charge boundary condition
γ_i	Acoustic radiation mode <i>i</i>
σ	Stress vector

Abbreviations

ASAC	Active structural acoustic control
DOF	Degree(s) of freedom
FEM	Finite element method
FRF(s)	Frequency response function(s)
GA(s)	Genetic algorithm(s)
MAC	Modal assurance criterion
MIMO	Multiple input, multiple output
PZT	Piezoceramic material (<i>lead zirconate titanate</i>)

RME	Radiation modal expansion
SISO	Single input, single output

Miscellaneous

∇^2	Differential operator
$\text{Re}(\)$	Real part
$\text{Im}(\)$	Imaginary part
x^*	Complex conjugate of x
$\dot{\mathbf{x}}$	Time derivative of \mathbf{x}
\mathbf{x}^T	Transpose of \mathbf{x}
\mathbf{x}^H	Hermitian of \mathbf{x} (complex conjugate transposed)

Appendix A

Additional Information on Piezoelectricity

A.1 Alternative constitutive equations

The piezoelectric constitutive equations can be written in four ways. These forms are given below, in matrix-vector notation.

Notation 1:

$$\begin{Bmatrix} \boldsymbol{\epsilon} \\ \mathbf{D} \end{Bmatrix} = \begin{bmatrix} \mathbf{S}^E & \underline{\mathbf{d}}^T \\ \underline{\mathbf{d}} & \underline{\boldsymbol{\epsilon}}^\sigma \end{bmatrix} \begin{Bmatrix} \boldsymbol{\sigma} \\ \mathbf{E} \end{Bmatrix}. \quad (\text{A.1})$$

Notation 2:

$$\begin{Bmatrix} \boldsymbol{\sigma} \\ \mathbf{D} \end{Bmatrix} = \begin{bmatrix} \mathbf{C}^E & -\underline{\mathbf{e}}^T \\ \underline{\mathbf{e}} & \underline{\boldsymbol{\epsilon}}^\epsilon \end{bmatrix} \begin{Bmatrix} \boldsymbol{\epsilon} \\ \mathbf{E} \end{Bmatrix}. \quad (\text{A.2})$$

Notation 3:

$$\begin{Bmatrix} \boldsymbol{\epsilon} \\ \mathbf{E} \end{Bmatrix} = \begin{bmatrix} \mathbf{S}^D & \underline{\mathbf{g}}^T \\ -\underline{\mathbf{g}} & \underline{\boldsymbol{\beta}}^\sigma \end{bmatrix} \begin{Bmatrix} \boldsymbol{\sigma} \\ \mathbf{D} \end{Bmatrix}. \quad (\text{A.3})$$

Notation 4:

$$\begin{Bmatrix} \boldsymbol{\sigma} \\ \mathbf{E} \end{Bmatrix} = \begin{bmatrix} \mathbf{C}^D & -\underline{\mathbf{h}}^T \\ -\underline{\mathbf{h}} & \underline{\boldsymbol{\beta}}^\epsilon \end{bmatrix} \begin{Bmatrix} \boldsymbol{\epsilon} \\ \mathbf{D} \end{Bmatrix}. \quad (\text{A.4})$$

In the above equations, $\boldsymbol{\epsilon}$ is the strain vector, $\boldsymbol{\sigma}$ is the stress vector, \mathbf{D} is the electric flux density vector, and \mathbf{E} is the electric field vector. Matrices \mathbf{S} and \mathbf{C}

contain the elasticity constants, $\underline{\epsilon}$ and $\underline{\beta}$ are the dielectric constants matrices. The piezoelectric coupling is expressed by matrices $\underline{\mathbf{d}}$, $\underline{\mathbf{e}}$, $\underline{\mathbf{g}}$ and $\underline{\mathbf{h}}$. The superscript symbols indicate values at E , ϵ , σ and D constant. For example, \mathbf{C}^E is the elasticity matrix for a constant electrical field. The coefficient matrices appearing in the four sets of constitutive equations are related as follows:

$$\begin{aligned} \mathbf{C}^E \mathbf{S}^E &= \mathbf{I}, & \mathbf{C}^D &= \mathbf{C}^E + \underline{\mathbf{e}}^T \underline{\mathbf{h}}, & \underline{\mathbf{e}} &= \underline{\mathbf{d}} \mathbf{C}^E, \\ \mathbf{C}^D \mathbf{S}^D &= \mathbf{I}, & \mathbf{S}^D &= \mathbf{S}^E - \underline{\mathbf{d}}^T \underline{\mathbf{g}}, & \underline{\mathbf{d}} &= \underline{\epsilon}^\sigma \underline{\mathbf{g}}, \\ \underline{\epsilon}^\epsilon \underline{\beta}^\epsilon &= \mathbf{I}, & \underline{\epsilon}^\sigma &= \underline{\epsilon}^\epsilon + \underline{\mathbf{d}} \underline{\mathbf{e}}^T, & \underline{\mathbf{g}} &= \underline{\beta}^\sigma \underline{\mathbf{d}}, \\ \underline{\epsilon}^\sigma \underline{\beta}^\sigma &= \mathbf{I}, & \underline{\beta}^\sigma &= \underline{\beta}^\epsilon - \underline{\mathbf{g}} \underline{\mathbf{h}}^T, & \underline{\mathbf{h}} &= \underline{\mathbf{g}} \mathbf{C}^D. \end{aligned}$$

A.2 PIC-151 material properties

The PZT patches used in the experiments are fabricated by *PI Ceramic*. The material type is PIC-151. The elastic compliance matrix under constant electric field, the piezoelectric charge coefficient matrix, and the dielectric matrix under constant stress are given by (supplied by *PI Ceramic*):

$$\mathbf{S}^E = 1 \cdot 10^{-12} \begin{bmatrix} 16.8 & -5.66 & -7.11 & 0 & 0 & 0 \\ -5.66 & 16.8 & -7.11 & 0 & 0 & 0 \\ -7.11 & -7.11 & 19.0 & 0 & 0 & 0 \\ 0 & 0 & 0 & 51.0 & 0 & 0 \\ 0 & 0 & 0 & 0 & 51.0 & 0 \\ 0 & 0 & 0 & 0 & 0 & 45.0 \end{bmatrix} \text{ m}^2/\text{N}, \quad (\text{A.5})$$

$$\underline{\mathbf{d}} = 1 \cdot 10^{-10} \begin{bmatrix} 0 & 0 & 0 & 0 & 6.10 & 0 \\ 0 & 0 & 0 & 6.10 & 0 & 0 \\ -2.14 & -2.14 & 4.23 & 0 & 0 & 0 \end{bmatrix} \text{ m/V}, \quad (\text{A.6})$$

$$\underline{\epsilon}^\sigma = 1 \cdot 10^{-8} \begin{bmatrix} 1.72 & 0 & 0 \\ 0 & 1.72 & 0 \\ 0 & 0 & 1.87 \end{bmatrix} \text{ F/m}. \quad (\text{A.7})$$

The storage order of the strains (and stresses) is according to the IEEE standard on piezoelectricity, i.e. $\epsilon = \{\epsilon_{11}, \epsilon_{22}, \epsilon_{33}, 2\epsilon_{23}, 2\epsilon_{31}, 2\epsilon_{12}\}^T$.

A.3 Thermopiezoelectricity

If the standard piezoelectric formulation is further expanded to a thermopiezoelectric formulation, two major effects are included, namely:

- The *pyroelectric* effect; the generation of electrical charge as a result of temperature variation, and vice versa.
- The *thermal strain* effect; the generation of mechanical strain as a result of temperature variation.

Thermopiezoelectric effects must be accounted for when piezoelectric materials are applied in environments with strong temperature variations, e.g. in aerospace applications. The constitutive equations for a linear thermopiezoelectric material are given by (in index notation) [106]:

$$\epsilon_{ij} = S_{ijkl}^{E,\theta} \sigma_{kl} + d_{kij}^{\theta} E_k + \lambda_{ij}^E \theta, \quad (\text{A.8a})$$

$$D_i = d_{ikl}^{\theta} \sigma_{kl} + \epsilon_{ik}^{\sigma,\theta} E_k + p_i^{\sigma} \theta, \quad (\text{A.8b})$$

$$\Delta = \lambda_{ij}^E \sigma_{kl} + p_k^{\sigma} E_k + \alpha \theta. \quad (\text{A.8c})$$

In these equations, θ is the temperature variation (from the stress-free reference temperature θ_0), Δ is the entropy per unit volume, λ_{ij}^E are the temperature strain coefficients, p_i^{σ} are the pyroelectric coefficients, and α is a material coefficient. The superscript symbols indicate values at E , σ and θ constant. The additional equation besides mechanical and electrical equilibrium equations (see Section 2.4) to describe thermopiezoelectric equilibrium is the heat conduction equation, which is given by:

$$h_i = -k_{ij} \theta_{,j}, \quad (\text{A.9})$$

where h is the heat flux vector, and k is the heat conduction tensor.

Appendix B

Additional Information on Beam Models

In this appendix, additional information on the beam model of Section 3.3 is presented. In Section B.1, the dynamic stiffness matrix (DSM) of a beam element with one surface bonded patch is derived. The validity of the assumption of a uniform electric field, which was used in the derivation of the beam model, is considered in Section B.2. In Section B.3, the implementation of a DSM model for the coupled longitudinal and transverse vibrations of a beam with surface bonded patches is considered.

B.1 Derivation of the dynamic stiffness matrix

A DSM element of a beam with one surface bonded patch is shown in Figure B.1. The equation of motion that is used as the basis for the dynamic stiffness matrix is, in frequency domain notation, given by (see Section 3.3.1):

$$-\omega^2(\rho A)_{\text{eq}} w + (EI)_{\text{eq}}^a \frac{d^4 w}{dx^4} = f, \quad (\text{B.1})$$

where w is the transverse displacement (i.e. complex amplitude), and f is an external transverse load. The nodal DOF vector \mathbf{w} and the nodal load vector \mathbf{f} are defined as:

$$\mathbf{w} = \begin{Bmatrix} w_i \\ \theta_i \\ w_{i+1} \\ \theta_{i+1} \end{Bmatrix}, \quad \mathbf{f} = \begin{Bmatrix} f_i \\ M_i \\ f_{i+1} \\ M_{i+1} \end{Bmatrix}, \quad (\text{B.2})$$

where w_i and $\theta_i = dw_i/dx$ are the displacement and rotation at node i , and f_i and M_i are the corresponding nodal shear force and bending moment. The sign convention is shown in Figure B.1. As well as the structural DOF and loads, this element also has an electric DOF and load, namely the voltage across the electrodes V , and the charge on the electrodes Q . Because these variables are independent of the coordinate along the beam, these variables are not defined at a node.

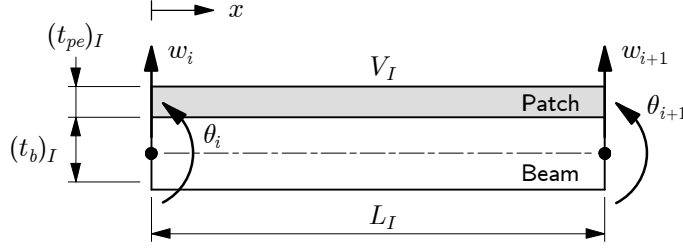


Figure B.1: Sign convention for a DSM element.

The general solution of equation (B.1) can be written as:

$$w = C_1 \sin(k_b x) + C_2 \cos(k_b x) + C_3 e^{k_b(x-L)} + C_4 e^{-k_b x} + w_p, \quad (\text{B.3})$$

where C_1 to C_4 are the integration coefficients, L is the element length, and the flexural wave number k_b is defined as:

$$k_b = \sqrt[4]{\omega^2 \frac{(\rho A)_{\text{eq}}}{(EI)_{\text{eq}}^a}}. \quad (\text{B.4})$$

The first four right hand side terms in equation (B.3) represent the homogeneous part of the solution, and w_p is the particular solution. The particular solution depends on the type of externally applied structural load. The nodal DOF can be expressed in terms of the integration coefficients and the particular solution by evaluating the general solution at the nodes, i.e. at $x = 0$ and $x = L$:

$$\mathbf{w} = \mathbf{G} \mathbf{c} + \mathbf{w}_p, \quad (\text{B.5})$$

where \mathbf{c} is the column vector with integration coefficients, \mathbf{w}_p is the column vector with the particular solution evaluated at the nodes. The transfer matrix

\mathbf{G} is given by:

$$\mathbf{G} = \begin{bmatrix} 0 & 1 & e^{-k_b L} & 1 \\ k_b & 0 & k_b e^{-k_b L} & -k_b \\ \sin(k_b L) & \cos(k_b L) & 1 & e^{-k_b L} \\ k_b \cos(k_b L) & -k_b \sin(k_b L) & k_b & -k_b e^{-k_b L} \end{bmatrix}. \quad (\text{B.6})$$

An equation similar to (B.5) exists for nodal the load vector \mathbf{f} . The bending moment M and the shear force F are given by:

$$M = (EI)_{\text{eq}}^a \frac{d^2 w}{dx^2} - E_{pe} Q_{pe} (1 - \gamma) \epsilon_{pe}, \quad \text{and} \quad F = -\frac{dM}{dx}. \quad (\text{B.7})$$

where $\gamma = E_{pe} A_{pe} / (EA)_{\text{eq}}$. The relation between the shear force and the bending moment is the mechanical rotary equilibrium for an infinitesimal part. Evaluating equations (B.7) at the nodes gives:

$$\mathbf{f} = \mathbf{H} \mathbf{c} + \mathbf{k}_{12} V + \mathbf{f}_p, \quad (\text{B.8})$$

where V is the electrode voltage, \mathbf{f}_p is the contribution of the particular solution,

$$\mathbf{H} = (EI)_{\text{eq}}^a k_b^2 \begin{bmatrix} -k_b & 0 & k_b e^{-k_b L} & -k_b \\ 0 & 1 & -e^{-k_b L} & -1 \\ k_b \cos(k_b L) & -k_b \sin(k_b L) & -k_b & k_b e^{-k_b L} \\ -\sin(k_b L) & -\cos(k_b L) & 1 & e^{-k_b L} \end{bmatrix}, \quad (\text{B.9})$$

and

$$\mathbf{k}_{12} = E_{pe} Q_{pe} (1 - \gamma) \frac{d_{31}}{t_{pe}} \begin{Bmatrix} 0 \\ 1 \\ 0 \\ -1 \end{Bmatrix}. \quad (\text{B.10})$$

The surface charge on the top electrode is defined as the integral of the average dielectric displacement (see Section 3.3.1):

$$Q = b_{pe} \int_0^L \left(\int_{t_b/2}^{t_b/2+t_{pe}} D_3 dz \right) dx, \quad (\text{B.11})$$

where

$$D_3 = d_{31} E_{pe} \left(\left[\frac{E_{pe} Q_{pe}}{(EA)_{\text{eq}}} - z \right] \frac{d^2 w}{dx^2} - \left[\frac{1 - k_{31}^2}{k_{31}^2} + \gamma \right] \epsilon_{pe} \right). \quad (\text{B.12})$$

Equation (B.11) can be rewritten in a form in which the charge is related to the nodal DOF and electrode voltage:

$$Q = \mathbf{k}_{21} \mathbf{w} + k_{22} V, \quad (\text{B.13})$$

where $\mathbf{k}_{21} = \mathbf{k}_{12}^T$, and

$$k_{22} = -\frac{b_{pe} l_{pe}}{t_{pe}} \epsilon_{33}^{\sigma} (1 - k_{31}^2 (1 - \gamma)). \quad (\text{B.14})$$

When equations (B.5), (B.8) and (B.13) are combined, the element matrix is found that relates the structural and electric DOF and loads:

$$\begin{bmatrix} \mathbf{K}_{11} & \mathbf{k}_{12} \\ \mathbf{k}_{21} & k_{22} \end{bmatrix} \begin{Bmatrix} \mathbf{w} \\ V \end{Bmatrix} = \begin{Bmatrix} \mathbf{f} \\ Q \end{Bmatrix} + \begin{Bmatrix} \mathbf{g} \\ 0 \end{Bmatrix}, \quad (\text{B.15})$$

where

$$\mathbf{K}_{11} = \mathbf{H} \mathbf{G}^{-1}, \quad \text{and} \quad \mathbf{g} = \mathbf{K}_{11} \mathbf{w}_p - \mathbf{f}_p.$$

The components of \mathbf{g} are defined by the particular solution and thus by the type of mechanical load on the element. The components of \mathbf{g} represent the equivalent nodal forces and moments. For a number of mechanical loads, the particular solutions are given in Table B.1.

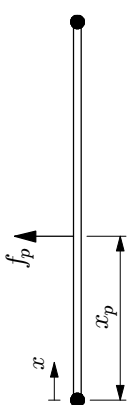
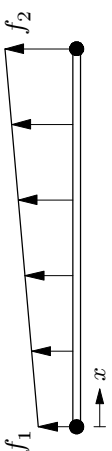
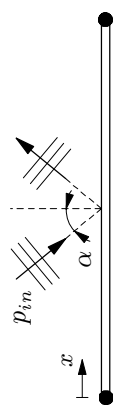
Load type	Load f	Solution w_p
 <p>Point</p>	$f_p \delta(x - x_p)$	$\frac{-j f_p (e^{-jk_b x-x_p } - j e^{-k_b x-x_p })}{4(EI)_{\text{eq}} k_b^3} \quad (\text{B.16})$
 <p>Linear</p>	$f_1 \left(1 - \frac{x}{L}\right) + f_2 \frac{x}{L}$	$\frac{-f_1 \left(1 - \frac{x}{L}\right) - f_2 \frac{x}{L}}{(EI)_{\text{eq}} k_b^4} \quad (\text{B.17})$
 <p>Plane wave</p>	$-2p_{in} e^{-jkx \sin(\alpha)}$	$\frac{-2p_{in} e^{-jkx \sin(\alpha)}}{(EI)_{\text{eq}} (k^4 \sin(\alpha)^4 - k_b^4)} \quad (\text{B.18})$

Table B.1: Load types.

B.2 Uniform electric field assumption

In the derivation of the beam model the electric field across the thickness of the patch was assumed to be uniform. In the analysis presented here, the electric field is solved with Maxwell's equation for the Euler-Bernoulli strain field. A similar approach was used in Section 2.5 for the longitudinal vibration of a piezoelectric bar.

The dielectric displacement across the patch for the Euler-Bernoulli strain field is given by:

$$D_3 = d_{31}E_{pe}(\epsilon_0 - \kappa z) + \epsilon_{33}^\sigma(1 - k_{31}^2)E_3, \quad (\text{B.19})$$

where $k_{31} = d_{31}\sqrt{E_{pe}/\epsilon_{33}^\sigma}$ is the electromechanical coupling factor. Substitution of this equation into Maxwell's equation for a one-dimensional electric field gives:

$$\frac{\partial^2 \phi}{\partial z^2} = -\frac{k_{31}^2}{d_{31}(1 - k_{31}^2)} \kappa, \quad (\text{B.20})$$

where the electric field has been replaced by $E_3 = -\partial\phi/\partial z$, with ϕ the electric potential. Double integration of this equation with respect to the z gives:

$$\phi = -\frac{k_{31}^2}{d_{31}(1 - k_{31}^2)} \kappa \frac{z^2}{2} + C_1 z + C_2. \quad (\text{B.21})$$

where C_1 and C_2 can be determined with the electrical boundary conditions. The following conditions apply:

$$\phi(t_b/2) = 0, \quad \phi(t_b/2 + t_{pe}) = V. \quad (\text{B.22})$$

For these boundary conditions, the electric potential distribution is:

$$\phi = -\frac{k_{31}^2}{d_{31}(1 - k_{31}^2)} \left(\frac{z^2}{2} - \frac{t_b + t_{pe}}{2} z + \frac{t_b(t_b + 2t_{pe})}{8} \right) \kappa + \frac{2z - t_b}{2t_{pe}} V, \quad (\text{B.23})$$

and the corresponding electric field is:

$$E_3 = \frac{k_{31}^2}{d_{31}(1 - k_{31}^2)} \left(z - \frac{t_b + t_{pe}}{2} \right) \kappa - \frac{V}{t_{pe}}. \quad (\text{B.24})$$

The first right hand side term represents the change of the electric field due to the deformation of the structure. The electric field is linear across the patch, whereas the distribution along the patch depends on the curvature κ .

The normal stress in the patch corresponding to the electric field in equation (B.24) is:

$$\sigma_{11}^{pe} = E_{pe} \left(\epsilon_0 - \left[z + \frac{k_{31}^2}{1 - k_{31}^2} \left(z - \frac{t_b + t_{pe}}{2} \right) \right] \kappa + \epsilon_{pe} \right), \quad (\text{B.25})$$

where $\epsilon_{pe} = d_{31}V/t_{pe}$. With equations (3.7) the normal force and bending moment become:

$$\begin{Bmatrix} N \\ M \end{Bmatrix} = \begin{bmatrix} (EA)_{\text{eq}} & -E_{pe}Q_{pe} \\ -E_{pe}Q_{pe} & E_bI_b + E_{pe}(I_{pe} + \frac{k_{31}^2}{1 - k_{31}^2}I_{pe}^*) \end{bmatrix} \begin{Bmatrix} \epsilon_0 \\ \kappa \end{Bmatrix} + \begin{Bmatrix} E_{pe}A_{pe} \\ -E_{pe}Q_{pe} \end{Bmatrix} \epsilon_{pe}, \quad (\text{B.26})$$

where $I_{pe}^* = (b_{pe}t_{pe}^3)/12$. This result and the result found for the uniform electric field assumption (see equation (3.8)) are similar, but the bending stiffness is different for the two cases:

$$\begin{aligned} \text{Uniform} \quad & (EI)_{\text{eq}} = E_bI_b + E_{pe}I_{pe}, \\ \text{Linear} \quad & (EI)_{\text{eq}}^* = E_bI_b + E_{pe} \left(I_{pe} + \frac{k_{31}^2}{1 - k_{31}^2} I_{pe}^* \right). \end{aligned}$$

In Figure B.2 the relative difference between the bending stiffness for a uniform and a linear electric field is shown as a function of the thickness ratio t_{pe}/t_b . The electromechanical coupling factor (for the d_{31} effect) for the material considered in this thesis is about 0.4 (see Appendix A). The results indicate that the error introduced by the uniform electric field assumption is very small. When only a small part of the beam is covered with a piezoelectric layer, the change in the overall bending stiffness due to the assumption is even smaller than shown in the figure. Therefore, the conclusion is that the assumption of a uniform electric field is allowed.

B.3 Model for the coupled longitudinal and transverse vibrations

The frequency domain representation of the equations of motion for the coupled longitudinal and transverse vibrations of a beam with an asymmetric patch (see Section 3.3.1) is given by:

$$-\omega^2 (\rho A)_{\text{eq}} u_0 + \omega^2 \rho_{pe} Q_{pe} \frac{dw}{dx} - (EA)_{\text{eq}} \frac{d^2 u_0}{dx^2} + E_{pe} Q_{pe} \frac{d^3 w}{dx^3} = 0, \quad (\text{B.27a})$$

$$-\omega^2 (\rho A)_{\text{eq}} w - E_{pe} Q_{pe} \frac{d^3 u_0}{dx^3} + (EI)_{\text{eq}} \frac{d^4 w}{dx^4} = 0, \quad (\text{B.27b})$$

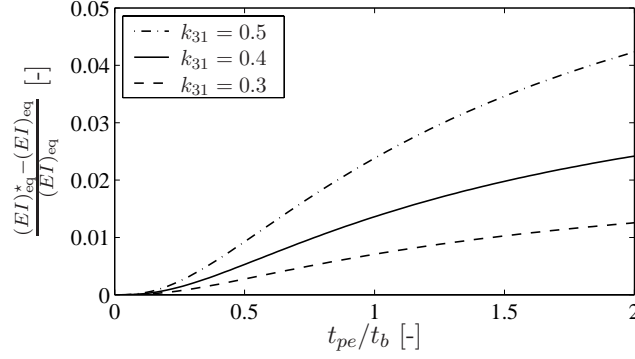


Figure B.2: Relative difference between the bending stiffness for a uniform and linear electric field versus the patch to beam thickness ratio ($E_{pe} = E_b$, $b_{pe} = b_b$).

where u_0 and w are the longitudinal and transverse displacements, respectively, of the beam mid-plane. By inserting a solution of the form:

$$u_0 = A e^{\lambda x}, \quad w = B e^{\lambda x}, \quad (\text{B.28})$$

the equations of motion reduce to the eigenvalue problem:

$$\begin{bmatrix} -k_l^2 - \lambda^2 & \frac{(\omega^2 \rho_{pe} Q_{pe} + E_{pe} Q_{pe} \lambda^2) \lambda}{(EA)_{eq}} \\ -\frac{E_{pe} Q_{pe} \lambda^3}{(EI)_{eq}} & -k_b^4 + \lambda^4 \end{bmatrix} \begin{Bmatrix} A \\ B \end{Bmatrix} = \begin{Bmatrix} 0 \\ 0 \end{Bmatrix}. \quad (\text{B.29})$$

The off-diagonal terms represent the coupling between the longitudinal and transverse vibrations. The non-trivial solutions of this equation can be solved from the characteristic equation:

$$(k_1 - 1) \lambda^6 + (k_2 - k_l^2) \lambda^4 + k_b^4 \lambda^2 + k_l^2 k_b^4 = 0, \quad (\text{B.30})$$

where

$$\begin{aligned} k_l^2 &= \omega^2 \frac{(\rho A)_{eq}}{(EA)_{eq}}, & k_b^4 &= \omega^2 \frac{(\rho A)_{eq}}{(EI)_{eq}}, \\ k_1 &= \frac{E_{pe}^2 Q_{pe}^2}{(EA)_{eq} (EI)_{eq}}, & k_2 &= \omega^2 \frac{\rho_{pe} E_{pe} Q_{pe}^2}{(EA)_{eq} (EI)_{eq}}. \end{aligned}$$

Note that k_l and k_b are the longitudinal and flexural wave numbers for the uncoupled problem. The characteristic equation has six roots, i.e. three conjugate pairs. For each root λ_i of the characteristic equation, the integration

coefficient A_i is related to coefficient B_i by the scalar α_i . The general solutions for the longitudinal and transverse vibrations can be written as:

$$u_0 = \sum_{i=1}^6 \alpha_i B_i e^{\lambda_i x}, \quad w = \sum_{i=1}^6 B_i e^{\lambda_i x}, \quad (\text{B.31})$$

where

$$\alpha_i = \frac{(EI)_{\text{eq}}(\lambda_i^4 - k_b^4)}{E_{pe} Q_{pe} \lambda_i^3}. \quad (\text{B.32})$$

The dynamic stiffness matrix for the coupled vibration model is derived similarly to the analysis presented in Section B.1. In this case the nodal DOF vector and nodal load vector are defined as:

$$\mathbf{w} = \begin{Bmatrix} u_i \\ w_i \\ \theta_i \\ u_{i+1} \\ w_{i+1} \\ \theta_{i+1} \end{Bmatrix}, \quad \mathbf{f} = \begin{Bmatrix} N_i \\ f_i \\ M_i \\ N_{i+1} \\ f_{i+1} \\ M_{i+1} \end{Bmatrix}, \quad (\text{B.33})$$

where u_i and N_i are longitudinal displacement and normal force, respectively, at node i . The sign convention for this element is shown in Figure B.3.

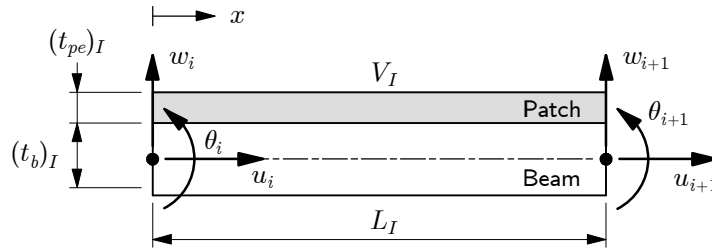


Figure B.3: Sign convention for a DSM element.

B.3.1 Test case

As a next step, the model for the coupled longitudinal and transverse vibrations is compared with the “uncoupled” model of Section B.1, which only describes the transverse vibration. The setup consists of an aluminium strip ($490 \times 30 \times 1.2$ mm) with two asymmetric bonded patches (see Figure B.4).

The patches have equal size ($l_{pe} \times 30 \times 1.2$ mm) and material properties. One patch is a voltage driven actuator (prescribed voltage) and the second patch is a voltage sensor (zero charge). The material properties of the strip and the patches can be found in Table 3.2.

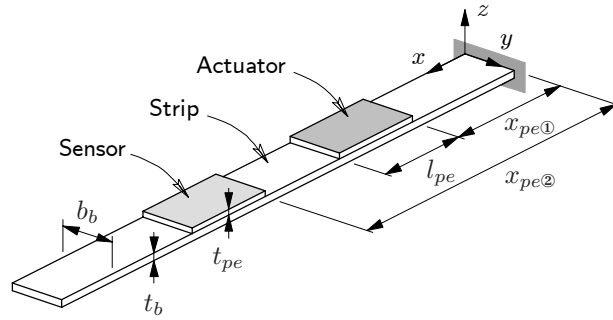


Figure B.4: Strip with two surface bonded patches.

In Figures B.5 and B.6 the results of a frequency domain analysis are presented for two configurations of the patches. The strip is clamped on *one* side. In the first configuration (Figure B.5) the patch lengths are relatively small compared to the strip length ($l_{pe} = 50$ mm) and in the second configuration (Figure B.6) the patches cover most of the strip surface ($l_{pe} = 200$ mm). The placement of the patches is given in Table B.2.

	l_{pe}	x_{pe1}	x_{pe2}	boundary condition
Figure B.5	50	130	310	clamped-free
Figure B.6	200	30	260	clamped-free
Figure B.7	50	130	310	clamped-clamped
Figure B.8	200	30	260	clamped-clamped

Table B.2: Patch lengths and locations (in mm).

In Figures B.5 and B.6 the FRF from the actuator voltage V_1 to the transverse tip displacement u_z , and the FRF from the actuator voltage to the sensor voltage V_2 are shown. In each subfigure the FRFs calculated with the coupled model (black solid line) and the uncoupled model (black dash-dotted line) are compared. The *coupled model* refers to the model for the coupled longitudinal and transverse vibrations and *uncoupled model* refers to the model where the longitudinal vibration is eliminated by assuming that the normal force is zero. For completeness, also the FRFs calculated with a *two-dimensional* FEM model are included in the results (gray solid line). The FEM model

describes the coupled longitudinal and transverse vibration. The FEM model is evaluated in the frequency range up to 1000 Hz, where the model is valid for the chosen discretization. More details on the numerical model can be found in Chapter 4.

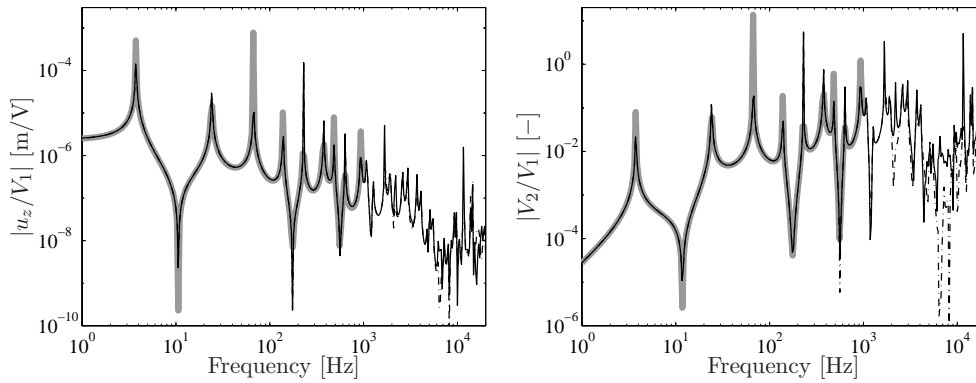


Figure B.5: FRFs calculated with the coupled model (—), uncoupled model (-----), and FEM model (—) for $l_{pe} = 50$ mm. The strip is clamped on *one* side.

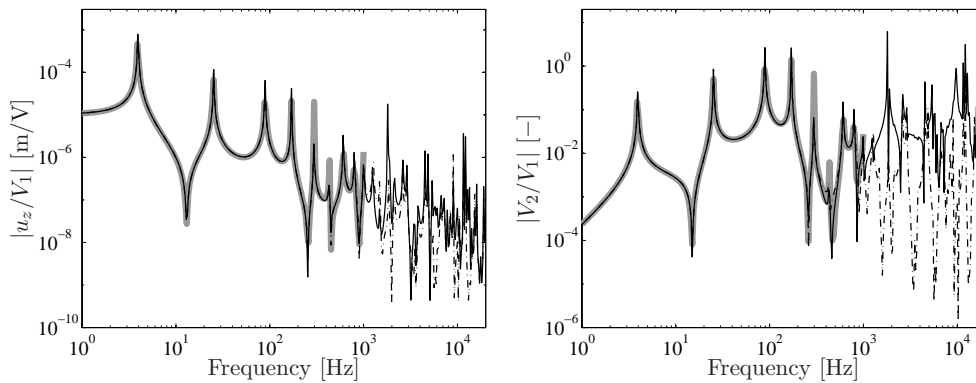


Figure B.6: FRFs calculated with the coupled model (—), uncoupled model (-----), and FEM model (—) for $l_{pe} = 200$ mm. The strip is clamped on *one* side.

As shown in Figures B.5 and B.6, there is a good correspondence between the FRFs predicted by the uncoupled and coupled model in the low frequency range. These results are furthermore in good agreement with the FEM results. At higher frequencies (> 1000 Hz), clear discrepancies between the uncoupled and coupled models are found, which are more pronounced for the configuration with large patches. It is noted that no damping is included in the models. Therefore, the differences between the levels of the FRFs close to

an eigenfrequency are mainly due the different discretizations of the frequency range.

It is important to note that the correspondence between the uncoupled and coupled model depends on the type of boundary condition. For the case that the strip is clamped on *both* sides, results are shown in Figures B.7 and B.8. In this case the transverse displacement of the strip at $x = x_{pe\otimes} + l_{pe}$ is considered rather than the the tip displacement. Now also in the low frequency range discrepancies between the coupled and uncoupled model can be observed, especially if the patches are large compared to the strip length. Still, the dynamical behaviour is accurately predicted by the uncoupled model if only a small part of the strip is covered with patches.

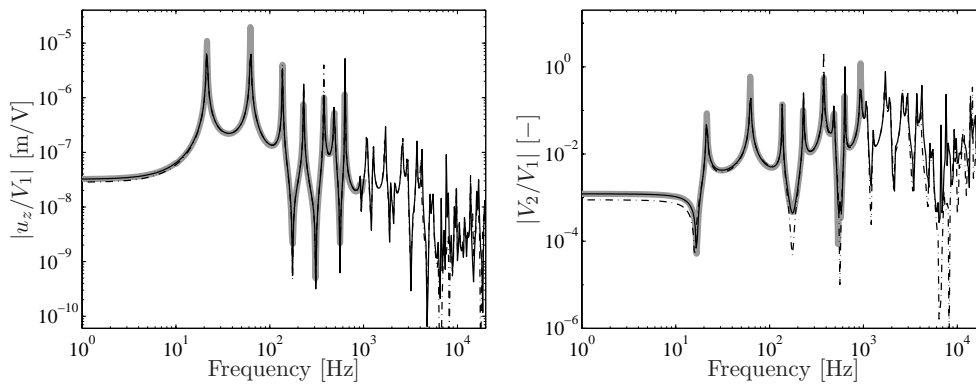


Figure B.7: FRFs calculated with the coupled model (—), uncoupled model (----) and FEM model (—) for $l_{pe} = 50$ mm. The strip is clamped on *both* sides.

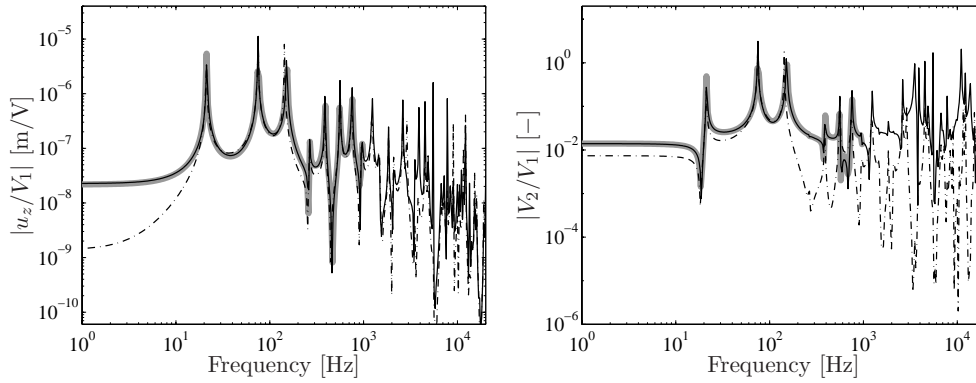


Figure B.8: FRFs calculated with the coupled model (—), uncoupled model (----) and FEM model (—) for $l_{pe} = 200$ mm. The strip is clamped on *both* sides.

Appendix C

A Plate with Surface Bonded Patches

C.1 Analytical model

In this section an analytical model of a plate with surface bonded piezoelectric patches is presented. The analysis is similar to the work of Dimitriadis, Fuller and Rogers [32] who considered the excitation of a simply supported plate by two patches bonded symmetrically on opposite sides of the plate. They determined the loads induced by the actuator pair with a static analysis, and used these results in an approximate dynamical analysis, in which the mass and stiffness of the pair were neglected. The same approach is applied here for a plate with asymmetrically bonded patches, which can serve either as actuator or sensor (see Figure C.1). An approximate dynamical model is derived for the

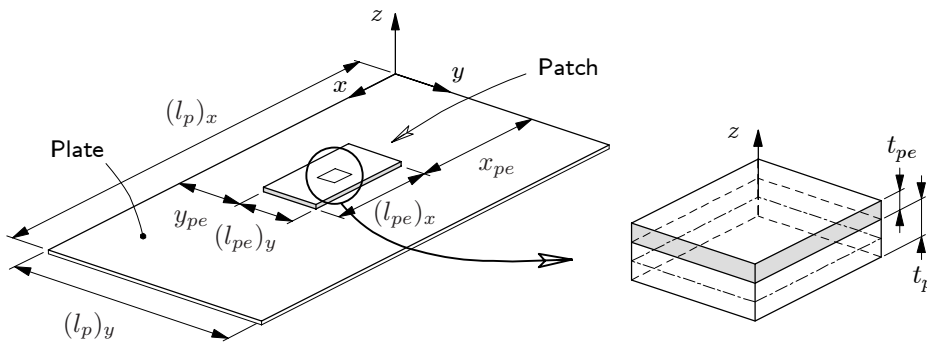


Figure C.1: A rectangular plate with a surface bonded patch (coordinate z is measured from the plate mid-plane).

transverse vibration of a plate with one or more PZT patches. The following assumptions are used:

- *Kirchhoff hypothesis*: a plane through the plate and patch perpendicular to the mid-plane of the plate remains straight and perpendicular to the mid-plane during deformation. Therefore, the strain is continuous at the bonding layer, i.e. *perfect bonding* is assumed.
- The electric field across the thickness of the patch is uniform.
- The plate and piezoelectric materials are homogeneous in the x - y plane.
- The mass and stiffness loading introduced by a patch is small.

In Chapter 4 the dynamic stiffness matrix method was applied to model beam-like structures with surface bonded patches. This method can not be used for plate-like problems, since no exact solution of the governing equation of motion is available. Therefore, an alternative model is derived, which does not account for the mass and stiffness of the patches.

The equation of motion for the transverse plate vibration is given by:

$$\rho_p t_p \frac{\partial^2 w}{\partial t^2} + \frac{E_p t_p^3}{12(1-\nu_p^2)} \left(\frac{\partial^2 w}{\partial x^4} + 2 \frac{\partial^4 w}{\partial x^2 \partial y^2} + \frac{\partial^4 w}{\partial y^4} \right) = f, \quad (\text{C.1})$$

where w is the plate mid-plane displacement in the transverse direction, ρ_p is the density of the plate material, t_p is the plate thickness, and f is an external distributed load on the plate. This equation follows from classical plate theory, i.e. the Kirchhoff hypothesis is used, and shear effects and rotary inertia effects are neglected.

The mode superposition method is used to solve equation (C.1). It is assumed that the solution is of the form:

$$w = \sum_{m=1}^{\infty} \sum_{n=1}^{\infty} \psi_{mn} q_{mn}, \quad (\text{C.2})$$

where ψ_{mn} are the mode shapes of the plate, q_{mn} are the mode participation factors, and m and n define the number of half waves in the x - and y -directions. When the modal expansion (C.2) is substituted into equation (C.1), and the result is multiplied by ψ_{mn} and integrated over the plate area S , a set of $m \times n$ uncoupled ordinary differential equations is obtained:

$$\Lambda_{mn} \ddot{q}_{mn} + \Lambda_{mn} \omega_{mn}^2 q_{mn} = r_{mn}, \quad (\text{C.3})$$

where ω_{mn} are the eigenfrequencies, and

$$\Lambda_{mn} = \int_S \rho_p t_p \psi_{mn}^2 dS, \quad (\text{C.4a})$$

$$r_{mn} = \int_S f(x, y) \psi_{mn} dS, \quad (\text{C.4b})$$

are the generalised masses and generalised loads, respectively. Equation (C.3) describes the structural vibration of the plate. The electromechanical interaction due to the piezoelectric effect is determined with a static analysis.

Plate loading

In the analysis that follows the indices p and pe refer to a variables related to the plate and piezoelectric patch, respectively. The linear strain field in the plate and the patch associated with the Kirchhoff hypothesis is given by:

$$\epsilon_{11} = \frac{\partial u_0}{\partial x} - z \frac{\partial^2 w}{\partial x^2} = \epsilon_{11}^0 - z \kappa_{11}, \quad (\text{C.5a})$$

$$\epsilon_{22} = \frac{\partial v_0}{\partial y} - z \frac{\partial^2 w}{\partial y^2} = \epsilon_{22}^0 - z \kappa_{22}, \quad (\text{C.5b})$$

$$\epsilon_{12} = \frac{1}{2} \left(\frac{\partial u_0}{\partial y} + \frac{\partial v_0}{\partial x} \right) - z \frac{\partial^2 w}{\partial x \partial y} = \epsilon_{12}^0 - z \kappa_{12}. \quad (\text{C.5c})$$

where u_0 , v_0 and w are the displacements of plate mid-plane in the x -, y - and z -directions, respectively, ϵ_{11}^0 , ϵ_{22}^0 and ϵ_{12}^0 are the mid-plane membrane strains, and κ_{11} , κ_{22} and κ_{12} are the curvatures. The uniform electric field across the thickness of the patch is described by:

$$E_3 = -\frac{V}{t_{pe}}, \quad (\text{C.6})$$

where V is the voltage across the electrodes and t_{pe} is the patch thickness. With the linear constitutive equations for plane stress, the stress field in the patch can be written as:¹

$$\begin{Bmatrix} \sigma_{11}^{pe} \\ \sigma_{22}^{pe} \\ \sigma_{12}^{pe} \end{Bmatrix} = \frac{E_{pe}}{1-\nu_{pe}^2} \begin{bmatrix} 1 & \nu_{pe} & 0 \\ \nu_{pe} & 1 & 0 \\ 0 & 0 & 1-\nu_{pe} \end{bmatrix} \left(\begin{Bmatrix} \epsilon_{11}^0 \\ \epsilon_{22}^0 \\ \epsilon_{12}^0 \end{Bmatrix} - \begin{Bmatrix} \kappa_{11} \\ \kappa_{22} \\ \kappa_{12} \end{Bmatrix} z \right) + \frac{E_{pe}}{1-\nu_{pe}} \begin{Bmatrix} 1 \\ 1 \\ 0 \end{Bmatrix} \epsilon_{pe}, \quad (\text{C.7})$$

¹In the model by Dimitriadis et al. [32] the stresses in the patch are assumed to have the same slope as in the plate. Consequently, the strains in the plate and patch have different slopes if the materials have different elastic properties. The present model does not make the constant stress slope assumption, as in the model presented by Kim and Jones [33].

where $\epsilon_{pe} = d_{31}V/t_{pe}$ is the free piezoelectric strain, E_{pe} is the Young's modulus, and ν_{pe} is Poisson's ratio (in-plane). The free piezoelectric strain ϵ_{pe} is equal in the x - and y -directions because the material is assumed to be homogeneous in the x - y plane ($d_{31} = d_{32}$). The stress field in the plate is described by a similar set of equations, but without piezoelectric coupling.

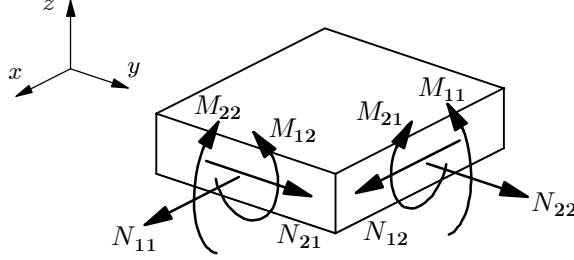


Figure C.2: Forces and moments in a Kirchhoff plate.

The stresses acting on a part of the plate with patch are equivalent with a set of forces $\mathbf{n} = \{N_{11}, N_{22}, N_{12}\}^T$ and moments $\mathbf{m} = \{M_{11}, M_{22}, M_{12}\}^T$, for which the positive senses are shown in Figure C.2. Integration of the stresses with respect to the z -coordinate gives a relation of the form:

$$\begin{Bmatrix} \mathbf{n} \\ \mathbf{m} \end{Bmatrix} = \begin{bmatrix} \mathbf{A} & \mathbf{B} \\ \mathbf{B} & \mathbf{C} \end{bmatrix} \begin{Bmatrix} \boldsymbol{\epsilon}_0 \\ \boldsymbol{\kappa} \end{Bmatrix} + \begin{Bmatrix} \mathbf{d} \\ \mathbf{e} \end{Bmatrix} \epsilon_{pe}, \quad (\text{C.8})$$

where $\boldsymbol{\epsilon}_0 = \{\epsilon_{11}^0, \epsilon_{22}^0, \epsilon_{12}^0\}^T$ and $\boldsymbol{\kappa} = \{\kappa_{11}, \kappa_{22}, \kappa_{12}\}^T$. For the case of static equilibrium in the absence of external loads, i.e. $\mathbf{n} = \mathbf{0}$ and $\mathbf{m} = \mathbf{0}$, equations (C.8) can be solved for the unknowns $\boldsymbol{\epsilon}_0$ and $\boldsymbol{\kappa}$. The resulting deformation is equal in the x - and y -directions:

$$\epsilon_{11}^0 = \epsilon_{22}^0 = C_\epsilon \epsilon_{pe}, \quad \kappa_{11} = \kappa_{22} = C_\kappa \epsilon_{pe}, \quad (\text{C.9})$$

where

$$C_\epsilon = \frac{-(t_p^2 + \beta^{-1}t_{pe}^2)}{(\beta + 4)t_p^2 + 6t_pt_{pe} + (\beta^{-1} + 4)t_{pe}^2}, \quad (\text{C.10a})$$

$$C_\kappa = \frac{6(t_p + t_{pe})}{(\beta + 4)t_p^2 + 6t_pt_{pe} + (\beta^{-1} + 4)t_{pe}^2}, \quad (\text{C.10b})$$

and

$$\beta = \frac{E_pt_p(1 - \nu_{pe})}{E_{pe}t_{pe}(1 - \nu_p)}. \quad (\text{C.11})$$

It can be seen in equation (C.7) that the electric field does not couple to the shear deformation, so $\epsilon_{12}^0 = 0$ and $\kappa_{12} = 0$.

The loads induced in the plate are found by integration of the stresses in equation (C.9) over the plate thickness. For a patch that covers only a part of the plate the induced loads can be written as [32]:

$$N_{pe} = \frac{E_p t_p}{1 - \nu_p} C_\epsilon \epsilon_{pe} [\text{h}(x - x_1) - \text{h}(x - x_2)] [\text{h}(y - y_1) - \text{h}(y - y_2)], \quad (\text{C.12a})$$

$$M_{pe} = \frac{E_p t_p^3}{12(1 - \nu_p)} C_\kappa \epsilon_{pe} [\text{h}(x - x_1) - \text{h}(x - x_2)] [\text{h}(y - y_1) - \text{h}(y - y_2)], \quad (\text{C.12b})$$

where $\text{h}(\cdot)$ is the unit step function, and

$$\begin{aligned} x_1 &= x_{pe}, & x_2 &= x_{pe} + (l_{pe})_x, \\ y_1 &= y_{pe}, & y_2 &= y_{pe} + (l_{pe})_y, \end{aligned} \quad (\text{C.13})$$

define the location and the size of the patch (see Figure C.1). An electric field across the patch induces a normal force distribution N_{pe} and moment distribution M_{pe} , which are equal in the x and y -direction and exist only in the proximity of the patch. The normal force distribution does not contribute to the transverse vibration of the plate and is therefore not further discussed. The forcing term in the equation of motion (C.1) is related to the moment distribution (C.12b) by [32]:

$$f = \frac{\partial^2 M_{pe}}{\partial x^2} + \frac{\partial^2 M_{pe}}{\partial y^2}, \quad (\text{C.14})$$

where

$$\frac{\partial^2 M_{pe}}{\partial x^2} = \frac{E_p t_p^3 C_\kappa}{12(1 - \nu_p)} \epsilon_{pe} [\delta'(x - x_1) - \delta'(x - x_2)] [\text{h}(y - y_1) - \text{h}(y - y_2)], \quad (\text{C.15a})$$

$$\frac{\partial^2 M_{pe}}{\partial y^2} = \frac{E_p t_p^3 C_\kappa}{12(1 - \nu_p)} \epsilon_{pe} [\text{h}(x - x_1) - \text{h}(x - x_2)] [\delta'(y - y_1) - \delta'(y - y_2)], \quad (\text{C.15b})$$

and $\delta'(\cdot)$ is the spatial derivative of the Dirac delta function. The load defined by equations (C.14) and (C.15) is equivalent with external line moments acting along the boundaries of the patch [32]. In the same way the excitation for in-plane vibration can be represented by line forces along the boundaries of the patch. A similar conclusion was drawn in Chapter 3 for the beam model.

Surface charge

Once the mode participation factors are known the plate response can be calculated with equation (C.2), using a limited number of modes in the expansion. It is furthermore possible to calculate the charges on the electrodes. The surface charge is obtained by integration of the electric flux density D_3 over the electrode area. For a Kirchhoff strain field and a uniform electric field the electric flux density can be written as:

$$D_3 = \frac{d_{31}E_{pe}}{1-\nu_{pe}} \left(\{1 \ 1 \ 0\} \left(\begin{Bmatrix} \epsilon_{11}^0 \\ \epsilon_{22}^0 \\ \epsilon_{12}^0 \end{Bmatrix} - \begin{Bmatrix} \kappa_{11} \\ \kappa_{22} \\ \kappa_{12} \end{Bmatrix} z \right) - \frac{1-2k_{31}^2}{k_{31}^2} \epsilon_{pe} \right), \quad (\text{C.16})$$

where $k_{31} = d_{31} \sqrt{E_{pe}/\epsilon_{33}^\sigma(1-\nu_{pe})}$ is the electromechanical coupling factor. The electric flux density is a function of both the mid-plane membrane strains and the curvatures. When it is assumed that the in-plane inertia forces and the in-plane external loads are small, the normal membrane strains can be expressed in terms of the curvatures and the free piezoelectric strain:

$$\epsilon_{ii}^0 = \frac{t_p + t_{pe}}{2(\beta + 1)} \kappa_{ii} - \frac{1}{\beta + 1} \epsilon_{pe}, \quad i = 1, 2. \quad (\text{C.17})$$

As for the beam model, the surface charge is evaluated using the *averaged* electric flux density. When equation (C.17) is substituted into equation (C.16) and the result is averaged over the thickness of the patch, the result is:

$$\bar{D}_3 = -\frac{d_{31}E_{pe}}{1-\nu_{pe}} \left[\frac{t_p + t_{pe}}{2} \frac{\beta}{\beta + 1} (\kappa_{11} + \kappa_{22}) + \left(\frac{1-2k^2}{k^2} + \frac{2}{\beta + 1} \right) \epsilon_{pe} \right]. \quad (\text{C.18})$$

By integration of this expression with respect to the electrode surface the surface charge Q is obtained:

$$Q = \int_{y_1}^{y_2} \int_{x_1}^{x_2} \bar{D}_3 \, dx \, dy. \quad (\text{C.19})$$

C.2 Numerical model: ANSYS implementation

In this work the commercial finite element program ANSYS was used. Unfortunately, no plate elements with piezoelectric capabilities are available in ANSYS [49]. The element types available for the modelling of strip-like and plate-like structures with piezoelectric patches are shown in Figure C.3. Two element types with piezoelectric capabilities are available: a two-dimensional

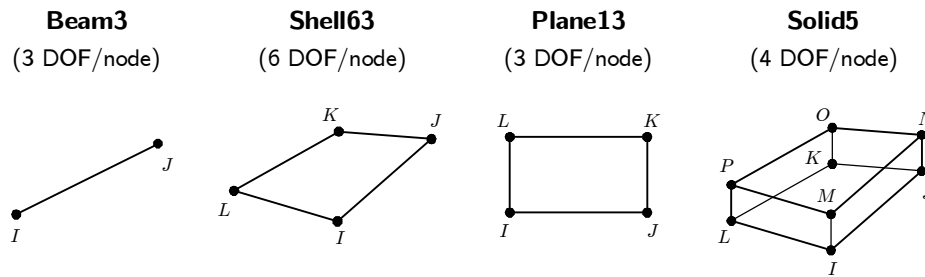


Figure C.3: Element types used to model beam or plate structures with patches.

four-node solid element (Plane13) and a three-dimensional eight-node solid element (Solid5). In ANSYS so-called extra shape functions are included to enhance the accuracy of solid elements in bending problems [50].

In Figure C.4 part of a FEM model representing a flat plate with a surface bonded rectangular patch is shown. The plate is modelled by four-node plate elements (Shell63), where each node has six DOF, i.e. three displacements and three rotations. The nodes of the piezoelectric solid elements (Solid5) each have four DOF, i.e. three displacements and the electric potential. Two-dimensional beam or strip problems can be modelled in ANSYS in a similar way with two-node beam elements (Beam3) and the two-dimensional piezoelectric elements (Plane13).

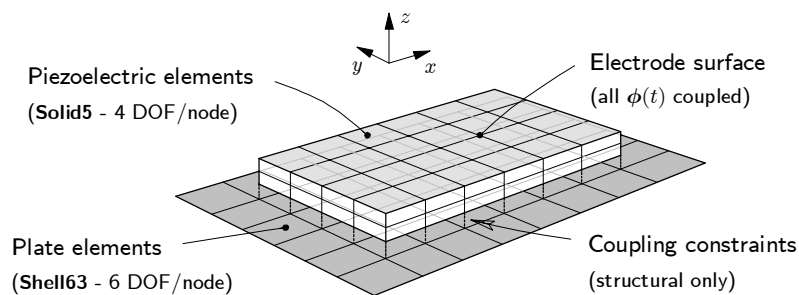


Figure C.4: Part of a FEM model of a plate with surface bonded patch.

The plate elements are defined in the plane corresponding with the mid-plane of the plate. Because the patch is bonded to the surface of the plate, there is an offset between the plate and piezoelectric elements, which is equal to half the plate thickness. The plate and piezoelectric elements are coupled with constraint equations. In order to make this an easy procedure, the mesh is such that the in-plane coordinates of the nodes defining the plate and piezoelectric elements are equal. For each node on the bottom side of the patch and the

corresponding node on the plate surface, the following *constraint equations* are introduced (see Figure C.5):

$$(u_{pe})_x = (u_p)_x + (\theta_p)_y t_p/2, \quad (\text{C.20a})$$

$$(u_{pe})_y = (u_p)_y - (\theta_p)_x t_p/2, \quad (\text{C.20b})$$

$$(u_{pe})_z = (u_p)_z. \quad (\text{C.20c})$$

In this equation u_p and θ_p denote the displacements and rotations of a node on the plate, u_{pe} refers to the displacements of the corresponding node on the patch, and t_p is the plate thickness.

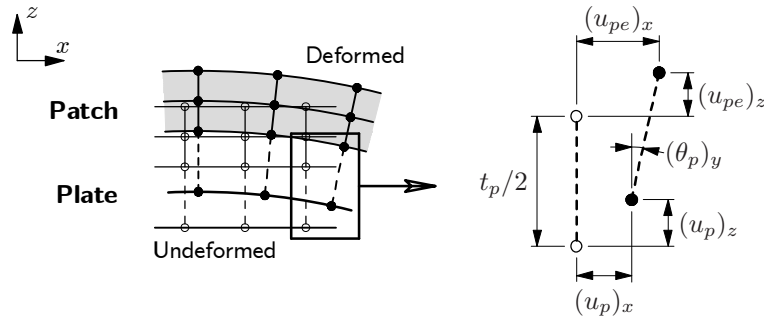


Figure C.5: Graphical representation (two-dimensional) of constraint equations (C.20) for coupling of plate and piezoelectric solid elements.

The electrodes on the top and bottom surfaces of a patch are very thin compared to the thickness of the piezoelectric material. It is therefore not necessary to account for the stiffness and mass introduced by the electrodes. The uniform distribution of the electric potential on an electrode is described in the FEM model by *equality constraints*, i.e. the electric potential of all nodes on a surface representing an electrode are coupled. If such an electrode is furthermore grounded, then the potential is set to zero.

C.3 Comparison

The analytical model presented in Section C.1 is used for validation of the “structural model” introduced in Chapter 4. The test case consists of a *simply supported* plate with two surface bonded patches, see Figure C.6. One patch is a voltage driven actuator and the other patch is a voltage sensor. The setup is equal to the one considered in Section 4.4.1, except that the plate is simply supported along all of its edges (rather than clamped). The two patches have

equal size ($50 \times 30 \times t_{pe}$ mm) and equal material properties. More details about this setup can be found in Figure 4.9.

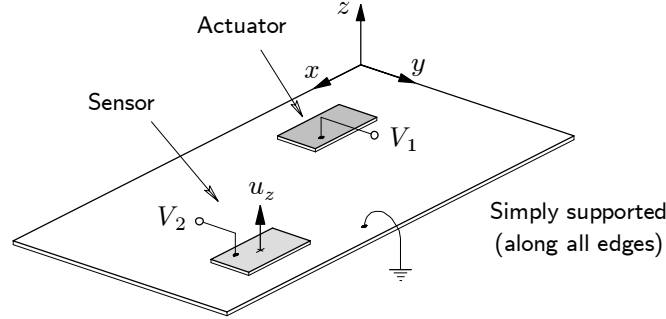


Figure C.6: Simply supported plate with two surface bonded patches.

For a plate with simply supported boundary conditions the mode shapes are given by:

$$\psi_{mn} = \sin(k_m x) \sin(k_n y), \quad (\text{C.21})$$

where $k_m = m\pi/(l_p)_x$ and $k_n = n\pi/(l_p)_y$. The corresponding eigenfrequencies are given by:

$$\omega_{mn} = (k_m^2 + k_n^2) \sqrt{\frac{E_p t_p^2}{12\rho_p(1-\nu_p^2)}}. \quad (\text{C.22})$$

For the simply supported boundary conditions, the generalised loads become:

$$r_{mn} = -\frac{E_p t_p^3}{1-\nu_p} C_\kappa \epsilon_{pe} \frac{k_m^2 + k_n^2}{k_m k_n} [\cos(k_m x_1) - \cos(k_m x_2)] [\cos(k_n y_1) - \cos(k_n y_2)]. \quad (\text{C.23})$$

The definitions of C_κ , x_1 , x_2 , y_1 and y_2 is given in equations (C.10) and (C.13). Equation (C.23) indicates that a mode can not be excited by an actuator patch if the edges of the patch are symmetrically with respect to a nodal line. For instance, a patch located at the center of the plate can excite only the even-even modes, i.e. 1-1, 3-1, 3-3, etc..

The analytical and numerical model are compared by means of two frequency response functions: the FRF from the actuator voltage V_1 to the normal sensor displacement u_z (i.e. the transverse displacement of the center of the patch) and the FRF from the actuator voltage to the sensor voltage V_2 . In Figures C.7 and C.8 these FRFs are shown for the cases that the thickness

of the patches is 0.1 mm and 1.0 mm, respectively. There is a good agreement between the results if the patches are thin compared to the plate (i.e. $t_{pe} = 0.1$ mm). However, if the thickness of the patches is comparable to the plate thickness (i.e. $t_{pe} = 1.0$ mm), the agreement between the FRFs corresponding to the analytical and numerical models is less. The discrepancies between the results are due to mass and stiffness of the patches, which are not accounted for in the analytical model.

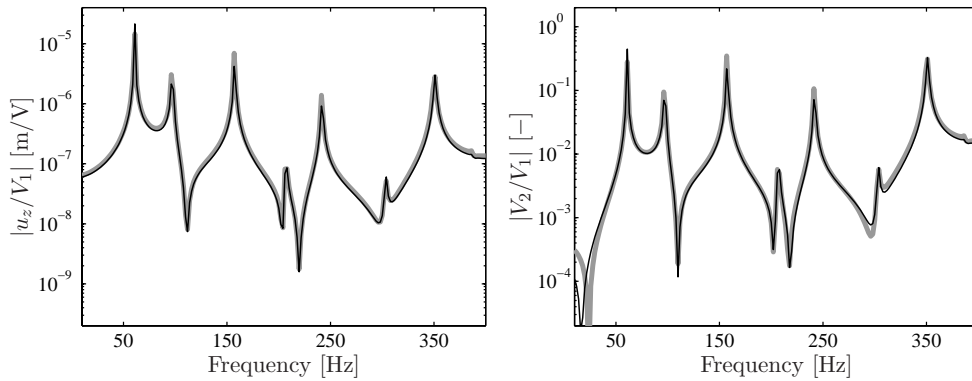


Figure C.7: FRFs for analytical (—) and numerical (---) models for $t_{pe} = 0.1$ mm.

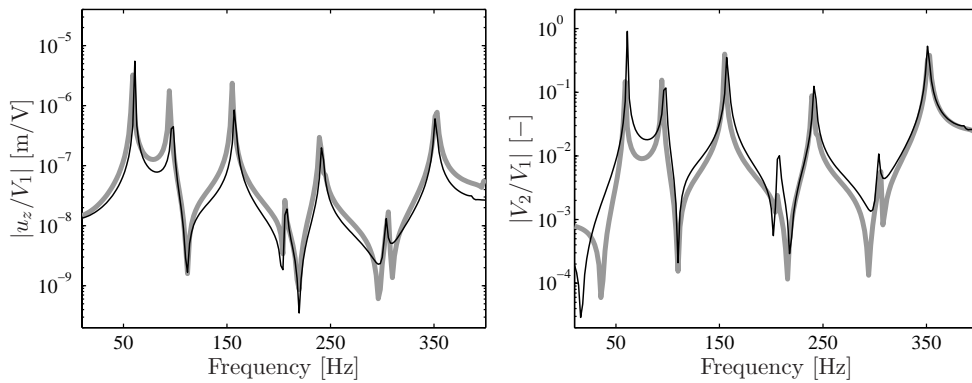


Figure C.8: FRFs for analytical (—) and numerical (---) models for $t_{pe} = 1.0$ mm.

Appendix D

Radiation Filters

A number of methods for capturing the sound radiation behaviour into a state space model have been reported in the literature. Such a model is referred to as a *radiation filter*. The radiation filter can be appended to the state space model of the structure yielding an efficient analysis tool for designing (modern) control systems and also to simulate the performance of various control strategies. Furthermore, a radiation filter enables the real-time implementation of sensing strategies for sound power estimation with structural or acoustic error sensors.

Baumann, Saunders and Robertshaw [61] introduced the idea of a radiation filter. They used a description of the sound power in terms of the *structural* modes to develop the radiation filter. More recently, Gibbs, Clark, Cox and Viperman [62] introduced an alternative approach termed *radiation modal expansion*. In contrast to the work of Baumann et al., they used a description of the sound power in terms of the *radiation* modes to create the radiation filter. These two approaches are discussed briefly in this appendix.

D.1 Derivation of the radiation filters

The general idea is to derive a state space model whose output is an estimate of the time-averaged radiated sound power. In the *frequency domain*, the sound power \bar{W} can be written as (see Section 4.3):

$$\bar{W} = \mathbf{v}_n^H \mathbf{R} \mathbf{v}_n, \quad (\text{D.1})$$

where \mathbf{R} is the radiation resistance matrix and \mathbf{v}_n is the vector with normal surface velocities of the elemental radiators. The radiation resistance matrix is evaluated at discrete frequencies. In order to predict the sound power over

a certain frequency band, the characteristics of \mathbf{R} must be captured over that band. A curve fit of each element in \mathbf{R} would lead to a very “large” state space model, which is impractical for control system design. The two approaches presented here are based on an approximation of the sound power.

In the approach followed by Baumann et al. [61], which is here referred to as “Baumann’s approach”, the basic equation is the expression of the radiated sound power in terms of the *structural* mode participation factors $\dot{\mathbf{q}}$:

$$\bar{W} = \dot{\mathbf{q}}^H \mathbf{M} \dot{\mathbf{q}}, \quad \text{where} \quad \mathbf{M} = \Psi_n^T \mathbf{R} \Psi_n, \quad (\text{D.2})$$

and Ψ_n is the matrix with the normal displacement components of the structural modes. It is important to note that the off-diagonal terms in \mathbf{M} cannot be neglected. It is possible to factorise the real, symmetric and positive definite matrix \mathbf{M} into the form $\mathbf{G}^H \mathbf{G}$, so the sound power can be written as:

$$\bar{W} = \dot{\mathbf{q}}^H \mathbf{G}^H \mathbf{G} \dot{\mathbf{q}} = \mathbf{z}^H \mathbf{z}. \quad (\text{D.3})$$

Matrix \mathbf{G} contains the frequency response functions (at discrete frequencies) of the radiation filters which operate on the mode participation factors to give \mathbf{z} . Some elements in \mathbf{G} have a small value and are set to zero to reduce the model size. As a next step, an s -domain (Laplace domain) transfer function, whose poles and zeros are located in the left half of the complex plane, is fitted to each non-zero element in \mathbf{G} to obtain $\mathbf{G}(s)$. The transfer function matrix is subsequently transformed into a state space representation. Baumann’s approach for creating a radiation filter is summarised in Figure D.1.

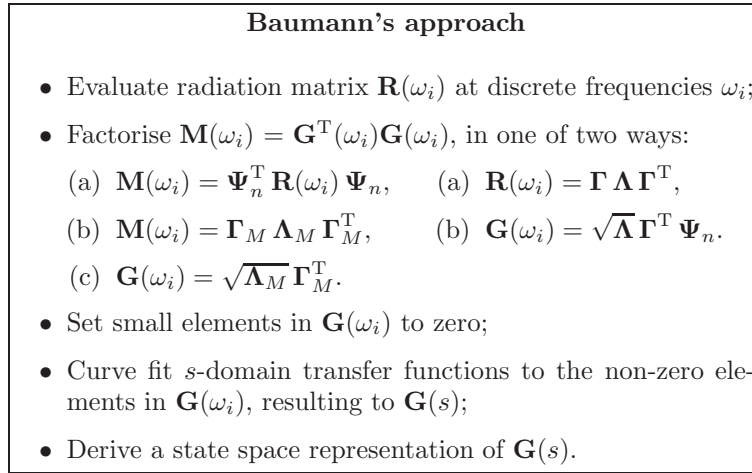


Figure D.1: Baumann’s approach for creating a radiation filter.

It is noted that there are other methods to obtain the radiation filter from \mathbf{M} than the method in Figure D.1 [61, 108].

The approach followed by Gibbs et al. [62], which is termed radiation modal expansion (RME), is based on the formulation of the sound power in terms of radiation modes and efficiencies. Because the radiation efficiencies fall off very rapidly with increasing radiation mode number, only a small number of radiation modes must be taken into account to accurately predict the sound power. A drawback is that the radiation modes depend on frequency. Borgiotti and Jones [109] showed that the most efficient radiation modes below some arbitrary frequency ω_{\max} can be synthesised by a linear combination of the radiation modes at ω_{\max} . This property is used in the RME technique. The velocity of the elemental radiators is written as $\mathbf{v}_n = \mathbf{\Gamma}_{\max} \tilde{\mathbf{a}}$, where $\mathbf{\Gamma}_{\max}$ is the matrix with a small number of radiation modes at frequency ω_{\max} . With substitution of this expression, the sound power can be written as:

$$\bar{W} = \tilde{\mathbf{a}}^H \tilde{\mathbf{\Lambda}} \tilde{\mathbf{a}}, \quad \text{where} \quad \tilde{\mathbf{\Lambda}} = \mathbf{\Gamma}_{\max}^T \mathbf{R} \mathbf{\Gamma}_{\max}. \quad (\text{D.4})$$

The radiation modes at ω_{\max} are not orthogonal with respect to the radiation modes at any other frequency. Therefore $\tilde{\mathbf{\Lambda}}$ is not a diagonal matrix (for $\omega \neq \omega_{\max}$). However, Gibbs et al. [62] assume that the contribution of the off-diagonal terms to the sound power is negligible. They denote the diagonal terms as the RME coefficients: $\psi_j^2 = \text{diag}(\tilde{\mathbf{\Lambda}})$. The corresponding approximation of the sound power is:

$$\bar{W} = \tilde{\mathbf{a}}^H \sqrt{\text{diag}(\tilde{\mathbf{\Lambda}})} \sqrt{\text{diag}(\tilde{\mathbf{\Lambda}})} \tilde{\mathbf{a}} = \mathbf{z}^H \mathbf{z}. \quad (\text{D.5})$$

In order to create the radiation filter it is only necessary to curve fit s -domain transfer functions to the RME coefficients ψ_j , and to transform the result into a state space representation. The radiation mode participation factors $\tilde{\mathbf{a}}$ are found by filtering the normal surface velocities by the matrix with “fixed frequency” radiation modes: $\tilde{\mathbf{a}} = \mathbf{\Gamma}_{\max}^T \mathbf{v}_n$. The RME approach for defining a radiation filter is summarised in Figure D.2.

It is important to note that in contrast to Baumann’s approach, RME leads to a radiation filter that only depends on the geometry, and not on other properties of the structure (e.g. material and boundary conditions). It is thus possible with RME to implement a sensing strategy for sound power estimation without using knowledge of the structure besides the geometry.

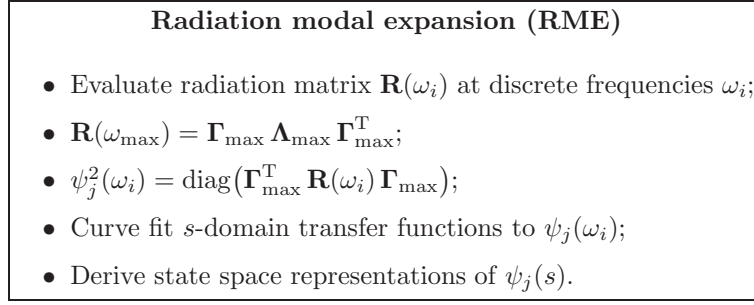


Figure D.2: Radiation modal expansion for creating a radiation filter.

D.2 Structural-acoustic model

The state space models obtained with the two approaches for designing a radiation filter have different input vectors. In Baumann's approach the input vector contains the time derivatives of the structural mode participation factors, $\dot{\mathbf{q}}(t)$. In the case of RME, the input vector contains the normal velocities of the elemental radiators $\mathbf{v}_n(t)$. For both radiation filters the input matrix and feedthrough matrix can be written in a form in which the input vector corresponds to $\mathbf{x}(t) = \{\mathbf{q}(t), \dot{\mathbf{q}}(t)\}^T$, which is the state vector of the state space representation of the structural model. Hence, the general state space representation of the radiation filter is given by:

$$\dot{\mathbf{r}}(t) = \mathbf{A}_f \mathbf{r}(t) + \mathbf{B}_f \mathbf{x}(t), \quad (\text{D.6a})$$

$$\mathbf{z}(t) = \mathbf{C}_f \mathbf{r}(t) + \mathbf{D}_f \mathbf{x}(t). \quad (\text{D.6b})$$

The length of the state vector $\mathbf{r}(t)$ is determined by the number of included structural or radiation modes, and the order of the s -domain transfer functions used for curve fitting. In the case of Baumann's approach, also the criterion for setting an element in \mathbf{G} to zero determines the number of states in the model. The time-averaged value of $\mathbf{z}(t)^T \mathbf{z}(t)$ is equal to the radiated sound power.

The radiation filter can be combined with the state space representation of the structural model to obtain a system model accounting for the structural-acoustic coupling. The state space model of the structure with piezoelectric patches is given by (see Section 4.2.4):

$$\dot{\mathbf{x}}(t) = \mathbf{A} \mathbf{x}(t) + \mathbf{B} \mathbf{v}(t), \quad (\text{D.7a})$$

$$\mathbf{y}(t) = \mathbf{C} \mathbf{x}(t) + \mathbf{D} \mathbf{v}(t), \quad (\text{D.7b})$$

where $\mathbf{v}(t)$ is the input vector (structural forces, voltage/charge driven actuators), and $\mathbf{y}(t)$ is the output vector (displacements, voltage/charge sensors). Equations (D.6) and (D.7) can be combined to give a state space model for the structural-acoustic system:

$$\begin{Bmatrix} \dot{\mathbf{x}}(t) \\ \dot{\mathbf{r}}(t) \end{Bmatrix} = \begin{bmatrix} \mathbf{A} & \mathbf{0} \\ \mathbf{B}_f & \mathbf{A}_f \end{bmatrix} \begin{Bmatrix} \mathbf{x}(t) \\ \mathbf{r}(t) \end{Bmatrix} + \begin{bmatrix} \mathbf{B} \\ \mathbf{0} \end{bmatrix} \mathbf{v}(t), \quad (\text{D.8a})$$

$$\begin{Bmatrix} \mathbf{y}(t) \\ \mathbf{z}(t) \end{Bmatrix} = \begin{bmatrix} \mathbf{C} & \mathbf{0} \\ \mathbf{D}_f & \mathbf{C}_f \end{bmatrix} \begin{Bmatrix} \mathbf{x}(t) \\ \mathbf{r}(t) \end{Bmatrix} + \begin{bmatrix} \mathbf{D} \\ \mathbf{0} \end{bmatrix} \mathbf{v}(t). \quad (\text{D.8b})$$

D.3 Test case

The two approaches for creating a radiation filter are compared by means of an “open-loop” frequency domain analysis of the sound power radiated by a clamped rectangular plate with two surface bonded piezoelectric patches. A detailed description of this setup can be found in Section 4.4.1. The sound power radiated by the plate (when excited by patch 1, see Figure 4.9) is estimated with radiation filters created with Baumann’s approach and RME. These results are compared to “exact” sound power, which is calculated with equation (D.1). In all three cases the structural model is identical.

A number of remarks are made regarding the implementation of the radiation filters. The starting point for both approaches was the radiation resistance matrix \mathbf{R} , which was calculated at 50 frequency steps in the range from 70 to 520 Hz. In Baumann’s approach matrix \mathbf{M} was factorised using a singular value decomposition of the radiation resistance matrix \mathbf{R} instead of a decomposition of \mathbf{M} (see Figure D.1, second bullet). It is possible to obtain \mathbf{G} in this way because the sound power is accurately predicted with a small number of radiation modes. The radiation filter was created with 6 structural modes and 5 radiation modes (the size of \mathbf{G} was 5×6). Thus, the number of structural modes included in the filter was less than the number of structural modes in the structural model. An element in \mathbf{G} was set to zero if the value of the element was less than 0.05 of the largest value in the associated row. With this criterion 13 out of 30 elements were set to zero. Using a third order transfer function to curve fit each (non-zero) element, the total number of states in the radiation filter was 51. The RME radiation filter was created with 5 radiation modes. The radiation modes at 520 Hz (highest frequency in the range of interest) were used to define the RME coefficients. With a third order transfer function to curve fit each RME coefficient, the number of states in the radiation filter was 15.

In MATLAB several procedures are available to curve fit an s -domain transfer function to frequency response data. A procedure was applied to fit a stable minimum phase transfer function to the *magnitude* of the the frequency response data (with MATLAB function `fitmag.m`, which is part of the μ -Analysis and synthesis toolbox). The resulting transfer function has (nearly) the same magnitude response as the frequency response data, but the phase response is different.

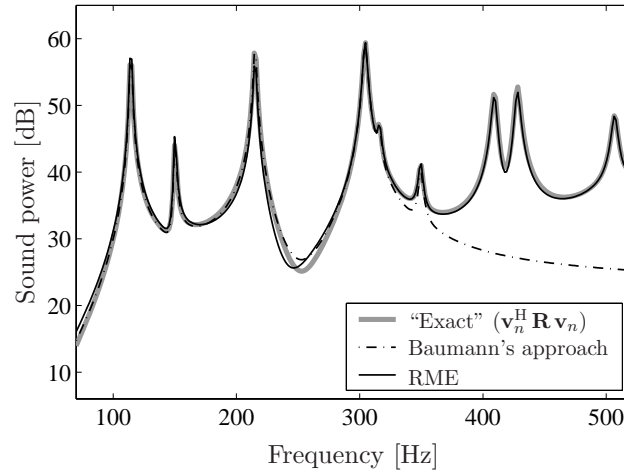


Figure D.3: Sound power estimations with Baumann’s approach and radiation modal expansion (excitation: patch 1, unit input).

The sound powers calculated with the radiation filters based on Baumann’s approach and RME are compared with the “exact” sound power in Figure D.3. It can be observed that both radiation filters give a good estimation of the sound power at low frequencies. The filter created with Baumann’s approach predicts the sound power up to the sixth resonance frequency (349 Hz) since it was constructed with six structural modes. The filter created with RME gives a good approximation of the sound power in the full range from 70 to 520 Hz. A further advantage of RME is that the radiation filter includes only 15 states, which is much less than the 51 states in the filter designed with Baumann’s approach. It is therefore concluded that RME is the more efficient technique to create a radiation filter. For the practical implementation of radiation filters in sound power sensing strategies, the radiation modes must be identified. A method to obtain these modes from experimental data is described by Berkhoff [110].

Appendix E

Adaptive Notch Filter

It is assumed that a continuous time domain signal $y(t)$ is sampled at a fixed rate to produce a sequence $y(n)$, where n is the sample number, which can only take integer values. The output from the error sensor is written as the superposition of the outputs from the primary and secondary paths (see equation (5.1)):

$$y(n) = y_d(n) + y_c(n), \quad (\text{E.1})$$

where the subscript d and c refer to the primary and secondary paths, respectively. The reference signal is defined as $x(n) = \sin(\omega_0 n)$, where $\omega_0 = T_s \omega$ and T_s is the time interval between two subsequent samples. The output from the error sensor due to the primary source operating alone can be written as:

$$y_d(n) = A_d \sin(\omega_0 n + \theta_d), \quad (\text{E.2})$$

where A_d and θ_d are the (*unknown*) amplitude and phase shift introduced by the primary path. This equation can also be written as:

$$y_d(n) = A_d \cos(\theta_d) \sin(\omega_0 n) + A_d \sin(\theta_d) \cos(\omega_0 n). \quad (\text{E.3})$$

Clearly, the output from the error sensor is zero if $y_c(n)$ has amplitude A_d and is shifted 180 degrees with respect to θ_d . The adaptive notch filter is realised using two reference signals: a sine wave and a cosine wave with a frequency equal to that of the primary excitation. The output from the digital filter, which is applied to the secondary source, is thus given by:

$$\begin{aligned} v_c(n) &= w_0(n) \sin(\omega_0 n) + w_1(n) \cos(\omega_0 n) \\ &= w_0(n) x_0(n) + w_1(n) x_1(n), \end{aligned} \quad (\text{E.4})$$

where $w_0(n)$ and $w_1(n)$ are the filter coefficients. The goal is to adjust the filter coefficients such that the output from the error sensor is cancelled. The error criterion is chosen equal to the instantaneous square of the error signal:

$$J(n) = y^2(n). \quad (\text{E.5})$$

This quantity is a quadratic function of the filter coefficients $w_0(n)$ and $w_1(n)$ and has a unique global minimum. A convenient way to converge to the optimum solution is by the steepest descent algorithm, which is given by [73]:

$$w_i(n+1) = w_i(n) - \mu x'_i(n) y(n), \quad i = 1, 2, \quad (\text{E.6})$$

where μ is the step size, which controls the convergence of the algorithm, and $x'_i(n)$ are the so-called filtered reference signals.¹ The filtered reference signals are found by passing the reference signals $x_i(n)$ through an estimate of the secondary path FRF:

$$\begin{Bmatrix} x'_0(n) \\ x'_1(n) \end{Bmatrix} = \begin{bmatrix} \hat{A}_c \cos(\hat{\theta}_c) & \hat{A}_c \sin(\hat{\theta}_c) \\ -\hat{A}_c \sin(\hat{\theta}_c) & \hat{A}_c \cos(\hat{\theta}_c) \end{bmatrix} \begin{Bmatrix} x_0(n) \\ x_1(n) \end{Bmatrix}, \quad (\text{E.7})$$

where \hat{A}_c and $\hat{\theta}_c$ are the amplitude and phase shift of the secondary path estimation at frequency ω_0 .

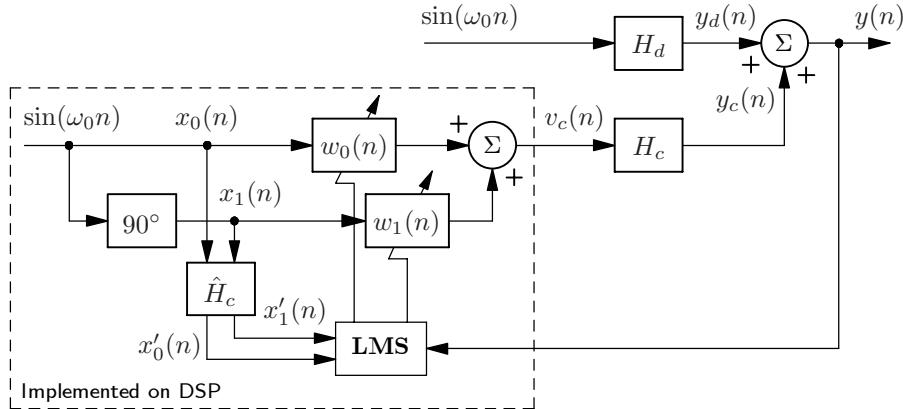


Figure E.1: Block diagram of an adaptive notch filter for narrowband feedforward control.

A block diagram representation of the adaptive notch filter is shown in Figure E.1. It is assumed that a sine wave signal generator is available on the

¹This type of algorithm is generally referred to as filtered- x LMS algorithm because the adaptation algorithm in equation (E.6) uses a “filtered” reference signal $x(n)$.

DSP. The cosine wave reference signal is obtained using a delay which corresponds to a phase shift of 90 degrees. The operation defined by equation (eqAE:update-algorithm) is performed in the block labelled with “LMS” and the new values of the filter are set accordingly. The estimation of the secondary path is denoted by \hat{H}_c . The methods for identification of the secondary path can be divided into *off-line* and *on-line* [73]. In off-line identification the secondary path is measured before operation of the active control system. This method can be used if the secondary path FRF is nearly time-invariant. However, if the secondary path is continuously changing in time, it is desirable to perform adaptive on-line identification.

The analysis of the adaptive notch filter was here restricted to the single channel case, i.e. for a control system with one secondary source and one error sensor. The extension to the multiple channel case can be found for instance in the book of Kuo and Morgan [73].

Appendix F

Description of the Genetic Algorithm

In this appendix the genetic algorithm (GA) is described in more detail. The main features of the current implementation are discussed in Section F.1. The way in which constraints are handled by the GA is addressed in Section F.2.

F.1 Genetic algorithm

A GA can be implemented in many ways. Differences between the various implementations can be found in the chromosome representation, creation of the initial population, selection function, genetic operators and termination criterion. These issues are briefly described in this section together with the choice of the GA parameter values.

F.1.1 Chromosome representation

Each individual in the population maintained by the GA is represented by a chromosome. A chromosome is made up of a sequence of genes from a certain alphabet. Each gene represents a design variable. The first GAs used a *binary* chromosome representation, i.e. the alphabet consisted of binary digits (0 or 1). However, an alphabet can also consist of floating point numbers, integers, characters, etc.. A guideline for choosing a representation is that more natural representations of the design variables are more efficient and produce better solutions. For example, for solving problems with real-valued design variables, better results are found with a floating point representation than with the binary representation [102].¹ Because the optimisation problem

of Section 7.5 is one involving real-valued design variables (i.e. the location of a patch), the current GA implementation uses a *floating point* representation. In the floating point representation each gene is a floating point number and the chromosome length is equal to the number of design variables.

F.1.2 Selection function

Selection of individuals is performed such that fitter individuals have an increased chance of being selected. A common selection approach is to assign a probability of being selected P_i to each individual i according to the fitness of the individual. The cumulative probability C_i for an individual i is:

$$C_i = \sum_{j=1}^i P_j. \quad (\text{F.1})$$

Next, a random number r between 0 and 1 is generated and compared against the cumulative probability. The individual i for which $C_i < r < C_{i+1}$ is selected. This is repeated in order to obtain a set of individuals with above average fitness (one particular can be selected more than once).

There are various methods for assigning probabilities to individuals, such as roulette wheel, linear ranking and geometric ranking. A ranking method is used here as it does not require scaling of the object function in contrast to some of the other methods. In a ranking method, the probability of being selected P_i is based on the rank of the individual i when all individuals are sorted with respect to their fitness. In *normalised geometric ranking selection*, which is the scheme used in this work, P_i is defined for each individual by:

$$P_i = \frac{q(1-q)^{R_i-1}}{1-(1-q)^N}, \quad (\text{F.2})$$

where q is a parameter between 0 and 1, N is the population size, and R_i is the rank of individual i , where one is the best. Larger values of q imply higher probabilities for fitter individuals (q is approximately the probability of selecting the best individual).

¹For converting a real-valued design variable into a binary number the design range must be discretized. The required precision determines the number of digits to describe one design variable, and thus the chromosome length.

F.1.3 Genetic operators

Genetic operators provide the basic search mechanism of the GA. The application of the genetic operators depends on the type of chromosome representation. In this subsection crossover and mutation functions based on a floating point representation are briefly described.

Crossover

From two parent chromosomes $\mathbf{x} = \{x_1, x_2, \dots, x_n\}$ and $\mathbf{y} = \{y_1, y_2, \dots, y_n\}$, with n the number of real-valued design variables (chromosome length), a crossover function produces the offspring chromosomes $\hat{\mathbf{x}}$ and $\hat{\mathbf{y}}$.

Simple crossover. The parent chromosomes are divided into two segments ($\mathbf{x} = \{\mathbf{x}_1 \mid \mathbf{x}_2\}$, where $\mathbf{x}_1 = \{x_1, \dots, x_p\}$ and $\mathbf{x}_2 = \{x_{p+1}, \dots, x_n\}$), and the offspring is created as follows:

$$\hat{\mathbf{x}} = \{\mathbf{x}_1 \mid \mathbf{y}_2\}, \quad (\text{F.3})$$

$$\hat{\mathbf{y}} = \{\mathbf{y}_1 \mid \mathbf{x}_2\}. \quad (\text{F.4})$$

The crossover point p , i.e. the point where the parent chromosomes are divided, is randomly selected.

Arithmetic crossover. The offspring are two complimentary linear combinations of the parents:

$$\hat{\mathbf{x}} = r \mathbf{x} + (1 - r) \mathbf{y}, \quad (\text{F.5})$$

$$\hat{\mathbf{y}} = (1 - r) \mathbf{x} + r \mathbf{y}, \quad (\text{F.6})$$

where r is a random number between 0 to 1.

Simple arithmetic crossover. A combination of simple crossover and arithmetic crossover:

$$\hat{\mathbf{x}} = \{\mathbf{x}_1 \mid r \mathbf{x}_2 + (1 - r) \mathbf{y}_2\}, \quad (\text{F.7})$$

$$\hat{\mathbf{y}} = \{\mathbf{y}_1 \mid (1 - r) \mathbf{x}_2 + r \mathbf{y}_2\}. \quad (\text{F.8})$$

Heuristic crossover. Assuming that \mathbf{x} has higher fitness than \mathbf{y} , a new individual is created and the best individual is maintained in the population:

$$\hat{\mathbf{x}} = \mathbf{x} + r (\mathbf{x} - \mathbf{y}), \quad (\text{F.9})$$

$$\hat{\mathbf{y}} = \mathbf{x}, \quad (\text{F.10})$$

where r is a random number between 0 to 1. Heuristic crossover differs from the previous crossover functions in two ways: the fitness of the parents is used in determining the search direction, and only one new individual is produced.

Mutation

A mutation function uses one individual $\mathbf{x} = \{x_1, x_2, \dots, x_n\}$ to produce an offspring $\hat{\mathbf{x}}$. One design variable of the parent, say x_k , is randomly selected for mutation. Let l_k and u_k be the lower and upper bound, respectively, for variable x_k .

Uniform mutation. The design variable is set to a random number within the boundaries:

$$\hat{x}_k = l_k + r(u_k - l_k), \quad (\text{F.11})$$

where r is a random number between 0 and 1.

Boundary mutation. The design variable is set equal to either its lower or upper boundary:

$$\hat{x}_k = \begin{cases} l_k & \text{if a random digit is 0,} \\ u_k & \text{if a random digit is 1.} \end{cases} \quad (\text{F.12})$$

This operator is very useful for solving problems in which the optimum is located either on or near the boundary of the search space.

Non-uniform mutation. The design variable is set equal to a random number within a range depending on the generation number:

$$\hat{x}_k = \begin{cases} x_k + (u_k - x_k) f(g) & \text{if a random digit is 0,} \\ x_k - (x_k - l_k) f(g) & \text{if a random digit is 1,} \end{cases} \quad (\text{F.13})$$

where $f(g) = r(1 - g/N)^b$, where g is the generation number, N is the total number of generations, b is a shape parameter (e.g. $b = 2$), and r is a random number between 0 and 1. Initially this operator searches the design space uniformly ($g \ll N$), but it searches more locally as the number of generations increases.

F.1.4 Initial population and termination

Two very basic methods are used to create an initial population and to terminate the GA. The initial population consists of randomly generated chromosomes, i.e. each gene is set to a random number within the boundaries of

the corresponding design variable. The criterion for terminating the GA is a specified maximum number of generations.

F.1.5 GA parameters

The values of the GA parameters used for solving the optimisation problem of Section 7.5 are given in Table F.1. The choice of these values was based on some guidelines found in the literature (e.g. reference [102]) and gave satisfactory results for some simple test problems (analytical object functions). It is generally recommended to use moderate population sizes (between 25 and 100 individuals), and to alter a relatively large portion of the chromosomes by crossover or mutation.

Crossover		Mutation		Other	
Simple	2	Uniform	1	Probability q (F.2)	0.1
Arithmetic	2	Boundary	0	Population size	30
Simple arithmetic	2	Non-uniform	2	Max. generation	50
Heuristic	4				

Table F.1: GA parameter values used for problem of Section 7.5.

In the case of a standard GA a crossover and mutation probability must be defined.² However, a slightly different type of GA was used in this work, which uses a fixed number of crossover and mutation operators. In each generation, first a specified number of (not necessarily distinct) parents with above average fitness are selected with the selection function. Next, a same number of (distinct) individuals with under average fitness are selected and removed from the population. This set is obtained with the same selection function, however with a reversed ranking order. The offspring produced with the parent chromosomes take the places of the removed individuals. This type of algorithm is referred to as the modified GA (“modGA”) in the book of Michalewicz [102] and has better performance than the standard GA, i.e. there is a smaller chance of convergence to a local optimum.

For the optimisation problem of Section 7.5, it is certain that the optimum is not near the boundary of the search space. Hence, the number of boundary mutations was set to zero.

²The crossover probability denotes the chance that a *chromosome* undergoes crossover, whereas the mutation probability denotes the chance that a *gene* is mutated. Although the mutation probability is generally much smaller than the crossover probability, the number of chromosomes changed by mutation and crossover are of the same order.

F.2 Handling constraints

The previous description of the GA is applicable to optimisation problems where each design variables is restricted to values within a given interval. However, in most real-life problems the design variables must satisfy some additional constraints. For example, when optimising the placement of PZT patches on a plate structure (see Section 7.5), there is the physical constraint that the patches may not overlap.

There are many ways to incorporate constraint handling in GAs of which a comprehensive overview was presented by Coello Coello [111]. In this work the probably most easy way to handle constraints is applied: *rejection of infeasible individuals* (also called “death penalty” method). It is implemented as follows: if an individual produced by one of the genetic operators is infeasible, i.e. does not satisfy all constraints, then the operation is repeated. In the next step, the “random parameter” (e.g. crossover point for simple crossover or random number r for uniform mutation) is redefined. This is repeated until a feasible solution is found or a maximum number of attempts is exceeded.³

The following issues are of importance for the problem of optimising the locations of piezoelectric patches:

- A relatively small portion of the plate area is covered with patches, i.e. the feasible search space constitutes a large portion of the whole search space.
- Evaluating the overlap constraint is computationally inexpensive (compared to an evaluation of the object function).
- The overlap constraint is not given in algebraic form; the algorithm returns whether or not an individual is feasible, but gives no estimation of the degree of infeasibility.
- It is not possible to evaluate an infeasible individual (that is, the FEM model cannot be defined).

As shown in Chapter 7 of the book by Michalewicz [102], the death penalty method must not be applied if the feasible search space is small compared to the whole search space. However, if this is not the case, a GA using the death penalty method produces results nearly equal to those found with GAs based on more advanced constraint handling techniques.

³In some cases this approach would result in an infinite loop if the number of iterations is not limited by a maximum.

Bibliography

- [1] D.A. Bies and C.H. Hansen. *Engineering Noise Control*. E & FN Spon, 2nd edition, 1996. ISBN 0-419-20430-X.
- [2] F.J.M. van der Eerden. *Noise Reduction with Coupled Prismatic Tubes*. PhD thesis, University of Twente, The Netherlands, 2000. ISBN 90-365-1521-1.
- [3] T.G.H. Basten. *Noise Reduction by Viscothermal Acousto-Elastic Interaction in Double Wall Panels*. PhD thesis, University of Twente, The Netherlands, 2001. ISBN 90-365-1597-1.
- [4] A. Preumont. *Vibration control of Active Structures*. Kluwer Academic Publishers, 1999. ISBN 0-7923-4392-1.
- [5] P. Lueg. Process of silencing sound oscillations. US Patent No. 2043416, 1936.
- [6] P.A. Nelson and S.J. Elliott. *Active Control of Sound*. Academic Press, 1992. ISBN 0-12-515425-9.
- [7] C.R. Fuller. Analysis of active control of sound radiation from elastic plates by force inputs. In *Proceedings of Inter-noise 88*, volume 2, pages 1061–1064, Avignon, France, 1988.
- [8] C.R. Fuller. Active control of sound transmission/radiation from elastic plates by vibration inputs: I. Analysis. *Journal of Sound and Vibration*, 136(1):1–15, 1990.
- [9] C.R. Fuller, C.H. Hansen, and S.D. Snyder. Active control of sound radiation from a vibrating rectangular panel by sound sources and vibration inputs: an experimental comparison. *Journal of Sound and Vibration*, 145(2):195–215, 1991.
- [10] C.R. Fuller, S.J. Elliott, and P.A. Nelson. *Active Control of Vibration*. Academic Press, 1996. ISBN 0-12-269440-6.
- [11] C.R. Fuller, C.H. Hansen, and S.D. Snyder. Experiments on active control of sound radiation from a panel using a piezoceramic actuator. *Journal of Sound and Vibration*, 150(2):179–190, 1991.

- [12] B.-T. Wang, C.R. Fuller, and E.K. Dimitriadis. Active control of noise transmission through rectangular plates using multiple piezoelectric or point force actuators. *Journal of the Acoustical Society of America*, 90(5):2820–2830, 1991.
- [13] J.P. Maillard and C.R. Fuller. Comparison of two structural sensing approaches for active structural acoustic control. *Journal of the Acoustical Society of America*, 103(1):396–400, 1998.
- [14] T.C. Sors and S.J. Elliott. Volume velocity estimation with accelerometer arrays for active structural acoustic control. *Journal of Sound and Vibration*, 258(5):876–883, 2002.
- [15] E.F. Sheta, R.W. Moses, L.J. Huttshell, and V.J. Harrand. An active smart material control system for F/A-18 buffet alleviation. In *Proceedings of IFASD 2003 - International Forum on Aeroelasticity and Structural Dynamics*, Amsterdam, The Netherlands, 2003.
- [16] S.C. Galea, T.G. Ryall, D.A. Henderson, R.W. Moses, E.V. White, and D.G. Zimcik. Next generation active buffet suppression system. In *AIAA/ICAS International Air & Space Symposium and Exposition*, Dayton, USA, 2003.
- [17] L.B. Scherer, C.A. Martin, M. West, J.P. Florance, C.D. Wieseman, A.W. Burner, and G.A. Fleming. DARPA/AFRL/NASA smart wing second wind tunnel test results. In *Proceedings of SPIE's 6th Annual International Symposium on Smart Structures and Materials*, Newport Beach, USA, 1999.
- [18] W.K. Wilkie, M.L. Wilbur, P.H. Mirick, C.E.S. Cesnik, and S. Shin. Aeroelastic analysis of the NASA/Army/MIT active twist rotor. In *Proceedings of the American Helicopter Society 55th Annual Forum and Technology Display*, Montreal, Canada, 1999.
- [19] M.L. Wilbur, W.T. Yeager Jr., W.K. Wilkie, C.E.S. Cesnik, and S. Shin. Hover testing of the NASA/Army/MIT active twist rotor prototype blade. In *Proceedings of the American Helicopter Society 56th Annual Forum and Technology Display*, Virginia Beach, USA, 2000.
- [20] A.P.F. Bernhard and I. Chopra. Analysis of a bending-torsion coupled actuator for a smart rotor with active blade tips. *Smart Materials and Structures*, 10:35–52, 2001.
- [21] B.S. Cazzolato. *Sensing systems for active control of sound transmission into cavities*. PhD thesis, University of Adelaide, Australia, 1999.
- [22] J. Holterman. *Vibration Control of High-Precision Machines with Active Structural Elements*. PhD thesis, University of Twente, The Netherlands, 2002. ISBN 90-365-1793-1.
- [23] A.A. Bent. *Active Fiber Composites for Structural Actuation*. PhD thesis, Massachusetts Institute of Technology, USA, 1997.

- [24] C.K. Lee. Theory of laminated piezoelectric plates for the design of distributed sensors/actuators. Part I: Governing equations and reciprocal relationships. *Journal of the Acoustical Society of America*, 87(3):1144–1158, 1990.
- [25] C.K. Lee, W.W. Chiang, and T.C. O’Sullivan. Piezoelectric modal sensor/actuator pairs for critical active damping vibration control. *Journal of the Acoustical Society of America*, 90(1):374–384, 1991.
- [26] K. Henriouille and P. Sas. Experimental validation of a collocated PVDF volume velocity sensor/actuator pair. *Journal of Sound and Vibration*, 265(3):489–506, 2003.
- [27] H.F. Tiersten. *Linear Piezoelectric Plate Vibrations*. Plenum Press, 1969.
- [28] W.G. Cady. *Piezoelectricity*. Dover Publications, 1964.
- [29] B. Jaffe, W.R. Cook Jr., and H. Jaffe. *Piezoelectric Ceramics*. Academic Press, 1971. ISBN 0-12-379550-8.
- [30] T. Bailey and J.E. Hubbard Jr. Distributed piezoelectric-polymer active vibration control of a cantilever beam. *Journal of Guidance*, 8(5):605–611, 1985.
- [31] E.F. Crawley and J. de Luis. Use of piezoelectric actuators as elements of intelligent structures. *AIAA Journal*, 25(10):1373–1385, 1987.
- [32] E.K. Dimitriadis, C.R. Fuller, and C.A. Rogers. Piezoelectric actuators for distributed vibration excitation of thin plates. *Journal of Vibration and Acoustics*, 113(1):100–107, 1991.
- [33] S.J. Kim and J.D. Jones. Optimal design of piezoactuators for active noise and vibration control. *AIAA Journal*, 29(12):2047–2053, 1991.
- [34] G.P. Gibbs and C.R. Fuller. Excitation of thin beams using asymmetric piezoelectric actuators. *Journal of the Acoustical Society of America*, 92(6):3221–3227, 1992.
- [35] F. Charette, C. Guigou, A. Berry, and G. Plantier. Asymmetric actuation and sensing of a beam using piezoelectric materials. *Journal of the Acoustical Society of America*, 96(4):2272–2283, 1994.
- [36] C. Park, C. Walz, and I. Chopra. Bending and torsion models of beams with induced-strain actuators. *Smart Materials and Structures*, 5:98–113, 1996.
- [37] C. Park and I. Chopra. Modeling piezoceramic actuation of beams in torsion. *AIAA Journal*, 34(12):2582–2589, 1996.
- [38] E.F. Crawley and E.H. Anderson. Detailed models of piezoceramic actuation of beams. *Journal of Intelligent Material Systems and Structures*, 1(1):4–25, 1990.
- [39] J. Pan, C.H. Hansen, and S.D. Snyder. A study of the response of a simply supported beam to excitation by a piezoelectric actuator. *Journal of Intelligent Material Systems and Structures*, 3:3–16, 1992.

- [40] J.F. Rivory, C.H. Hansen, and J. Pan. Further studies of the dynamic response of a simply supported beam excited by a pair of out-of-phase piezoelectric actuators. *Journal of Intelligent Material Systems and Structures*, 5:654–664, 1994.
- [41] S.K. Ha and Y.H. Kim. Analysis of a piezoelectric multimorph in extensional and flexural motions. *Journal of Sound and Vibration*, 253(5):1001–1014, 2002.
- [42] Y.-S. Lee, P. Gardonio, and S.J. Elliott. Coupling analysis of a matched piezoelectric sensor and actuator pair for vibration control of a smart beam. *Journal of the Acoustical Society of America*, 111(6):2715–2726, 2002.
- [43] A.N. Daniai, J.F. Doyle, and S.A. Rizzi. Dynamic analysis of folded plate structures. *Journal of Vibration and Acoustics*, 118(4):591–598, 1996.
- [44] U. Lee. Vibration analysis of one-dimensional structures using the spectral transfer matrix method. *Engineering Structures*, 22:681–690, 2000.
- [45] D.R. Mahapatra, S. Gopalakrishnan, and T.S. Sankar. Spectral-element-based solutions for wave propagation analysis of multiply connected unsymmetric laminated composite beams. *Journal of Sound and Vibration*, 237(5):819–836, 2000.
- [46] S. Gopalakrishnan and J.F. Doyle. Wave propagation in connected wave guides of varying cross-section. *Journal of Sound and Vibration*, 175(3):347–363, 1994.
- [47] F.J. Fahy. *Sound and Structural Vibration*. Academic Press, 1985. ISBN 0-12-247670-0.
- [48] A. Benjeddou. Advances in piezoelectric finite element modelling of adaptive structural elements: A survey. *Computers and Structures*, 76:347–363, 2000.
- [49] Computational Applications and System Integration Inc, 2004 S. Wright Street, Urbana, IL 61821, USA. *Ansys User Manual*, 5.7 edition, 2000.
- [50] R.L. Taylor, P.J. Beresford, and E.L. Wilson. A non-conforming element for stress analysis. *International Journal for Numerical Methods in Engineering*, 10:1211–1219, 1976.
- [51] G.F. Franklin, J.D. Powell, and A. Emami-Naeini. *Feedback Control of Dynamic Systems*. Addison-Wesley, 3rd edition, 1994. ISBN 0-201-53487-8.
- [52] F.J. Fahy. *Foundations of Engineering Acoustics*. Academic Press, 2001. ISBN 0-12-247665-4.
- [53] M.N. Currey and K.A. Cunefare. The radiation modes of baffled finite plates. *Journal of the Acoustical Society of America*, 98(3):1570–1580, 1995.
- [54] G.V. Borgiotti. The power radiated by a vibrating body in an acoustic fluid and its determination from boundary measurements. *Journal of the Acoustical Society of America*, 88(4):1884–1893, 1990.
- [55] K.A. Cunefare. The minimum multimodal radiation efficiency of baffled finite beams. *Journal of the Acoustical Society of America*, 90(5):2521–2529, 1991.

- [56] K. Naghshineh, G.H. Koopmann, and A.D. Belegundu. Material tailoring of structures to achieve a minimum radiation condition. *Journal of the Acoustical Society of America*, 92(2):841–855, 1992.
- [57] S.J. Elliott and M.E. Johnson. Radiation modes and the active control of sound power. *Journal of the Acoustical Society of America*, 94(4):2194–2204, 1993.
- [58] A.P. Berkhoff. Sensor scheme design for active structural acoustic control. *Journal of the Acoustical Society of America*, 108(3):1037–1045, 2000.
- [59] K.A. Cunefare and M.N. Currey. On the exterior acoustic radiation modes of structures. *Journal of the Acoustical Society of America*, 96(4):2302–2312, 1994.
- [60] K.A. Cunefare, M.N. Currey, M.E. Johnson, and S.J. Elliott. The radiation efficiency grouping of free-space acoustic radiation modes. *Journal of the Acoustical Society of America*, 109(1):203–215, 2001.
- [61] W.T. Baumann, W.R. Saunders, and H.H. Robertshaw. Active suppression of acoustic radiation from impulsively excited structures. *Journal of the Acoustical Society of America*, 90(6):3202–3208, 1991.
- [62] G.P. Gibbs, R.L. Clark, D.E. Cox, and J.S. Vipperman. Radiation modal expansion: Application to active structural acoustic control. *Journal of the Acoustical Society of America*, 107(1):332–339, 2000.
- [63] F.J. Fahy. *Sound Intensity*. E & FN Spon, 2nd edition, 1995.
- [64] J.W. Parkins, S.D. Sommerfeldt, and J. Tichy. Error analysis of a practical energy density sensor. *Journal of the Acoustical Society of America*, 108(1):211–222, 2000.
- [65] B.S. Cazzolato and C.H. Hansen. Errors in the measurement of acoustic energy density in one-dimensional sound fields. *Journal of Sound and Vibration*, 236(5):801–831, 2000.
- [66] F. Jacobsen. A note on finite difference estimation of acoustic particle velocity. *Journal of Sound and Vibration*, 256(5):849–859, 2002.
- [67] S.M. Kirkup. *The Boundary Element Method in Acoustics*. Integrated Sound Software, 1998.
- [68] R. Visser. Experimental validation of a boundary element solver for exterior acoustic radiation problems. In *Proceedings of the Tenth International Congress on Sound and Vibration*, Stockholm, Sweden, 2003.
- [69] R.A. Burdisso and C.R. Fuller. Dynamic behavior of structural acoustic systems in feedforward control of sound radiation. *Journal of the Acoustical Society of America*, 92(1):277–286, 1992.
- [70] R.A. Burdisso and C.R. Fuller. Theory of feedforward controlled system eigenproperties. *Journal of Sound and Vibration*, 153(3):437–451, 1992.

- [71] M.E. Johnson and S.J. Elliott. Active control of sound radiation using volume velocity cancellation. *Journal of the Acoustical Society of America*, 98(4):2174–2186, 1995.
- [72] A. Francois, P. De Man, and A. Preumont. Piezoelectric array sensing of volume displacement: A hardware demonstration. *Journal of Sound and Vibration*, 244(3):395–405, 2001.
- [73] S.M. Kuo and D.R. Morgan. *Active Noise Control Systems*. John Wiley & Sons, 1996. ISBN 0-471-13424-4.
- [74] J.S. Vipperman and R.L. Clark. Implementation of an adaptive piezoelectric sensor/actuator. *AIAA Journal*, 34(10):2102–2109, 1996.
- [75] S.J. Elliott, P. Gardonio, T.C. Sors, and M.J. Brennan. Active vibroacoustic control with multiple local feedback loops. *Journal of the Acoustical Society of America*, 111(2):908–915, 2002.
- [76] P. Gardonio, Y.-S. Lee, S.J. Elliott, and S. Debost. Analysis and measurement of a matched volume velocity sensor and uniform force actuator for active structural acoustic control. *Journal of the Acoustical Society of America*, 110(6):3025–3031, 2001.
- [77] B. Petitjean, I. Legrain, F. Simon, and S. Pauzin. Active control experiments for acoustic radiation reduction of a sandwich panel: feedback and feedforward investigations. *Journal of Sound and Vibration*, 252(1):19–36, 2002.
- [78] G. Clark Smith and R.L. Clark. The influence of frequency-shaped cost functionals on the structural acoustic performance of static, output feedback controllers. *Journal of the Acoustical Society of America*, 104(4):2236–2244, 1998.
- [79] J.S. Vipperman and R.L. Clark. Multivariable feedback active structural acoustic control using adaptive piezoelectric sensor/actuators. *Journal of the Acoustical Society of America*, 105(1):219–225, 1999.
- [80] P. Gardonio, E. Bianchi, and S.J. Elliott. Smart panel with multiple decentralised units for the control of sound transmission. Part I: Theoretical predictions. In *Proceedings of Active 2002*, pages 471–486, Southampton, UK, 2002.
- [81] P. Gardonio, E. Bianchi, and S.J. Elliott. Smart panel with multiple decentralised units for the control of sound transmission. Part II: Design of the decentralised control units. In *Proceedings of Active 2002*, pages 487–498, Southampton, UK, 2002.
- [82] E. Bianchi, P. Gardonio, and S.J. Elliott. Smart panel with multiple decentralised units for the control of sound transmission. Part III: Control system implementation. In *Proceedings of Active 2002*, pages 499–510, Southampton, UK, 2002.
- [83] M.Z. Ren, K. Seto, and F. Doi. Feedback structure-borne sound control of a flexible plate with an electromagnetic actuator: the phase lag problem. *Journal of Sound and Vibration*, 205(1):57–80, 1997.

- [84] S. Griffin, C.H. Hansen, and B.H. Cazzolato. Feedback control of structurally radiated sound into enclosed spaces using structural sensing. *Journal of the Acoustical Society of America*, 106(5):2621–2628, 1999.
- [85] B. Bingham, M.J. Atalla, and N.W. Hagood. Comparison of structural-acoustic control designs on an active composite panel. *Journal of Sound and Vibration*, 244(5):761–778, 2001.
- [86] Y.-S. Lee, P. Gardonio, and S.J. Elliott. Volume velocity vibration control of a smart panel using a uniform force actuator and an accelerometer array. *Smart Materials and Structures*, 11(6):863–873, 2002.
- [87] R.L. Clark and D.E. Cox. Multi-variable structural acoustic control with static compensation. *Journal of the Acoustical Society of America*, 102(5):2747–2756, 1997.
- [88] S.L. Padula and R.K. Kincaid. Optimization strategies for sensor and actuator placement. Technical Report NASA/TM-1999-209126, NASA Langley Research Center, Hampton, Virginia, USA, 1999.
- [89] M.I. Frecker. Recent advances in optimization of smart structures and actuators. *Journal of Intelligent Material Systems and Structures*, 2002. Accepted for publication.
- [90] C.J. Damaren. Optimal location of collocated piezo-actuator/sensor combinations in spacecraft box structures. *Smart Materials and Structures*, 12(3):494–499, 2003.
- [91] P. De Fonseca, P. Sas, and H. Van Brussel. A comparative study of methods for optimising sensor and actuator locations in active control applications. *Journal of Sound and Vibration*, 221(4):651–679, 1999.
- [92] R.L. Clark and C.R. Fuller. Optimal placement of piezoelectric actuators and polyvinylidene fluoride error sensors in active structural acoustic control approaches. *Journal of the Acoustical Society of America*, 92(3):1521–1533, 1992.
- [93] B.-T. Wang, R.A. Burdisso, and C.R. Fuller. Optimal placement of piezoelectric actuators for active structural acoustic control. *Journal of Intelligent Material Systems and Structures*, 5(1):67–77, 1994.
- [94] B.-T. Wang. Optimal placement of microphones and piezoelectric transducer actuators for far-field sound radiation control. *Journal of the Acoustical Society of America*, 99(5):2975–2984, 1996.
- [95] J. Kim, V.V. Varadan, and V.K. Varadan. Finite element-optimization methods for the active control of radiated sound from a plate structure. *Smart Materials and Structures*, 4(4):318–326, 1995.
- [96] V.V. Varadan, J. Kim, and V.K. Varadan. Optimal placement of piezoelectric actuators for active noise control. *AIAA Journal*, 35(3):526–533, 1997.

- [97] Y.K. Kang, H.C. Park, W. Hwang, and K.S. Han. Optimum placement of piezoelectric sensor/actuator for vibration control of laminated beams. *AIAA Journal*, 34(9):1921–1926, 1996.
- [98] P. De Man, A. Francois, and A. Preumont. Robust feedback control of a baffled plate via open-loop optimization. *ASME Journal of Vibration and Acoustics*, 124:154–157, 2002.
- [99] X. Li, C.H. Hansen, and X. Qiu. Optimal sizes and locations of piezoelectric actuators for curved panel sound sources. *International Journal of Acoustics and Vibrations*, 2(4):161–166, 1996.
- [100] K.H. Baek and S.J. Elliott. Natural algorithms for choosing source locations in active control systems. *Journal of Sound and Vibration*, 186(2):245–267, 1995.
- [101] P. De Boe, D. Simon, and J.-C. Golinval. Strategies for distributed piezoelectric actuator/sensor placement by noise effect minimisation and modal controllability/observability. In *Proceedings of ISMA 25*, volume 1, pages 53–60, Leuven, Belgium, 2000.
- [102] Z. Michalewicz. *Genetic Algorithms + Data Structures = Evolution Programs*. Springer-Verlag, 3rd edition, 1994. ISBN 3-540-60676-9.
- [103] D.E. Goldberg. *Genetic Algorithms in Search, Optimization and Machine Learning*. Addison-Wesley, 1989. ISBN 0-201-15767-5.
- [104] M.H.H. Oude Nijhuis and A. de Boer. Optimization strategy for actuator and sensor placement in active structural acoustic control. In *Proceedings of Active 2002*, Southampton, UK, 2002.
- [105] J.S. Vipperman and R.L. Clark. Implications of using colocated strain-based transducers for output active structural acoustic control. *Journal of the Acoustical Society of America*, 106(3):1392–1399, 1999.
- [106] H.S. Tzou and R. Ye. Pyroelectric and thermal strain effects of piezoelectric (PVDF and PZT) devices. *Mechanical Systems and Signal Processing*, 10(4):459–469, 1996.
- [107] L. Meirovitch. *Elements of Vibration Analysis*. McGraw-Hill Book Company, 2nd edition, 1986. ISBN 0-07-100271-5.
- [108] W. Dehandschutter, K. Henriouille, J. Swevers, and P. Sas. State space feedback control of sound radiation using structural sensors and structural control inputs. In *Proceedings of Active 97*, pages 979–993, Budapest, Hungary, 1997.
- [109] G.V. Borgiotti and K.E. Jones. Frequency independence property of radiation spatial filters. *Journal of the Acoustical Society of America*, 96(6):3516–3524, 1994.
- [110] A.P. Berkhoff. Broadband radiation modes: estimation and active control. *Journal of the Acoustical Society of America*, 111(3):1295–1305, 2002.

- [111] C.A. Coello Coello. Theoretical and numerical constraint-handling techniques used with evolutionary algorithms: A survey of the state of the art. *Computer Methods in Applied Mechanics and Engineering*, 191:1245–1287, 2002.

Nawoord

Dit was het dus. Ruim drie jaar lang met veel plezier onderzoek doen, en vervolgens een jaar lang ploeteren om het proefschrift te voltooien. Dat alleen mijn naam op de kaft van dit boekje staat, doet misschien vermoeden dat de totstandkoming ervan geheel mijn werk is. Niets is minder waar. Meerdere personen hebben direct of indirect bijgedragen aan dit proefschrift.

Ten eerste is dat André de Boer, voor wie mijn promotie zijn vuurdoop als promotor is. Ik bedank hem voor zijn begeleiding, steun en hulp bij de afronding van dit proefschrift. Tevens bedank ik Henk Tijdeman, onder andere voor het feit dat hij me na mijn afstuderen wist te strikken voor een promotieplaats.

De overige “mannen van de Dynamica”, Ruud Spiering, Peter van der Hoogt, Bert Wolbert en Ysbrand Wijnant bedank ik voor de enorme bijdrage die zij hebben geleverd aan dit boekje.

Zonder de hulp van Debbie Vrieze (Zimmerman van Woesik), Tanja van Scherpenzeel en Jacqueline Emmerich zou de promotie waarschijnlijk pas in 2004 plaatsvinden.

Alle overige collega's van de vakgroep Technische Mechanica (en Kunststoffen) bedank ik voor de prima sfeer in de Noord-vleugel van het WB-gebouw.

De (ex-)promovendi van de leerstoel, Frits van der Eerden, Tom Basten, Hedzer Tillema, René Visser, Clemens Beijers, Rob Huls, Marieke Hannink en Ekke Oosterhuis bedank ik voor de gezellige tijd, alle hulp, de correcties van het proefschrift, maar ook voor de getoonde interesse in de klootschietsport!

Ook de studenten, die met hun afstudeeropdracht een steentje hebben bijgedragen aan dit proefschrift, Ivo Reinink, Rob Huls, Ivar Voetelink, Toby de Kort en Wouter Sonderen, wil ik bij deze bedanken.

Tenslotte bedank ik mijn familie en vrienden voor van alles en nog wat. Vanaf nu heb ik weer meer tijd om jullie te helpen, of om aan de bar te staan!

Allemaal onmeunig bedankt!

Marco

